HAL open science

Magnetism in spin-1 Bose-Einstein condensates with antiferromagnetic interactions

Vincent Corre

To cite this version:

Vincent Corre. Magnetism in spin-1 Bose-Einstein condensates with antiferromagnetic interactions. Physics [physics]. Ecole Normale Supérieure de Paris, 2014. English. NNT : . tel-01117109v1

HAL Id: tel-01117109

https://theses.hal.science/tel-01117109v1

Submitted on 16 Feb 2015 (v1), last revised 18 Apr 2016 (v2)

HAL is a multi-disciplinary open access archive for the deposit and dissemination of scientific research documents, whether they are published or not. The documents may come from teaching and research institutions in France or abroad, or from public or private research centers.

L'archive ouverte pluridisciplinaire **HAL**, est destinée au dépôt et à la diffusion de documents scientifiques de niveau recherche, publiés ou non, émanant des établissements d'enseignement et de recherche français ou étrangers, des laboratoires publics ou privés.

Laboratoire Kastler Brossel

Ecole Normale Supérieure
Collège de France
UPMC
CNRS

THÈSE DE DOCTORAT DE L'ECOLE NORMALE SUPERIEURE

Spécialité : Physique Quantique

présentée par

Vincent CORRE

pour obtenir le grade de

DOCTEUR de l'ECOLE NORMALE SUPERIEURE

Magnetism in spin-1 Bose-Einstein condensates with antiferromagnetic interactions

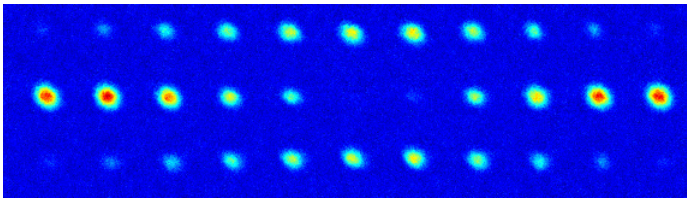

Soutenue le 15 décembre 2014
devant le jury composé de :

M.	Luis SANTOS	Rapporteur
M.	Antoine BROWAEYS	Rapporteur
M.	Jean-Claude GARREAU	Examinateur
M.	Jean-Noël FUCHS	Examinateur
M.	Jean DALIBARD	Directeur de thèse
M.	Fabrice GERBIER	Co-directeur de thèse

Contents

Remerciements **7**

Introduction **11**

1 Spin-1 Bose-Einstein condensates **17**
1.1 Bose-Einstein condensates with an internal degree of freedom 17
1.2 Bose-Einstein condensation in scalar gases 18
1.2.1 Bose-Einstein transition in an ideal gas 18
1.2.2 Effect of the interactions: ground-state 19
1.2.3 Effect of the interactions: excited states 21
1.3 Spin-1 Bose-Einstein condensates: spin Hamiltonian 23
1.3.1 Single spin-1 particle 23
1.3.2 Two-body scattering of two spin-1 particles 25
1.3.3 Many-body Hamiltonian 27
1.3.4 Effect of applied magnetic fields 29
1.4 Mean-field theory of spin-1 condensates 30
1.4.1 Single-mode approximation 30
1.4.2 Mean-field approximation 31
1.4.3 Ground-state in the Single-mode approximation 32
1.4.4 Validity of the single-mode approximation 35
1.4.5 Excitations in a spinor condensate 40
1.5 Conclusion 43

2 Production, manipulation and detection of a spin-1 Bose-Einstein condensate of Sodium **45**
2.1 Experimental methods 45
2.1.1 The experimental chamber and the atomic source 46
2.1.2 Magneto-Optical Trap 46
2.1.3 Resonant laser 48
2.1.4 Loading in a Crossed Dipole Trap and two-step evaporation 48
2.1.5 Condensation in the dimple trap 54
2.2 Diagnostic of the spinor gas 58
2.2.1 Application of magnetic fields 58
2.2.2 Stern Gerlach separation 59
2.2.3 Imaging set-up 63
2.2.4 Calibration of the scattering cross-sections 64
2.2.5 Imaging noise 67
2.3 Preparation of a controlled magnetization 70
2.3.1 Magnetic fields control 71

2.3.2 Spin-mixing . . . 73
2.3.3 Spin distillation . . . 74
2.4 Conclusion . . . 77

3 Mean-field study of an antiferromagnetic spinor condensate 79
3.1 Nematic order in spinor condensates . . . 80
3.1.1 Definition of the nematic order parameter . . . 80
3.1.2 Application to mean-field states . . . 83
3.1.3 Nematic order of a mean-field ground-state . . . 85
3.2 Experimental study of the phase diagram . . . 88
3.2.1 Experimental sequence . . . 88
3.2.2 Results . . . 89
3.3 Detection of spin-nematic order . . . 91
3.3.1 Rotation of the spinor wavefunction . . . 92
3.3.2 Experimental implementation of three-level Rabi oscillations . . . 95
3.3.3 Evidence for phase-locking . . . 97
3.4 Conclusion . . . 101

4 Spin fragmentation in a spin-1 Bose gas 103
4.1 Fragmentation of a spinor condensate at zero field . . . 103
4.1.1 Fragmented Bose-Einstein condensates . . . 103
4.1.2 Spin fragmentation in an antiferromagnetic spinor BEC at $T = 0$ . . . 105
4.1.3 Spin fragmentation at finite temperatures . . . 107
4.2 The broken-symmetry picture . . . 109
4.2.1 Broken-symmetry picture at $T = 0$ . . . 109
4.2.2 Broken-symmetry approach at finite temperatures . . . 112
4.2.3 $SU(3)$ coherent states . . . 112
4.2.4 Broken symmetry description of a spin-1 gas with constrained magnetization . . . 114
4.3 Connection to spontaneous symmetry breaking . . . 121
4.3.1 Spontaneous symmetry breaking in the thermodynamic limit . . . 122
4.4 Conclusion . . . 125

5 Observation of spin fragmentation and spin thermometry 127
5.1 Observation of spin fluctuations . . . 128
5.1.1 Experimental sequence . . . 128
5.1.2 Data acquisition . . . 129
5.1.3 Measured moments of n_0 . . . 130
5.2 Statistical analysis of the distributions of n_0 and m_z . . . 133
5.2.1 Model and method . . . 134
5.3 Spin temperature and condensed fraction during the evaporation . . . 139
5.3.1 Temperatures at fixed trap depth . . . 144
5.4 Two spinor fluids isolated from each other . . . 145
5.4.1 Comparison of spin and kinetic temperatures . . . 145
5.4.2 Large q: the condensate and the thermal gas are coupled . . . 146
5.4.3 Low q: condensate at equilibrium but decoupled from the thermal gas 147
5.5 Conclusion . . . 148

Conclusion and perspectives 151

A Numerical methods for the spinor Gross-Pitaevskii equations 155
A.1 Gross-Pitaevskii equations in imaginary time 155
A.1.1 The imaginary time propagation method 155
A.1.2 Dimensionless coupled Gross-Pitaevskii equations 156
A.2 Propagation of the finite differences scheme 157
A.3 Numerical implementation 159

B Geometrical representation of a spin-1 state 161
B.1 Bloch-Rabi representation 161
B.2 Application to the mean-field ground state 162

C Three-level Rabi oscillation 165

D Generalized coherent states 167
D.1 Construction of generalized coherent states 167
D.2 Spin coherent states 168
D.3 $SU(3)$ coherent states 169
D.4 Diagonal representation of few-body operators in the $SU(3)$ coherent states basis 170

E Spin fragmentation of Bose-Einstein condensates with antiferromagnetic interactions 171

Bibliography 191

Remerciements

Je tiens ici à remercier les personnes qui m'ont accompagné et soutenu durant ces trois années, scientifiquement ou humainement, les deux se mêlant souvent. Elles ont une part évidente dans cette thèse et dans la personne que je suis aujourd'hui.
En premier lieu, je voudrais remercier mon directeur de thèse, Jean Dalibard. Ce sont ses grandes qualités d'enseignant, l'enthousiasme et l'esthétique de ses cours à l'Ecole Polytechnique qui d'abord m'ont amené vers la physique, à laquelle je ne me destinais pas jusque là. En m'accueillant ensuite en stage de recherche puis un an plus tard en thèse dans son groupe, il m'a permis de rejoindre un environnement de travail exceptionnel. Pendant ces années j'ai pu profiter de la grande valeur scientifique de son jugement et de ses conseils, mais aussi de sa gentillesse, de sa patience et de son indéfectible bonne humeur. Ce mélange de hauteur de vue sur les problèmes physiques et de proximité avec ces étudiants a régulièrement permis de surmonter sans douleur les caprices de l'expérience (ou les erreurs de l'expérimentateur).
Je souhaite également remercier chaleureusement Fabrice Gerbier, qui dirige quotidiennement l'expérience Sodium, et à qui je dois à peu près tout ce que je comprends aujourd'hui de la physique des atomes froids. Au milieu de son travail, Fabrice est toujours prêt à répondre à une question, à se plonger dans un programme mal écrit, et n'a jamais hésité à m'expliquer patiemment (et presque chaque fois, à me ré-expliquer, un peu plus patiemment encore) différents points de théorie. D'autre part, le bon fonctionnement de la manip Sodium tient pour beaucoup aux précieux conseils de Fabrice, à son implication et à son étonnante mémoire de l'histoire de l'expérience. Je ne compte plus les fois où face à une incongruité expérimentale non identifiée, Fabrice a immédiatement cité un précédent survenu il y a deux, trois, quatre ans, et prescrit un remède, la plupart du temps efficace. Enfin, je tiens à souligner les qualités humaines de Fabrice, qui parfois nécessitent de le côtoyer quotidiennement pour être pleinement appréciées. D'abord, Fabrice perd rarement une occasion d'exercer son humour piquant, souvent associé au temps de la francophonie à cette perle idiomatique (bordelaise?) : le "gonze", qui aura suscité quantité de rires en S6. Par ailleurs, sa gestion humaine de l'équipe s'est révélée avec les années efficace et juste. Et finalement, je tiens à le remercier pour m'avoir guidé vers "l'après-thèse", ce qui n'a été facile pour aucun de ceux qui ont essayé.
J'ai réalisé ma thèse au sein du laboratoire Kastler Brossel sur deux sites, l'Ecole Normale Supérieure, rue Lhomond, et l'institut de physique du Collège de France. Je tiens à remercier les directeurs de ces institutions - Paul Indelicato puis Antoine Heidmann, Serge Haroche - de m'y avoir accueilli, ainsi que les services technique et administratif sans qui ce travail de recherche n'aurait pu voir le jour.
Je remercie Luis Santos, Antoine Browaeys, Jean-Claude Garreau et Jean-Noël Fuchs d'avoir accepté d'examiner mon travail de thèse et d'avoir fait le voyage jusqu'au Collège de France pour assister à la soutenance.
Je remercie aussi toutes les personnes que j'ai côtoyées sur la manip Sodium durant ces

trois années. David et Luigi d'abord, qui m'ont initié au fonctionnement de l'expérience et m'ont appris les premières techniques expérimentales. Leur bonne humeur et leur complicité a marqué ma première année de thèse. Je remercie Lingxuan pour son travail de programmation des fonctions de fit (et leur nomenclature si poétique). Je voudrais remercier très particulièrement Tilman et Camille qui m'ont accompagné ces deux dernières années dans les moments joyeux comme dans ceux plus difficiles. Travailler au labo avec eux a été un réel plaisir. Ma compréhension de la physique a beaucoup profité de nos discussions et je remercie en particuliers Tilman pour ces moments de réflexion à deux où progressivement un problème s'éclairait (ou pas). Un grand merci aussi à lui pour son aide durant la semaine précédant ma soutenance. Tilman s'est volontairement infligé six répétitions de ma présentation, qui doit énormément à ces conseils et remarques. Je suis reconnaissant à Camille de la saine émulation qu'il a su entretenir quant à l'heure d'arrivée au labo. La réputation de l'équipe Sodium était déjà acquise, son avenir est désormais assuré. Je le remercie également et avant tout pour son soutien précieux hors du labo dans les moments un peu pénibles de ma dernière année de thèse. Les longues soirées improvisées à deux autour de x bouteilles m'ont apporté un peu de courage et de recul, et certainement pas mal d'heures de sommeil supplémentaires. Je les remercie surtout tous deux de la joyeuse ambiance qu'ils ont su instaurer en S6 puis au Collège, entre débats passionnés sur la meilleure boisson houblonnée, sur la valeur calorique d'un sandwich libanais ou sur nos goûts musicaux respectifs (plus rarement sur la position d'une lentille ou sur l'intérêt d'une mesure), et blagues plus ou moins fines et répétitives. Merci à tous les deux, j'espère que notre amitié perdurera, et le plus activement possible. Notre expérience a récemment accueilli en thèse le jeune Andrea qui s'est distingué par sa rapidité à adopter les habitudes de ses prédécesseurs. Je lui souhaite bonne chance pour la suite de sa thèse.

Je souhaite aussi remercier les membres des autres équipes du groupe "Atomes froids", pour les moments joyeux partagés au labo ou autour de quelques verres. Je remercie notamment les Rubidium qui, malgré leur constante propension à délocker notre laser et leurs tendances à noyer ou brûler S6, se sont révélés de très sympathiques voisins. Je remercie en particuliers Rémi avec qui j'ai partagé de nombreux bons moments, au pub quizz ou à Brewberry, en organisant un Friday bar, lors d'un tour sur sporcles ou d'un déménagement à Zürich. Je le remercie aussi pour son soutien et sa compréhension, et espère que nous continuerons à nous voir régulièrement. Merci aussi aux autres Rubidium, Lauriane et sa gentillesse, Christof et son humour, Laura et sa motivation, plus tard rejoints par Tom, David, Katharina et Jean-Loup. Merci aussi aux occupants de l'autre extrémité du couloir pour leur enthousiasme: Igor, Benno, Andrew, Alexandre, Matthias et Daniel (pour les parties de foot ou de basket), Quentin, Marion, Sébastien, Wilfried, Davide et ses true stories, Leonid, Chayma, Tian, Manel, ... Je remercie particulièrement Lauriane pour avoir partagé cette difficile année de la rédaction et pour tous ses efforts pour nous la rendre meilleure. Outre en escalade j'ai grâce à elle également fait cette année de gros progrès en géographie des vins et des fromages, notions généralement très obscures pour un Breton. Je la remercie pour les moments heureux qu'elle a su construire et pour sa patience entre eux.

Je remercie enfin toutes les personnes extérieures au labo qui m'ont accompagné durant ces trois années. En premier lieu je remercie Boulc'h pour tout ce que nous avons partagé depuis bien plus que trois ans, en Maunoury, à Montrouge ou boulevard Auguste Blanqui, à Paris ou dans notre Finistère, au volant d'une 106 surchauffée, sur des skis ou dans un champs carhaisien. Merci aussi aux 2007 que j'ai pu continuer à voir (même si trop peu souvent): Mathilde pour les séances à Arkose, Janus et Jérémy pour leur bonne humeur,

Tobi pour l'alliance de la culture et de la bière, Boz pour son altitude, Papy Jean pour sa sagesse, Louis, Kippelen, Alexis, Etienne pour ses cheveux, Lambix pour les régates saucisson et sa friteuse, le corse, les judokas plus ou moins gros, les PêCheurs plus ou moins sobres, et tous les autres. Je remercie la peu sérieuse troupe des jeunes Rennais ou assimilés pour leur joie de vivre communicative: Greg, Cécile, Louna, Joss, l'arabe, Marcus, Madec, l'enfant Cherpi, Dupré... Je remercie aussi Laure pour m'avoir supporté et soutenu pendant mes deux premières années de thèse. Je remercie les coureurs du PUC - Thomas, Anthony, Raphaël, Maxime, Céline, Marine, Jardin, Elise, Maïté et les autres - pour toutes ces soirées où j'oubliais tout pour ne plus compter que les tours de piste et les secondes. Merci aussi à mes colocs non déjà cités: Coralie et l'apathique Aristote, Arnaud et ses histoires improbables, Joujou et sa gastronomie. Je remercie enfin mes parents et mes frères et soeurs pour leurs encouragements constants et leur aide. Les colis de crêpes et de pâté Hénaff m'ont permis de surmonter les dernières fatigues de la rédaction. Je remercie en particuliers Pauline qui a largement contribué au succès de mon pot de thèse, et Grégoire pour l'optimisme qu'il a su me transmettre et pour sa complicité. Je leur souhaite bonne chance dans leur thèse respective. Bon courage aussi aux deux futurs médecins et à Bibi.

Introduction

The progress of trapping and cooling techniques of atomic clouds[1] in the last thirty years have paved the way for major developments in atomic physics. At the extremely low temperatures that are now achievable, quantum properties of gaseous matter are dramatically enhanced. One of the important predictions of quantum statistical mechanics states that in a gas at temperature T, particles behave as wave packets with a typical extension given by the thermal de Broglie wavelength $\lambda_T \propto 1/\sqrt{T}$. When the temperature is low enough, this size becomes on the order of the inter-particle spacing and the wave packets overlap. In the case of non or weakly interacting bosonic particles (particles with an integer spin) the interference of their wave packets lead to the emergence of a giant matter wave corresponding to the accumulation of a significant fraction of the atoms in the single-particle state of minimal energy. The macroscopic quantum object thus created is called a Bose-Einstein condensate (BEC), after Einstein who theoretically predicted it in 1925, extending to non-interacting massive particles the work of Bose on photons [1].

Bose-Einstein condensation was experimentally observed in dilute gases for the first time in 1995 [2, 3]. These pioneering realizations[2] triggered a rapid and continuous development of both experimental and theoretical research in this field. BECs indeed represent a remarkable tool to study the quantum world, for they combine simplicity (the underlying theory is well understood and they are almost perfectly isolated from their environment) and versatility (a large numbers of various physical problems can be addressed). In an ultra-cold trapped atomic gas, particles do interact with each other. But due to the low-densities at stake, these interactions are weak, and BECs are very well described by a simple mean-field theory where all the atoms occupy the same quantum state. On the contrary, in superfluid ^{4}He that provided the first experimental evidence of Bose-Einstein condensation (at the temperature considered ^{4}He is a liquid, not a gas) the strong inter-particle interactions led to only 10% of the atoms occupying the same state [4, 5]. Soon after the first realizations of atomic BECs, experiments performed in this mean-field framework explored the coherence properties of ultra-cold gases. Matter wave interference has been observed between two overlapping condensates [6] and in a continuous beam of atoms escaping from a condensate (which represents the atomic analog of a laser) [7]. Evidence for the superfluid behavior of these gases has been provided by the formation of quantized vortices in rotating gases [8]. Note that fermions have also been cooled down to the quantum degenerate regime using similar techniques as for bosons [9, 10].

The consistent interest in ultra-cold gases also originates from the fine control of experimental parameters accessible to experimentalists. Thus, numerous different physical

[1] The importance of these advances has been recognized by the Nobel prize awarded in 1997 to S.Chu, C.Cohen-Tannoudji and W.D.Philips.

[2] W.Ketterle, E.Cornell and C.Wieman have been awarded the 2001 Nobel prize for these first experimental realizations of BEC in dilute gases.

situations can be engineered and investigated. In particular, interactions between particles can be tuned both in sign (attractive or repulsive) and in strength through the use of Feschbach resonances. The geometry of the potential landscape confining the atoms can also be adjusted by the application of chosen optical or magnetic fields. These tools allow one to study many-body quantum phenomena where inter-particles interactions play a key role. Feschbach resonances made it possible for instance to study gases of fermions both in the regime of strong attractive interactions [11] (where weakly bound molecules are formed that undergo a Bose-Einstein condensation) and of weak attractive interactions [12] (where they form a superfluid phase well described by the BCS theory).
The controllability of the trapping potential allowed to realize the textbook example of a box potential [13] or to design systems of lower dimensionality (1D and 2D) by strongly confining them in the remaining dimensions. The Tonks-Girardeau gas has been produced in a one-dimensional gas [14] while in two-dimensional gases a transition from a normal to a superfluid state has been observed (the Berezinski-Kosterlitz-Thouless transition) [15]. Using the interference pattern created by the superimposition of several laser beams, it is also possible to generate a regular lattice potential in which the atoms arrange themselves periodically like in a crystal. Changing the depth of the potential wells it is possible to tune the strength of the interactions, which led to the observation of the phase transition between a superfluid phase and an insulating Mott phase [16, 17]. On the opposite, a disordered potential is obtained by shining a laser beam through a diffusive plate. Imposing the resulting speckle pattern on a BEC allows one to investigate the localization of matter waves predicted in a general framework by Anderson[3] [20, 21].

Another direction that arised in the field of ultra-cold gases is the study of multi-components gases. Mixtures of superfluids have actually been a long-time appealing goal. First experiments involved mixtures of ^{4}He and ^{6}He [22] in 1953, but the superfluid behavior of ^{6}He could not be observed due to its low concentration. The realization of BEC in dilute gases has revived the interest in multi-component superfluids. In the following years, mixtures of BECs in different hyperfine states have been produced [23, 24, 25], followed by the mixture of a BEC mixed with a degenerate Fermi gas [26, 27]. A particular class of multi-component superfluids is composed of superfluids with an internal degree of freedom. Such systems are rare. The first studies considered liquid ^{3}He, where spin 1/2 atoms form weakly bound pairs in the triplet spin manifold [28, 29]. The development of ultra-cold gases physics gave access to a new family of such fluids: spinor Bose-Einstein condensates. In a spinor BEC, the simultaneous trapping of all Zeeman sublevels of an hyperfine state allows atoms in different spin states to coexist in the condensate. This coexistence leads to a spin-dependent interaction that manifests itself for instance in coherent spin oscillations [30, 31, 32] or in parametric spin amplification [33]. Additionally the spin degree of freedom couples to the external magnetic fields. The combination of the spin interaction and the magnetic coupling gives rise to a wealth of phenomena. In the presence of a static magnetic field, spinor condensates become magnetically ordered. Spin textures [34] and metastable spin domains [35] have been observed in spinor condensates immersed in a gradient of magnetic field. Besides, depending on the nature (ferromagnetic or antiferromagnetic) of the spin interaction and on the total spin of the atomic species, Bose-Einstein condensation is expected to result in different possible magnetic phases [36, 37], which places spinor condensates at the interface between atomic and condensed matter physics.

[3]The Anderson localisation has also been observed in systems equivalent to disordered potentials, in particular in a quasi-periodic optical lattice [18] and in the quasi-periodic kicked-rotor system [19].

Spinor condensates have also emerged as a candidates for the realization of non classical states which are particularly interesting for atomic interferometry, metrology and quantum information. The spin-exchange interaction indeed induces strong correlations in the spin degree of freedom of the condensate [38, 39]. Using these spin correlations, squeezed spin states have been observed [40, 41]. These states are characterized by a reduction of the noise in one component of their total spin below the standard quantum limit.

The project of our team at laboratoire Kastler Brossel is to use spinor condensates to produce different kinds of strongly correlated quantum states. One of the long term goal is the realization of Schrödinger cat states, which correspond to the coherent superposition of a condensate in two different spin state [42]. These maximally correlated states have already been realized with a few photons [43] or trapped ions [44], but not yet in a mesoscopic ensemble of particles. Another kind of strongly correlated states that we want to achieve are twin states: Fock states in which half of the atoms occupy one spin state and the other half occupy another spin state. To produce these states we chose to work with Sodium atoms. The spin interaction in spinor condensates of Sodium is indeed advantageous for its nature (it is antiferromagnetic) and for its strength (it is significantly more intense than in Rubidium for instance, which is commonly used in the field of spinor condensates). The project has been initiated in 2006 by Fabrice Gerbier and Jean Dalibard. The construction of the experimental set-up for the production of Sodium BECs has been carried out by E. Mimoun and L. de Sarlo, who designed in particular an all-solid state laser for the cooling of Sodium [45][46]. Then joined D. Jacob and L. Shao, who completed the construction step and contributed to the obtention of the first BECs [47]. This work presents the consecutive studies of spinor condensates of Sodium at thermodynamic equilibrium. We investigate in particular the properties of this equilibrium state under various conditions of magnetic field and of spin distribution.

Outline

- In chapter 1 we give the first elements of the theory of spinor condensates, focusing on the case of spin-1 condensates (which is the case of Sodium). We derive the expression of the spin interaction between two spin-1 particles and explicit the coupling of these particles to an external magnetic field. From these ingredients we deduce the many-body Hamiltonian describing spin-1 BECs, and in particular its component acting in the spin space. We then introduce the important single-mode approximation that decouples the spin and orbital degrees of freedom of the system. We use this approximation to investigate the ground-state within a mean-field approach. We find that spin-1 condensates in their ground-state can exist in two different magnetic phases. In order to check the relevance of this result for our experimental system, the validity of the single-mode approximation is confirmed by a numerical calculation. We finally study the effect of the spin degree of freedom on the elementary excitations of the condensate.

- Chapter 2 details the experimental methods to produce, prepare and probe our spinor condensates. We describe our experimental set-up and the sequence that we perform to bring a cloud of Sodium atoms initially at high temperature to the regime of quantum degeneracy. We explain how we load a magneto-optical trap from a background pressure in our vacuum chamber, and how the atomic cloud is

then successively transferred in two optical dipole traps, where it is cooled down by evaporative cooling. We characterize the evolution of the temperature, of the number of trapped atoms and of the frequencies of our trap during this evaporation. The second part of the chapter is devoted to our imaging procedure. We resort to absorption imaging combined with a Stern-Gerlach experiment to first spatially separate the different spin components. A calibration of the scattering cross-sections of the different spin states is presented, as well as a noise analysis. The last part deals with the control of the internal degree of freedom. The magnetization of a spin-1 condensate (the difference between the populations in the two extremal spin state) is conserved during a Hamiltonian evolution and it is a crucial parameter in the thermodynamic properties of the system. We explain how we can prepare a cloud of chosen magnetization using two different techniques that we denote as spin-mixing and spin distillation.

- Chapter 3 focuses on the properties of the mean-field ground-state of an antiferromagnetic spin-1 condensate. We highlight in particular the existence in such states of a spin nematic order. This spin nematic order characterizes the symmetry of the ground-state and provides a geometrical understanding of the mean-field magnetic phase diagram. We then present an experimental investigation of the phase diagram in terms of the spin populations at equilibrium. In a third part we show a method to probe the nematic order. This method is based on the measurement of the fluctuations of the magnetization after a rotation of the total spin of the state, and provides evidence for such a magnetic order.

- In the measurement of the phase diagram presented in chapter 3, we observed huge spin fluctuations in the region of low magnetization and low magnetic field. Although these fluctuations are not expected in the simple mean-field theory, they reflect the tendency of the system to restore the spin rotational symmetry (which is broken in the simple mean-field approximation). In this situation Bose-Einstein condensation occurs simultaneously in several spin states. The condensate is said to be fragmented. In chapter 4 we introduce the phenomenon of fragmentation and show by a diagonalization of the Hamiltonian that, in antiferromagnetic spinor condensates, it manifests itself in the two first moments of the population with zero spin projection along the quantization axis. We then develop an approximative but very efficient approach to describe a spin-1 Bose gas at low temperature. The spin state of the condensate is here described by a statistical mixture of mean-field states analogous to spin coherent states. We introduce here the notion of spin temperature. This approach allows to recover the manifestation of fragmentation, but without the numerical complexity of an exact diagonalization. We are able to study the continuous evolution of the spin state of the condensate from a fragmented state at low magnetic field to a mean-field state at larger magnetic field. In a last part we point out the similarity between this transition and the concept of spontaneous symmetry breaking.

- Finally, in chapter 5 we report on the experimental investigation of spin fragmentation in our spinor condensates. We prepare clouds with vanishing magnetization and measure the spin populations and their fluctuations at equilibrium. We perform these experiments at different "kinetic" temperatures (temperature of the thermal cloud) by changing the duration of the evaporative cooling. We then analyze the distributions of the spin populations using the theory presented in chapter 4, and are

able to deduce a spin temperature for the different values of our experimental parameters. We compare the spin and kinetic temperatures and find that they do not coincide. We interpret this as an evidence for the lack of thermalization between the spin degrees of freedom of the condensate and the spatial thermal component, which each arrive independently at a pseudo-thermal equilibrium by different relaxations mechanisms.

Chapter 1

Spin-1 Bose-Einstein condensates

1.1 Bose-Einstein condensates with an internal degree of freedom

Bose-Einstein condensation in an atomic gas is a phase transition defined by the macroscopic accumulation of atoms in the same single-particle state: if the gas is confined by an external potential, the atoms condense in the ground-state of the trap due to their bosonic statistics. They are then described by a giant wavefunction. The first experimental realizations of Bose-Einstein condensates in laser-cooled gases has been achieved in 1995 with alkali atoms [2, 3]. Even though these atomic species have an hyperfine structure with non-zero total spin in their electronic ground state, the use of magnetic traps imposed that all the atoms remain in low-field seeking states. For atoms with a nuclear spin $I = 3/2$ such as ^{87}Rb and ^{23}Na, only the $|F = 1, m_F = -1\rangle$ state of the lower hyperfine manifold and the $|F = 2, m_F = 1, 2\rangle$ states of the upper one can be trapped. The condensate was actually polarized in a single magnetic state: the spin degree of freedom was frozen [1]. The condensation is characterized in this case by a scalar wavefunction, describing the external degrees of freedom .

However the development of optical trapping techniques since 1997 allows to equally trap all the sublevels of an hyperfine manifold [48, 49], releasing the constraint on the internal degree of freedom and thus opening the possibility of creating Bose-Einstein condensates with several distinguishable components. Such condensates where the atoms are allowed to occupy any of the magnetic sublevels of a single hyperfine manifold F are called spinor condensates and are represented by a $(2F + 1)$-component wavefunction. Multi-component condensates are realized in other systems. The mixture of condensates from different bosonic species is also described by a multi-component wavefunction, as well as the mixture of condensates occupying N different hyperfine states of the same isotope, for instance the $|F = 1, m_F = -1\rangle$ and $|F = 2, m_F = +1\rangle$ states of ^{87}Rb, which realizes a pseudo-spin $(N - 1)/2$ system. Yet spinor condensates differ in major ways from other kinds of multi-component condensate. The key feature of spinor condensates is the vectorial nature of their wavefunction which expresses the possibility of population transfers between their different components. Mixtures of condensates do not possess this property. Associated with the internal rotational symmetry of the system, the vectorial transforma-

[1] A notable exception is the case of the $|F = 1, M_F = -1\rangle$ and $|F = 2, m_F = +1\rangle$ states of ^{87}Rb, whose mixture survives due to the fortunate near-equality of the singlet and triplet scattering lengths that almost suppresses spin-changing collisions. The mixture of condensates of these two hyperfine states realizes a pseudo-spin 1/2 system.

tion of the wavefunction dramatically affects the inter-atomic interactions. In particular, a characteristic of spinors that is not shared by other multi-component systems is the coherent internal-state dynamics driven by spin-exchange collisions. This coherent spin-mixing makes spinor condensates different from an uncoherent overlap of $2F+1$ condensates and gives access to a rich variety of phenomena. For instance, spin-1 condensates constitute a suitable non-linear medium to create non-classical state of matter, similarly to the creation of non-classical states of light in quantum optics. Using this similarity, parametric spin amplification [33] and spin squeezing [50] have been experimentally demonstrated. The coherence of the spin collisions also appears in the Josephson junction dynamics of spin oscillations [32, 51].

Bose-Einstein condensation is a purely quantum phase transition in the sense that it is a consequence of the quantum statistics of the atoms and not of their interactions. Still in spinor gases interactions between different spin states lead the atoms to condense in several possible phases. This is possible in spite of the weakness of the spin-dependent interaction (which contributes roughly to 1nK of energy per atom, much less than the typical 100nK temperature of the condensate) because of the bosonic enhancement provided by the Bose-Einstein condensate. Because of these enhanced interactions, spinor Bose gases become magnetically ordered below the condensation threshold. The interplay between spin-interactions and magnetic fields in the condensate give rise to magnetic phase transitions. We demonstrate in the following the existence of such a phase transition in spin-1 condensates with antiferromagnetic interactions.

In this chapter, we give first elements of theory of the spinor Bose gas that constitute the basis of the experimental and theoretical developments presented in the rest of this work. We first recall some basic properties of the Bose-Einstein condensation in a scalar gas confined in an harmonic trap. In particular we discuss the ground-state and the low-lying excited states of a weakly interacting gas. In a second part we turn to spinor condensates. We derive the interaction Hamiltonian and introduce two important approximations to simplify its treatment: the single-mode and the mean-field approximations. We then combine them to discuss the ground-state of the antiferromagnetic spin-1 Bose gas, which we experimentally studied in ^{23}Na condensates. The validity of the single-mode approximation is investigated. Finally we show that new modes of excitations associated to the internal degree of freedom, analogous to spin waves in magnetic materials, arise.

1.2 Bose-Einstein condensation in scalar gases

1.2.1 Bose-Einstein transition in an ideal gas

We consider a gas of N non-interacting atoms confined in an harmonic potential:

$$V_{\text{ext}}(\mathbf{r}) = \frac{1}{2}m(\omega_x^2 x^2 + \omega_y^2 y^2 + \omega_z^2 z^2) \tag{1.1}$$

where m is the mass of one atom and $\omega_{i=x,y,z}$ are the trapping frequencies along the three directions of space. The ground state wavefunction is obtained from the time-independent Schrődinger equation:

$$\phi(\mathbf{r}) = \left(\frac{m\bar{\omega}}{\pi\hbar}\right)^{3/4} \exp\left[-\frac{m}{2\hbar}(\omega_x x^2 + \omega_y y^2 + \omega_z z^2)\right] \tag{1.2}$$

where we defined the averaged frequency $\bar{\omega} = (\omega_x \omega_y \omega_z)^{1/3}$. The wavefunction ϕ satisfies the normalization condition $\int d^3\mathbf{r}|\phi(\mathbf{r})|^2 = 1$. The size of the condensate is independent of N and is set by the harmonic oscillator length

$$a_{ho} = \left(\frac{\hbar}{m\bar{\omega}}\right)^{1/2} \tag{1.3}$$

The standard procedure to introduce the Bose-Einstein condensation is to consider the bosonic occupation numbers of all the excited states, sum them and show that this sum has an upper bound independent of N [52]. The maximum number of atoms that can populate the excited states decreases with the temperature T of the gas, so that below a critical temperature T_c that depends on the atom number N, the atoms have no choice but to occupy the ground-state. This point marks the onset of the Bose-Einstein condensation. As the temperature is further lowered the atoms accumulate in the ground-state whose population N_0 becomes a macroscopic fraction of N. The fraction of atom in the ground-state N_0/N is denoted as the condensed fraction. A semi-classical approximation valid when the thermal energy is large compared to the level spacings set by the harmonic oscillator ($k_B T \gg \hbar\omega_{x,y,z}$) gives a critical temperature

$$k_B T_c = \hbar\bar{\omega}\left(\frac{N}{g_3(1)}\right)^{1/3} \simeq 0.94\hbar\bar{\omega}N^{1/3} \ , \tag{1.4}$$

where we introduced the family of Bose functions $g_\alpha(z) = \sum_{k=0}^{\infty} \frac{z^k}{k^\alpha}$. When we let $N \to +\infty$, the proper thermodynamic limit is to let at the same time $\bar{\omega} \to 0$, while keeping the product $N\bar{\omega}^3$ constant, so that the critical temperature (1.4) stays well defined.

The semi-classical approximation also allows one to calculated the spatial density of the thermal atoms populating the excited states. One finds:

$$n_T(\mathbf{r}) = \lambda_T^{-3} g_{3/2}(e^{\beta(\mu - V_{\text{ext}}(\mathbf{r}))}) \tag{1.5}$$

where $\lambda_T = h/\sqrt{2\pi m k_B T}$ is the De Broglie wavelength and μ is the chemical potential.

1.2.2 Effect of the interactions: ground-state

Even though we consider dilute gases of typical densities ranging from 10^{13} to 10^{15}cm^{-3}, the interactions between atoms can not be neglected. We recall in this section how they modify the ground-state of the condensate [52].

Two-body interactions

Because of the low density, the atoms interact almost exclusively through binary collisions. Furthermore, the temperature of the gas is low enough to allow for the "cold collisions" approximation: collisions are well described by s-wave scattering only. In this conditions, the interactions are characterized by a single parameter, the s-wave scattering length a. As the details of the two-body scattering potential are irrelevant, instead of the real (generally unknown) potential, one typically uses a simple model potential with the same scattering length. A popular choice for short range interactions is the so-called Fermi potential:

$$\hat{V}(\mathbf{r}, \mathbf{r}') = \frac{4\pi\hbar^2 a}{m}\delta(\mathbf{r} - \mathbf{r}') \tag{1.6}$$

where δ is the Dirac distribution. In the following we note $g = 4\pi\hbar^2 a/m$. Using such a contact potential to build a many-body theory is valid as long as the s-wave scattering length is much smaller than the mean inter-particle distance, which gives the condition $n|a|^3 \ll 1$ where n is the total density. In this dilute limit, two-boy scattering is essentially unaffected by the presence of other atoms and proceeds as if the two colliding atoms were alone. Positive and negative values of a correspond respectively to an effective repulsion and attraction between the atoms. From now on we only consider positive values of a.

Gross-Pitaevskii equation

In an ideal gas the many-body ground state is simply obtained by putting all the particles in the single-particle ground-state. This is not true any more for interacting particles, and the exact many-body particles ground-state is usually hard to calculate exactly. A very successful approach to describe the interacting Bose gas is the Hartree-Fock approximation which assumes that all the atoms share the same single-particle wavefunction. In this case we can derive an equation for the ground-state wavefunction ϕ by minimizing the free energy $\langle H \rangle - \mu N$. We obtain the Gross-Pitaevskii equation:

$$\left(-\frac{\hbar^2}{2m}\nabla^2 + V_{\text{ext}}(\mathbf{r}) + gN|\phi(\mathbf{r})|^2\right)\phi(\mathbf{r}) = \mu\phi(\mathbf{r}) \tag{1.7}$$

The chemical potential μ corresponds mathematically to the Lagrange multiplier associated with the conservation of the total atom number N. In equation (1.7) ϕ is normalized to unity: $\int \mathrm{d}\mathbf{r}|\phi(\mathbf{r})|^2 = 1$.

Thomas-Fermi approximation

To estimate the importance of the effect of the interactions on the ground state wavefunction we compare the interaction energy E_{int} to the kinetic energy E_{kin} of the system. One finds that the ratio of the two energies is given by:

$$\frac{E_{\text{int}}}{E_{\text{kin}}} \approx N\frac{a}{a_{ho}} \tag{1.8}$$

If this number is large, the ground state is essentially determined by the interaction and the kinetic term can be neglected compared to the interaction one in the Gross-Pitaevskii equation. This is the Thomas-Fermi approximation. From (1.7) we find the density of the condensate:

$$n(\mathbf{r}) = |\phi(\mathbf{r})|^2 = g^{-1}\max\left[\mu - V_{\text{ext}}(\mathbf{r}), 0\right] \tag{1.9}$$

Due to the shape of the trapping potential, the density of the condensate is parabolic. (For non-interacting atoms it was gaussian). The chemical potential is calculated by integrating (1.9) over space and equaling it to N:

$$\mu = \frac{\hbar\bar{\omega}}{2}\left(15N\frac{a}{a_{ho}}\right)^{2/5} \tag{1.10}$$

We then obtain the radius of the condensate $R_i = \sqrt{2\mu/m\omega_i^2}$:

$$R_i = a_{ho}\frac{\bar{\omega}}{\omega_i}(15N\frac{a}{a_{ho}})^{1/5} \tag{1.11}$$

for $i = (x, y, z)$. Since we assume $Na/a_{ho} \gg 1$, the size of the condensate is much larger than the size of the non-interacting ground state a_{ho}. This is an effect of the repulsive interaction between the atoms.

1.2.3 Effect of the interactions: excited states

We now consider the effect of the interactions on the excited states. In a non-interacting condensate, elementary excitations consist in the promotion of atoms of the condensate to single-particle excited states of the trap. Their spectrum is then the one of an harmonic oscillator. Interactions modify this spectrum. Low-lying excitations can be derived following a procedure introduced by Bogoliubov [53]. For simplicity we here consider the case of an homogeneous gas of N atoms in a volume V.

In second quantization a generic many-body Hamiltonian reads:

$$\hat{H} = \int \mathrm{d}\mathbf{r}\hat{\Psi}^\dagger(\mathbf{r})\left(-\frac{\hbar^2}{2m}\nabla^2\right)\hat{\Psi}(\mathbf{r}) + \frac{1}{2}\int \mathrm{d}\mathbf{r}\mathrm{d}\mathbf{r}'\hat{\Psi}^\dagger(\mathbf{r})\hat{\Psi}^\dagger(\mathbf{r}')\hat{V}(\mathbf{r}-\mathbf{r}')\hat{\Psi}(\mathbf{r}')\hat{\Psi}(\mathbf{r}) \tag{1.12}$$

In the following we replace the two-body interaction operator $\hat{V}$ by expression (1.6).

For uniform systems it is convenient to expand the atomic-field operator in the basis of plane-waves. We assume that a macroscopic fraction of the atoms are in the condensate, which is defined by the $\mathbf{k} = 0$. We note N_0 the number of atoms in this mode.The commutator of the associated creation and annihilation operators is much smaller than their action on the state of the condensate (on order $\sqrt{N_0}$), so that these operators can be approximated by c-numbers:

$$\hat{a}_0^\dagger \simeq \hat{a}_0 \simeq \sqrt{N_0} \tag{1.13}$$

Separating the $\mathbf{k} = 0$ mode from the others, and retaining only terms which are at least quadratic in $\hat{a}_0^\dagger$ and $\hat{a}_0$, the Hamiltonian becomes:

$$\hat{H} \approx \frac{gN^2}{2V} + \sum_{\mathbf{k}\neq 0}(\epsilon_k + \frac{gN}{V})\hat{a}_{\mathbf{k}}^\dagger\hat{a}_{\mathbf{k}} + \frac{gN}{2V}\sum_{\mathbf{k}\neq 0}(\hat{a}_{\mathbf{k}}^\dagger\hat{a}_{-\mathbf{k}}^\dagger + \hat{a}_{\mathbf{k}}\hat{a}_{-\mathbf{k}}) \tag{1.14}$$

where $\epsilon_k = \hbar^2k^2/2M$. The first term is the energy of the condensate (due to interaction since the kinetic energy is zero). The factor in front of $\hat{a}_{\mathbf{k}}^\dagger\hat{a}_{\mathbf{k}}$ has two terms: the kinetic energy and the interaction with the condensate. The last term comes from processes where two atoms of the condensate are scattered into states of momenta $+\mathbf{k}$ and $-\mathbf{k}$, and the inverse process where two atoms with momenta $+\mathbf{k}$ and $-\mathbf{k}$ are scattered into the condensate.

The Hamiltonian (1.14) can be diagonalized by a Bogoliubov transformation. We introduce new operators $\hat{\alpha}_k$ defined by:

$$\hat{\alpha}_{\mathbf{k}}^\dagger = u_{\mathbf{k}}\hat{a}_{\mathbf{k}}^\dagger + v_{\mathbf{k}}\hat{a}_{-\mathbf{k}} \tag{1.15}$$

where $u_{\mathbf{k}}$ and $v_{\mathbf{k}}$ are amplitudes to determine. We impose that these new operators obey the bosonic commutation relations:

$$[\hat{\alpha}_{\mathbf{k}}, \hat{\alpha}_{\mathbf{k}'}^\dagger] = \delta_{\mathbf{k},\mathbf{k}'},\ [\hat{\alpha}_{\mathbf{k}}, \hat{\alpha}_{\mathbf{k}'}] = [\hat{\alpha}_{\mathbf{k}}^\dagger, \hat{\alpha}_{\mathbf{k}'}^\dagger] = 0 \tag{1.16}$$

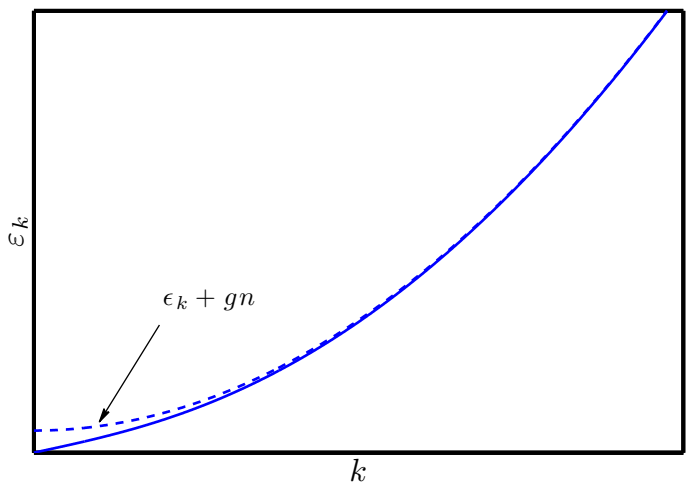

Figure 1.1: Spectrum of Bogoliubov excitations. The solid line shows the energy ε_k, the dashed line shows $\epsilon_k + gn$.

Inserting (1.15) into the Hamiltonian (1.14), we determine $u_{\mathbf{k}}$ and $v_{\mathbf{k}}$ such that the Hamiltonian becomes diagonal. We obtain:

$$\hat{H} = E_0(N/V) + \sum_{\mathbf{k}\neq 0} \varepsilon_k \hat{\alpha}^\dagger_{\mathbf{k}} \hat{\alpha}_{\mathbf{k}} \tag{1.17}$$

where $E_0(N/V)$ is the energy of the ground-state. We note $n = N/V$ the density. The excited states correspond to creations of quasiparticles with an energy ε_k given by:

$$\varepsilon_k = \sqrt{\epsilon_k(\epsilon_k + 2gn)} \tag{1.18}$$

For long wavelength excitations ($k \ll mgn/\hbar^2$) we find the phonon dispersion law $\varepsilon \approx c_s \hbar k$, where $c_s = \sqrt{gn/m}$ is the sound velocity, whereas in the opposite limit the short wavelength excitations ($k \gg mgn/\hbar^2$) are free particles excitations with energy $\varepsilon_k \approx \epsilon_k + gn$. The spectrum at high energies resemble the one of a non-interacting system, and excitations are there single-particle excitations (the amplitude $v_{\mathbf{k}}$ goes to zero for large k). On the other hand, the lowest modes are collective modes involving more than one particle.

In a box with periodic boundary conditions, the possible values of the components of $\mathbf{k}$ are discrete: $k_i = 2\pi/L_i$, where $i = x, y, z$ and L_i is the size of the box in direction i. In an harmonic potential, the complete calculation of elementary excitations is tedious, but we can still estimate the energy of the phonon modes, approximating the harmonic trap by a box. We take for the size of the box twice the radius of the condensate in the Thomas-Fermi regime $R_{TF} = \sqrt{2\mu/m\omega^2} = \sqrt{2gn/m\omega^2}$, where ω is here the frequency of the harmonic potential that we assume isotropic for simplicity. If we calculate the energy of the first phonon mode we get:

$$\varepsilon_1 \sim \frac{\hbar c_s}{R_{TF}} \sim \hbar\omega \tag{1.19}$$

We find that the first phonon mode has an energy on the order of $\hbar\omega$, the quantum of energy associated to the harmonic potential. This is confirmed by a more rigorous analysis [52, 54].

1.3 Spin-1 Bose-Einstein condensates: spin Hamiltonian

We now consider a Bose-Einstein condensate with an internal degree of freedom, and in particular the case of a condensate of particles of spin 1. We first look at the single particle level, and describe the internal structure and how it couples to external fields. We then move to the level of two particles and discuss how they interact before finally deriving the many-body Hamiltonian.

1.3.1 Single spin-1 particle

Internal structure

We describe here the electronic structure of ^{23}Na. The fine structure results from the coupling of the electron spin $\mathbf{S}$ to its orbital angular momentum $\mathbf{L}$. We note the total electron angular momentum $\mathbf{J} = \mathbf{S} + \mathbf{L}$. The ground state $3^2S_{1/2}$ corresponds to $L = 0$ so that $J = 1/2$. The two first excited states $3^2P_{1/2}$ and $3^2P_{3/2}$ correspond to $L = 1$ and have $J = 1/2$ and $J = 3/2$ respectively. The two transitions $3^2S_{1/2} \to 3^2P_{1/2}$ and $3^2S_{1/2} \to 3^2P_{1/2}$ form a fine structure doublet noted D_1 and D_2. Each of these three levels have an hyperfine structure resulting from the coupling of the total electron angular momentum $\mathbf{J}$ to the nuclear angular momentum $\mathbf{I}$. We note the total angular momentum $\mathbf{F} = \mathbf{J}+\mathbf{I}$. In ^{23}Na the nucleus has an angular momentum $I = 3/2$ so that the ground state $J = 1/2$ splits into two levels of total spin $F = 1$ and $F = 2$. The hyperfine splitting in the ground state is $\Delta E_{hfs} \approx 1.77$ GHz [55]. The $3^2P_{1/2}$ and $3^2P_{3/2}$ states split respectively in two ($F = 1, 2$) and four levels ($F = 0, 1, 2, 3$). Each of these hyperfine level contains $2F + 1$ Zeeman sublevels labeled my the projection of the total angular momentum on the quantization axis, $m_F = -2F, -2F + 1, ..., 2F$. In absence of external magnetic field these levels are degenerate.

Zeeman effect

We now consider the effect of an external magnetic field oriented along the quantization axis and of amplitude B. The angular momentum of a particle couples to the magnetic field and the degeneracy of the Zeeman sublevels is then broken. In the electronic ground state the shifts of the Zeeman sub levels are given by the Breit-Rabi formula [55]:

$$E_{m_F} = -m_F g_I \mu_I B - \frac{1}{2}\sqrt{1 + m_F\alpha + \alpha^2} \tag{1.20}$$

where $\alpha = (g_J - g_I)\mu_B B/\Delta E_{hfs}$, μ_I is the nuclear magneton, μ_B is the Bohr magneton, g_I and g_J are respectively the nuclear and electronic Landé g-factors.

Typical magnetic fields used experimentally are on the order of a few G, so that the Zeeman shifts are small compared to ΔE_{hfs}. One can expand the Breit-Rabi formula up to order 2 in α, and neglecting g_I compared to g_J we get:

$$E_{m_F} = m_F p + m_F^2 q \tag{1.21}$$

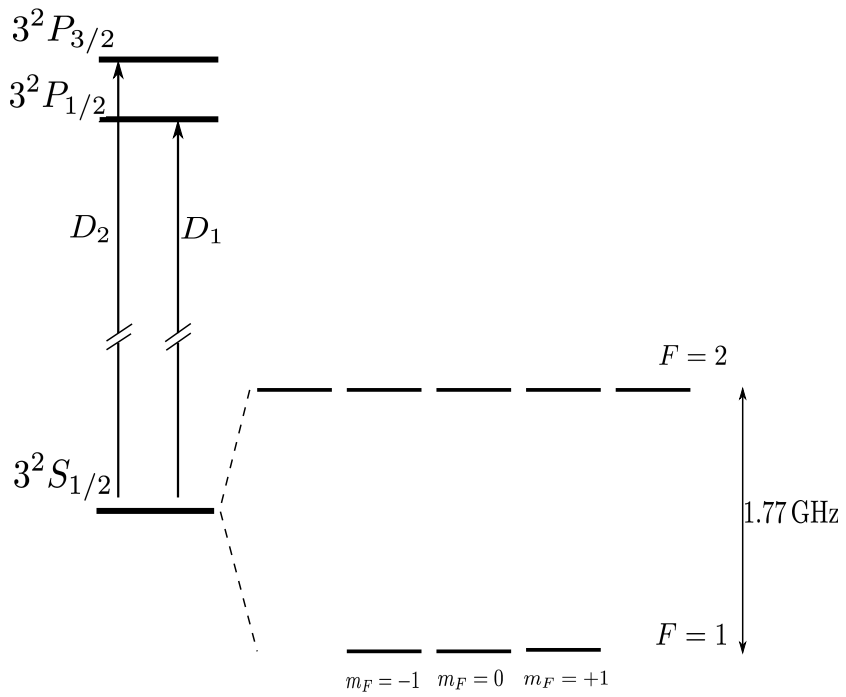

Figure 1.2: Fine structure and hyperfine structure of the electronic ground state of Sodium.

with

$$p = g_F \mu_B B \ , \ q = \frac{(g_F \mu_B B)^2}{\Delta E_{hfs}} \tag{1.22}$$

where $g_F = -1/2$ for the $F = 1$ hyperfine manifold is calculated from g_J and g_I. Numerically one has $\mu_B/2 \approx h \times 700\,\mathrm{kHz/G}$, and $\mu_B^2/4\Delta_{hf} \approx h \times 277\,\mathrm{Hz/G^2}$.

Optical trapping

We now discuss the interaction between spin-1 particles and the electric field of a laser beam. The motivation is that the production of a spinor condensate requires that the different spin states of an hyperfine manifold see the same trapping potential. Such a spin-independent potential is provided by an optical dipole trap. The electric field of a red-detuned focused laser beam induces in polarizable atoms a dipole moment whose interaction with the same electrical field creates the trapping potential. For a laser which is far-off resonant to the atomic transition of interest, this interaction is described by the Hamiltonian

$$\hat{H}_{\mathrm{dip}} = -\hat{\mathbf{E}}^{(-)}.\alpha.\hat{\mathbf{E}}^{(+)} \tag{1.23}$$

where $\hat{\mathbf{E}}^{(\pm)}$ are the electric field operators creating and annihilating photons in the laser mode, and α is the atomic polarizability tensor given by

$$\alpha = -\sum_{F,F'} \frac{\hat{P}_F \hat{\mathbf{d}} \hat{P_{F'}} \hat{\mathbf{d}}^\dagger \hat{P}_F}{\hbar \Delta_{FF'}} \tag{1.24}$$

F (F') labels the angular momentum of the ground (excited) states manifold. $\hat{P}_F$ is the projector on the manifold F, $\hat{\mathbf{d}}$ is the electric dipole operator,and $\Delta_{FF'} = \omega_L - \omega_{FF'}$ is the detuning of the laser frequency to the atomic transition $F - F'$. The polarizability tensor α can be understood in terms of a scattering interaction: an atom from the ground

state manifold F is virtually promoted to the manifold F' by the raising dipole operator $\hat{d}^\dagger$ and at the same time a photon is annihilated by $\hat{\mathbf{E}}^{(+)}$. The atom then decays back to the manifold F (possibly in an other state) and a photon is created. The polarizability α is built as the dyadic product of two vector operator, and so is a rank-2 tensor that can decomposed in the sum of irreducible operators of rank 0,1 and 2. It follows that the Hamiltonian $\hat{H}$ can as well be written:

$$\hat{H}_{\text{dip}} = \hat{H}^{(0)}_{\text{dip}} + \hat{H}^{(1)}_{\text{dip}} + \hat{H}^{(2)}_{\text{dip}} \tag{1.25}$$

where $\hat{H}^{(i)}$ is the component of rank i. If we restrict the ground states of the atoms to one manifold F we have [56]

$$\hat{H}^{(0)}_{\text{dip}} \propto \mathbf{E}^{(-)}.\mathbf{E}^{(+)}.\mathbb{1}_F \tag{1.26}$$

$$\hat{H}^{(1)}_{\text{dip}} \propto (\mathbf{E}^{(-)} \times \mathbf{E}^{(+)}).\hat{\mathbf{F}} \tag{1.27}$$

$$\hat{H}^{(2)}_{\text{dip}} \propto E^{(-)}_i E^{(+)}_j \left(\frac{1}{2}(F_i F_j + F_j F_i) - \frac{F(F+1)}{3}\mathbb{1}_F \right) \tag{1.28}$$

where $\mathbf{F}$ is the total angular momentum of the atoms. The weight of these different contributions are respectively given by $1/\Delta_{FF'}$, $\Delta_{fs}/\Delta^2_{FF'}$ and $\Delta_{hfs}/\Delta^2_{FF'}$, where Δ_{fs} is the fine structure splitting of the excited states and Δ_{hfs} the hyperfine structure splitting. If the detuning of the laser to the atomic transition is large compared to hyperfine splitting, the rank-2 contribution of the polarizability becomes negligible. Besides, if the laser light is linearly polarized the vector term vanishes. In these conditions, only the scalar part of the Hamiltonian remains, that acts as a state-independent light shift. The three spin states then see the same trapping potential. Conversely, reducing the detuning or using circularly polarized light allows to manipulate the atoms in a spin-dependent way. In the following we consider the trapping potential is independent of the spin state and note it $V_{\text{ext}}(\mathbf{r})$.

1.3.2 Two-body scattering of two spin-1 particles

We derive here the Hamiltonian describing the interaction of two atoms of spin 1. For atoms with an internal degree of freedom, collisions connect asymptotic incoming and outgoing states that are a product of an orbital and an internal state. Internal and orbital states are labeled by quantum numbers, in particular by their total angular momentum. As we explained in the previous section, in dilute gases at very low temperature, binary s-wave collisions prevail, and we can make the cold-collisions approximation: the wavefunction of the relative motion of the two atoms has then zero total angular momentum.
We assume the interaction is rotationally invariant in real and in spin space[2] . This is exact in the absence of symmetry breaking due in particular to applied magnetic fields. Nonetheless, this approximation remains valid at low magnetic fields. As a consequence the total angular momentum is conserved. We additionally make the approximation that orbital and internal degrees of freedom do not couple during the collision. Then orbital and spin angular momentum are independently conserved.
The wave-function of bosons has to be symmetric under the exchange of any two particles. Because of the s-wave approximation, the orbital part of the wavefunction is symmetric under such exchange. Its internal part then also has to be symmetric. The parity of

[2]Making this assumption we neglect non-rotationally symmetric interactions, in particular the magnetic dipole-dipole interaction. See footnote 3 next page for a justification of this approximation in the case of a gas of Sodium atoms.

the wave-function is $(-1)^F$, so that for two colliding spin-1 particles there only exists two scattering channels: $F = 0$ and $F = 2$. Because of the rotational symmetry of the interaction, the two atoms stay in the same channel during the collision.
As in the scattering of two polarized particle we already discussed, the interaction potential is characterized by the s-wave scattering length alone. We decide to model its spatial part by a Fermi contact potential of same scattering length. Since the scattering channel is conserved during the collision we can write the interaction operator as:

$$\hat{V} = \delta(\mathbf{r}_1 - \mathbf{r}_2) \otimes \sum_{F=0,2} \frac{4\pi\hbar^2 a_F}{m} \hat{P}_F \tag{1.29}$$

where $\hat{P}_F$ is the projector on the total spin F state, and a_F is the scattering length associated with the scattering channel of total spin F. This generic form respects the symmetry under exchange of two particles and is rotationally symmetric.

This operator may be expressed in terms of one-particle spin operators. First we write the total spin of the atom pair:

$$(\hat{\mathbf{S}}_1 + \hat{\mathbf{S}}_2)^2 = \hat{\mathbf{S}}_1^2 + \hat{\mathbf{S}}_2^2 + 2\hat{\mathbf{S}}_1.\hat{\mathbf{S}}_2 = \sum_F F(F+1)\hat{P}_F = 6\hat{P}_2 \tag{1.30}$$

We note $\hat{I}_{1,2}$ the identity operator in the internal Hilbert space of the particule 1,2. Considering that $\hat{I}_1 \otimes \hat{I}_2 = \hat{P}_0 + \hat{P}_2$ we get:

$$\hat{P}_0 = \frac{\hat{I}_1 \otimes \hat{I}_2 - \hat{\mathbf{S}}_1.\hat{\mathbf{S}}_2}{3}, \ \hat{P}_2 = \frac{2\hat{I}_1 \otimes \hat{I}_2 + \hat{\mathbf{S}}_1.\hat{\mathbf{S}}_2}{3} \tag{1.31}$$

We then obtain for the spin part of the two-particle interaction operator (1.29):

$$\hat{V}_s = c_0 \hat{I}_1 \otimes \hat{I}_2 + c_2 \hat{\mathbf{S}}_1.\hat{\mathbf{S}}_2 \tag{1.32}$$

with

$$c_0 = \frac{4\pi\hbar^2}{m}\frac{a_0 + 2a_2}{3}, \ c_2 = \frac{4\pi\hbar^2}{m}\frac{a_2 - a_0}{3} \tag{1.33}$$

We note $\bar{a} = (a_0 + 2a_2)/3$ and $a_s = (a_2 - a_0)/3$. These two lengths determine the nature and the strength of the interactions. In particular the sign of a_s determines the ferromagnetic or antiferromagnetic behavior of the spinor gas, as it energetically favors either the alignment or the anti-alignment of the spins. In the following, when dealing with Sodium we will use the most accurate known values of these scattering lengths, determined in [57] using a combination of Feschbach spectroscopy and coupled-channel calculations. They found $\bar{a} = 52.66(40)a_B$ and $\bar{a} - a_s = 50.78(40)a_B$, where a_B is the Bohr radius. This gives $\bar{a} \approx 2.79(2)$ nm and $a_s \approx 0.10(2)$ nm. Spin-dependent interactions in Sodium are thus antiferromagnetic. From this we also deduce the relative strength of the spin-dependent and spin-independent terms in the interaction operator (1.32) for Sodium[3]:

$$\frac{a_s}{\bar{a}} \approx 0.036 \tag{1.35}$$

[3]We can now also estimate the relative strength of the spin-dependent interaction and of the dipole-dipole interaction. The order of magnitude of the strength of the long-range dipole-dipole interaction between two particles of magnetic moment μ_1 and μ_2 is given by

$$V_{dd} \sim \frac{\mu_0}{4\pi}\frac{\mu_1\mu_2}{r^3}$$

In many atomic species, the atomic magnetic moment is relatively small, on the order of the Bohr magneton μ_B. The ratio of the dipole-dipole energy per atom to the spin-dependent contact interaction is independent

1.3.3 Many-body Hamiltonian

Spin-dependent interaction

From the two-body interaction operator $\hat{V}_s$ we derive the many-body interaction Hamiltonian $\hat{H}_{int}$. The operator $\hat{V}_s$ is a sum of two terms, so is $\hat{H}_{int}$. The first term in $\hat{V}_s$ gives a spin-independent part:

$$\bar{H} = \frac{c_0}{2} \sum_{ij} \int \mathrm{d}\mathbf{r} \hat{\Psi}_i^\dagger(\mathbf{r}) \hat{\Psi}_j^\dagger(\mathbf{r}) \hat{\Psi}_i(\mathbf{r}) \hat{\Psi}_j(\mathbf{r}) \tag{1.36}$$

and the second one a spin-dependent part:

$$\hat{H}_s = \frac{c_2}{2} \sum_{ijkl} \int \mathrm{d}\mathbf{r} \mathbf{S}_{ik}.\mathbf{S}_{jl} \hat{\Psi}_i^\dagger(\mathbf{r}) \hat{\Psi}_j^\dagger(\mathbf{r}) \hat{\Psi}_k(\mathbf{r}) \hat{\Psi}_l(\mathbf{r}) \tag{1.37}$$

where the atomic field operator $\hat{\Psi}_i^\dagger(\mathbf{r})$ creates a particle at position $\mathbf{r}$ in the $|F=1, m_F=i\rangle$ Zeeman state, and where $\mathbf{S}_{ij}$ are the (i,j) components of the spin-1 operator $\hat{\mathbf{S}}$ in the standard basis $|m_F=i\rangle$: $\mathbf{S}_{ij} = ((S_x)_{ij}, (S_y)_{ij}, (S_z)_{ij})^T$, with:

$$S_x = \frac{1}{\sqrt{2}} \begin{pmatrix} 0 & 1 & 0 \\ 1 & 0 & 1 \\ 0 & 1 & 0 \end{pmatrix}, \; S_y = \frac{i}{\sqrt{2}} \begin{pmatrix} 0 & -1 & 0 \\ 1 & 0 & -1 \\ 0 & 1 & 0 \end{pmatrix}, \; S_z = \begin{pmatrix} 1 & 0 & 0 \\ 0 & 0 & 0 \\ 0 & 0 & -1 \end{pmatrix} \tag{1.38}$$

Calculating explicitly the spin-dependent Hamiltonian (1.37) and gathering identical terms from (1.36) we find the expression for the full interaction Hamiltonian:

$$\begin{aligned} \hat{H}_{int} \;=\; & \frac{1}{2} \int \mathrm{d}\mathbf{r} (c_0 + c_2) \hat{\Psi}_{+1}^\dagger \hat{\Psi}_{+1}^\dagger \hat{\Psi}_{+1} \hat{\Psi}_{+1} + c_0 \hat{\Psi}_0^\dagger \hat{\Psi}_0^\dagger \hat{\Psi}_0 \hat{\Psi}_0 + (c_0 + c_2) \hat{\Psi}_{-1}^\dagger \hat{\Psi}_{-1}^\dagger \hat{\Psi}_{-1} \hat{\Psi}_{-1} \\ & + 2(c_0 + c_2) \hat{\Psi}_{+1}^\dagger \hat{\Psi}_0^\dagger \hat{\Psi}_{+1} \hat{\Psi}_0 + 2(c_0 + c_2) \hat{\Psi}_{-1}^\dagger \hat{\Psi}_0^\dagger \hat{\Psi}_{-1} \hat{\Psi}_0 + 2(c_0 - c_2) \hat{\Psi}_{+1}^\dagger \hat{\Psi}_{-1}^\dagger \hat{\Psi}_{+1} \hat{\Psi}_{+1} \\ & + 2c_2 (\hat{\Psi}_{+1}^\dagger \hat{\Psi}_{-1}^\dagger \hat{\Psi}_0 \hat{\Psi}_0 + \hat{\Psi}_0^\dagger \hat{\Psi}_0^\dagger \hat{\Psi}_{+1} \hat{\Psi}_{-1}) \end{aligned} \tag{1.39}$$

where the terms proportional to c_0 come from the spin-independent part, whereas the terms proportional to c_2 come from the spin-dependent part.

Introducing the two operators $\hat{\rho}(\mathbf{r}) = \sum_i \hat{\Psi}_i^\dagger(\mathbf{r}) \hat{\Psi}_i(\mathbf{r})$ for the total number density and $\hat{\mathbf{S}}(\mathbf{r}) = \sum_{i,j} \mathbf{S}_{ij} \hat{\Psi}_i^\dagger(\mathbf{r}) \hat{\Psi}_j(\mathbf{r})$ for the spin density, and commuting the field operators in (1.36) and (1.37) we get:

$$\bar{H} = \frac{c_0}{2} \int \mathrm{d}\mathbf{r} (\hat{\rho}^2(\mathbf{r}) - \hat{\rho}(\mathbf{r})) \tag{1.40}$$

and

$$\hat{H}_s = \frac{c_2}{2} \int \mathrm{d}\mathbf{r} (\hat{\mathbf{S}}^2(\mathbf{r}) - 2\hat{\rho}(\mathbf{r})) \tag{1.41}$$

Terms appear that only depend on the total atom number $N = \int \mathrm{d}\mathbf{r} \hat{\rho}(\mathbf{r})$. This number is supposed fixed, and these terms merely account for a shift of the energy reference. We will drop them from now on. By construction, this Hamiltonian is rotationally symmetric.

---

of the density:

$$\epsilon = \frac{\mu_0 \mu_B^2 m}{(4\pi)^2 \hbar^2 a_s} \tag{1.34}$$

For ^{23}Na we calculate $\epsilon \approx 2 \times 10^{-2}$, and we can neglect the dipole-dipole interactions. This is not true in atomic species with large magnetic moment, such as Chromium [58].

Therefore the projection of the angular momentum on the quantization axis is conserved by the spin-dependent interaction. This quantity is referred to as the longitudinal magnetization of the system and reads

$$M_z = \int \mathrm{d}\mathbf{r} \left(\hat{\Psi}^\dagger_{+1}(\mathbf{r})\hat{\Psi}_{+1}(\mathbf{r}) - \hat{\Psi}^\dagger_{-1}(\mathbf{r})\hat{\Psi}_{-1}(\mathbf{r}) \right) \tag{1.42}$$

The longitudinal magnetization corresponds to the difference in the populations of the $|m_F = +1\rangle$ and $|m_F = -1\rangle$ states. Its conservation also appears in (1.39), where the terms of the two first lines correspond to the energy shift due to elastic collisions, whereas the terms of the third line describe inelastic collisions that produce a pair of atoms in $|m_F = +1\rangle$ and $|m_F = -1\rangle$ from two atoms in $|m_F = 0\rangle$, or the opposite process. These inelastic collisions are the only allowed spin-changing collisions. They represent a major feature of spinor gases, as they express the coherence between the three spin components and are at the origin of a rich variety of phenomena.

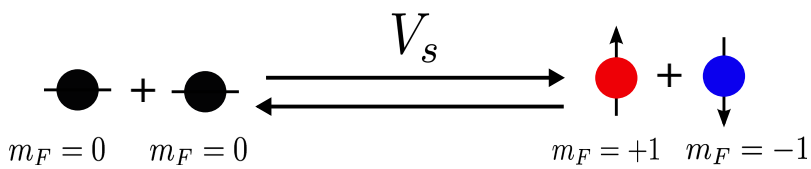

Figure 1.3: The only spin-changing processes are the collision where two atoms in the $|m_F = 0\rangle$ state give one atom in $|m_F = +1\rangle$ and one in $|m_F = -1\rangle$, and the opposite process. These collisions conserve the projection of the total spin on the quantization axis.

Another property originating from the spin-dependent interaction in antiferromagnetic spinor condensates is the immiscibility of the $|m_F = 0\rangle$ state with the $|m_F = +1\rangle$ and $|m_F = -1\rangle$ states. Let's consider a two-component condensate mixture. We label these components A and B. Its interaction energy is given by [59]:

$$E = \frac{1}{2} \int \mathrm{d}\mathbf{r} \left(n_A^2 g_A + n_B^2 g_B + 2 n_A n_B g_{AB} \right) \tag{1.43}$$

n_A and n_B are the densities of the two component, the g coefficients are defined by $g_i = 4\pi\hbar^2 a_i/m, (i = A, B, AB)$, where a_A and a_B are the same-species scattering lengths and a_{AB} is the cross-scattering length. Recalling the expression of c_0 and c_2 (1.33) we can identify the different scattering lengths from (1.39):

	$m_F = +1$	$m_F = 0$	$m_F = -1$
$m_{F=+1}$	a_2	a_2	$(a_2 + 2a_0)/3$
$m_{F=0}$	a_2	$(2a_2 + a_0)/3$	a_2
$m_{F=-1}$	$(a_2 + 2a_0)/3$	a_2	a_2

Table 1.1: Scattering lengths describing collisions in the $F = 1$ spinor gas.

We assume that each of the two component A and B has a population N and fills a volume V. The interaction energy if the two components are mixed is:

$$E = \frac{N^2}{2V} \left(g_A + g_B + 2 g_{AB} \right) \tag{1.44}$$

If they separate in two distinct phases, the interaction energy becomes:

$$E = \frac{N^2}{2}(\frac{g_A}{V_A} + \frac{g_B}{V_B}) \tag{1.45}$$

the two volumes V_A and V_B being determined by the condition of equal pressure:

$$g_A(\frac{N}{V_A})^2 = g_B(\frac{N}{V_B})^2 \tag{1.46}$$

Comparing these two results, we find that the two component will mix if $g_{AB} < \sqrt{g_A g_B}$, or equivalently if $a_{AB} < \sqrt{a_A a_B}$, and that they will phase separate if $a_{AB} > \sqrt{a_A a_B}$. In the case of sodium, $a_2 > a_0$, so that $a_{+1,0} > \sqrt{a_{0,0} a_{+1,+1}}$, and so the Zeeman components $m_F = \pm 1$ and $m_F = 0$ are immiscible. Conversely the states $m_F = -1$ and $m_F = +1$ are miscible.

1.3.4 Effect of applied magnetic fields

We introduced previously the effect of an external magnetic field on a single spin-1 particle. We now consider its effect on the many-body Hamiltonian.

Let us first compare the importance of the Zeeman energy of one atom (1.21) with the spin interaction discussed above. The spin-dependent interaction in trapped spinor gases is associated with typical energies on the order of $h \times 100$Hz, which correspond to a magnetic field of 140μG for the linear Zeeman energy, so that even for small fields this effect largely dominates the spin-dependent interaction. If the longitudinal magnetization was free, the ground-state would consist in accumulating all the atoms in the magnetic state of lowest linear Zeeman energy. But the magnetization is fixed, and consequently so is the linear Zeeman energy. The linear Zeeman effect only acts as an offset in the energy, and so has no effect on the ground-state properties of the spinor gas: it is irrelevant and can be ignored. This is a crucial point: without longitudinal spin conservation, all the interesting phenomena associated with the spin-dependent interaction would be screened.

The Zeeman effect enters the Hamiltonian through its much smaller quadratic part. Since q is positive, this effect shifts the states $|m_F = +1\rangle$ and $|m_F = -1\rangle$ up compared to $|m_F = 0\rangle$, and so favors the latter. Taking the $|m_F = \pm 1\rangle$ states as a reference for the energy shifts of the quadratic Zeeman effect, we can write the magnetic Hamiltonian:

$$\hat{H}_{\text{zee}} = -q\hat{N}_0 \tag{1.47}$$

where $\hat{N}_0$ is the population operator of the $|m_F = 0\rangle$ state. Obviously, this quadratic shift breaks the rotational symmetry of the spin Hamiltonian by favoring a particular axis of the space (the quantization axis, defined by the direction of the applied field).

So far we have considered homogeneous fields. If the linear Zeeman effect is effectively canceled by the longitudinal spin conservation in the case of an homogeneous magnetic field, this is not true for a non-uniform field. The application of a gradient of magnetic field, by making the spin Hamiltonian space-dependent, may create spin domains in the condensate [59].

Finally, we point out that the magnetic field defines a local quantization axis for the spin state of the atoms. To be able to define the spin state of our atoms and study their

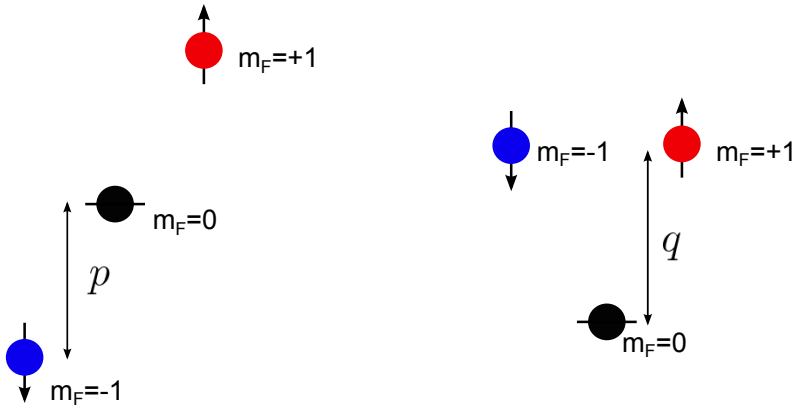

Figure 1.4: Effect of an homogeneous external magnetic field on the structure of the $F = 1$ manifold. Linear and quadratic Zeeman shifts (respectively left and right) are represented on a different energy scale, p being much larger than q for a given field.

magnetic properties, we need that the spin state of the atoms follows adiabatically in time and in space the evolution of the magnetic field. If the field varies too rapidly the atoms may undergo spin-flip transitions [60]. The condition for adiabaticity is discussed more quantitatively in chapter 2.

1.4 Mean-field theory of spin-1 condensates

In the previous section we derived the Hamiltonian of the spin-1 Bose gas in the presence of an external magnetic field. We now want to determine its ground state. The exact treatment is in general complex. A first simplification is to use a mean-field approach. To further simplify the problem we also introduce the so-called single-mode approximation. We are then able to find the ground state of the system under these two approximations. Finally, to evaluate if these results apply in our experimental conditions we quantitatively check the validity of the single-mode approximation.

1.4.1 Single-mode approximation

In the presence of a magnetic field, the spin Hamiltonian reads

$$\hat{H}_s = \frac{c_2}{2} \int d^3\mathbf{r}\hat{\mathbf{S}}^2(\mathbf{r}) - q\hat{N}_0 \tag{1.48}$$

Due to the coupling of the orbital and internal degrees of freedom, the exact ground state can generally not be calculated analytically. The problem is however much simplified by the widely used single-mode approximation (SMA) [61]. This approximation assumes that the different Zeeman states in the Bose-Einstein condensate share the same spatial mode:

$$\phi_{+1}(\mathbf{r}) = \phi_0(\mathbf{r}) = \phi_{-1}(\mathbf{r}) = \psi(\mathbf{r}) \tag{1.49}$$

The single-mode wavefunction ψ is the solution of the Gross-Pitaevskii equation

$$\left(-\frac{\hbar^2\nabla^2}{2m} + V_{\text{ext}}(\mathbf{r}) + c_0 N|\psi(\mathbf{r})|^2\right)\psi(\mathbf{r}) = \mu\psi(\mathbf{r}) \tag{1.50}$$

The spin and external degrees of freedom are now decoupled. As the three spin states contribute the same way to the spin-independent part of the energy (1.54) it is fixed by ψ

and all the properties of the condensate now come from the minimization of its energy in spin space.

We can factor out the spatial part of the wavefunction in the spin Hamiltonian $\hat{H}_s$ and get:

$$\hat{H}_s = \frac{U_s}{2N}\hat{\mathbf{S}}^2 - q\hat{N}_0 \tag{1.51}$$

where $U_s = Nc_2 \int d^3\mathbf{r}|\psi(\mathbf{r})|^4$ is the spin interaction energy per atom, and $\hat{\mathbf{S}}$ is the total spin operator.

In the case of sodium, we have $a_2 > a_0$ and so the parameter c_2 is positive. The spin-dependent interactions therefore favor the state of minimum total spin and is denoted as antiferromagnetic. Other species such as ^{87}Rb have $a_2 < a_0$: the spin interactions are then ferromagnetic and favor the parallel alignment of the spins. The magnetic field on the other hand favors the $|m_F = 0\rangle$ state through the quadratic Zeeman effect. The interplay between these two effects under the constraint that the magnetization is conserved determines the ground-state of the spinor condensate. In the following we focus on the antiferromagnetic case only which is realized for Sodium atoms that we study experimentally.

1.4.2 Mean-field approximation

We here present the mean-field approximation, independently of the SMA. We will combine the two in section 1.4.3.

In the presence of a magnetic field, the total Hamiltonian is the sum of the spin-dependent Hamiltonian $\hat{H}_s$ (1.48) and of the spin-independent Hamiltonian

$$\hat{H}_0 = \sum_i \int d^3\mathbf{r}\hat{\Psi}_i^\dagger(\mathbf{r})\left[-\frac{\hbar^2}{2m}\nabla^2 + V_{\text{ext}}(\mathbf{r})\right]\hat{\Psi}_i(\mathbf{r}) + \bar{H} \tag{1.52}$$

where $\bar{H}$ is defined in expression (1.40). The mean-field approximation assumes that all the atoms share the same single-particle state $\phi = (\phi_{+1}, \phi_0, \phi_{-1})^T$. Each component ϕ_i plays the role of the wavefunction of the atoms in the spin state $|m_F = i\rangle$. We can generally write the N-body state of the condensate as

$$|\Psi\rangle_N = \frac{1}{\sqrt{N!}}\left(\hat{a}_\phi^\dagger\right)^N|0\rangle \tag{1.53}$$

where $\hat{a}_\phi^\dagger$ creates one atom in the single-particle state ϕ. This state is normalized: $\int \phi(\mathbf{r})^*.\phi(\mathbf{r})\mathrm{d}\mathbf{r} = 1$. By inserting this N-body state in the total Hamiltonian $\hat{H}_0 + \hat{H}_s$ we obtain the energy functional

$$\begin{aligned} E_{\text{tot}}[\phi_{+1}, \phi_0, \phi_{-1}] = &\sum_{i=\pm1,0}\left[\frac{\hbar^2}{2m}\int|\nabla\phi_i|^2 + \int V_{ext}|\phi_i|^2 + \frac{c_0}{2}\int|\phi_i|^4\right] \\ &+\frac{c_2}{2}\int\left(|\phi_{+1}|^2 - |\phi_{-1}|^2\right)^2 + 2|\phi_0|^2\left(|\phi_{+1}|^2 + |\phi_{-1}|^2\right) + 2\left(\phi_0^2\phi_{+1}^*\phi_{-1}^* + c.c\right) \\ &+\sum_{i=\pm1,0} E_i\int|\phi_i|^2 \end{aligned} \tag{1.54}$$

The first line corresponds to the spin-independent part of the energy: the kinetic energy, the potential energy and the spin-independent interaction energy. The second line corresponds to the spin-dependent interaction energy and the third line to the Zeeman energy. From the variational minimization of the free energy $E_{\text{tot}} - \mu\langle N\rangle - \eta\langle S_z\rangle$ with respect to the ϕ_i one obtains a set of coupled Gross-Pitaevskii (GP) equations for the wavefunction of the ground state:

$$(\mu+\eta)\phi_{+1} = (\mathcal{H} + E_{+1} + c_2(n_{+1}+n_0-n_{-1}))\,\phi_{+1} + c_2\phi_0^2\phi_{-1}^* \tag{1.55}$$

$$\mu\phi_0 = (\mathcal{H} + E_0 + c_2(n_{+1}+n_{-1}))\,\phi_0 + 2c_2\phi_0^*\phi_{+1}\phi_{-1} \tag{1.56}$$

$$(\mu-\eta)\phi_{-1} = (\mathcal{H} + E_{-1} + c_2(n_{-1}+n_0-n_{+1}))\,\phi_{-1} + c_2\phi_0^2\phi_{+1}^* \tag{1.57}$$

where:

$$\mathcal{H} = -\frac{\hbar^2\nabla^2}{2m} + V_{\text{ext}}(\mathbf{r}) + c_0 n_{\text{tot}} \tag{1.58}$$

We have noted $n_i = |\phi_i|^2$, $n_{\text{tot}} = n_{+1}+n_0+n_{-1}$, and E_i is the energy shift of the state $|m_F = i\rangle$ due to the quadratic Zeeman effect and is given by $E_i = qi^2$. η is the Lagrange factor associated to the conservation of the magnetization, exactly in the same way that the chemical potential μ is associated to the conservation of total atom number. In these equations the last term corresponds to the spin-exchange part of the interactions and is responsible for the redistribution of the atoms between the three spin states when out of equilibrium.

1.4.3 Ground-state in the Single-mode approximation

We now consider the mean-field and the single-mode approximations together. As we already mentioned, a key characteristic of the spinor gas is the conservation of its magnetization. This constraint has dramatic consequences on the thermodynamic properties of the system and has to be considered in the search for its ground-state. In particular the mean-field solution we derive here is not an absolute ground state where the magnetization is let free but describes the states effectively accessible to the system in experimental conditions. After having obtained an expression for the mean-field solution we highlight the existence of a phase transition.

In the SMA the spatial part of the spinor wavefunction is factorized out and we can then focus on the spin part of the single particle state $|\phi\rangle$. We write

$$|\phi(\mathbf{r})\rangle = \psi(\mathbf{r}) \otimes |\boldsymbol{\zeta}\rangle \tag{1.59}$$

The spin state $|\boldsymbol{\zeta}\rangle$ can be parametrized in the standard basis by

$$|\boldsymbol{\zeta}\rangle = \begin{pmatrix} \sqrt{n_{+1}}e^{i\theta_{+1}} \\ \sqrt{n_0}e^{i\theta_0} \\ \sqrt{n_{-1}}e^{i\theta_{-1}} \end{pmatrix} \tag{1.60}$$

We have here 6 real parameters: three relative populations $n_{\pm1,0}$, and three phases $\theta_{\pm1,0}$. The state $|\boldsymbol{\zeta}\rangle$ verifies $\langle\hat{N}_i\rangle = n_i N$. One population can be dropped because of the normalization condition $n_{+1}+n_{-1}+n_0 = 1$. One phase also disappears if we consider it as an irrelevant global phase. We are left with 4 truly free parameters: 2 amplitudes and 2 phases. We choose the parametrization:

$$\begin{array}{cc} x = n_{+1}+n_{-1} & m_z = n_{+1}-n_{-1} \\ \Theta = \theta_{+1}+\theta_{-1}-2\theta_0 & \alpha = \theta_{+1}-\theta_{-1} \end{array} \tag{1.61}$$

to make the average reduced magnetization $m_z = \langle N_{+1} - N_{-1}\rangle/N$ clearly appear. The normalization of the state imposes the relations $0 \leq x \leq 1$ and $|m_z| \leq x$. The spinor wavefunction becomes (up to a global phase):

$$|\boldsymbol{\zeta}\rangle = \begin{pmatrix} \sqrt{(x+m_z)/2}e^{i(\Theta+\alpha)/2} \\ \sqrt{1-x} \\ \sqrt{(x-m_z)/2}e^{i(\Theta-\alpha)/2} \end{pmatrix} \tag{1.62}$$

We insert this expression in the SMA Hamiltonian (1.51) and get the spin-energy functional:

$$\frac{E_{\text{spin}}}{NU_s} = \frac{1}{2}\left(m_z^2 + 2x(1-x) + 2\cos\Theta(1-x)\sqrt{x^2-m_z^2}\right) + \tilde{q}x \tag{1.63}$$

where we defined $\tilde{q} = q/U_s$. We now minimize this quantity with the only free parameters x and Θ, as the phase α does not appear, and the magnetization m_z is fixed. $\tilde{q}$ is an external parameter imposed to the system. We immediately see that in the case of antiferromagnetic interactions ($U_s > 0$) the energy is always minimized by $\Theta = \pi$, independently of the value of m_z and x. On the contrary the solution for x depends on the magnetization and on the quadratic Zeeman effect.

- If $m_z = 0$ the energy functional reduces to $E_{\text{spin}} = Nqx$, so that $x = 0$ as soon as $q > 0$. In this case all the atoms are in the spin state $|m_F = 0\rangle$.
  At zero magnetization and zero field, the Hamiltonian is rotationally invariant and x can take any value from 0 to 1. This defines a whole family of degenerate ground states characterized by $n_{+1} = n_{-1}$. Due to the rotational symmetry these states are all the states with eigenvalue $m_F = 0$ relatively to one arbitrary direction of space. We note θ and ϕ the polar angles defining this direction. The degenerate ground states correspond to all the rotations $\mathcal{R}(\theta,\phi)$ of the $|m_F = 0\rangle^{\otimes N}$ spin state. They are referred to as polar states and are represented in the standard basis by the vector

$$|\vec{\zeta}_{\theta,\phi}\rangle = \mathcal{R}(\theta,\phi)\begin{pmatrix} 0 \\ 1 \\ 0 \end{pmatrix} = \begin{pmatrix} -\frac{1}{\sqrt{2}}\sin\theta e^{-i\phi} \\ \cos\theta \\ \frac{1}{\sqrt{2}}\sin\theta e^{i\phi} \end{pmatrix}. \tag{1.64}$$

- If $m_z > 0$, the result of the minimization depends on the value of q. We define the critical value q_c:

$$q_c = U_s\left(1 - \sqrt{1-m_z^2}\right) \tag{1.65}$$

  The form of the mean-field ground state depends on how q compares to q_c:

  - if $q \leq q_c$, then E_{spin} is minimum for $x = 1$. The ground-state reads:

$$|\vec{\zeta}\rangle = \begin{pmatrix} \sqrt{(1+m_z)/2}e^{i\phi} \\ 0 \\ \sqrt{(1-m_z)/2}e^{-i\phi} \end{pmatrix} \tag{1.66}$$

    The quadratic Zeeman effect is not strong enough to overcome the immiscibility of $|m_F = 0\rangle$ with $|m_F = \pm 1\rangle$. The ground state is determined by the minimization of the spin-dependent interaction energy which is obtained by mixing

only $|m_F = +1\rangle$ and $|m_F = -1\rangle$. The state $|m_F = 0\rangle$ is not populated and the population of the two others $|m_F = +1\rangle$ and $|m_F = -1\rangle$ is determined by the value of the magnetization m: $n_{\pm 1} = (1 \pm m_z)/2$.

– if $q > q_c$, then x is the solution of the equation $\partial E_{\text{spin}}/\partial x = 0$ which reads:

$$(1-2x)(\sqrt{x^2 - m_z^2} - x) + \frac{q}{U_s}\sqrt{x^2 - m_z^2} = m_z^2 \tag{1.67}$$

A fraction of the atoms now populates the $m = 0$ state, due to the stronger quadratic Zeeman effect: adding some atoms in $|m_F = 0\rangle$ now removes more Zeeman energy than it adds interaction energy. Asymptotically, for very large q the ground state is found by minimizing the quadratic Zeeman energy, so that $x \to m_z$ or equivalently $n_0 \to 1 - m_z$ when $q \to +\infty$.

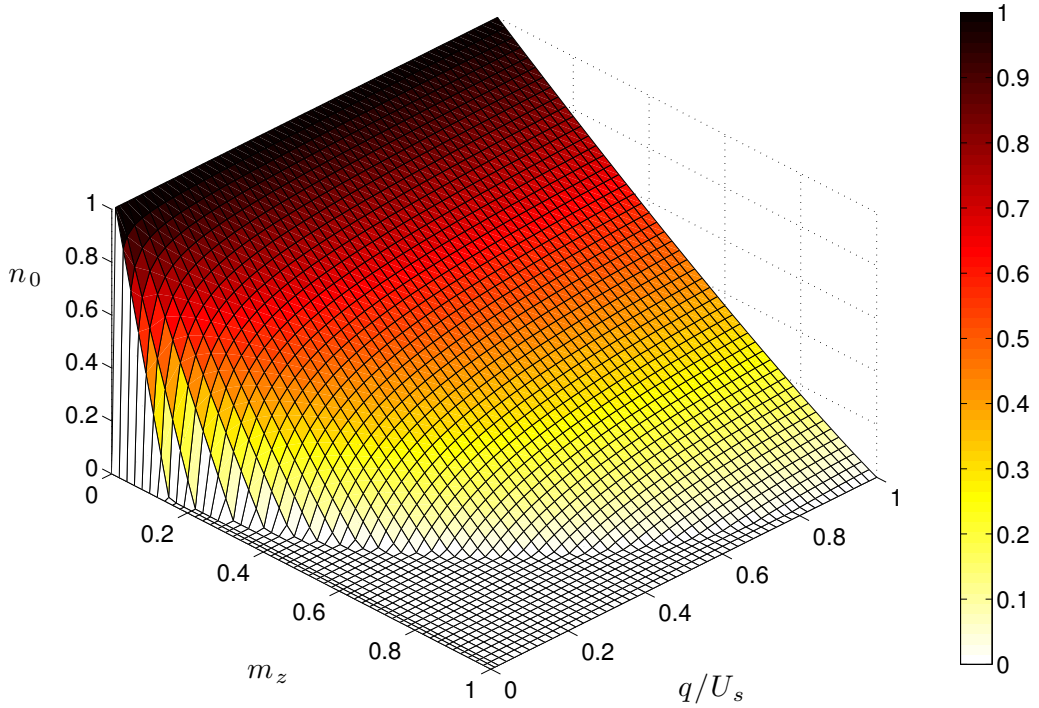

Figure 1.5: Magnetic phase diagram of an antiferromagnetic spin-1 Bose-Einstein condensate in the single mode approximation. The relative population of the $|m_F = 0\rangle$ state in the mean-field ground state is represented as a function of the magnetization m_z and the reduced quadratic Zeeman energy q/U_s. We clearly see two phases: one where $n_0 = 0$ and the second where $n_0 > 0$.

Two different phases are thus possible: in the first one, at low magnetic field, the spin-dependent interactions dominate over the quadratic Zeeman effect and prevents the accumulation of atoms in the $|m_F = 0\rangle$. The atoms distribute between the states $|m_F = \pm 1\rangle$ in order to fulfill the condition $n_{+1} - n_{-1} = m_z$. We call this phase antiferromagnetic. On the contrary in the second phase, when the quadratic Zeeman effect gets larger than the critical value q_c the gain in Zeeman energy brought by some occupation of the $|m_F = 0\rangle$ state prevails over its cost in interaction energy. When q reaches the

value q_c the population of $|m_F = 0\rangle$ in the ground state starts to rise. Then as q gets larger this population increases and finally reaches an asymptotic value defined by the constraint of fixed magnetization that imposes a minimum occupation of the state $|m_F = +1\rangle$ equal to m_z. We call this phase the broken-axisymmetry phase. Thus we here identified a phase transition described by the order parameter n_0: n_0 is zero in the antiferromagnetic phase, and continuously increases with q to $1 - m_z$ in the broken-axisymmetry phase. The phase transition is of second order.

1.4.4 Validity of the single-mode approximation

As we have seen previously, due to the spin-dependent interactions atoms in the spin states $|m_F = \pm 1\rangle$ and atoms in the state $|m_F = 0\rangle$ are not miscible in a flat potential. When in a trap, atoms in different spin states may then also prefer to spatially separate to minimize their spin-dependent energy. The formation of such spin domains of course violates the single-mode approximation. Indeed, the assumption of a common mode has been shown not to be rigorously verified in an harmonic trap in the presence of an external magnetic field [62], and the resort to this approximation needs to be carefully justified. In this section we want to check that the deviation to the SMA are negligible in our experimental conditions, so that we can compare our experimental results to the SMA predictions derived in the previous section, in particular for the magnetic phase diagram whose experimental measurement is presented in chapter 3.

We can give a first qualitative argument to estimate the validity of the single-mode approximation. The three spin states will share the same spatial mode if the spatial deformation of the different wavefunctions cost more kinetic energy than it reduces the interaction energy. The minimum size of a spin domain can be evaluated by the spin healing length, which corresponds to the scale on which the spin wavefunctions recover from a perturbation. It is given by

$$\xi_s = \sqrt{\frac{\hbar^2}{2mc_2 n}} \tag{1.68}$$

where n is the atomic density. If the size of the condensate is smaller than or of the same order as the spin healing length, the three spin components can not phase separate and we expect the single-mode approximation to be verified. For a given trap geometry, increasing the atom number brings the condensate in the Thomas-Fermi regime where its size is given by $R_{TF} = \sqrt{2\mu/m\omega^2}$, with the chemical potential $\mu \simeq c_0 n$. The condition $R_{TF} \lesssim \xi$ then becomes

$$\frac{\mu}{\hbar\omega} \lesssim \sqrt{\frac{c_0}{c_2}} \tag{1.69}$$

This condition defines an upper bound for the chemical potential and so for the atom number, for the SMA to be valid. Besides, in an anisotropic trap the relation (1.69) may hold in some directions and fail in the others. For a typical density of $n = 4 \times 10^{14}\,\mathrm{cm}^{-3}$, the spin healing length in a sodium condensate is on the order of $1\,\mu$m, comparable to the size of our experimental atomic sample.

To justify more precisely the validity of the single-mode approximation in our experiment, we calculate numerically the spatial mode of the three spin states in a Bose-Einstein condensate of Sodium under the constraint of conserved total atom number and of conserved magnetization, and in the presence of an external magnetic field. If we do not make

the single-mode approximation, the spinor condensate at zero temperature is represented in a mean-field description by a vector $(\phi_{+1}(\mathbf{r}), \phi_0(\mathbf{r}), \phi_{-1}(\mathbf{r}))^T$, whose components are the wavefunctions of the three spin states and obey the set of coupled Gross-Pitaevskii equations (1.55) to (1.57). For simplicity we consider here an isotropic trapping potential: $V_{\text{ext}}(\mathbf{r}) = \frac{1}{2}m\omega^2 r^2$, so that the problem is rotationally symmetric in real space and the wavefunctions of the ground state are functions of the only radial variable r. We note ψ the SMA wavefunction, solution of equation (1.50).

The wavefunctions in the ground state minimize the energy functional (1.54). From this expression we can already examine the validity of the SMA in two situations: when the magnetization is zero, and when the gas is polarized.

- In the first case, one has $\eta = 0$. The symmetric role of ϕ_{+1} and ϕ_{-1} in the GP equations then imposes $\phi_{+1} = \phi_{-1}$. We can show that under this condition the spin-dependent part of E_{tot} reduces to the Zeeman energy. If a magnetic field is applied, one has $q > 0$ and the minimization of E_{tot} imposes $\phi_{+1} = \phi_{-1} = 0$. The wavefunction ϕ_0 is then found from the minimization of the spin-independent terms, which corresponds to the definition (1.50) of the SMA wavefunction. In the case $q = 0$ the Zeeman energy vanishes and the three wavefunctions verify (1.50). At zero magnetization the SMA is thus exact.

- In the case of a polarized cloud, one finds that the wavefunction ϕ_{+1} verifies an equation similar to (1.50), but with an interaction parameter $c_0 + c_2 = 4\pi\hbar^2 a_2/m$ instead of $c_0 = 4\pi\hbar^2\bar{a}/m$. The deviation to the SMA is due to the term c_2 which is very small compared to c_0, so that the deviation to the wavefunction ψ is also small. (Strictly speaking the notion of a common mode has little meaning in this case, since two of the three spin components are absent. We here consider the deviation of this mode to ψ.). In all the other situations, the validity of the SMA has to be tested numerically.

Similarly to the scalar case, a set of time-dependent GP equations can be derived that describe the evolution in time of the wavefunctions of the condensate. They are given in Appendix A. To calculate numerically the ground-state wavefunctions we propagate these coupled GP equations in imaginary time using a Backward Euler Finite Difference scheme [63]. One of the major difference in the numerical resolution compared to the scalar GP equation is the necessity to ensure the conservation of the magnetization throughout the propagation in imaginary time. This can be done by introducing a Lagrange multiplier, which has to be continuously re-adjusted to maintain a steady magnetization. We rather follow the method developped in [64], where the wavefunctions are properly projected after each propagation step on the subspace of adequate magnetization. The numerical methods are described in Appendix A.

We use this algorithm to calculate the solution of the coupled GP equations for a condensate in a spherical trap of frequency $\omega = 2\pi \times 600\,\text{Hz}$ (which is close to the geometry of the trap we use in our experiments). To investigate the validity of the single mode approximation in our experimental conditions we compute the wavefunction of the three spin components for an atom number $N = 5000$, for positive magnetizations and varying magnetic fields. The figure (1.6) shows an example of numerical solution of the GP equation (calculated for a magnetic field of 200 mG and a magnetization of 0.3). The three spatial modes are similar, and are also close to the SMA solution ψ (that we did not plot for clarity). To quantify the deviation of the three wavefunctions to the SMA solution ψ

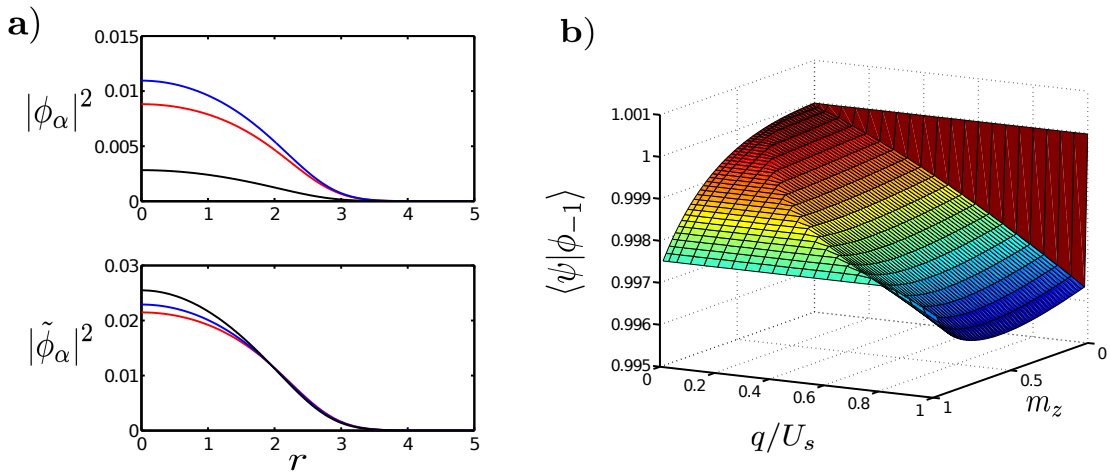

Figure 1.6: **a**): Original (top figure) and normalized (bottom figure) density profiles of the three spin components in a spherical trap of frequency $\omega = 2\pi \times 600\,\text{Hz}$. The red curve corresponds to the $m_F = +1$ spin state, the black one to $m_F = 0$ and the blue one to $m_F = -1$. The radius r is given in units of the oscillator length a_{ho}. The parameters are $N = 10^3$, $q/U_s = 0.2$ and $m_z = 0.3$. **b**): magnetization and magnetic field dependence of the overlap integral $\langle\Psi_{SMA}|\Psi_{-1}\rangle$, for $N = 10^3$ and $\omega = 2\pi \times 600\,\text{Hz}$.

we calculate the overlap integrals $\langle\psi|\tilde{\phi}_i\rangle = \int d\mathbf{r}\psi^*(\mathbf{r})\tilde{\phi}_i(\mathbf{r})$, where $\tilde{\phi}_i = \phi_i/\sqrt{N_i}$ are the normalized wavefunctions. The figure (1.6) shows the results for the state $|m_F = -1\rangle$ as a function of the magnetic field B and the magnetization m_z. One sees that the overlap integral goes down with B, but stays above 0.99 for field lower than 1 G. For the states $|m_F = +1\rangle$ and $|m_F = 0\rangle$, the overlap integral is equal to unity within 1.10^{-3}. We check that the SMA is exactly verified for $m_z = 0$.

The effect of the deviation of the actual wavefunctions to the SMA prediction is evaluated by the change it causes in the total energy of the system. We note $E_{SMA} = E_{\text{tot}}(\psi, \psi, \psi)$ the total energy of the system in the SMA, which we calculate using the results we derived previously for the ground-state in this approximation. We then consider the difference $\Delta E_{\text{tot}} = E_{\text{tot}} - E_{SMA}$, normalized to E_{SMA}. We find that this relative difference stays very small in the whole diagram, on the order of 10^{-4}, which actually corresponds to the energy resolution of our algorithm. Thus, up to the precision of our calculation we do not measure any difference with the SMA solution from the energetic point of view. We additionally check that the variation of the spin-independent part of the energy (corresponding to the terms of the first line of (1.54)) is negligible compared to the spin-dependent energy (the two other lines). This condition is required to state that the ground-state is determined by the minimization of the spin-dependent energy only, as done in the previous section. From the results of our numerical simulation we find that the spin-independent energy varies over the whole phase diagram by less than $5 \times 10^{-4}\hbar\omega$, while the spin energy is everywhere much larger but in a very narrow region arrow the point $B = 0, m_z = 0$ where it vanishes. The two parts of the energy are shown in figure (1.7).

We now look at the phase and population of the three spin components. First we check

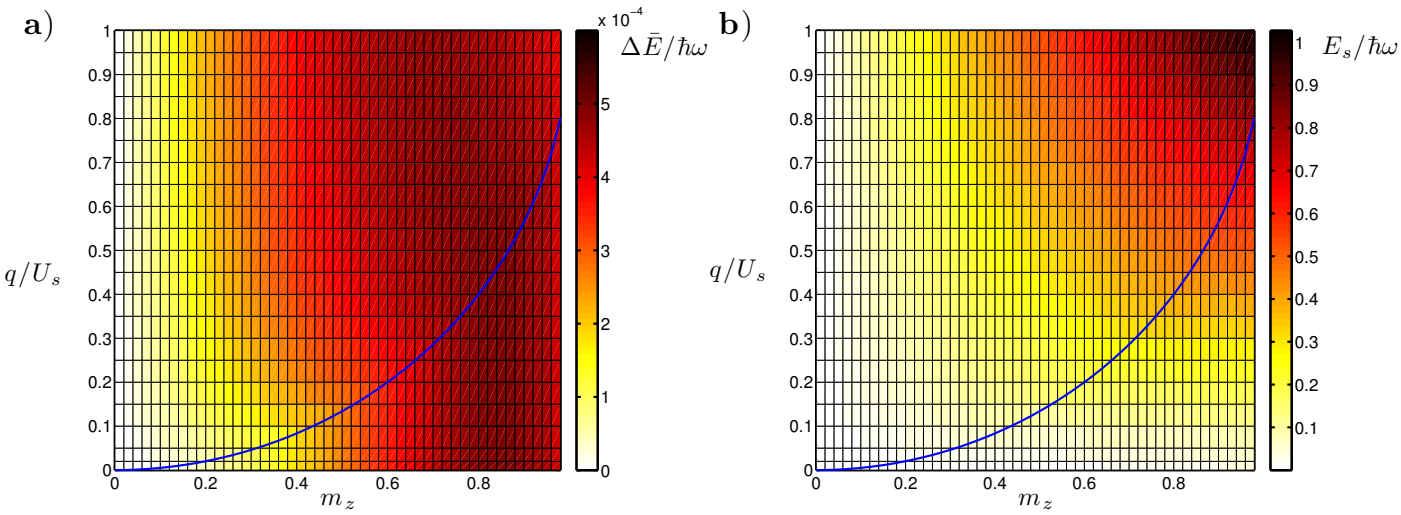

Figure 1.7: **a**): Variation of the spin-independent energy (kinetic+potential+interaction) $\Delta\bar{E} = \bar{E} - \bar{E}_0$, where $\bar{E}_0$ is the energy at $m_z = 0$ and $q = 0$. **b**): Spin-dependent energy (Zeeman+spin interaction) E_s. The spin energy E_s is everywhere much larger than the variation of $\bar{E}$, which allows to decouple the spin and spatial degrees of freedom and to determine the ground state from the minimization of the spin energy. Note the different colorscales. The blue line each time represents the SMA prediction of the critical q. The parameters are $\omega = 2\pi \times 600\,\text{Hz}$ and $N = 5000$ atoms.

that the three wavefunctions have uniform phases and that the relation $\Theta = \pi$ holds for all fields and magnetizations. Considering the energy functional (1.54) it appears that space-dependent phases would only add energy (kinetic and spin energy due to the spin exchange term). The minimization of the spin energy then fixes $\Theta = \pi$ as in the SMA. But our main interest in calculating the GP solution was the difference in n_0 between the SMA prediction and this solution, as the measurement of the magnetic phase diagram is a direct way of experimentally checking the mean-field theory of spinor gases (see chapter 3). This difference in the phase diagram is shown in figure (1.8), as well as the population n_0 obtained from the GP equations. The deviation to the SMA prediction essentially lies around the phase transition, but remains on the percent level with our choice of parameters. Close to the transition we expect that the derivative $\partial E_{\text{tot}}/\partial n_0$ is very small. Because of this, the precision of the algorithm in n_0 is decreased at these points and here again we conclude that, up to our numerical precision, we can not find a difference in the value of the critical magnetic field.

Finally, we also use our numerical simulation to consider the effect of the atom number N on the validity of the SMA in our trap. If we increase N and keep the frequency ω constant the chemical potential increases as well, and according to the condition (1.69) we expect the precision of the SMA to decay with N. We consider a given point in the phase diagram where we can expect the three spin states to be populated, and solve the GP equations for an increasing atom number while keeping the trap frequency constant. We choose $B = 0.3\,\text{G}$ ($q = 25\,\text{Hz}$) and $m_z = 0.5$. The results are presented in figure (1.9) for $N = 10^3, 10^4$ and 10^5. We can calculate the chemical potential μ from the solution of

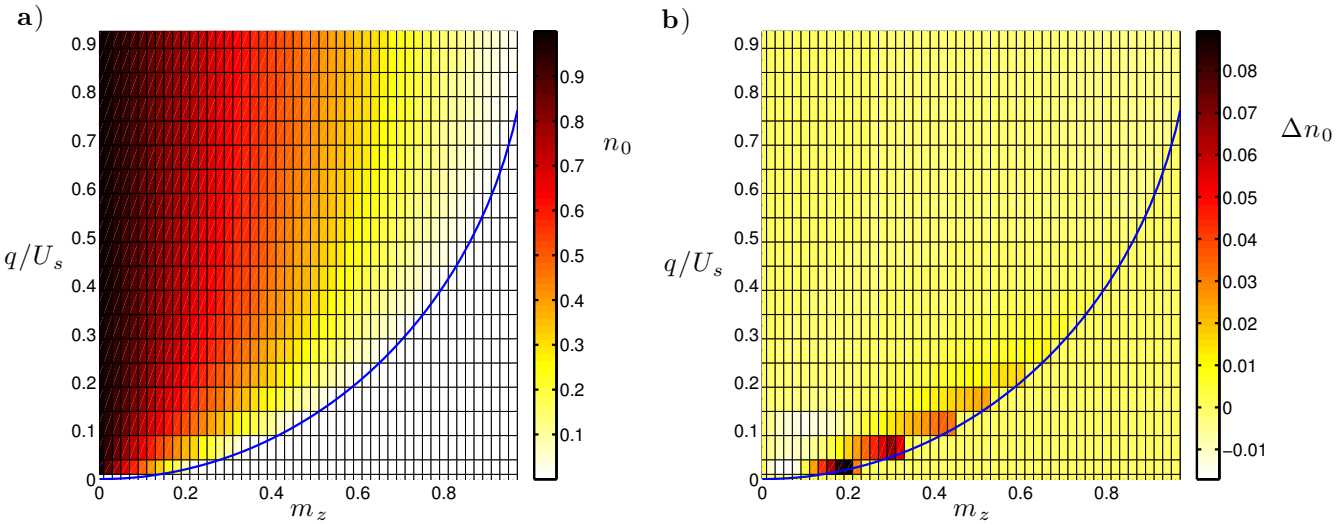

Figure 1.8: **a**): Relative population n_0 obtained from the numerical resolution of the Gross-Pitaevskii equations, as a function of the magnetic field B and the magnetization m_z. The blue solid line corresponds to the SMA prediction of the critical field. **b**): Difference of the relative population n_0 calculated from the Gross-Pitaevskii equations to the one calculated in the SMA. The blue line is the same as in **a**). The deviation is localized close to the phase transition. The parameters are $\omega = 2\pi \times 600\,\text{Hz}$ and $N = 5000$ atoms.

the GP equation (1.56):

$$N_0\mu = \int \phi_0^* \mathcal{H}\phi_0 + c_2(n_{+1} + n_{-1})n_0 + 2c_2(\phi_0^*)^2\phi_{+1}\phi_{-1} \tag{1.70}$$

where $\mathcal{H}$ is defined in (1.58). For Sodium we have $\sqrt{c_0/c_2} \approx 5.28$. As it appears in figure (1.9), the normalized radial wave functions differ more and more as N increases, and become significantly different already for $N = 10^4$. Yet, they mainly differ in the region of small r, so that once multiplied by an elementary volume and integrated, the difference becomes very small, as shown in table (1.2). For this reason the substantial difference of the radial wave functions does not make a substantial difference for energetics.

From all this we conclude that the SMA describes well our experimental system.

N	1.10^3	1.10^4	1.10^5
$U_s/\hbar\omega$	0.037	0.113	0.297
$\mu/\hbar\omega$	2.24	3.98	6.86
$1 - \langle\psi\|\phi_{-1}\rangle$	8×10^{-4}	3.6×10^{-3}	7.8×10^{-3}
$\Delta E_{tot}/E_{SMA}$	$\simeq 1 \times 10^{-4}$	3×10^{-4}	9×10^{-4}

Table 1.2: Spin energy U_s, chemical potential μ, overlap integral $\langle\psi|\phi_{-1}\rangle$ and difference ΔE_{tot} of the total energy to the SMA energy for $N = 10^3, 10^4$ and 10^5.

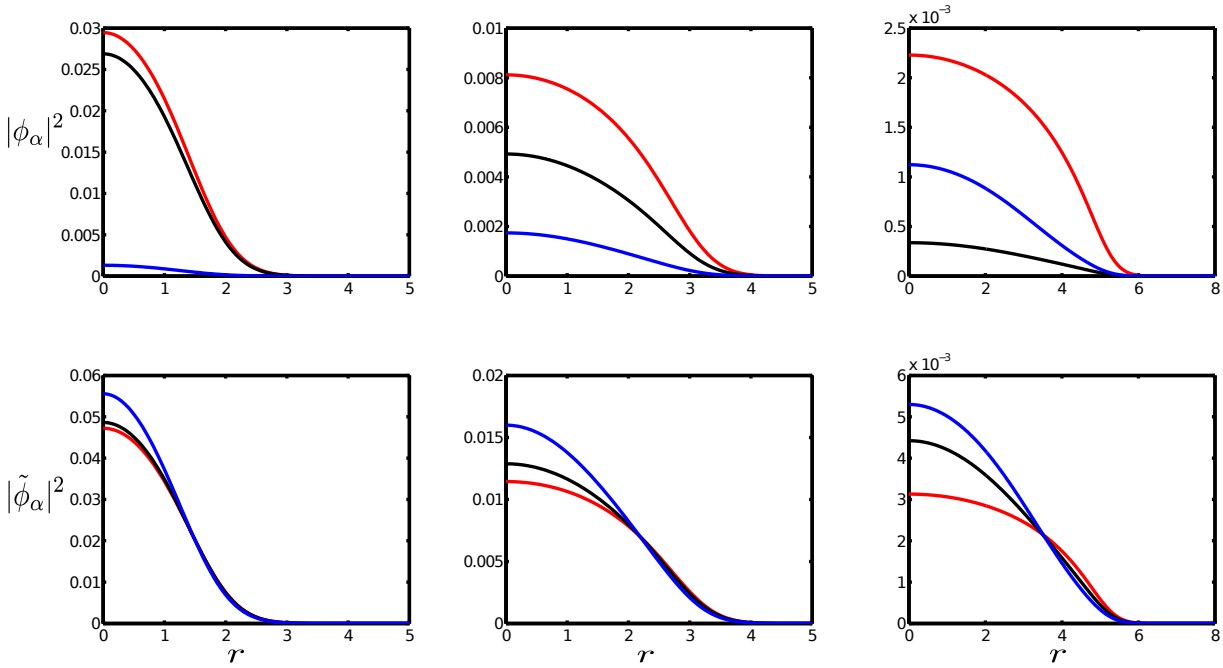

Figure 1.9: Original (upper line) and renormalized (lower line) density profiles of the three spin components in a spherical harmonic trap of frequency $\omega = 2\pi \times 600$ Hz, for atom number $N = 10^3, 10^4$ and 10^5 (from left to right). The color code is the same as in figure (1.6). The parameters are $B = 0.3$ G and $m_z = 0.5$. Note the different scale of the radial axis of the third column. The density are expressed in unit of a_{ho}^{-3}, the radius r is expressed in unit of a_{ho}.

1.4.5 Excitations in a spinor condensate

We now want to derive the collective excitations in a spinor condensate. We follow the same procedure as for the scalar Bose gas explained in section 1.2.3. For simplicity reasons, we consider a box potential with periodic boundary conditions, and will then decompose the atomic field operator in the basis of plane waves. We additionally assume that the condensate is in the polar state directed along the z axis, meaning all the condensed atoms are in the $|m_F = 0\rangle$ state. (For a complete treatment of the Bogoliubov theory of spinor condensates see for instance [65] and [36]). We can write the field operator as:

$$\hat{\Psi}(\mathbf{r}) = \begin{pmatrix} 0 \\ \phi_0(\mathbf{r}) \\ 0 \end{pmatrix} + \begin{pmatrix} \delta\hat{\Psi}_{+1}(\mathbf{r}) \\ \delta\hat{\Psi}_0(\mathbf{r}) \\ \delta\hat{\Psi}_{-1}(\mathbf{r}) \end{pmatrix} \tag{1.71}$$

where ϕ_0 is the wavefunction of the condensate and corresponds to the mode $\mathbf{k} = 0$. $\delta\hat{\Psi}_\alpha$ represents the non-condensed atoms in the spin state $|m_F = \alpha\rangle$ and can be developed on the plane wave basis:

$$\delta\hat{\Psi}_\alpha = \frac{1}{\sqrt{V}} \sum_{\mathbf{k}\neq 0} e^{i\mathbf{k}.\mathbf{r}} \hat{a}_{\alpha,\mathbf{k}} \tag{1.72}$$

where V is the volume of the box. We insert this expression in the total Hamiltonian

$$\hat{H} = \int \mathrm{d}\mathbf{r}\hat{\Psi}^\dagger(\mathbf{r})(-\frac{\hbar^2}{2m}\nabla^2)\hat{\Psi}(\mathbf{r}) + \frac{c_0}{2}\hat{\rho}^2(\mathbf{r}) + \frac{c_2}{2}\hat{\mathbf{S}}^2(\mathbf{r}) \tag{1.73}$$

As for the scalar gas, we retain only terms that are at least quadratic in $\hat{a}_{0,\mathbf{k}=0}$ and $\hat{a}^\dagger_{0,\mathbf{k}=0}$ (there are no condensed atoms in the $|m_F = \pm 1\rangle$ states). We then make the Bogoliubov approximation and take $\phi_0(\mathbf{r}) = \sqrt{N_{0c}/V}$, where N_{0c} denotes the number of condensed atoms. Finally, we do the replacement $N_{0c} = N - \sum_{\alpha,\mathbf{k}\neq 0} \hat{a}^\dagger_{\alpha,\mathbf{k}}\hat{a}_{\alpha,\mathbf{k}}$. After some algebra we find:

$$\begin{aligned}\hat{H} = \frac{c_0 N^2}{2V} &+ \sum_{\mathbf{k}\neq 0}(\epsilon_k + \frac{c_0 N}{V})\hat{a}^\dagger_{0,\mathbf{k}}\hat{a}_{0,\mathbf{k}} + \frac{c_0 N}{V}\sum_{\mathbf{k}\neq 0}(\hat{a}^\dagger_{0,\mathbf{k}}\hat{a}^\dagger_{0,-\mathbf{k}} + \hat{a}_{0,\mathbf{k}}\hat{a}_{0,-\mathbf{k}}) \\ &+ \sum_{\substack{\mathbf{k}\neq 0\\ \alpha=\pm 1}}(\epsilon_k + \frac{c_2 N}{V})\hat{a}^\dagger_{\alpha,\mathbf{k}}\hat{a}_{\alpha,\mathbf{k}} + \frac{c_2 N}{V}\sum_{\mathbf{k}\neq 0}(\hat{a}^\dagger_{+1,\mathbf{k}}\hat{a}^\dagger_{-1,-\mathbf{k}} + \hat{a}_{+1,\mathbf{k}}\hat{a}_{-1,-\mathbf{k}})\end{aligned} \tag{1.74}$$

where $\epsilon_k = \hbar^2 k^2/2m$. The excitations in the state $|m_F = 0\rangle$ are decoupled from the excitations of the two other states, and the restriction of the Hamiltonian to this state has a structure similar to the Hamiltonian we derived in the case of the scalar condensate. We can then perform an equivalent Bogoliubov transformation. To diagonalize the part of the Hamiltonian involving the $|m_F = \pm 1\rangle$ states the Bogoliubov transformation is slightly more complicated as it requires to define two additional operators:

$$\hat{a}_{0,\mathbf{k}} = h_k\hat{d}_{\mathbf{k}} - g_k\hat{d}^\dagger_{-\mathbf{k}} \tag{1.75}$$

$$\hat{a}_{+1,\mathbf{k}} = u_k\hat{s}_{+,\mathbf{k}} - v_k\hat{s}^\dagger_{-,-\mathbf{k}} \tag{1.76}$$

$$\hat{a}_{-1,\mathbf{k}} = u_k\hat{s}_{-,\mathbf{k}} - v_k\hat{s}^\dagger_{+,-\mathbf{k}} \tag{1.77}$$

h_k, g_k, u_k and v_k are amplitudes that can be chosen real. The operators $\hat{d}_{\mathbf{k}}$, $\hat{s}_{+,\mathbf{k}}$ and $\hat{s}_{-,\mathbf{k}}$ obey bosonic commutation relations similar to (1.16), which implies $h_k^2 - g_k^2 = 1$ and $u_k^2 - v_k^2 = 1$. We insert these expressions in the Hamiltonian and choose the amplitudes so that the non-diagonal terms vanish. We end up with:

$$\hat{H} = E_0 + \sum_{\mathbf{k}\neq 0}\varepsilon_{d,k}\hat{d}^\dagger_{\mathbf{k}}\hat{d}_{\mathbf{k}} + \sum_{\pm,\mathbf{k}\neq 0}\varepsilon_{s,k}\hat{s}^\dagger_{\pm,\mathbf{k}}\hat{s}_{\pm,\mathbf{k}} \tag{1.78}$$

where E_0 the energy of the ground state and with the spectrum of excitations:

$$\varepsilon_{d,k} = \sqrt{\epsilon_k(\epsilon_k + 2c_0 n)} \tag{1.79}$$

$$\varepsilon_{s,k} = \sqrt{\epsilon_k(\epsilon_k + 2c_2 n)} \tag{1.80}$$

where $n = N/V$. There are three Bogoliubov modes. The mode associated with the $m_F = 0$ state corresponds to density excitations of the condensate. It has the same properties than the Bogoliubov mode of the scalar gas: short wavelength excitations are free particle excitations, whereas long wavelength excitations are phonons, associated with the sound speed $c_d = \sqrt{c_0 n/m}$. The two other modes, associated with the particles in the states $m_F = \pm 1$ are spin-wave modes. They have a dispersion law similar to density waves, but a lower energy, as $c_2 \ll c_0$. The associated speed $c_s = \sqrt{c_2 n/m}$ is then also lower. For a typical density $n \sim 10^{14}\,\mathrm{cm}^{-3}$ one finds in Sodium $c_d \sim 0.5\,\mathrm{cm.s}^{-1}$ and $c_s \sim 0.1\,\mathrm{cm.s}^{-1}$. As we did for the scalar gas in the first section we can estimate the energy of the first

spin-wave mode in a spherical trap of frequency ω by taking for the size of the box twice the Thomas-Fermi radius. We obtain :

$$\varepsilon_{s,1} \sim \frac{\hbar c_s}{R_{TF}} \sim \sqrt{\frac{c_2}{c_0}}\hbar\omega \tag{1.81}$$

These three Bogoliubov modes are gapless modes. The existence of a gapless mode expresses the spontaneous breaking of a continuous symmetry of the Hamiltonian of the system. Here the density excitations are associated to the breaking of the $U(1)$ gauge symmetry, similarly to the scalar condensate. The two spin-wave modes are associated to the spontaneous breaking of two symmetry generators of the spin Hamiltonian. In the absence of external magnetic field, the spin Hamiltonian obeys the $SO(3)$ symmetry corresponding to the invariance under spin rotations. The $SO(3)$ group admits three generators: the three spin operators $\hat{S}_x, \hat{S}_y, \hat{S}_z$, that generate the rotations around the three axis x, y, z. We considered here a condensate in the nematic state oriented along the z axis (all the atoms in the $|m_F = 0\rangle$ spin state). This state is symmetric by rotation about the z axis but breaks the symmetry by rotation about the x and y axis, thus leading to the existence of two gapless modes.

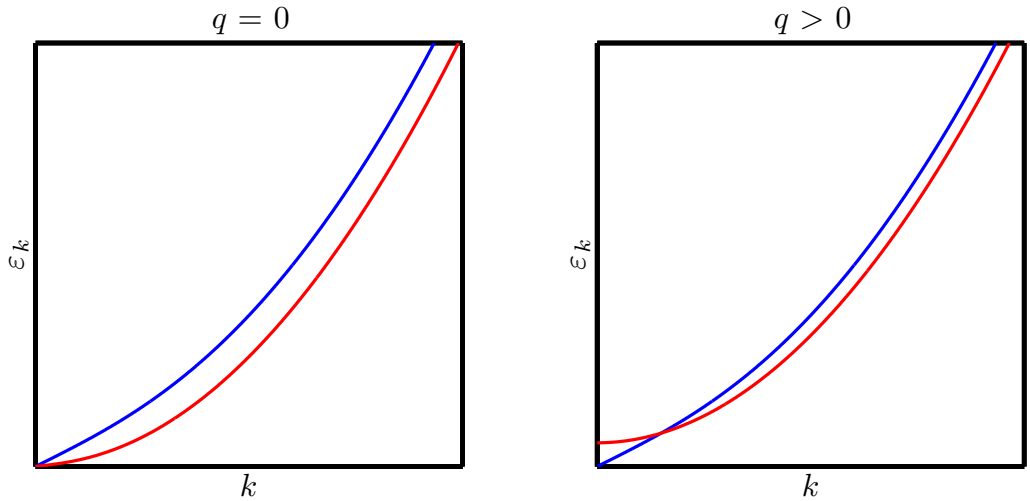

Figure 1.10: Spectrum of Bogoliubov excitations in a spinor Bose gas, calculated for a zero magnetic field (left) and for a strictly positive magnetic field (right). The blue line represents the density excitations, the red line represents the two spin-wave modes. In the presence of a magnetic field, these modes develop a gap.

In the presence of a magnetic field, the quadratic Zeeman effect simply adds a term $+q\sum_{\alpha=\pm,\mathbf{k}} \hat{a}^\dagger_{\alpha,\mathbf{k}}\hat{a}_{\alpha,\mathbf{k}}$. It is easy to see that the density mode is not affected, and that the spin wave modes now have an energy

$$\varepsilon_{s,k} = \sqrt{(\epsilon_k + q)(\epsilon_k + q + 2c_2 n)} \tag{1.82}$$

At zero momentum the spin wave modes thus develop a gap $\sqrt{q(q + 2c_2 n)}$. In this case the magnetic field explicitly breaks the $SO(3)$ symmetry of the Hamiltonian. There is no spontaneous symmetry breaking, so no gapless mode (apart from the density excitations associated to the broken $U(1)$ symmetry.)

1.5 Conclusion

In this chapter we presented the first ingredients of the theory of spinor condensates. We established the expression of the spin-dependent interaction and found that it conserves the magnetization of the system. This conservation is a key feature of spinor condensates, and has important consequences on the thermodynamic properties of these condensates. We derived the many-body Hamiltonian of this system in the presence of an external magnetic field. We then introduced the single-mode approximation that decouples the internal and spatial degrees of freedom and thus greatly simplifies the theory. We developed a mean-field approach to determine the ground state of the antiferromagnetic spin-1 Bose gas under the constraint of conserved magnetization. We numerically checked that the SMA was valid in our experimental conditions, which allows us to compare our experimental results to the SMA predictions. This will be the aim of chapter 3. In the rest of this work we always consider that the SMA applies in the condensate. Finally we also studied the spectrum of the collective modes of a spinor condensate. We found that, in addition to the density mode present in scalar condensates, two spin-wave modes arise due to the existence of the spin-degree of freedom. We will use these results in chapter 4 and chapter 5 where we consider the effect of the finite temperature of our gases.

Chapter 2

Production, manipulation and detection of a spin-1 Bose-Einstein condensate of Sodium

In chapter 1 we derived the mean-field ground state of a spin-1 Bose gas under the constraint of conserved magnetization, and we now want to experimentally check these predictions. But before presenting our results on the measurement of the ground state we discuss in this chapter how we produce spinor Bose-Einstein condensates, how we manipulate them and finally how we detect them. In the first part we describe the experimental set-up we use to trap and cool the atomic gas. The first step of the experiment takes place in a magneto-optical trap. The atomic cloud is then transferred in a conservative optical trap and further cooled to the degenerate regime by evaporative cooling. In the first part of this chapter we present this experimental sequence. We then detail the techniques to manipulate the internal degree of freedom of the gas. In particular we explain how we control its magnetization, which is then a conserved quantity and plays a crucial role in its equilibrium properties. We finally explain how we probe the condensate and how we analyse the information we can extract from it.

2.1 Experimental methods

In the long term, the objective of our experiment is to work with spinor condensates of very small atom number (on the order of one hundred atoms) in order to create and study strongly correlated states [42]. These states are extremely sensitive to decoherence and the control of the experimental environment, and in particular of the external magnetic field, is crucial. For this reason it was planned from the beginning that at some point the whole experimental set-up should be embedded in a magnetic shield (not installed yet). The set-up we use is consequently very compact: we do not use a Zeeman slower for instance (which besides would have been hardly compatible with our magnetic fields requirements). All the experiment takes place in a single vacuum chamber. Our experimental set-up was thoroughly described in the thesis of Emmanuel Mimoun [42] and David Jacob [66]. Here we recall its main characteristics and send the reader to these two references for a detailed description. In all the following we define three directions x, y, z in the frame of the laboratory as indicated further in the figure (2.2).

2.1.1 The experimental chamber and the atomic source

We use a custom-made UHV chamber made of titanium. Titanium has a very low magnetic susceptibility, so that no magnetization develops in the core of the chamber when external magnetic fields are applied. The optical access to the center of the chamber is possible through several windows with an anti-reflection coating at 589 nm and 1064 nm. Two opposite flanges entering the chamber at its top and bottom allow an high numerical aperture access to the center of the chamber. All the pieces (windows, seals, screws) are made of amagnetic materials.
The quality of the vacuum inside the chamber is of major importance, as collisions with particles from the background pressure can heavily degrade the lifetime of the condensate. Two pumps are connected to the chamber: a "getter" pump close to the experiment, and an ionic pump which is placed at the end of a 40 cm pipe, for it contains a permanent magnet. The residual pressure in the chamber is on the order of 10^{-11} mbar.

The constraint of a single-chamber experiment imposes that the source of Sodium atoms is placed inside the chamber. We resort to *dispensers*, which are metallic enveloppe containing oxyde of Sodium (in our experiment). At room temperature they are chemically inert, but high temperatures activate an oxydo-reduction reaction that releases Sodium atoms. The increase of the temperature is done by sending an electric current of a few amperes (typically 3.5 A in our case) through the metallic enveloppe. Activating the dispensers causes a large increase in the Sodium pressure inside the chamber, on a time scale of a few seconds. Then, as they are disabled the pressure decays, corresponding to the binding of the Sodium atoms to the walls of the chamber and mostly to its windows. This decay happens on the minute timescale. Because the background pressure remains too high during this time and would hinder the cooling of the atoms we do not use the dispensers before every experimental run. Instead we control the pressure of sodium in the chamber using light-induced atomic desorption. Using power LEDs we shine UV light through several windows inside the chamber. Similarly to the photo-electric effect, atoms are released from the surface they are stuck to by absorbing a UV photon. This technique allows one to increase the pressure of Sodium by a factor 40 with respect to the background pressure. After the extinction of the desorbing light a low background pressure is restored in less than 100 ms [67].

2.1.2 Magneto-Optical Trap

A Magneto-Optical Trap (MOT) is an apparatus that traps atoms from a background gas at room temperature and cool them down to temperatures on the order of a few tens of microKelvin [68]. Its working principle is based on the viscous friction and on the spring force produced on the atoms by three pairs of contra-propagating laser beams, red-detuned and non-saturating compared to a closed atomic transition on the one hand. The friction force relies on the combination of Doppler effect and of the average effect of many photon absorption-emission processes. The spring force is created by the association of the radiation pressure and of a gradient of magnetic field. The stochastic nature of these processes sets a minimum temperature that can be achieved in a MOT, much larger than the critical temperature defining the threshold for Bose-Einstein condensation.

The atomic transition we consider in our experiment is the D_2 line of ^{23}Na, which has a wavelength of 589.158 nm and a natural linewidth $\Gamma = 2\pi \times 9.795$ MHz. The hyperfine structure of this line is represented in figure (2.1). We denote by $|F\rangle$ the states belonging

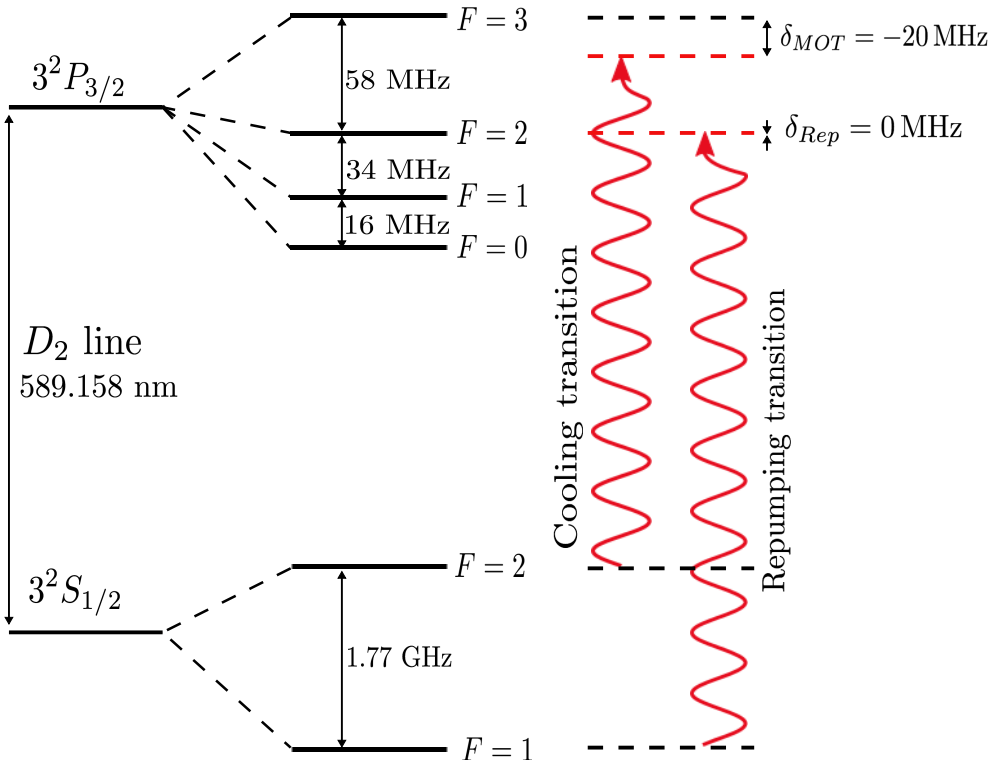

Figure 2.1: Hyperfine structure of the D_2 transition in Sodium. The cooling beam is detuned to the red of the transition $|F = 2\rangle \rightarrow |F' = 3\rangle$ by 20 MHz. The repumper beam is resonant with the transition $|F = 1\rangle \rightarrow |F' = 2\rangle$.

to the $S_{1/2}$ manifold and by $|F'\rangle$ the ones belonging to the $P_{3/2}$ manifold. We use as cooling transition the transition $|F = 2\rangle \rightarrow |F' = 3\rangle$. The MOT laser beams are detuned to the red of this transition by 20 MHz. To bring in the cooling cycle atoms initially in the state $|F = 1\rangle$ and those that decayed to this state after a non-resonant transition $|F = 2\rangle \rightarrow |F' = 2\rangle$ we need a *repumper* beam, which is resonant with the transition $|F = 1\rangle \rightarrow |F' = 2\rangle$.

Experimentally the six MOT beams are collimated with a radius of 11 mm and a power of 1.2 mW, corresponding to an intensity of $0.1\,I_{\mathrm{sat}}$ per beam. The repumper beams are superimposed with the MOT ones and have a power of $300\,\mu$W. The magnetic field gradient is created by a pair of water-cooled coils in anti-Helmoltz configuration placed on both side of the chamber on the y axis. When a current of 120 A passes through, the gradient of magnetic field on the strong y axis is equal to $15\,\mathrm{G.cm}^{-1}$. With an optimized alignment of the six beams and an illumination of the chamber with UV light as homogeneous as practically possible[1], we are able to load around 2.10^7 atoms in the MOT in 6 s.

[1]We observed that when the LEDs were placed on the upper windows of the chamber, the loading rate of the MOT was progressively and slowly decreasing. We suppose that in this configuration, the UV light mainly desorb atoms from the top part of the chamber (the divergence of the LEDs is very large). As the atoms then redistribute in average isotropically on the walls and windows of the chamber, after some time they accumulate in its bottom part. The partial pressure of Sodium when the UV LEDs are switched on is then decreased, which results in a lower loading rate of the MOT. We solved this issue by adding LEDs in front of all the accessible viewports.

2.1.3 Resonant laser

The source of resonant light we use was described in detail in the thesis of E.Mimoun [42]. We briefly give here its main characteristics.

We developed a solid-state laser at 589 nm based on the sum of two lasers at 1064 nm and 1319 nm in a non-linear crystal. The infrared lasers are two YAGs lasers outputing respectively 1.2 W and 0.5 W. The crystal is a periodically-poled KTP crystal placed in a cavity resonant with the two infrared wavelength. This configuration produces 650 mW of yellow light in a gaussian mode, which allows one to couple it efficiently in optical fibers. The frequency of this laser is locked to a line of iodine located 467 MHz above the D_2 line of Sodium through a saturated absorption scheme. The beam coming out of the cavity is split in two parts. One is shifted in frequency to the cooling transition using an acousto-optic modulator. The second forms the repumper beam and has to be shifted in frequency by 1.7 GHz, corresponding to the hyperfine splitting between the $|F = 1\rangle$ and $|F = 2\rangle$ states. For this we use a high frequency acousto-optic modulator, which has a low diffraction efficiency (about 20%), but which contrary to an electro-optic modulator spatially separates the shifted beam from the main beam. This allows us to switch on and off the repumper very fast, on the microsecond timescale. The yellow light leeking through one mirror of the cavity is used to form two probe beams for the imaging. All these beams are coupled into optical fibers and brought to the chamber.

2.1.4 Loading in a Crossed Dipole Trap and two-step evaporation

It is not possible to reach the degeneracy threshold using the MOT alone. The phase space density at the end of this step is typically on the order of $10^{-5} - 10^{-6}$, while the degenerate regime occurs at phase space densities of order unity. The standard technique developed in ultra-cold atoms experiments to get to the degenerate regime uses evaporative cooling in a conservative trap. We then need to transfer the atomic cloud from the MOT into such a trap. Since we want to confine the three Zeeman sublevels of the $F = 1$ manifold of the electronic ground state, a magnetic trap is forbidden. It would only trap the low-field seeking states ($|F = 1, m_F = -1\rangle$ for Sodium). We then use the dipolar confinement created by a far-off red-detuned laser beam. As we have seen in chapter 1, if the laser is linearly polarized the trapping potential is independent of the spin state of the atom [69].

The Crossed Dipole Trap

We use a 1070 nm fiber laser whose output power can be controlled from 1 to 40 W. Its polarization is linear and well-defined by a Glan-Taylor polarizer. The laser beam goes through the chamber in an horizontal plane. It is focused at the center of the chamber by a 125 mm lens on a waist $w_0 = 40\,\mu$m, recollimated, folded back on itself with an angle $\theta = 45°$ and focused again at the same position with the same waist, thus crossing the first arm of the beam, as depicted in the figure (2.2.a). A waveplate is placed between the two arms that rotates the polarization by 90° to avoid interference effects. This crossed dipole trap (CDT) creates a trapping potential V_{CDT} which is the sum of the potentials created by its two arms:

$$V_{CDT}(x, y, z) = \frac{V^0_{CDT}}{2}\left[\left(\frac{w_0}{w(x)}\right)^2 e^{-\frac{2(y^2+z^2)}{w^2(x)}} + \left(\frac{w_0}{w(u)}\right)^2 e^{-\frac{2(v^2+z^2)}{w^2(u)}}\right] \tag{2.1}$$

where we introduced the rotated coordinates $(u, v) = (-x\sin\theta + y\cos\theta, x\cos\theta + y\sin\theta)$ and the waists along the two propagation axis $w(x)$ and $w(u)$. Each arm creates a potential

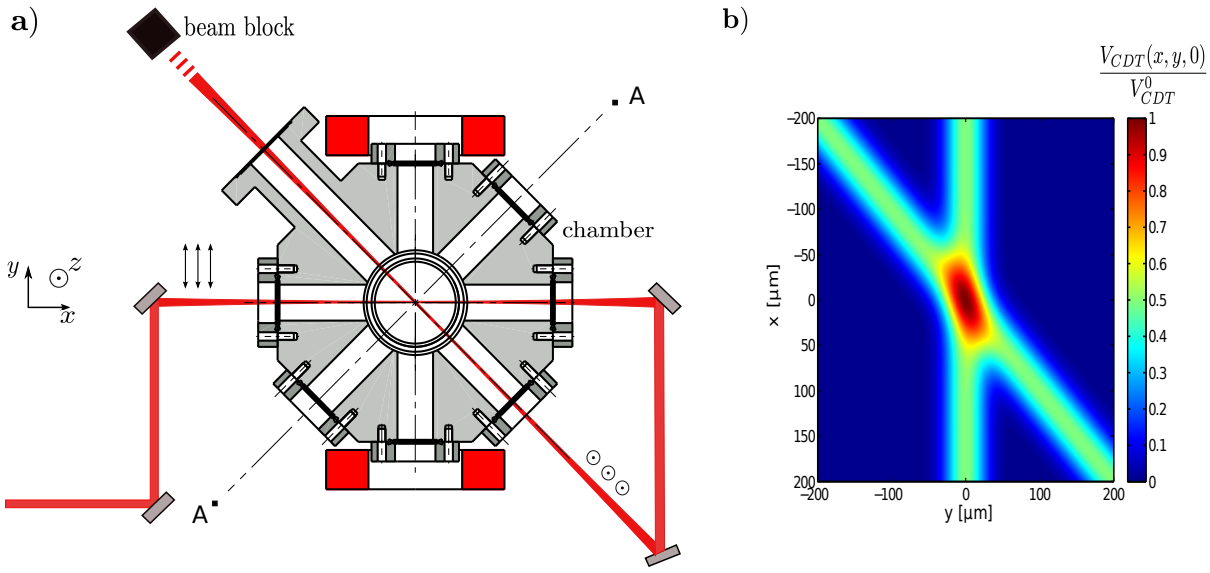

Figure 2.2: **a**): Path of the crossed dipole trap in the experiment chamber seen from above. The arrows next to each arm of the laser beam before it enters the chamber indicates the light polarization.**b**): Potential created by the crossed dipole trap in the horizontal plane $z = 0$, calculated for a waist $w_0 = 40\,\mu$m and a power $P = 36$ W. The arms and crossing region of the trap are clearly visible.

of maximal depth $V^0_{CDT}/2$ proportionnal to the light intensity in its center $I_0 = 2P_0/\pi w_0^2$, where P_0 is the power laser beam. The potential V_{CDT} is calculated in the figure (2.2.b) for $P_0 = 40\,$W. The depth of the CDT is then approximately $V_0 = 2\,$mK. In the central region the potential can be approximated by a 3D harmonic potential. Further away from the center, the two arms are strongly confining in their respective transverse direction, and very weakly confining along their respective axis.

Stabilization of the alignment

The precise crossing of the two arms of the CDT is capital: a misalignement perturbs the trapping potential which degrades the number of atoms loaded and then jeopardizes the evaporation. Yet the alignement of the laser does drift on a day time, mainly because of thermal drifts in its fiber (when we switch it on two hours are usually necessary before it stabilizes) or in the laboratory itself[2], that can cause changes of several tens of μm in the position the beams. To correct for it we installed a commercial active pointing stabilization system[3]. This system consists of two position sensitive detectors and of two actuators. The position sensitive detectors are two quadrant photodiodes placed after the chamber on the path of the transmission of the laser through a mirror. One is positioned at the focus of a lens and is sensitive mainly to drifts of the laser in angle, while the second is off focus and is sensitive mainly to drifts in position. They are integrated in a servo loop: the system compares the measured signals on the two detectors to pre-registered reference values (corresponding to the correct alignment of the beam) and reacts on the pointing of the beam with two motorized mirrors in the beam path before the chamber. This system can be run in principle continuously as long as the intensity of the laser stays above some threshold. Because in our case the intensity is varied to very low values we only use it

[2]We note that these drifts significantly decreased after moving the experiment to Collège de France.
[3]*Aligna 4D* by TEM Messtechnik GmbH, Hannover, Germany

during the MOT when the intensity of the CDT is kept constant. This is sufficient to prevent long terms (presumably thermal) drifts that are the main concern for us.

Control of the power

To precisely control the depth of the trapping potential we also need to control the power of the laser beam through a servo loop [70]. The error signal is easily constructed by substracting the power of a fraction of the beam (practically the power transmitted through a mirror) measured on a photodiode to the setpoint. To react on the power of the laser we have the possibility to use two different actuators. We can directly control the current of the pump diodes of the laser as long as it stays above the lasing threshold. We can also change the angle of a motorized rotating half-wave plate which, associated with a fixed quarter-wave plate in the path of the laser beam allows us to vary the power transmitted through the Glan-Taylor polarizer. These two actuators have very different bandwidths: 50 kHz for the current control, 10 Hz for the rotating waveplate. To benefit from the higher bandwitdh of the current control and still be able to get low powers (below the lasing threshold) we associate the two actuators in the following way. We consider the general situation where we want the power of the laser to be described by some function f of the time t. The motorized waveplate is placed outside the servo loop and receives through a programmable microcontroller the appropriate command such that, for some given value of the diode current, the laser power would in principle evolve in time as wanted. The command sent to the microcontroller determines the angular position θ of the wave-plate, where θ is defined with respect to the p-polarization axis of the polarizer. Given the configuration of the polarizer the transmitted power P writes

$$\begin{aligned} P(t) &= P_0 \cos^2[\theta(t)] = P_0 \cos^2[\alpha V(t) + \beta] \\ &= P_0 f(t) \end{aligned} \tag{2.2}$$

where P_0 is the maximal transmitted power, obtained when $\theta = 0$. The calibration factor α characterizes the response of the waveplate to the command voltage V, β is a constant voltage. Knowing the parameters α and β the command function $V(t)$ is easily deduced from the desired power function $f(t)$. The servo-loop then uses the current of the pump diode to correct for the remaining fluctuations of the laser power around this theoretical evolution (due to mechanical noise in the waveplate or to thermal fluctuations in the fiber that change the polarization of the laser, for example). In this configuration, most of the work is done by the waveplate in the sense that the current of the diodes only experiences small amplitude variations around some fixed value, but the servo loop still inherits from the high bandwidth of the current control. For a fixed value of the current of the diodes, the rotating waveplate alone allows us to reach an extinction of the transmitted power of 0.5%.

Optimization of the loading

The temperature of the atomic cloud in the MOT ($\sim 200\,\mu$K) is too high compared to the depth of the CDT to efficiently load it. To optimize the transfer of the atoms into the CDT we modify the experimental parameters of the MOT in two steps. First we lower the power of the repumper beams to depump the atoms in the $F = 1$ hyperfine state. This suppresses light-induced collisions and multiple photon scattering, which results in an increase of the atomic density in the trap. This step lasts 100 ms. Then, to further cool the cloud the frequency of the MOT beams is changed to a detuning of 38 MHz. At

the end of these two steps the temperature of the cloud is approximately 50 μK.

The confining potential created by the dipole trap can be interpreted as an AC-Stark effect that shifts the energy levels of the atom proportionally to the intensity of the trapping laser. Since the ground and excited states have different polarizabilities, the light shifts they experience are also different. This implies that the atomic transitions, which are defined by the difference between two hyperfine levels, are modified by the presence of the dipole trap, in particular the cooling and repumping transitions. The dipole trap obviously has to be superimposed to the MOT at some point. The effect we described may then degrade the efficiency of the cooling in the MOT, especially for high powers of the CDT. We can compensate for this effect by shifting the frequency of the cooling and repumping beams, but only partially because of the spatial dependence of the light shifts [47]. We can make the cooling mechanisms work for example in the central region of the CDT, but they are then much less efficient in the outer region. This phenomenon explains that the loading of the CDT is not optimal when we set it to its maximal power. There is an optimal loading power which we experimentally determine to be 13.5 W by counting the atoms loaded in the central region of the CDT 100 ms after the cooling beams are switched off.

Evaporation in the CDT

When we switch off the MOT (i.e. the cooling and repumping beams and the magnetic field gradient), the CDT is at its loading power of 13.5 W (corresponding to a depth of 0.7 mK approximately). At this power, the trapping potential is such that a significant fraction of the atoms are trapped in the arms of the CDT. As the CDT is formed by two gaussian laser beams, ramping up its power results in an increase of the trapping frequencies. We observe that if we compress the trap this way the atoms accumulate in the central region of the CDT, thus increasing the density and consequently the collision rate. We therefore ramp the power of the laser from 13.5 W to its maximum power, which corresponds to 36 W on the atoms, in a linear ramp of two seconds. After this compression, around 10^5 atoms are trapped in the CDT which is well described by a spherical harmonic trap of frequency $\omega = 2\pi \times 6.2$ kHz and of depth 1.9 mK. The temperature of the cloud is approximately 100 μK. This is a good starting point for the evaporative cooling.

Still, the compression has a detrimental side effect. The increase of the laser power indeed causes some heating of the optics it passes through, even though these are specially coated. This heating deforms the surface of the optics and is responsible for a thermal lensing effect. We identified this effect in particular in the lens we use to focus the first arm of the laser. The observable consequences of this thermal lensing are a modification of the focal length of the lens and, to a lesser extent, a misalignment of the laser beam. These two effects happen on a time scale shorter than that of the compression, meaning that the beam and its focus moves during the compression. We account partially for this displacement by optimizing the position of the focalizing lens in order to maximize the number of atoms after the compression.

The evaporative cooling is driven by lowering the depth of the trapping potential such that the most energetic atoms escape the trap. Inter-particle collisions then allow the remaining atoms to thermalize to a lower temperature, as the average thermal energy per particle is now smaller. This technique implies a loss of atoms but the gain in temperature is such that the phase space density can be increased by several orders of magnitude,

provided the collision rate stays high enough to maintain an effective rethermalization. However, due to the optical nature of the trap the lowering of the trap depth U goes with a lowering of the trapping frequencies: in a gaussian beam one has $\omega \propto \sqrt{U}$ (this is not the case in a magnetic trap where the depth and the frequencies are independent). This decompression of the trap decreases the collision rate and limits the efficiency of the evaporative cooling. By optimizing the final phase space density we found that the best way to lower the trap potential was a decreasing exponential ramp which brings the power of the laser from 30 W to 100 mW in 2 s, with a time constant of 500 ms. However the phase space density stays below unity: the evaporative cooling in the CDT does not allow to reach the degeneracy threshold. The solution we implemented to bypass this limitation and get to the degenerate regime is to add a second dipolar trap of smaller volume where a stronger confinement makes the evaporative cooling more efficient.

Transfer and evaporation in a small volume dipole trap

In a dipolar potential created by a gaussian beam, the trapping frequencies evolves as the square root of the light intensity. Thus, with a given power, by focusing a laser beam on a smaller waist we can obtain a stronger confinement. The idea to reach the degenerate regime is to transfer the atoms from the CDT to a second dipolar trap of smaller volume called the *dimple* trap where we then continue the evaporative cooling [47]. This second dipolar trap consists of two laser beams created by two different infrared power lasers at 1064 nm. They are transmitted through acousto-optic modulators and optical fibers to the chamber. The first beam propagates through the chamber vertically and is focused on the atomic cloud by an objective of large numerical aperture placed in the lower entring flange. Its waist is 9 μm. We denote this beam as *vertical dimple*. The second beam propagates in the horizontal plane perpendicularly to the second beam of the CDT (see figure (2.2) and (2.3)) and is focused at the same position by a 200 mm lens on a waist of 11 μm. We denote it as *horizontal dimple*. Here again the precise crossing of the two beams and the superposition of the two waists is crucial. The vertical dimple is kept fixed at all time, and we adjust the pointing of the horizontal dimple with a motorized mirror and a lens mounted on a translation stage. The dimple trap is actually the spatially most stable of all our traps, and its position is used as the reference position on which the alignment of the CDT and of the MOT is optimized.
At its maximum level the dimple trap has a depth of 54 μK. It is then negligible compared to the confinement induced by the MOT and does not perturb neither the potential created by CDT before its evaporation. The dimple trap is switched on from the beginning of the experimental sequence but is of little effect until the CDT is evaporated. Then, during this step as the depth of the CDT decreases the presence of the dimple is progressively revealed and forms a narrow peaked potential at the center of the softer CDT potential, as shown in figure (2.3). In the same time it is filled by the least energetic atoms that fall in it. At the end of the evaporation of the CDT the atoms are mainly held by the dimple potential. Once the CDT is switched off the evaporative cooling can now start in the dimple trap.

As the dimple trap is created by two different laser beams, the powers of these two lasers have to be lowered simultaneously. In order to keep the ratio of the trapping frequencies constant and to preserve the shape of the trap the ratio of the powers of the two lasers is also kept constant during the evaporation. In the experimental results we will describe in this work two different sequences have been used to lower the trap depth. For the experiments presented in the chapter 3 an exponential ramp has been used, while

T_{evap}	$\omega_x/2\pi$ [kHz]	$\omega_x/2\pi$ [kHz]	$\omega_x/2\pi$ [kHz]	$\bar{\omega}/2\pi$ [kHz]	$V[\mu K]$
$T_{evap} = 0$	4.86	6.38	8.02	6.30	1.9×10^3
$T_{evap} = 2$ s	4.06	4.68	2.33	3.54	54

Table 2.1: Trapping frequencies and trap depth V before the evaporation of the CDT ($T_{evap} = 0$) and after the evaporation, once the CDT is switched off and the atoms fill the dimple trap at its maximum power ($T_{evap} = 2\,\mathrm{s}$). The trap deth is lowered by a factor 35 while the trap frequencies stay high ($\bar{\omega}$ is only divided by 2).

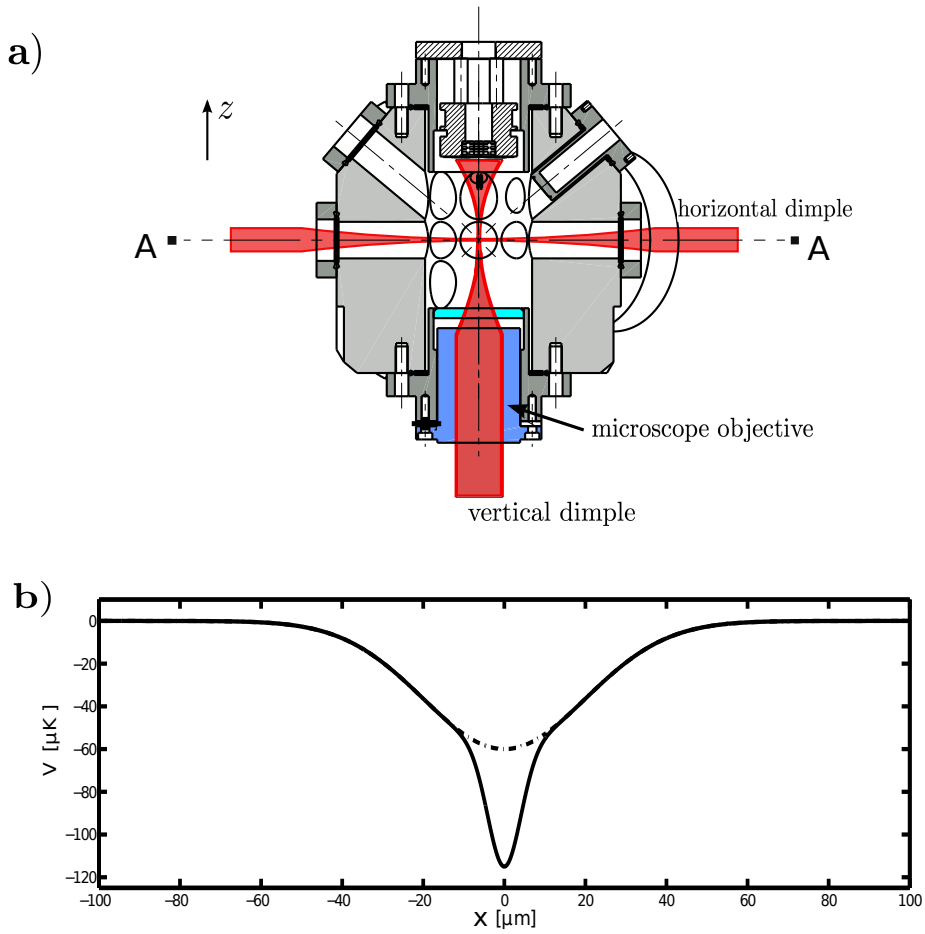

Figure 2.3: **a**):Path of the two laser beams forming the dimple trap. The plane of the figure contains the z axis and the A-A axis defined in the figure (2.2). The two entring flanges appear, in particular the bottom one that contains the microscope objective of large numerical aperture. **b**):Trapping potential during the evaporation of the CDT. The solid line shows the potential created by the superposition of the CDT and the dimple trap. The dashed line shows the potential created by the CDT only. The power of the CDT is 1 W, while the dimple trap is at its maximum power.

in the experiments described in chapter 5 the ramp is linear. Both ramps have the same initial and final powers, and have been optimized in terms of the final phase space density. The exponential ramp brings the depth of the dimple from 54 μK to 1.4 μK in 3.5 s with a time constant of 1.5 s. In the linear ramp the trap depth varies between the two same

point in 1 s. Because in the exponential ramp the opening of the trap is much faster at the beginning of the evaporation, smaller three-body losses are expected. Both sequences produce quasi-pure Bose-Einstein condensates of about 6.10^3 atoms. For experiments like the ones described in chapter 5 where we need to accumulate a lot of data in a short time, we prefer to use this linear ramp which is faster. In the following we characterize the evolution of the atomic cloud during the evaporative cooling. We concentrate on the linear ramp.

2.1.5 Condensation in the dimple trap

Characterization of the trap

To study the behavior of our atomic system during the evaporative cooling we need to characterize how the trapping potential evolves. In particular we want to determine its frequencies and its depth as functions of the evaporation time.

Since in an optical trap formed by a gaussian beam the intensity of the laser and the trapping frequencies are related, the knowledge of the frequencies and of the laser power allows to determine precisely the waist of the two beams. The depth of the trap is then easily calculated from the power. The power of the two beams forming the dimple trap is directly measurable. To access the trap frequencies we use the following technique. We prepare a cloud polarized in $|m_F = +1\rangle$ (see next section) and apply a strong magnetic gradient and a bias magnetic field directed along one of the main axes of the trap. This creates a force in this direction on the cloud which is displaced in the trapping potential. The force is then suddenly switched off and we measure the oscillation of the center of mass of the cloud in the harmonic potential of the trap. We directly extract the frequency along the direction of the force by a Fourier analysis of this motion. We do this experiment for the two horizontal axis of the trap, and for different evaporation time. Knowing the corresponding powers of the beams that we suppose gaussian and perfectly overlapped at their waist, we can fit the value of these waists. We find a waist of $9.0 \pm 0.5\,\mu$m for the vertical dimple and a waist of $11.0 \pm 0.5\,\mu$m for the horizontal dimple. The measurement are summarized in figure (2.4).

Temperature and condensed fraction

Above the degeneracy threshold the atomic density in the trap is described by a Bose function (1.5). When the degeneracy threshold is reached the condensate forms on top of the thermal distribution. The density of the thermal fraction is then modified by the interaction with the condensed atoms. At zero temperature in the Thomas-Fermi approximation the condensate density has the parabolic shape (1.9).

In a time-of-flight experiment the trapping potential is switched off and the atoms are released. The thermal fraction expands mostly ballistically due to its high kinetic energy, and the condensate expands mainly due to the release of interaction energy that converts in kinetic energy on a timescale on the order of the trap period. In the two limits of a purely thermal gas and of a condensate in the Thomas-Fermi regime, the atomic density during the expansion is deduced from the density in the trap by a scaling law [71]. For a partially condensed gas, the interactions between the thermal and condensed fractions make it hard to compute the evolution of their respective distribution. The standard procedure is then to take advantage of the bimodality of the total atomic density and to describe its two components by the two limiting cases described above. We note $\sigma_{i,\mathrm{th}}$ (resp

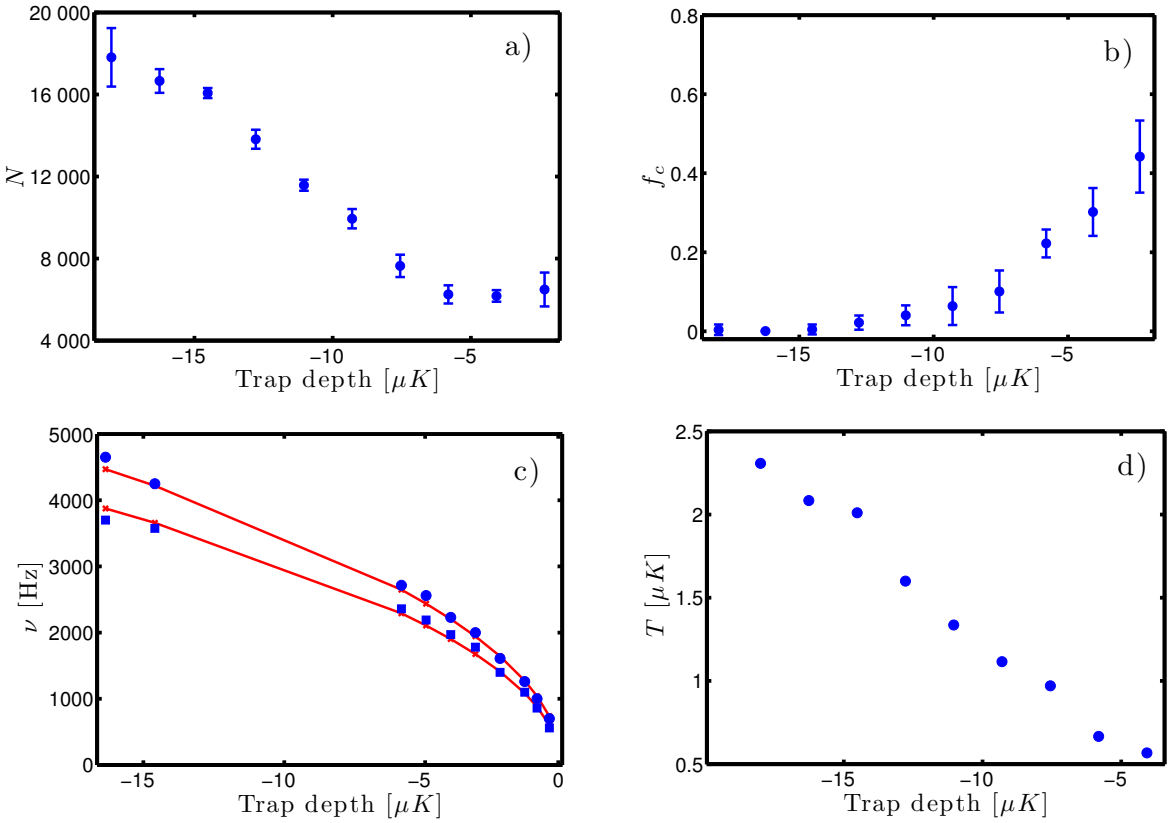

Figure 2.4: Characterization of the evaporative cooling with the 1 s linear ramp. The trap depth is the depth of the horizontal dimple trap. **a**): Atom number during the evaporation as a function of the trap depth. **b**): Condensed fraction during the evaporation, deduced by fitting measured ToF profiles (see text). The method has a large systematicc error (see text) that makes it unreliable for $f_c \gtrsim 0.3$.**c**):Frequencies of the dimple as a function of the trap depth during evaporative cooling. Blue squares and circles correspond to the measured frequency in the two horizontal axis of the dimple. The red lines are fits supposing the dimple is made of two gaussian beams crossing at their waists. The trap depth is calculated from the results of these fits. **d**): Temperature during the evaporation, measured with the plateau method. We find a parameter $\eta = U/k_B T \approx 7$ (where U is the trap depth).

$\sigma_{i,c}$) the size of the thermal (resp condensed) distribution on the axis i after a time of flight t, and ω_i the trap frequency on this axis. Using absorption imaging (see next section of this chapter) we can access the column density of the atomic cloud, corresponding to its density integrated along the z axis. We fit this column density in the $x-y$ plane by a bimodal distribution which is the sum of two terms:

$$\tilde{n}_{\rm th}(x,y) = \frac{\tilde{n}_{th}(0,0)}{g_2(1)} g_2\left(-\frac{x^2}{2\sigma_{x,\rm th}^2} - \frac{y^2}{2\sigma_{y,\rm th}^2}\right) \tag{2.3}$$

$$\tilde{n}_c(x,y) = \tilde{n}_c(0,0)\max\left(1 - \frac{x}{2\sigma_{x,c}^2} - \frac{y}{2\sigma_{y,c}^2}\right) \tag{2.4}$$

where g_2 is a Bose function as defined in chapter 1. This choice correctly describes our atomic samples as long as the thermal and condensed components have significantly dif-

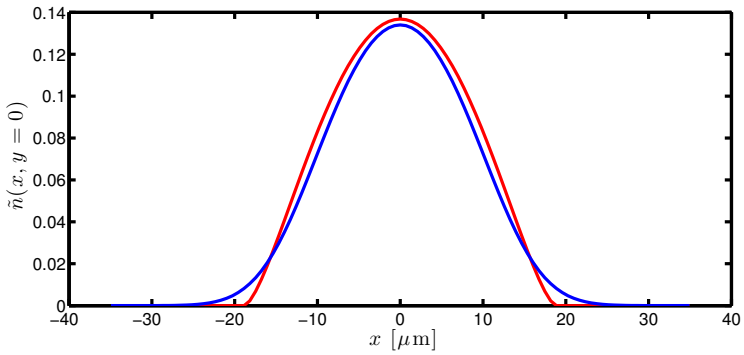

Figure 2.5: Cut along the x axis of the atomic column density $\tilde{n}$ after a time-of-flight of 2.5 ms for the solution of the Gross-Pitaevskii equation (blue) and for the Thomas-Fermi solution (red). The parameters are $N = 5000$ and $(\omega_x, \omega_y, \omega_z) = 2\pi \times (560, 700, 385)$ Hz.

ferent sizes. However, when the two size become comparable it fails, as we explain now. Because of our relatively small atom number, the condensate in the trap is in our case not well in the Thomas-Fermi regime. The resolution of the Gross-Pitaevskii equation with our experimental parameters shows in particular that it exhibits wings, while the Thomas-Fermi parabola has sharp edges. These wings are small in the trap but are revealed in the time-of-flight expansion, and may be associated to the thermal Bose distribution by the fitting algorithm. In this case the fitting procedure fails to distinguish the two component of the gas. Figure (2.5) compares the solution of the Gross-Pitaevskii equation and the Thomas-Fermi solution for $N = 5000$ atoms and for the trap frequencies measured at the end of the evaporation in our experimental system.

In the condition where our fit model works, the size $\sigma_{i,\mathrm{th}}$ is given by $\sigma_{i,th} = \sigma^0_{i,\mathrm{th}}\sqrt{1+\omega_i^2 t^2}$ [72], where $\sigma^0_{i,\mathrm{th}} = \sqrt{k_B T/m\omega_i^2}$, even with the Bose fonction. In the limit $\omega_i t \gg 1$ the thermal cloud expands isotropically with a velocity $\sigma^0_{i,th}\omega_i$. To extract the temperature of the cloud we thus vary the time of flight t and fit the size of the thermal distribution by a function $\sigma_{i,\mathrm{th}}(t) = \sqrt{{\sigma^0_{i,\mathrm{th}}}^2 + v^2 t^2}$, with the two fit parameters $\sigma^0_{i,\mathrm{th}}$ and v. We then obtain the temperature by $T = mv^2/k_B$.

Practically, for a given absorption image of the atomic cloud, we specify a region around the center of the atomic distribution (a disc that we call the mask) outside which the analysis algorithm fits a thermal distribution of the form (2.3). The difference between the whole image and the result of this first fit is then fitted by a Thomas-Fermi distribution (2.4). The robustness of this method lies in the clear bimodality of the actual atomic distribution. But as we just explained, after a time-of-flight expansion this bimodality may not appear, for the condensate density in the trap differs from the Thomas-Fermi solution. If the mask is too small and does not include all the condensate distribution, the fitting algorithm is not able to recognize its wings and may attribute them to the thermal fraction, inducing a bias in the fitted thermal fraction and underestimating the condensed fraction. To circumvent this issue we fit the same image several time, systematically increasing the size of the mask at each fit round. First the mask is too small and does not contain the whole condensate. The fitted size of the thermal fraction then changes from round to round. Once the condensate is completely included in the mask, the algorithm fits with a Bose function the true thermal distribution. Further increasing the size of the mask then

does not change the result of this fit, and we observe a plateau in the value of the size of the fitted thermal distribution as a function of the size of the mask, as illustrated by the figure (2.6). For very large masks however the atomic signal outside the mask gets on the order of the imaging noise and the fit algorithm fails. The fitted sizes of the distribution above a certain mask size are then meaningless. To extract the value of the plateau we decide to consider the fits up to to the point where the integrated optical density inside the mask reaches 95% of the total integrated optical density. We then fit the relevant sizes of the thermal distribution with a law of the form $\sigma(s) = -a\exp(-s^3/2b^3) + d$, with fit parameters a, b and d, which reproduces well the behavior of the size of the distribution σ when we increase the size of the mask s. This method allows to reliably determine the size of the thermal distribution and then to deduce the temperature as explained above.

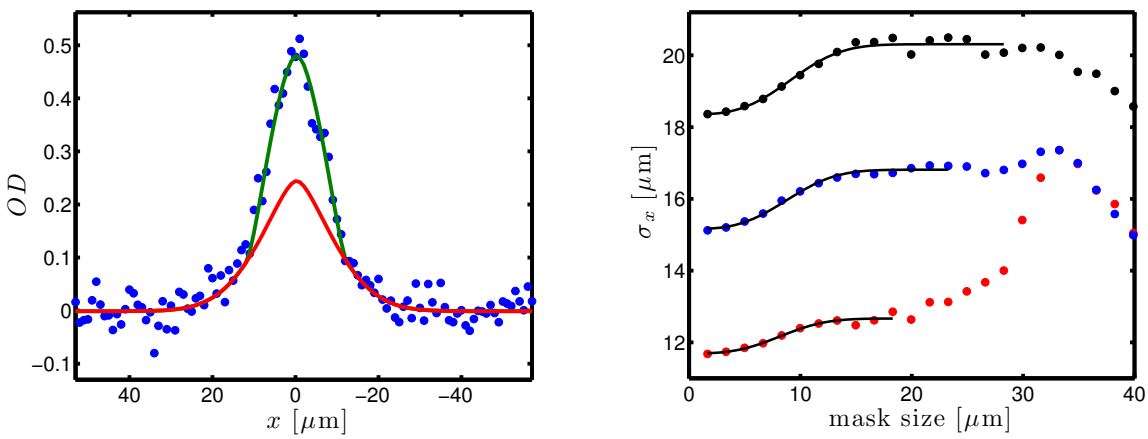

Figure 2.6: **On the left:** Cut along the x axis of a bimodal fit of the atomic density in an absorption image. The blue points show the measured optical density of the atomic cloud, the red and green curves correspond respectively to the fitted Bose function and Thomas-Fermi function. The evaporation point is 700 ms. **On the right:** Size (along the x axis) of the Bose function fitted outside the mask as a function of the mask size for an evaporation time of 600 ms. The three sets of points - red, blue and black - correspond to three different absorption images taken at different times of flight: from bottom to top 0.6 ms, 0.8 ms and 1 ms. The solid curves fit each set of points by a function of the form $d - a\exp(-x^3/2b^3)$, from which we extract the value of the plateau.

The condensed fraction is easily deduced from a bimodal fit, as the ratio of the integrated condensed distribution to the integrated total distribution. Yet, for highly condensed clouds the thermal and condensed fractions have comparable sizes and our algorithm is not able to reliably distinguish them. This results in a systematic underestimation of the condensed fraction. The results of the bimodal fit are trustworthy only as long as the size of the condensed distribution is significantly smaller than the size of the thermal one, which corresponds to condensed fraction $f_c \lesssim 0.3$. The evolution of the temperature and of the condensed fraction during the evaporation of the dimple trap is shown in figure (2.4).

Experimental check of the single-mode approximation

We have introduced the single-mode approximation in chapter 1, and numerically checked its validity in conditions similar to ours (in term of atom number and trap frequencies). Here we confirm experimentally the validity of the approximation. For this we prepare a cloud at very low temperature where the three spin states are populated (see last section of this chapter) and image them separately using a Stern-Gerlach separation (see next section). We can this way access the spatial distribution of the three spin states. We fit these distributions by three gaussians f_i, $i = +1, 0, -1$. We then compare the mode of the three spin states by calculating the overlap integrals of the recentered and normalized gaussians $\int \tilde{f}_i \tilde{f}_j$, where $\tilde{f}_i = f_i / \int f_i$. We find that these three integrals are on the order of 0.9, which supports the validity of the single-mode approximation in our system.

2.2 Diagnostic of the spinor gas

To study the magnetic properties of a spinor condensate we need to be able to probe its spin state. Two main techniques are used in spinor experiments.

A first technique uses dispersive imaging and takes advantage of the dependence of the dielectric tensor of the atomic sample in its local spin state. By sending a far off-resonant linearly polarized laser beam through the atomic gas, and by measuring the rotation of its polarization we can retrieve the local magnetization of the cloud. This technique allows one to acquire several images from the same experimental run. It was demonstrated in [73] where the authors relied on its principle to characterize the three components of the local spin of the gas.

A second technique consists in performing a Stern-Gerlach experiment followed by absorption imaging. The application of a gradient of magnetic field associated with an homogeneous bias field realises a spin-dependent force on the atoms that allows to spatially separate the three Zeeman states during a time-of-flight experiment. Absorption imaging then gives access to the populations of the three spin states and to their spatial distribution. This technique is destructive.

These two techniques give different informations on the spin state of the atomic sample. The Stern-Gerlach method being easier to implement, we choose to use this technique, before additionally implementing the dispersive imaging in the future.

2.2.1 Application of magnetic fields

The Stern-Gerlach experiment requires the application of external magnetic fields. We here briefly describe our coil system which we use to create these fields. The calibration of the field created by these coils is presented in section 2.3.1.

We are able to apply an homogeneous static magnetic field at the center of the chamber using three pairs of coils in Helmoltz configuration placed around the chamber along the three axis x, y, z and that create the three components of a controllable field (B_x, B_y, B_z).

We are also able to create a quadrupolar magnetic field using the pair of coils already used for the MOT. The strong axis of this quadrupolar field is along the y direction.

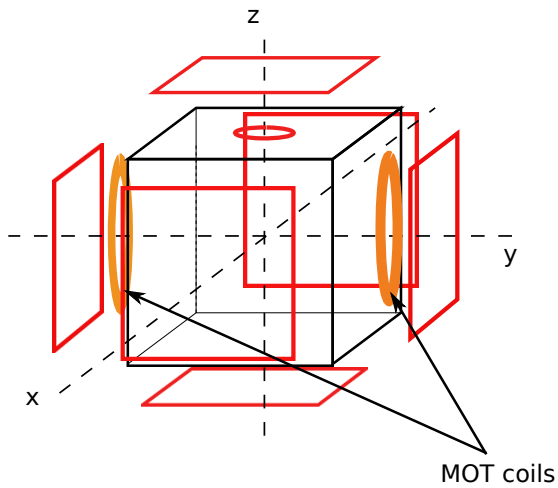

Figure 2.7: Geometry of the coil system. Along each of the x, y, z axes, a pair of rectangular coils in Helmoltz configuration creates at the atoms position an homogeneous static field in the corresponding direction. An additional single smaller coil on the z axis allows us to control more quickly the z component of the magnetic field. Two circular coils placed along the $y$axis in anti-Helmoltz configuration creates the quadrupolar field needed for the MOT.

Additionally, a single coil is placed on top of the chamber on the z axis.This coil creates a magnetic field which is not strictly homogeneous at the center of the chamber, but can be considered as homogeneous on the spatial scale of our clouds after the evaporative cooling, when the clouds are small (some tens of μm). The advantage of this single coil is that, due to its lower inductance compared to a pair of coils, the current establishes faster, and it then allows a faster control of the magnetic field.

2.2.2 Stern Gerlach separation

We first recall the principle of a Stern-Gerlach experiment, and then describe how we implement it in our case.

Principle of the Stern-Gerlach separation

An atom with a total spin $\mathbf{F}$ in the presence of a magnetic field $\mathbf{B}$ sees a potential

$$V_{\text{mag}} = \frac{\mu_B}{\hbar} g_F \mathbf{F}.\mathbf{B} \tag{2.5}$$

where g_F is the Landé factor and μ_B is the Bohr magneton. If we look at times long compared to the Larmor frequency the total spin $\mathbf{F}$ stays aligned with the magnetic field which defines a local quantization axis, and the potential now reads

$$V_{\text{mag}} = \frac{\mu_B}{\hbar} g_F m_F ||\mathbf{B}|| \tag{2.6}$$

If the field $\mathbf{B}$ is not homogeneous a particle experiences (in a semi-classical picture) a spin-dependent force

$$\mathbf{F}_{\text{mag}} = -\frac{\mu_B}{\hbar} m_F \nabla ||\mathbf{B}|| \tag{2.7}$$

The gradient of magnetic field created by the MOT coils can thus be used to apply such a force on our atomic cloud and spatially separate the different spin components. Since the

Landé factor g_F is negative for the $F = 1$ hyperfine manifold of Sodium, the atoms in the $|m_F = -1\rangle$ spin state feel a force directed toward the region of weak magnetic field, while the atoms in the $|m_F = +1\rangle$ state feel a force of same amplitude but opposite direction. This effect is the basis of the Stern-Gerlach experiment [74].
The magnetic field created by the two anti-Helmoltz MOT coils writes in the cartesian frame of the laboratory:

$$\mathbf{B}(x, y, z) = \begin{pmatrix} bx/2 \\ -by \\ bz/2 \end{pmatrix} \tag{2.8}$$

As the atomic cloud stands around the zero of the quadrupolar field (or close to it), the direction of the gradient of magnetic field, and therefore the direction of the force varies with the position of the atoms. To obtain a force approximately linear with coordinate, we need to add a large bias magnetic field that sends the zero of the quadrupolar field far away from the cloud, so that the gradient appears homogeneous on the spatial scale of the atomic cloud. We consider the situation where we add a homogeneous magnetic field $B_0\mathbf{e}_y$ directed along the strong axis of the gradient. The modulus of the total field is given by:

$$||\mathbf{B}(x, y, z)|| = |B_0|\sqrt{\frac{b^2}{B_0^2}(x^2 + z^2) + (1 - \frac{2b}{B_0}y)^2} \tag{2.9}$$

We note L the characteristic spatial extension of the atomic cloud, which at the end of the evaporation is on the order of $10\,\mu$m. If we take B_0 large enough such that $bL/|B_0| \ll 1$, then to first order in this quantity we have

$$\nabla||\mathbf{B}(x, y, z)|| = -\text{sign}(B_0)2b\mathbf{e}_y \tag{2.10}$$

where $\text{sign}(B_0) = B_0/|B_0|$, and atoms in the state $|m_F\rangle$ experience a force

$$\mathbf{F}_{\text{mag}} = -\frac{\mu_B}{\hbar}m_F\text{sign}(B_0)b\mathbf{e}_y \tag{2.11}$$

where we used $g_F = -1/2$ for the $F = 1$ hyperfine manifold of ^{23}Na. The amplitude of the force is determined by the gradient of magnetic field, and not by the bias field, which only sets the direction of the force. If the bias field is directed along one of the axes of the gradient, then the force has the same direction. To maximize the force it is then advantageous to apply the force along the strong axis of the quadrupolar field as we did here, to benefit from the stronger gradient on this axis.

Slow opening of the trap

In a time-of-flight experiment the optical confinement is switched off and the atoms of the three Zeeman states separate under the action of the magnetic force. On the spatial scale of the separation that can be achieved, this force is homogeneous, so that the atoms in the $|m_F = \pm 1\rangle$ states are uniformly accelerated in opposite directions. The magnetic force does not act on the atoms in $|m_F = 0\rangle$. Additionally to its global movement, each cloud expands ballistically due to its kinetic and interaction energy. This expansion is linear in time in the limit where the time of flight is large compared to the inverse of all the trap frequencies. To correctly count the three spin populations and analyse their spatial modes, the three clouds have to be clearly spatially separated. As the distance between the clouds grows quadratically in time, while the size of each cloud only grows linearly, the

condition that the clouds do not overlap can in principle be met by increasing the time of flight. However, technical issues limit the recourse to this solution. When switched on at the beginning of the time of flight with a set point $2b = 15\,\mathrm{G.cm^{-1}}$, the gradient of magnetic field does not reach this value instantaneously but has a characteristic rising time of 5 ms. If we integrate the effect of the time-dependent magnetic force during this time we find that the separation of the three clouds is on the order of their size. If we further increase the time of flight, then the absorption signal becomes too weak. An other solution would be to use a larger magnetic field gradient to increase the magnetic force, but we are here limited by the electronic set-up. To avoid this difficulty we do not switch off suddenly the trapping potential at the beginning of the time of flight, but instead we lower it by ramping down the laser power exponentially in 5.5 ms. At this point we switch off the dipole trap and start a "true" time of flight experiment. During this attenuation of the laser power the gradient of magnetic field and the separation field are turned on.

The attenuation has two main effects. First it gives the magnetic force the time to build up while the atoms are still held in the optical trap. This way, the force experienced by the atoms once they are released is increased and they separate faster. On the other hand, the attenuation of the power of the lasers also induces a relaxation of the trapping frequencies, which results in a slower expansion of the atomic clouds during the time of flight.

The experimental sequence is the following. The time $t = 0$ refers to the beginning of the attenuation. Before we start the attenuation, the homogeneous bias field that defines the direction of the magnetic force (we call it the separation field) is ramped up. In order to maximize the magnetic force, this field is set on the strong axis of the quadrupolar field, which is the y axis. The rise up time of the magnetic field created by the pair of coils on this axis is quite low, presumably because of eddy currents: the field needs around 7 ms to settle when the command is brought from zero to 2.5 G in a step. We start to ramp the separation field at $t = -7\,\mathrm{ms}$. At $t = -1\,\mathrm{ms}$ we ramp up the gradient of magnetic field, from 0 to its maximum value $2b = 15\,\mathrm{G.cm^{-1}}$. At $t = 0$ we start to lower the power of the dimple trap, using an exponential ramp of time constant 3 ms that brings the power to 5% of its initial value in a time $T = 5.5\,\mathrm{ms}$. At this time the trap is switched off, releasing the atoms. The bias magnetic field applied in the x direction since the evaporation, whose value depends on the experiment, is brought to zero during the attenuation. As the atoms are still held in the trap at that time, the separation axis of the Stern-Gerlach experiment is not affected by this field, and is purely in the y direction.

The position of the dimple trap in the chamber does not coincide exactly with the zero of the quadrupolar field. This results in a tilt of the direction of the magnetic force in the Stern-Gerlach experiment with respect to the desired y axis. We calibrated this bias field using a spectroscopic method described in section 2.3.1 and found that its main component is in the z direction. To compensate for it we ramp up the current in the single coil on the z axis (for it has a much faster response than the pair of coils on this axis) to the adequate value. We check that the three clouds actually lie in the same horizontal plane at the time of the imaging. The current in this coil is then set to a higher value for the imaging, as will be explained in the following. This experimental sequence is summarized in the figure (2.8).

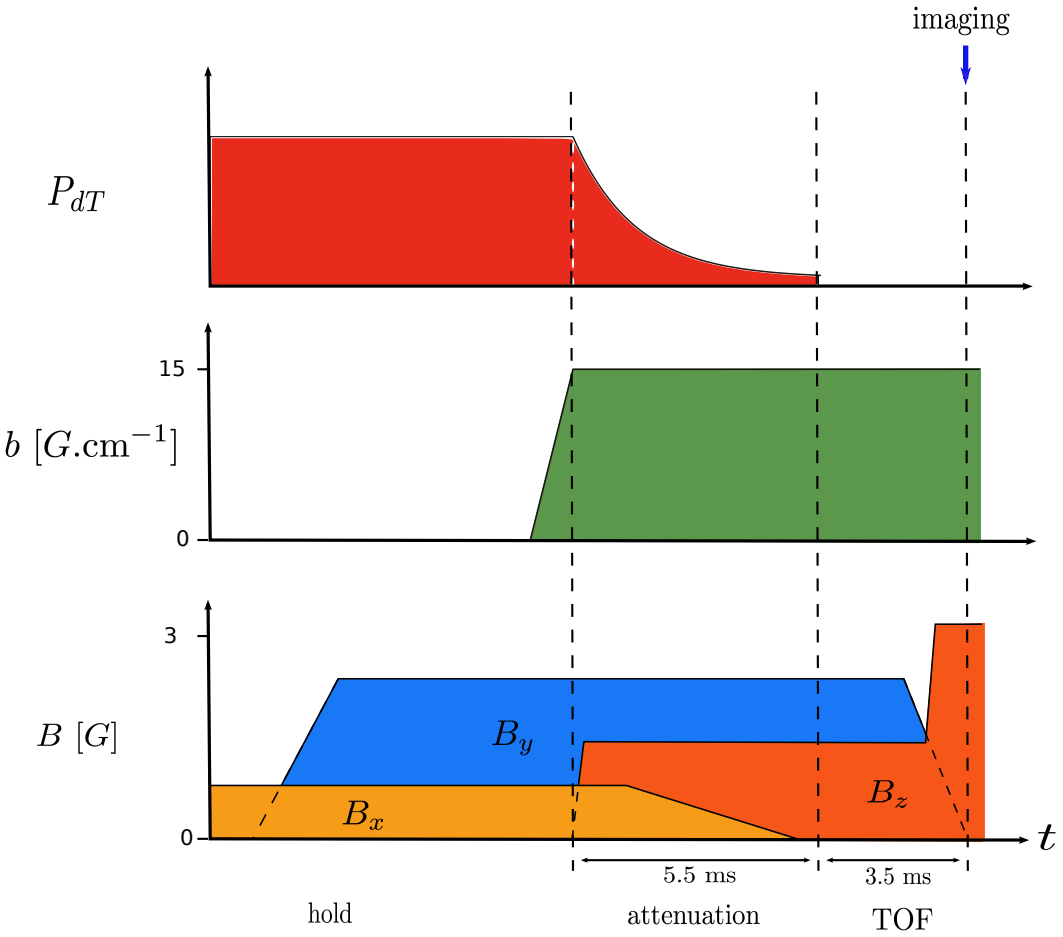

Figure 2.8: Experimental sequence during the Stern-Gerlach separation of the three spin states. The top plot shows the qualitative evolution of the laser power of the dimple trap. The middle one shows the gradient of magnetic field, represented by the parameter b defined in the expression (2.8). The bottom plot shows the three component of the applied magnetic field. The component B_x of the magnetic field is typically used to apply an arbitrary static homogeneous field during the experiment. Its value is changed depending on the purpose of the experiment. The component B_y defines the axis of the Stern-Gerlach separation. The component B_z compensates the offset field due to the quadrupolar field during the attenuation, and is then ramped up to define the quantization axis during the imaging.

Effect of the attenuation

Each experiment that we perform aims at measuring one or several thermodynamical variables of the atomic cloud: atom number, condensed fraction, temperature, etc. The experimental conditions under which we want to probe these variables are defined by the values of the experimental variables before the Stern-Gerlach separation of the three spin species. To be able to reliably perform such measurements, the corresponding variables have to stay unchanged during the attenuation.

We checked experimentally that the total atom number was the same with or without the Stern-Gerlach separation. At low temperatures we also checked with polarized clouds that the condensed fraction measured after the Stern-Gerlach experiment was compati-

ble within the errorbars with the one measured without attenuation and Stern-Gerlach experiment.

On the contrary the temperature cannot be measured by a time of flight experiment after a Stern-Gerlach separation, as the attenuation slows down the expansion of the atomic cloud, which is directly related to its temperature.

2.2.3 Imaging set-up

In the experiments that we describe in the next chapters, we are interested in the populations of the three spin states, and in their spatial modes (to check the single-mode approximation). A suitable technique to probe our atomic samples is then absorption imaging. For this purpose we implemented an imaging system using two CCD cameras: one placed along the x axis (to image the $y-z$ plane of the atoms), one along the z axis (to image the $x-y$ plane). The plane of the CCD chip of each camera is optically conjugated to the plane of the atomic cloud by a pair of lens (x axis) or by an achromatic doublet associated to the microscope objective of large numerical aperture that we also use to focus the vertical dimple (z axis). The magnifications on the two axes were calibrated against gravity and measured respectively at 1.6 and 7.6. The area of one pixel in the object plane is respectively $(4.0\,\mu\text{m})^2$ and $(1.7\,\mu\text{m})^2$.

The resonant light required for the two imaging probes is derived from the yellow laser described in section 2.1.3 and brought to the experimental chamber on the two imaging axes through optical fibers. Before the fiber they are coupled to AOMs that allow us to switch on and off the probe light on a microsecond timescale and to control its intensity.

Absorption imaging relies on the scattering of photons by the atoms when illuminated by resonant light. To image our system we need to take successively two pictures: one with the atoms and probe light, one without the atoms and with probe light. In the presence of the atomic sample, part of the light is scattered and the first picture shows the projected shadow of the sample on the CCD chip. The second image shows the complete probe pattern and is needed to normalize the intensity of the first image. The pixel by pixel division of the two pictures allows to retrieve the optical density of the cloud (see next section)[4].

The microscope objective of large numerical aperture ($NA \approx 0.33$) confers to the vertical imaging a spatial resolution of at least $2\,\mu$m, calibrated by imaging the smallest atomic cloud that we can produce. Besides, the camera[5] on this axis can be used in frame transfer mode. In this mode, only part of the CCD chip is exposed (in our case 1/6 of its total area), the rest being physically hidden by a razor blade. Once the first image is acquired, the corresponding rows on the chip are not read out but shifted to the neighbouring unexposed part. A new picture can then be taken and this operation can be repeated until all the chip is used. The transfer time being much shorter than the read-out time, this mode allows us to shorten the time between the two absorption images from 300 ms to 4 ms. The noise due to spatial variations of the probe beam is then vastly reduced. For

[4] A third image taken without atoms and without probe may be used to substract to the two first an offset intensity due to stray light. In our set-up the CCD chip is protected from stray light by a tube of 10 cm approximately, and the intensity background in the absence of probe is negligible.

[5] Pixis1024, Princeton Instruments, USA

these reasons we use preferentially the vertical imaging to probe cold and small clouds.

The atomic transition we use for the imaging is the same as the cooling transition: $|F = 2\rangle \rightarrow |F' = 3\rangle$. Before imaging the atoms we then have to repump them from $|F = 1\rangle$ to $|F = 2\rangle$. The imaging sequence is the following. We want to image the atoms at the end of the time of flight experiment noted $t = 0$. At $t = -30\,\mu$s a pulse of repumping light of $20\,\mu$s is shined on the atoms, followed at $t = 0$ by a pulse of probe light of $10\,\mu$s. At this moment we take the first image by exposing the chip of the CCD camera. A time of 4 ms is then needed to perform the frame transfer on the CCD chip. The same sequence is repeated to take the second image without atoms. The chip is then read-out.
To obtain a higher signal, the probe is polarized σ_+ (the Clebsh-Gordan coefficients are more favorable for this polarization). As the probe propagates along the z axis, the quantization axis has to be set to this axis before the imaging. We ramp up the magnetic field in this direction during the time of flight, using the faster single coil. As the large gradient of magnetic field is still on, and the separation field is not yet down to zero when we ramp the imaging field, the Larmor frequency is large and allows a fast but still adiabatic rotation of the magnetic field.

2.2.4 Calibration of the scattering cross-sections

We describe in this section how the atomic density is extracted from the two absorption images. We note $I_1(x, y)$ the intensity measured on the first image (with atoms) and $I_2(x, y)$ the intensity on the second image (without atoms). The atomic density is noted $n(x, y, z)$. We suppose that the probe beam propagates along the z axis.

Atom-light interaction model

We consider first the simple model of a two-level atom, with a transition of wavelength λ_0 and linewidth Γ. In the presence of quasi-resonant light of intensity I, the scattering cross-section reads

$$\sigma(I) = \frac{\sigma_0}{1 + 4(\delta/\Gamma)^2 + I/I_{\text{sat}}} \tag{2.12}$$

where δ is the detuning of the incident light to the atomic transition and I_{sat} is the saturation intensity of the transition. The resonant cross section σ_0 is given by $\sigma_0 = 3\lambda_0^2/2\pi$. The Beer-Lambert law $\mathrm{d}I/\mathrm{d}z = -n\sigma(I)I$ then gives the optical density as

$$OD(x, y) = \sigma_0 \int n(x, y, z)\mathrm{d}z = -\ln\left(\frac{I_1(x, y)}{I_2(x, y)}\right) + \frac{I_2(x, y) - I_1(x, y)}{I_{\text{sat}}} \tag{2.13}$$

which shows how the column density $\tilde{n}(x, y) = \int n(x, y, z)\mathrm{d}z$ is extracted from the two pictures. In the low-intensity regime, where $I/I_{\text{sat}} \ll 1$, this expression reduces to the logarithmic term.

Experimentally, this simple model does not describe rigorously the interaction of our atoms with the probe light. The atoms are not two-level atoms but rather have a more complex electronic structure with several excited states. The expression (2.12) is then not exact. The probe-atom interaction could in principle be treated exactly, but this would require the precise knowledge of the probe polarization (on which depends I_{sat}) and of the atomic state after repumping, which are both hard to determine[6]. We follow the empirical

[6]We use the same configuration of repumper as in the MOT, so that the polarization at the atom position is unknown. The repumping mechanisms may lead to a different distribution of the atoms in the

method of [75], and model the light-atom interaction by the expression (2.12) but we account for all the effects we mentioned by defining for each Zeeman state $|m_F = i\rangle$ a different effective saturation intensity $I^{\text{eff}}_{\text{sat},i}$ and a coefficient α_i such that

$$\sigma_i(I) = \frac{\sigma_0/\alpha_i}{1 + 4(\delta/\Gamma)^2 + I/I^{\text{eff}}_{\text{sat},i}} \tag{2.14}$$

One finds then that the optical density for the Zeeman state $|m_F = i\rangle$ is given by:

$$OD_i(x,y) = \sigma_0 \int n_i(x,y,z)\mathrm{d}z = -\alpha_i \ln\left(\frac{I_1(x,y)}{I_2(x,y)}\right) + \frac{I_2(x,y) - I_1(x,y)}{I^{\text{eff}}_{\text{sat},i}} \tag{2.15}$$

To correctly image our atomic samples we need to know these six coefficients, the three α_i and the three saturation intensities $I^{\text{eff}}_{\text{sat},i}$. As this model is an empirical description of our system, these coefficients have to be determined experimentally.

Determination of the parameters

The method we use to determine the six parameters is based on the two simple remarks that the real atom number does not depend neither on the intensity of the incident light nor on its distribution among the three spin states. We denote by $(\alpha_i^*, I^{\text{eff}*}_{\text{sat},i})$ the true values of the two parameters (which of course assumes that our system is well describe by this model), and we note $OD_i^*(x,y)$ the corresponding optical density.

In a first step we repeat the same experimental sequence a large number of times in conditions where the populations of the three states are expected to be stable. Each time we image the three clouds of the three Zeeman states but vary the intensity of the probe from shot to shot. Integrating the optical density (2.15) locally around each cloud we obtain the populations N_i of the three clouds as a function of the probe intensity I_2 and of the parameters α_i and $I^{\text{eff}}_{\text{sat},i}$. According to our previous remark, the three curves $N_i(I_2)$ should be flat. Let's consider the effect of the two parameters on the behavior of these curves in the limits of very low and very strong saturation.
If the incoming probe light is very low compared to the saturation intensity ($I_1, I_2 \ll I^{\text{eff}}_{\text{sat}}$), the optical density is given by the logarithmic term only and the value we calculate for two given parameters α_i and $I^{\text{eff}}_{\text{sat},i}$ is related to the true optical density by

$$OD(x,y,\alpha_i, I^{\text{eff}}_{\text{sat},i}) \approx \frac{\alpha_i}{\alpha_i^*} OD_i^*(x,y) \tag{2.16}$$

In the regime of high intensity ($I_1, I_2 \gg I^{\text{eff}}_{\text{sat}}$), the scattering rate saturates and the number of photons scattered by the atoms becomes independent of the probe intensity. We can write $I_1(x,y) = I_2(x,y) - C(x,y)$, where $C(x,y)$ is proportional the local atomic density. In this case the optical density we calculate is

$$OD(x,y,\alpha_i, I^{\text{eff}}_{\text{sat},i}) \approx \frac{\alpha_i C(x,y)}{I_2(x,y)} + \frac{C(x,y)}{I^{\text{eff}}_{\text{sat,i}}} \approx \frac{C(x,y)}{I^{\text{eff}}_{\text{sat},i}} \tag{2.17}$$

as the ratio $C/I_2 \to 0$ when $I_2 \to +\infty$. We see that the atom number we measure in the state $|m_F = i\rangle$ is determined at low intensity by the parameter α_i and at high intensity by $I^{\text{eft}}_{\text{sat},i}$. As the true atom number does not depend on the intensity, these two values should

Zeeman states of the $F = 2$ manifold depending on their initial Zeeman state in the $F = 1$ manifold.

be matched. We adjust the parameters $I^{\text{eff}}_{\text{sat},i}$ to cancel the average slope of the curves $N_i(I_2)$. If the model (2.15) describes correctly our system, the measured atom numbers should now be a constant function of the intensity.

We now need to determine the three α_i. From expression (2.16) we see that these parameters will now determine the absolute value of the atom number. To determine the value of the α_i we use the fact that the total atom number we measure should not depend on its distribution in the three spin states. A suitable experiment to test this are Rabi oscillations. (We describe in the next chapter how we realize these experiments.) In the Rabi oscillations, the real total atom number stays constant, but the three relative populations oscillate. Demanding that the total atom number we measure stays constant throughout the oscillation imposes relations on the way we count the three states relatively to one another (at a given probe intensity), and so imposes relations between the different α_i. For example making the measured total atom number a constant function of the measured atom number in $|m_F = 0\rangle$ during the Rabi oscillation fixes the ratios $\alpha_0/(\alpha_{+1} + \alpha_{-1})$. The same reasoning[7] for the three species allows to determine all the ratio α_i/α_j. If we fix one of the α parameters, for instance α_{-1}, we can then derive from this procedure the values of α_0/α_{-1} and α_{+1}/α_{-1}. Note that, to preserve the independence of the measured atom number on the intensity as we change the parameters α_i we also have to readjust the $I^{\text{eff}}_{\text{sat,i}}$.

At this stage the two conditions we required previously on the measured atom number are met: it is independent of the probe intensity and of its distribution in the three spin states. The relative values of the three populations are known, only the absolute atom number is left to fix. This will be done by the determination of the last α_{-1} parameter using an independent method.

Calibration of the total atom number

We want to determine the absolute atom number N of an atomic cloud polarized in $|m_F = +1\rangle$. The natural method consists in calibrating it against some quantity which depends on it in a known way and that we can measure absolutely, for example the critical temperature [66]. For condensates in the Thomas-Fermi regime one possibility is to calibrate N against the size of the cloud: the Thomas-Fermi radius R_{TF} depends on N with a power law, with an exponent 1/5 (see expression (1.11)) and the time-of-flight expansion that only multiplies it by a scaling factor that we can calculate [71]. As we said earlier and illustrate in figure (2.5), our condensates are not well described by the Thomas-Fermi approximation and we can not use this law. Still the size of the condensate depends on its atom number. To calculate this dependance we numerically solve the Gross-Pitaevskii equation for a polarized (scalar) gas using our experimental trap frequencies, and varying the atom number. We then calculate how the atomic distribution evolves in a time of flight experiment, following the method developed in [71]. The behavior of the size of the atomic distribution with N is close to the power law of the Thomas -Fermi regime. So, to

[7] We actually resort to two different Rabi oscillations that differ in their initial state: one starts from a state fully polarized in $|0\rangle$ and the other from a state fully polarized in $|+1\rangle$. The first one shows large oscillations of the three spin states but the populations in the $|+1\rangle$ and $|-1\rangle$ states oscillate in parallel, which makes impossible the determination of the ration α_{+1}/α_{-1}. For this we use the second oscillation where they oscillate in phase opposition. The second oscillation could not be used alone because there the population in $|0\rangle$ oscillates with a small amplitude that does not allow a precise determination of the ration $\alpha_0/\alpha_{\pm1}$. In principle an oscillation where the three states are initially populated could be used alone, but experimentally this kind of oscillation is subject to more noise as explained in chapter 3.

be consistent with the analysis of the experimental data we fit the atomic distribution corresponding to each value of N with a Thomas-Fermi distribution, extract a radius $R(N)$, an fit these sizes with a power law of the form $R_{GP}(N) = (a^2 + b^2 N^{2c})^{1/2}$. We obtain from this fit for the x direction $a = 12.4 \pm 0.3\,\mu$m, $b = 1.01 \pm 0.20\,\mu$m and $c = 0.31 \pm 0.02$. (The Thomas-Fermi solution corresponds to $a = 0\,\mu$m, $b \approx 3.6\,\mu$m for these parameters and $c = 0.2$. The parameter b is calculated from expression (1.11) and from the solution of the scaling law describing the evolution of the atomic density in time of flight.)

In parallel with this numerical calculation we experimentally produce and image cold clouds, varying their atom number by changing the MOT loading time. We fit the atomic distributions thus obtained by a Thomas-Fermi distribution and extract from it a size R_{exp} and an atom number N calculated with α_{-1}. We then fit the correction factor α_{-1} that best adjust the experimental points $R_{exp}(\alpha_{-1}N)$ to the calculated law $R_{GP}(N)$. We find

$$\alpha_{-1} = 2.09 \pm 0.33 \tag{2.18}$$

meaning that the actual atom number of our clouds (polarized in $|-1\rangle$) is around 2 times larger than the number calculated using the two-level model. We are now able to determine all the α_i and $I^{\text{eff}}_{\text{sat,i}}$. The results are summarized in table (2.2).

m_F	$+1$	0	-1
α	2.80	2.37	2.09
$I^{\text{eff}}_{\text{sat}}$ [counts]	1370	1375	1540

Table 2.2: Imaging parameters α_i and $I^{\text{eft}}_{\text{sat,i}}$ determined by the methods described above. The effective saturation intensity is left in counts because we did not calibrate the attenuation of the probe intensity between the plane of the atoms and the CCD chip of the camera, and so we can not reliably infer the intensity on the atoms from the counts measured on the chip. Several effects could cause a loss of photons from the probe beam, in particular the optics and the razor blade.

2.2.5 Imaging noise

The atomic density is deduced from the mathematical operations on the two absorption images defined by the expression (2.15). Any source of noise on these two images is transformed in a noise in the density, and so after integration in a noise in the atom number. We can identify several sources of noise.

Sources of noise and fringe removal

The first source of noise stems from the quantum nature of the photons of the imaging probe and is called shot noise. The number of photons from the probe that hit each pixel of the CCD chip has a Poissonian distribution around its mean value N_{ph}, meaning that this number fluctuates with a standard deviation $\sqrt{N_{\text{ph}}}$. The other major source of noise is the fluctuation of the pattern of the probe. In the plane of the atomic sample the profile of the probe is not uniform, but instead exhibits some particular geometrical pattern with fringes where high intensity regions alternate with lower intensity ones. These fringes originate from interference effects and from diffraction of the probe on the defects of the optics it goes through or on the dust accumulated on the windows of the chamber.

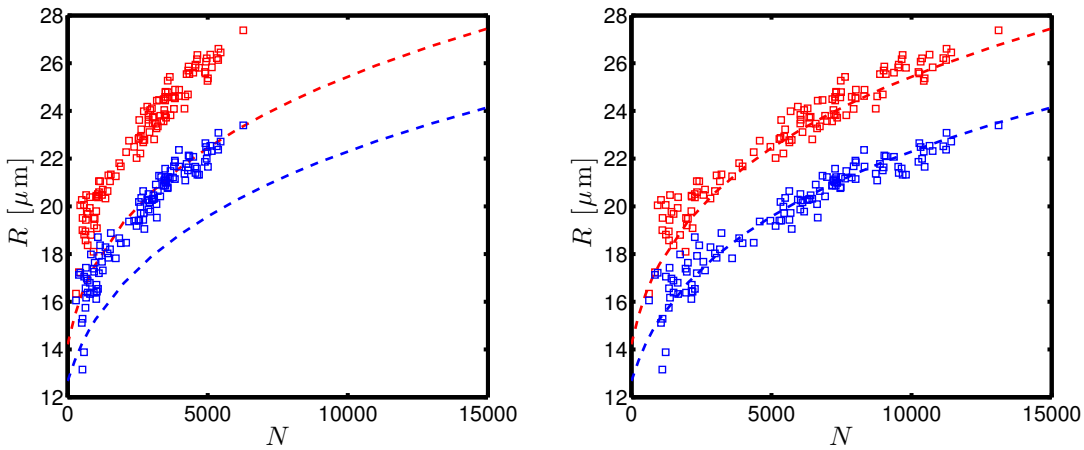

Figure 2.9: **On the left:** Measured sizes of the atomic cloud obtained from a Thomas-Fermi fit after a time of flight of 2.5 ms plotted against the measured atom number deduced from the ideal cross section. The red and blue squares correspond to the sizes measured experimentally in the two horizontal directions. The red and blue solid lines correspond to the sizes obtained in the same two directions from a Thomas-fermi fit of the exact solution of the Gross-Pitaevskii equation. **On the right:** The same measured sizes plotted against the measured atom number corrected by the factor deduced from the fit procedure explained previously. The red and blue solid lines are the same as on the left plot.

Because of various mechanical noises, this pattern fluctuates in time, and in particular it may be globally shifted by some pixels between the two absorption images, leading to an imperfect normalization of the intensity of the first image. These fluctuations of the probe pattern are stochastic, as they come from high frequency mechanical noise (typically tens of kHz) that do not stay coherent over the 4 ms separating the two images. This induces a noise of the measured optical density when we repeat the experiment. This noise is more pronounced in the region of the probe pattern with a larger gradient of intensity, where fringes in the optical density appear and form reproducible structures.

To reduce this noise we use during the analysis of the two raw pictures a fringe-removal algorithm. This algorithm builds for each first absorption image I_1 (i.e. with atoms) the best second image $I_{2,\mathrm{opt}}$ (i.e. without atoms) by linearly combining a large set of second pictures $I_{2,k}$:

$$I_{2,\mathrm{opt}} = \sum_k c_k I_{2,k} \tag{2.19}$$

The coefficients c_k are determined by the minimization of the least square difference $\sum_{x\in S} (I_1(x) - c_k I_{2,k}(x))^2$, where x labels the pixels of the images and S is a subset of pixels excluding the atom region. This minimization is equivalent to the resolution of a large linear system, which can be performed efficiently using the LU decomposition. The algorithm is fast and needs approximately ten seconds to determine hundreds of best reference images out of a set of the same size. This technique allows one to account for the vibrations of the second image compared to the first one, and thus vastly reduces the fringe amplitude [76].

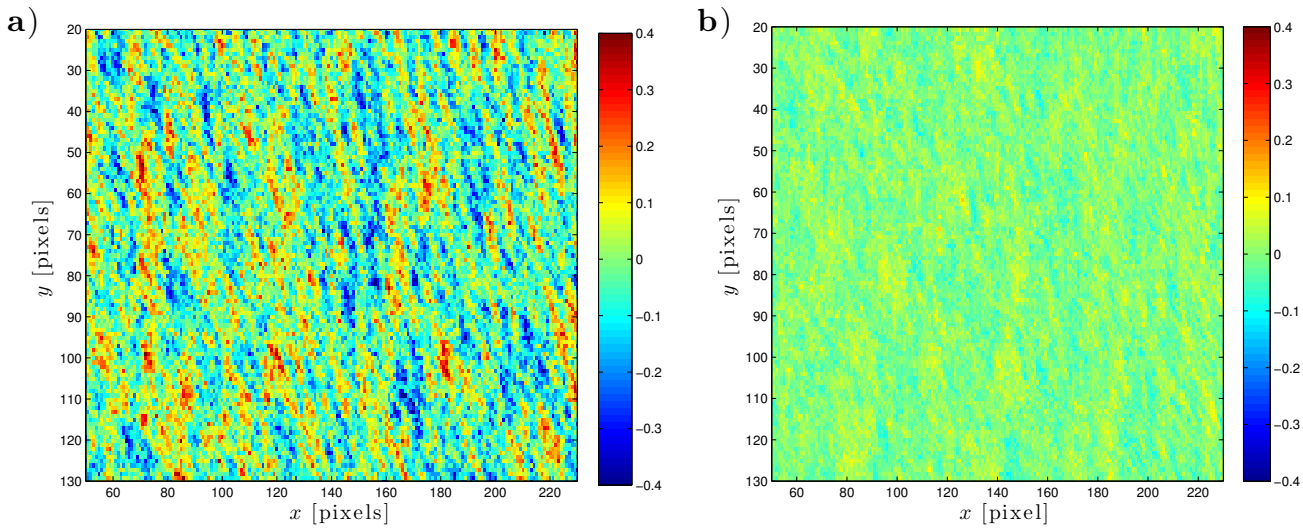

Figure 2.10: **a**): Absorption image without atoms analyzed without using the fringe-removal algorithm. **b**): The same image analyzed with the fringe-removal algorithm, using a set of 200 reference pictures.

Dependence on the imaging intensity

We now look how these sources of noise impact the measured optical density. We write the intensity of the absorption images as

$$I_i^\gamma(\mathbf{r}) = \bar{I}_i(\mathbf{r}) + \delta I_i^\gamma(\mathbf{r}) \tag{2.20}$$

where $i = 1$ or 2, $\mathbf{r} = (x, y)$ and γ labels one experimental realization. $\bar{I}_i(\mathbf{r})$ corresponds to the average over the experimental realization $\langle I_i^\gamma(\mathbf{r})\rangle$, and $\delta I_i^\gamma(\mathbf{r})$ denotes the fluctuations around this average and contains the shot noise and the spatial noise described above. To make these two contributions appear we write to first order:

$$I_i^\gamma(\mathbf{r}) = \bar{I}_i f_i(\mathbf{r}) + \delta I_i^\gamma f_i(\mathbf{r}) + \bar{I}_i \delta f_i^\gamma(\mathbf{r}) \tag{2.21}$$

where $\bar{I}_i$ represents the average intensity in picture i and δI_i^γ the difference to this average of the experiment γ, and $f_i(\mathbf{r})$ represents the average spatial mode of the probe intensity in picture i and δf_i^γ the difference of the spatial mode in experiment γ to this average mode. We insert this expression in the definition of the optical density (2.15) and develop it to first order in $\delta I_i^\gamma/\bar{I}_i$ and $\delta f_i^\gamma(\mathbf{r})/f_i(\mathbf{r})$. We obtain:

$$\begin{aligned} OD(\mathbf{r}) \approx & -\alpha\left[\ln\left(\frac{\bar{I}_1 f_1(\mathbf{r})}{\bar{I}_2 f_2(\mathbf{r})}\right) + \frac{\delta I_1^\gamma}{\bar{I}_1} - \frac{\delta I_2^\gamma}{\bar{I}_2} + \frac{\delta f_1^\gamma(\mathbf{r})}{f_1(\mathbf{r})} - \frac{\delta f_2^\gamma(\mathbf{r})}{f_2(\mathbf{r})}\right] \\ & + \frac{\bar{I}_2 f_2(\mathbf{r}) + \delta I_2^\gamma f_2(\mathbf{r}) + \bar{I}_2 \delta f_2^\gamma(\mathbf{r}) - \bar{I}_1 f_1(\mathbf{r}) - \delta I_1^\gamma f_1(\mathbf{r}) + \bar{I}_1 \delta f_1^\gamma(\mathbf{r})}{I_{\text{sat}}^{\text{eff}}} \end{aligned} \tag{2.22}$$

The terms $\delta I_i^\gamma/\bar{I}_i$ correspond to the shot noise and have a variance $1/\bar{I}_i$. The terms $\delta f_i^\gamma(\mathbf{r})/f_i(\mathbf{r})$ correspond to all the fluctuations of the spatial mode of the probe intensity, and have a variance that depends on the mode f_i. Considering that the two mean intensities of the two pictures on one side, and the two average spatial modes on the other are close, we note $\bar{I}_1 \approx \bar{I}_2 = I_0$ and $f_1(\mathbf{r}) \approx f_2(\mathbf{r}) = f(\mathbf{r})$. Taking the variance of the optical

density over γ and supposing that the noise between different realizations is not correlated we obtain after some calculations:

$$\Delta\left(OD(\mathbf{r})\right)^2 = 2\alpha\left(1+\frac{f(\mathbf{r})}{\alpha}\frac{I_0}{I_{\text{sat}}^{\text{eff}}}\right)^2\left(\frac{1}{N_{\text{ph}}}+\frac{(\delta f(\mathbf{r}))^2}{f(\mathbf{r})^2}\right) \tag{2.23}$$

where $N_{\text{ph}} = I_0\sigma\Delta t/\hbar\omega = N_{\text{counts}}/\eta g$ is the average number of photons of energy $\hbar\omega$ hitting the pixel $\mathbf{r}$ of area σ during the exposure time Δt. N_{count} is the number of counts on the pixel of the CCD chip, $\eta = 0.95$ and $g = 1e^-/\text{count}$ are the quantum efficiency and the gain of the camera. The noise in atom number on the pixel $\mathbf{r}$ is given by $\Delta N = (\sigma/\sigma_0)\Delta OD(\mathbf{r})$ (σ_0 is the resonant scattering cross-section). Two regimes can be identified. For low intensities of the probe ($I_0 \ll I_{\text{sat}}$) the noise on the measured atom number is dominated by the shot noise that scales as $1/\sqrt{I_0}$. For large intensities on the other hand, it is dominated by the term $\delta f(\mathbf{r})I_0/I_{\text{sat}}^{\text{eff}}$ and so increases like I_0. This increase of the noise at high intensities is due to the fluctuations of the spatial mode. Consider the intensity at one particular position of the spatial mode of the probe, and then the intensity at this same position but after the spatial mode was shifted. The difference between the two is proportional to the global intensity of the probe, and this noise enters directly in the second term of the optical density. The boundary between the two regimes depends on the value of α and of $(\delta f)^2/f^2$, which is a characteristic of the experimental set-up. To determine the probe intensity I_0 that minimizes the noise in our case, we take a serie of pictures where we make sure that no atoms are present (by disabling the UV LEDs for example) and where we vary the probe intensity. We then count the number of atoms and look at its fluctuation when we scan I_0. The results are presented in the figure (2.11) where the standard deviation of the atom number counted in the three clouds is plotted against the local intensity of the probe expressed in counts on the CCD chip. We observe that the noise first decreases at very low intensities, due to the gain in shot noise. Then the additionnal noise due to fluctuations of the probe overtakes this gain and the total noise increases again with the incoming intensity, in an approximately linear way. An intensity is then identified that gives the minimum noise on the atom number, in this case $I \approx 3000$ counts. This optimal intensity depends critically on the term $\delta f/f$, which is characteristic of the probe pattern, and so should be re-evaluated each time this pattern changes (for instance when we realign the probe beam).

We can estimate the noise we expect from the shot noise only at the intensity $I = 3000$ counts by setting $\delta f = 0$ in expression (2.23). The signal is integrated over a region of 40×40 pixels, so the noise in atom number reads

$$\Delta N = \sqrt{N_{\text{pixel}}}\sqrt{2\alpha}\left(1+\frac{I_0}{I_{\text{sat}}^{\text{eff}}}\right)\frac{1}{\sqrt{N_{\text{ph}}}}\frac{\sigma}{\sigma_0} \tag{2.24}$$

with $\sqrt{N_{\text{ph}}} = \sqrt{N_{\text{count}}/\eta g} \approx 56$ and σ the size of one pixel in the plane of the atoms. From the determination of the imaging parameters we found that the three α are close to 2, and the $I_{\text{sat}}^{\text{eff}}$ on the order of 1500 counts. With these numbers we obtain $\Delta N \approx 52$ atoms. On figure (2.11) we measure a noise between 60 and 80 atoms. As the sources of noise add quadratically we deduce that the noise due to the fluctuations of the probe pattern and the shot noise are of the same order at this intensity.

2.3 Preparation of a controlled magnetization

As explained in the first chapter, the magnetization of a spinor gas of Sodium is to a very good approximation a conserved quantity in an Hamiltonian evolution. As it determines

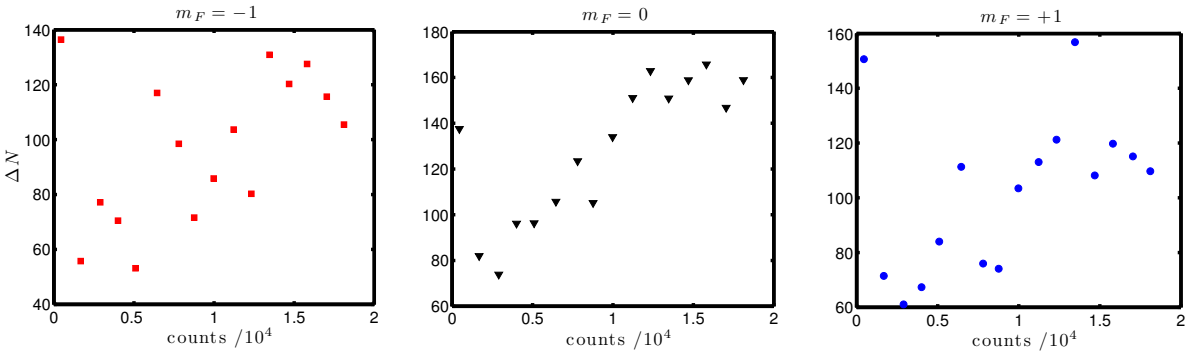

Figure 2.11: Standard deviation of the measured atom number in the three spin states as a function of the number of counts on the CCD chip. The UV LEDs were disabled during the experiment so that no atom was actually present in the pictures. The number of counts is averaged over a region of 40×40 pixels around each of the three clouds (when they are present). This number is proportional to the local intensity. We see that the noise first decreases at low intensities (shot noise), has a minimum around 3000 counts and then increases again (spatial noise).

important properties of the system (in particular the mean-field ground state, as will be evidenced in chapter 3), the investigation of its behavior at equilibrium requires to be able to control the magnetization of the atomic cloud.

Important remark: The states $|m_F = +1\rangle$ and $|m_F = -1\rangle$ play exactly symmetric roles in the thermodynamic properties of the spin-1 Bose gas. It turned out that the naturally most populated state in our samples (meaning the most populated state if we do not act on the internal degree of freedom) is the $|m_F = -1\rangle$ state, as evidenced by our polarization process presented in this section. Yet for simplicity reason we prefer to consider positive magnetizations. In the following we will then mostly consider the absolute value of the magnetization.

If we run an experimental sequence as described in the first section, the magnetization of the cloud turns to be always close to -0.7, a value presumably determined by the combined effects of the optical pumping and of the magnetic field at stake during the MOT phase. Due to the symmetry of the problem in spin space, we can restrict our experimental studies to negative magnetizations. We then need to be able to increase the absolute magnetization of the cloud from its "natural" value 0.7 to unity, and to decrease it to zero. We use for each case a different technique that we describe here. As both techniques impose a precise control of the magnetic field we first describe how we achieve it.

2.3.1 Magnetic fields control

The external magnetic field is a key parameter in the physics of spinor condensate. To manipulate and to probe our system we need to vary it, both in amplitude and in direction. The single particle spin Hamiltonian is parametrized by the magnetic field through the Zeeman effect $\hat{H} = -\hat{\boldsymbol{\mu}}.\mathbf{B}$ (where $\boldsymbol{\mu}$ is the magnetic moment of one particle), and the time dependence of the field automatically makes the single particle spin eigenstates also time-dependent, as well as their energy. Let us suppose that at $t = 0$ the magnetic

field $\mathbf{B}$ points in the z direction. The spin eigenstates are the states $|+1\rangle_z, |0\rangle_z$ and $|-1\rangle_z$. If at $t > 0$, the field $\mathbf{B}$ turns, the eigenstates also continuously rotate in spin space. We want that the spin state of our atomic cloud stays at every time the same compared to the time-dependent quantization axis defined by $\mathbf{B}$. This imposes that our system adiabatically follows the variations of the magnetic field. In our case the condition of adiabatic following is expressed by the fact that the Larmor frequency ω_L is much larger than the typical angular frequency ω_B at which the magnetic field rotates in space. In other words, the magnetic moment precesses rapidly about the direction of the field compared to its angular speed. This condition for adiabaticity writes

$$\omega_L = |g_F| \frac{\mu_B}{\hbar} ||\mathbf{B}(t)|| \gg \omega_B \tag{2.25}$$

In the $F = 1$ hyperfine manifold of Sodium one has $|g_F| = 1/2$, so that $|g_F|\mu_B/\hbar \approx 2\pi \times 700\,\mathrm{kHz.G^{-1}}$.

We illustrate this condition with a simple example. We consider the situation where the magnetic field lies in the $x - z$ plane and varies in time according to

$$\mathbf{B}(t) = \begin{pmatrix} B_0 \\ 0 \\ bt \end{pmatrix}. \tag{2.26}$$

Here B_0 is expressed in G and b in $\mathrm{G.s^{-1}}$. As t goes from $-\infty$ to $+\infty$ the direction of the magnetic field turns from $-\mathbf{e}_z$ to $+\mathbf{e}_z$, as illustrated in the figure (2.12). We define θ the angle between $\mathbf{B}(t)$ and $\mathbf{e}_z$. The rotation speed of the field is given by the time derivative of θ,

$$\dot{\theta} = \frac{b}{B_0} \cos^2 \theta. \tag{2.27}$$

It is maximum for $\theta = 0$, which corresponds to the time $t = 0$. On the other side, the Larmor frequency is minimum at the same time and is equal to $\omega_L = \mu_0 B_0/2$. The adiabaticity condition then writes

$$\frac{\omega_L}{\dot{\theta}_{max}} = \frac{\mu_0 B_0^2}{2b} \gg 1. \tag{2.28}$$

Experimentally the coefficient b can reach values on the order of $\mathrm{G.ms^{-1}}$. In this case and for fields B_0 up to tens of mG the condition (2.28) is not verified. The adiabatic following of the spins is not guaranteed and we have to take a special care of the way we vary the magnetic fields, especially when we work with small applied felds, on the level of a few mG. Besides, the adiabatic following obviously fails if at some point the magnetic field vanishes. The atoms then experience spin-flip (or Majorana) transitions that project the initial spin state onto some random final state [60]. In particular the magnetization is not conserved during this process. For this reason we have to take care not to cross the point of zero magnetic field during the experimental sequence. A precise calibration of the ambient magnetic field is then necessary to ensure this is the case.

We calibrate the field created by each pair of coils and the components of the stray field by performing radio-frequency (rf) spectroscopy on the atoms. During the experimental sequence, on top of the evaporation of the CDT we send a known current I in one pair of coils, thus lifting the degeneracy of the Zeeman states through the linear Zeeman effect. At the same time we apply a pulse of oscillating magnetic field of chosen frequency ω,

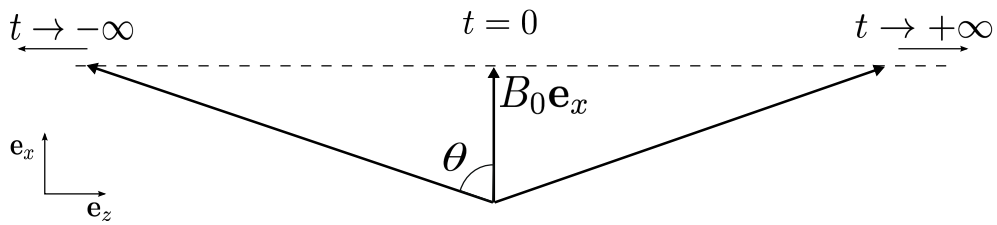

Figure 2.12: Time evolution of the magnetic field described by the expression (2.26). We define θ the angle between $\mathbf{B}(t)$ and $\mathbf{e}_x$.

using an antenna placed close to the chamber. If the frequency ω is close to the Larmor frequency ω_L, the atoms experience Rabi oscillations. We cannot resolve the oscillations, but if we apply a long pulse compared to their coherence time, the oscillations dephase and we observe a mixing of the three spin states. This mixing depends on the detuning $\delta = \omega - \omega_L$, and is maximum at resonance. We apply a pulse of 500 ms, much longer than the coherence time. To broaden the resonance we also sweep the frequency ω between $\omega - \Delta/2$ and $\omega + \Delta/2$ during the pulse, where $\Delta = 2\pi \times 10\,\text{kHz}$. At the end of the sequence we measure the three spin populations. We repeat this experiment, scanning the frequency ω, and observe the resonance in terms of the magnetization which varies from a positive value when the detuning δ is large to zero at resonance. We can then determine the field created at the atoms position by the current I. We repeat this procedure for several values of the current, positive and negative. We fit the measured magnetic fields by a law

$$B(I) = \sqrt{B_\perp^2 + (B_{0,i} + \alpha_i I)^2} \tag{2.29}$$

with the fit parameters $B_\perp$ that describe the offset field in the plane orthogonal to the axis i, the component of the stray field on the i axis $B_{0,i}$, and the calibration factor α_i in G/A that describes the response of the pair of coils. This method is illustrated by figure (2.13)

axis	x	y	z
α [G.A^{-1}]	1.434 ± 0.008	0.496 ± 0.008	1.796 ± 0.015

Table 2.3: Calibration factors of the three pairs of coils deduced from the RF spectroscopy.

The field created at the position of the atoms by the single coil on the vertical axis is calibrated with the same spectroscopic method.

2.3.2 Spin-mixing

We have seen in the previous section that dephased rf transitions between the three spin states induces a mixing of the spin populations. To lower the magnetization from the "natural" magnetization down to zero we use the same principle. At the beginning of the evaporation, we apply a static bias magnetic field $\mathbf{B} = B\mathbf{e}_x$ to lift the degeneracy of the Zeeman sublevels. We then apply a pulse of magnetic field oscillating at the Larmor frequency $\omega_L = \mu_B B/2\hbar$ using the same antenna as mentionned earlier for the atomic spectroscopy. The atoms then undergo Rabi oscillations between the Zeeman sublevels. The amplitude of the bias field B is chosen small enough to neglect the quadratic Zeeman effect compared to the Rabi frequency. As before we apply a rf pulse long compared to the

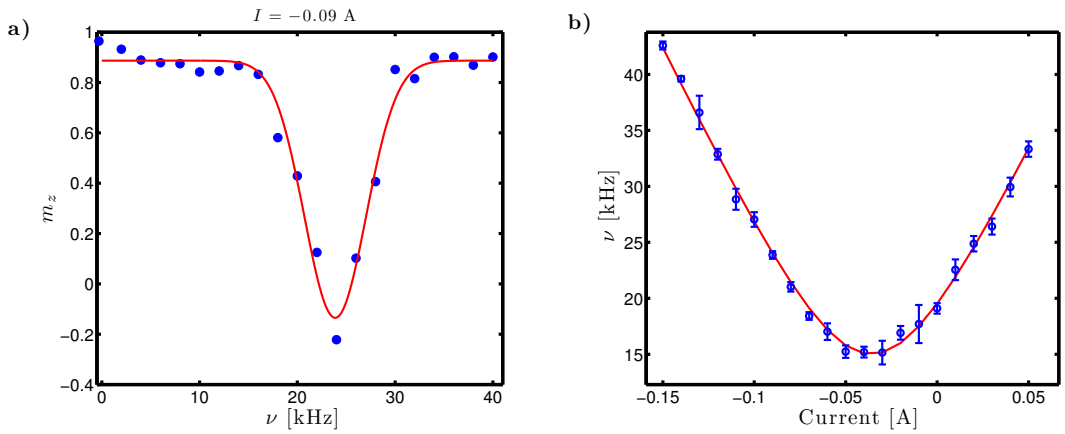

Figure 2.13: **a**): Magnetization of the atomic cloud when we scan the RF frequency around the Larmor Frequency. A current $I = -90$ mA is sent through the y-pair of coils. We determine the position of the resonance by the gaussian fit (solid red line). **b**): Fitted Larmor frequency (blue points) as a function of the current in the y pair of coils. The current in all other coils is kept unchanged. Each point is determined by a resonance similar to the one shown in **a**).The red line is a fit with the law (2.29) and allows one to extract the value of the offset field in the y direction and the calibration factor α_y. In this case we find an offset $B_{0y} = 17 \pm 2\,\mathrm{mG}$. The calibration factors are summarized in table 2.3.

coherence time of the Rabi oscillations, so that the Rabi oscillations dephase. The duration of the pulse is fixed to 200 ms. In this case we do not want to control the mixing of the populations with the frequency of the oscillating magnetic field: this method would be too sensitive to magnetic field fluctuations. A more robust and reproducible technique uses the power of the rf pulse as control parameter. To decrease the sensitivity to magnetic field fluctuations we add a gradient of magnetic field to inhomogeneously broaden the transitions, and sweep the frequency of the rf pulse as we explained in the previous section, with the same value of $\Delta = 10\,\mathrm{kHz}$. The inhomogeneity of the Larmor frequency induces a faster dephasing of the oscillations. Here we benefit from the large size of the atomic cloud at this time of the experiment to speed up the dephasing (the cloud is still held by the CDT). We can then vary the power of the rf pulse by varying the command voltage sent to the rf amplifier. We observe the magnetization decrease as a function of the command voltage, as illustrated in figure (2.14). With this technique we can control the magnetization of the atomic cloud from -0.7 to 0 with a typical precision of 5%. In the particular case where we want to prepare a cloud of zero magnetization the precision is as good as to 3%, as we can use a very large rf power to reach the asymptotic behavior of the magnetization.

2.3.3 Spin distillation

The natural magnetization of the cloud once the resonant light is switched off is about 0.7. To increase it we take advantage of the effect of a gradient of magnetic field on the trapping potential seen by atoms in different Zeeman sublevels.

As we have seen in the section on the Stern-Gerlach separation, the superposition of a gradient of magnetic field and of an homogeneous bias field creates a spin-dependent force

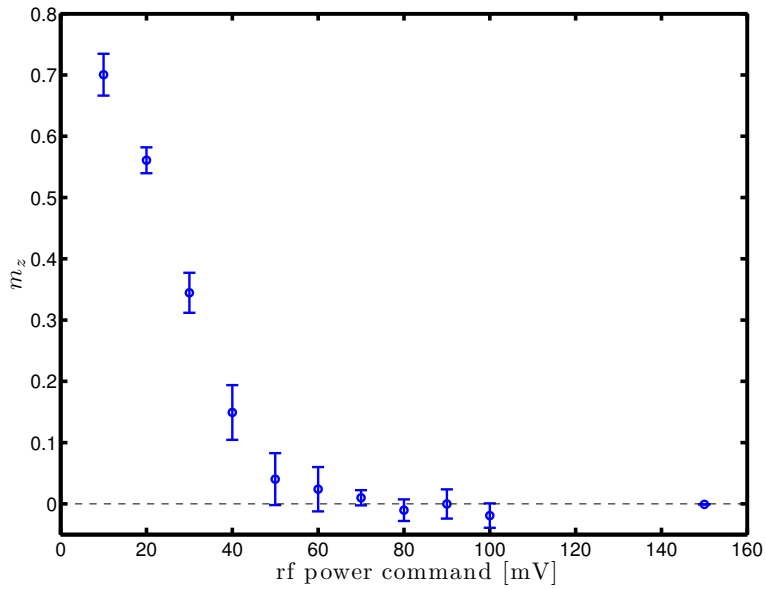

Figure 2.14: Evolution of the magnetization m of the atomic cloud as a function of the command controling the power of the RF pulse. The Larmor frequency is 190 kHz.

on the atoms. Previously we added the bias field along the strong axis of the gradient. We now add a bias magnetic field $B_0\mathbf{e}_z$ directed along the z axis. As we did before, we note L the characteristic spatial extension of the atomic cloud. The calculations are similar and we find to first order in bL/B_0:

$$\nabla||\mathbf{B}(x,y,z)|| = \text{sign}(B_0)b\mathbf{e}_z \tag{2.30}$$

The three spin states thus see a magnetic potential

$$V_{\text{mag}}(\mathbf{r}) = \text{sign}(B_0)m_F\frac{\mu_B b}{\hbar}g_F z \tag{2.31}$$

This potential adds up to two other terms: first to the confining potential created by the optical trap which is identical for the three spin states and is gaussian along the z axis:

$$V_{\text{trap}}(\mathbf{r}) = U_0(x,y)e^{-2z^2/w_z^2} \tag{2.32}$$

where w_z is the waist of the laser beam in the z direction, and second the gravitational potential $V_{\text{gr}}(\mathbf{r}) = mgz$, where m is the mass of one atom of Sodium, and g the acceleration of gravity. The leading term is the trapping potential which is symmetric along the z axis about the point $z = 0$. The effect of the gravitation is to lower one edge of the potential in the z direction, and to raise the other one. Now we add the magnetic potential (2.31). By choosing the proper value of b and sign of B_0 we can make this potential such that it cancels the effect of the gravitation for one of the two spin states $|m_F = \pm 1\rangle$, and increases it for the other state. The $|m_F = 0\rangle$ state stays unaffected. We can evaluate the gradient of magnetic field required by

$$\frac{\mu_B b}{2\hbar} = mg \tag{2.33}$$

We find that we need to apply a gradient $b \approx 8$ G.cm^{-1} to compensate the gravity. If we choose $B_0 > 0$ (resp. < 0) and note ΔU the shift in the trapping potential due to

the gravity, the total potential is equal to the confining optical potential for atoms in the low-field seeking state $|m_F = -1\rangle$ (resp. $|m_F = +1\rangle$), it is lowered by ΔU for atoms in $|m_F = 0\rangle$ and lowered by $2\Delta U$ for atoms in $|m_F = +1\rangle$ (resp. $|m_F = -1\rangle$), as shown in figure (2.15). If we apply the gradient of magnetic field and the bias field in z during the evaporation of the optical trap, the two spin states seeing a lowered potential leave the trap at a faster rate than the third one, resulting in a polarization of the atomic cloud in the state $|m_F = -1\rangle$ or $|m_F = +1\rangle$. We call this technique spin distillation, as we polarize our cloud by preferentially trapping one state and discarding the others.

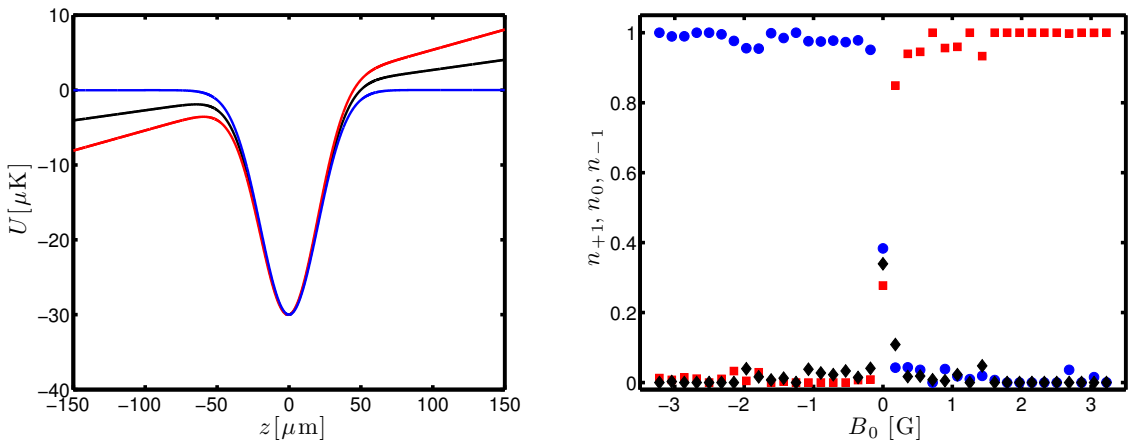

Figure 2.15: **On the left**: Potential seen by the three spin states along the z axis in the lower part of the evaporation of the CDT (the power of the CDT is 550 mW here), when the bias magnetic field $B_0 < 0$. The red, black and blue curves correspond respectively to the state $m_F = +1, 0, -1$. **On the right**: relative populations of the three spin states after the spin distillation as a function of the bias magnetic field B_0. Red squares represent the population in $|m_F = +1\rangle$, black losanges in $|m_F = 0\rangle$ and blue circles in $|m_F = -1\rangle$. The distillation is here realized after the full evaporation, when the atomic cloud is small (some tens of μm).The magnetic trapping has no effect at this length scale and the symmetric role of the states $m_F = \pm 1$ clearly appears.

The symmetry of the two states $|m_F = \pm 1\rangle$ with respect to this technique is actually not exact, but only approximate in the limit $bL/|B_0| \gg 1$. Indeed the quadrupolar magnetic field created by the anti-Helmoltz coils induces in the two other directions x and y a potential which is confining for the atoms in $|m_F = -1\rangle$ but anti-confining for the ones in $|m_F = +1\rangle$ at the beginning of this section. This effect is negligible in our case when the atomic cloud is loaded in the dimple trap, as L is then small enough, on the order of $10\,\mu$m. The two states $|m_F = \pm 1\rangle$ play there symmetric roles and we are able to polarize the cloud in either of them by choosing the sign of B_0, as shown in figure (2.15). On the contrary, when the cloud is still in the CDT and in particular when the arms of the CDT are still filled, the size L is then much larger and this effect is clearly observable. If at this point we try to polarize in the $|m_F = +1\rangle$ state, the distillation process and the quadrupolar magnetic anti-trapping compete. The result is a global loss of atoms, and an imperfect polarization. On the contrary if we try to polarize in the $|m_F = -1\rangle$ state the two effects add up and we can obtain almost fully polarized samples (with an absolute magnetization $|m_z| = 0.99 \pm 0.01$). For simplicity reasons we perform the polarization step at the same time of the experimental sequence as the depolarization one (and exchange one for the

other depending on the magnetization we aim at). We do it at high temperatures, in the CDT. The polarization mechanism is then not symmetric, and this technique only allows us to realize magnetizations with a given sign.

The spin distillation can also be used to produce atomic cloud almost purely in the $|m_F = 0\rangle$ spin state. We may want to realize this spin state for example as the initial state for Rabi oscillations as we detail in chapter 3. We first depolarize the cloud using the spin mixing technique described previously. The magnetization of the cloud is then zero within 3 %, the spin populations being distributed between the three spin states. To have all the atoms accumulate in the $|m_F = 0\rangle$ state we apply during the two-step evaporation a large magnetic field, typically 1 G, and then hold the cloud for one second in the dimple trap. As will be discussed in the next chapter, due to the large quadratic Zeeman effect the mean-field ground state in spin space for N atoms in these conditions is $|m_F = 0\rangle^{\otimes N}$. But the fluctuations of the magnetization around zero and the existence of a thermal fraction lead to the presence of a small fraction of atoms in the $|m_F = \pm 1\rangle$ states. To discard these atoms we perform two successive distillation[8] steps with the bias magnetic field B_0 in turns positive and negative. This technique allows to produce clouds with less than 1% of atoms in the $|m_F = \pm 1\rangle$ states.

2.4 Conclusion

In this chapter we described how we produce quasi-pure Bose-Einstein condensates of Sodium. Starting from a MOT we load the atoms in a large volume crossed dipole trap where we start the evaporative cooling. To conserve high trapping frequencies necessary to maintain an efficient thermalization during the evaporation we add a second small-volume optical dipole trap. The atoms fill this dimple trap where we pursue the evaporative cooling. We presented the methods to measure the temperature and the condensed fraction of the cloud during the evaporation. In the end we obtain a cloud of approximately 6000 atoms with a condensed fraction larger than 0.9. We then explained how we detect the three spin components of the condensate, using a combination of Stern-Gerlach separation and absorption imaging. We studied our imaging noise and showed how we can reduce it, by choosing the optimal probe light intensity and by using a fringe-removal algorithm. Finally we described the techniques to control the magnetization of our samples. The spin-mixing technique based on the dephasing of Rabi oscillations allows one to decrease the absolute magnetization down to zero. We are also able to polarize our clouds using a spin distillation, based on the spin-dependent potential created by a gradient of magnetic field. We now have all the tools to investigate the mean-field theory of spinors that we exposed in the first chapter, and in particular to explore the magnetic phase diagram. This investigation is the subject of chapter 3.

[8] In this case it rather corresponds to a spin "filtering" as we do not use a differential evaporation rate but really spill away the atoms.

Chapter 3

Mean-field study of an antiferromagnetic spinor condensate

In chapter 1 we developed a mean-field description of the spinor Bose-Einstein condensate. In particular we introduced the important single mode approximation (SMA) and checked its validity in our system. This reduced the problem of the spinor condensate to a pure spin problem, the spatial mode entering only to determine the interaction energy U_s. In this context we derived the mean-field ground state of an antiferromagnetic condensate in the presence of an external magnetic field, and we identified a phase transition resulting from the competition between the spin interactions and the quadratic Zeeman effect. In this chapter we experimentally investigate these predictions. The mean-field ground state can be represented by a single-particle spin state of the form

$$|\boldsymbol{\zeta}\rangle = \begin{pmatrix} \sqrt{\frac{1-n_0+m_z}{2}}e^{i(\Theta+\alpha)/2} \\ \sqrt{n_0} \\ \sqrt{\frac{1-n_0-m_z}{2}}e^{i(\Theta-\alpha)/2} \end{pmatrix} \tag{3.1}$$

where n_i is the average relative population in the $|m_F = i\rangle$ state, $m_z = n_{+1} - n_{-1}$ is the average magnetization and Θ and α are two phases. We give here the expectation values of some spin operators in this state (to leading order in the atom number N). These results will be used in this chapter.

$$\langle \hat{S}_x \rangle = \sqrt{2n_0 n_{+1}} \cos\left(\frac{\Theta+\alpha}{2}\right) + \sqrt{2n_0 n_{-1}} \cos\left(\frac{\Theta-\alpha}{2}\right) \tag{3.2}$$

$$\langle \hat{S}_y \rangle = -\sqrt{2n_0 n_{+1}} \sin\left(\frac{\Theta+\alpha}{2}\right) + \sqrt{2n_0 n_{-1}} \sin\left(\frac{\Theta-\alpha}{2}\right) \tag{3.3}$$

$$\langle \hat{S}_x^2 + \hat{S}_y^2 \rangle = 2n_0(1-n_0) + 2\cos(\Theta)\sqrt{(1-n_0)^2 - m_z^2} \tag{3.4}$$

$$\langle \hat{S}_z \rangle = m_z \tag{3.5}$$

$$\langle \hat{S}_z^2 \rangle = m_z^2 \tag{3.6}$$

where we used $n_{\pm 1} = \sqrt{(1 - n_0 \pm m_z)/2}$ for shortness. We note that in the mean-field approximation, to order $1/N$ we have $\langle \hat{S}_i^2 \rangle \approx \langle \hat{S}_i \rangle^2$ $(i = x, y, z)$. Experimentally the different spin populations are directly measurable using absorption imaging. The mean-field theory predicts the existence of two magnetic phases characterized by the occupancy of the

$|m_F = 0\rangle$ state. We show in this chapter a measurement of the magnetic phase diagram in terms of the population n_0.
The mean-field approximation also implies that in the ground state the phase Θ takes a fixed value (equal to π), while the phase α does not enter the energy functional and is then expected to be random. Contrary to the populations, the phases are not directly accessible. However the phase Θ can be revealed by a noise analysis of the magnetization that we present in the last section of this chapter. The locking of Θ to π is actually a signature of the existence of a spin nematic order in the system. By confirming this locking of Θ we thus provide direct evidence for this spin nematic ordering. This order suggests a more geometrical understanding of the ground-state in the phase diagram, and we introduce it in the first part of this chapter.

3.1 Nematic order in spinor condensates

The magnetic phase transition between the antiferromagnetic and the broken-axisymmetry phases is revealed by the presence or the absence of the $m_F = 0$ component. We understood these two phases as the consequence of the predominance of the spin interactions (which favors the coexistence of $|m_F = +1\rangle$ and $|m_F = -1\rangle$) in the first one and of the predominance of the quadratic Zeeman effect (which favors $|m_F = 0\rangle$) in the second one (see chapter 1). The phase diagram actually hides a more profound order. The study of spin correlations allows to describe the transition in terms of an orientational order of the total spin of the system. The two competing effects indeed favor different kinds of spin anisotropy: the spin interactions favor a nematic ordering of the spin while the quadratic Zeeman effect favors transverse ferromagnetism. In this section we first define the nematic order parameter for a mean-field spin state and then calculate it in the case of an antiferromagnetic spin-1 condensate.

3.1.1 Definition of the nematic order parameter

In this section we first derive the expression of the nematic tensor for a single spin 1 and then extend it to many-particles mean-field states.

Cartesian basis

We first introduce the convenient cartesian basis $\{|x\rangle, |y\rangle, |z\rangle\}$ defined in the standard one by:

$$|x\rangle = \frac{1}{\sqrt{2}}(|-1\rangle - |+1\rangle) \tag{3.7}$$

$$|y\rangle = \frac{i}{\sqrt{2}}(|-1\rangle + |+1\rangle) \tag{3.8}$$

$$|z\rangle = |0\rangle \tag{3.9}$$

We consider the single-particle spin-1 operators $\hat{\mathbf{s}} = (\hat{s}_x, \hat{s}_y, \hat{s}_z)$. The cartesian basis verifies the relation

$$\hat{s}_a|b\rangle = i\epsilon_{abc}|c\rangle \tag{3.10}$$

where $a, b, c \in \{x, y, z\}$ and ϵ_{abc} is the fully antisymmetric tensor. In particular $|a\rangle$ is the eigenvector with eigenvalue zero of the operator $\hat{s}_a$.

We now consider a generic single-particle spin-1 state $|\boldsymbol{\zeta}\rangle = \zeta_x|x\rangle + \zeta_y|y\rangle + \zeta_z|z\rangle$ ($\boldsymbol{\zeta}$ is a unit vector with complex components). One then easily obtains for the expectation value of the spin in this state:

$$\langle\hat{\mathbf{s}}\rangle = \begin{pmatrix} \langle\hat{s}_x\rangle \\ \langle\hat{s}_y\rangle \\ \langle\hat{s}_z\rangle \end{pmatrix} = -i\boldsymbol{\zeta}^* \times \boldsymbol{\zeta} \tag{3.11}$$

We separate the real and imaginary parts of $\boldsymbol{\zeta}$:

$$\boldsymbol{\zeta} = \mathbf{u} + i\mathbf{v} \tag{3.12}$$

where $\mathbf{u}$ and $\mathbf{v}$ are real vectors. Since $\boldsymbol{\zeta}$ is normalized, one has:

$$|\mathbf{u}|^2 + |\mathbf{v}|^2 = 1 \tag{3.13}$$

Besides, the gauge symmetry allows one to take $\mathbf{u}$ and $\mathbf{v}$ orthogonal and such that $|\mathbf{u}| \geq |\mathbf{v}|$. Using the relation (3.11) one finds the mean spin vector in terms of these two vectors:

$$\langle\hat{\mathbf{s}}\rangle = 2\mathbf{u} \times \mathbf{v} \tag{3.14}$$

Single-particle quadrupolar spin tensor

We wish to characterize the spin correlations in a spin-1 state. The first natural idea would be to consider the average spin $\langle\hat{\mathbf{s}}\rangle$. However, our aim is to extend this characterization to mean-field states, and in a spinor condensate this quantity is constraint by the condition of fixed magnetization. To study how the spins organize themselves in their remaining degrees of freedom we have to look at higher order moments. Still considering a single spin 1 we then introduce the spin fluctuation tensor $\langle\hat{s}_i\hat{s}_j\rangle$. As $\hat{\mathbf{s}}$ is a spin-1 object, this dyadic tensor can be decomposed as the sum of irreducible tensors of rank 0,1 and 2:

$$\hat{T}_{ij} = \hat{T}^{(0)}_{ij} + \hat{T}^{(1)}_{ij} + \hat{T}^{(2)}_{ij} \tag{3.15}$$

The scalar part is $\hat{T}^{(0)}_{ij} = 2\delta_{ij}$. The rank-1 part is the antisymmetric tensor

$$\hat{T}^{(1)}_{ij} = \frac{1}{2}\langle\hat{s}_i\hat{s}_j - \hat{s}_j\hat{s}_i\rangle = i\epsilon_{ijk}\langle s_k\rangle \tag{3.16}$$

and the rank-2 part is the symmetric tensor

$$\hat{T}^{(2)}_{ij} = \frac{1}{2}\langle\hat{s}_i\hat{s}_j + \hat{s}_j\hat{s}_i\rangle - 2\delta_{ij} \tag{3.17}$$

The information on the anisotropy of the spin state is carried by the first term in $T^{(2)}$. We finally define the spin quadrupole (or covariance) tensor

$$Q_{ij} = \frac{1}{2}\langle\hat{s}_i\hat{s}_j + \hat{s}_j\hat{s}_i\rangle - \langle\hat{s}_i\rangle\langle\hat{s}_j\rangle \tag{3.18}$$

In atomic physics a non-zero average spin $\langle\hat{\mathbf{s}}\rangle$ is known as "orientation" while a non-zero Q is referred to as "alignment". The quadrupolar tensor Q is symmetric and so can be diagonalized. After some calculations we find:

$$Q_{ij} = \delta_{ij} - (u_iu_j + v_iv_j) - \langle\hat{s}_i\rangle\langle\hat{s}_j\rangle \tag{3.19}$$

This expression immediately reveals one basis which diagonalizes Q. Indeed, if we define the vectors

$$\underline{\mathbf{u}} = \frac{\mathbf{u}}{|\mathbf{u}|} \quad , \quad \underline{\mathbf{v}} = \frac{\mathbf{v}}{|\mathbf{v}|} \quad , \quad \mathbf{w} = \frac{\langle \hat{\mathbf{s}} \rangle}{|\langle \hat{\mathbf{s}} \rangle|} \tag{3.20}$$

it is clear from (3.14) that $\mathbf{w} = \underline{\mathbf{u}} \times \underline{\mathbf{v}}$, so that $\{\underline{\mathbf{u}}, \underline{\mathbf{v}}, \mathbf{w}\}$ form an orthonormal basis, and that we can express Q as:

$$Q = \mathbb{1} - |\mathbf{u}|^2 \underline{\mathbf{u}} \otimes \underline{\mathbf{u}} - |\mathbf{v}|^2 \underline{\mathbf{v}} \otimes \underline{\mathbf{v}} - |\langle \hat{\mathbf{s}} \rangle|^2 \mathbf{w} \otimes \mathbf{w} \tag{3.21}$$

The vectors $\underline{\mathbf{u}}, \underline{\mathbf{v}}, \mathbf{w}$ are eigenstates[1] of Q with the respective eigenvalues $1 - |\mathbf{u}|^2, 1 - |\mathbf{v}|^2$ and $1 - |\langle \hat{\mathbf{s}} \rangle|^2$. These eigenvalues take their values between 0 and 1. They are related by the relations (3.13) and (3.14), so that the anisotropy of the spin is characterized by one of them only.

Mean-field quadrupolar spin tensor

We now consider N spin 1 particles. We can define the total spin operators

$$\hat{S}_i = \sum_{\alpha=1}^{N} \hat{s}_i^{(\alpha)} \tag{3.22}$$

where $i = x, y, z$ and where the operator $\hat{s}_i^{(\alpha)}$ acts as $\hat{s}_i$ on the particle α and as identity on the others. If the N particles form a mean-field condensate, they are all described by the same single-particle state $|\boldsymbol{\zeta}\rangle$ and one obtains

$$\langle \hat{S}_i \rangle = N \langle \hat{s}_i \rangle \tag{3.23}$$

where $\langle \hat{s}_i \rangle = \langle \boldsymbol{\zeta} | \hat{s}_i | \boldsymbol{\zeta} \rangle$. The treatment of product operators demands a bit more care, since for instance we have

$$\hat{S}_i \hat{S}_j = \sum_{\alpha=1}^{N} \sum_{\beta=1}^{N} \hat{s}_i^{(\alpha)} \hat{s}_j^{(\beta)} \neq \sum_{\alpha=1}^{N} \hat{s}_i^{(\alpha)} \hat{s}_j^{(\alpha)} \tag{3.24}$$

However, because we consider spin states of the form $|\boldsymbol{\zeta}\rangle^{\otimes N}$ we have

$$\langle \hat{S}_i \hat{S}_j \rangle = \sum_{\alpha \neq \beta} \langle \hat{s}_i^{(\alpha)} \hat{s}_j^{(\beta)} \rangle + \sum_{\alpha} \langle \hat{s}_i^{(\alpha)} \hat{s}_j^{(\alpha)} \rangle \tag{3.25}$$

$$= N(N-1) \langle \hat{s}_i \rangle \langle \hat{s}_j \rangle + N \langle \hat{s}_i \hat{s}_j \rangle \tag{3.26}$$

We now define the N-particles spin quadrupolar tensor

$$Q_{ij}^{(N)} = \frac{1}{2} \langle \hat{S}_i \hat{S}_j + \hat{S}_j \hat{S}_i \rangle - \langle \hat{S}_i \rangle \langle \hat{S}_j \rangle. \tag{3.27}$$

Using (3.23) and (3.26) we obtain for a mean-field state:

$$Q_{ij}^{(N)} = N \left(\frac{1}{2} \langle \hat{s}_i \hat{s}_j + \hat{s}_j \hat{s}_i \rangle - \langle \hat{s}_i \rangle \langle \hat{s}_j \rangle \right) \tag{3.28}$$

The anisotropy of a mean-field spin state is then expressed by the corresponding single-particle quadrupolar tensor. This tensor is then called the nematic tensor. It plays the role of an order parameter that characterizes the amount of alignment of a mean-field spin state, as we illustrate in the following.

[1] If $\mathbf{u} = 0$ (resp. $\mathbf{v} = 0$), then $\mathbf{w} = 0$. Zero is then a double eigenvalue of Q and the eigenvectors can be chosen as any orthonormal basis of the plane orthogonal to the non-zero vector $\mathbf{v}$ (resp. $\mathbf{u}$).

3.1.2 Application to mean-field states

In the following we only consider single-particle spin operators, which we denote by $\hat{\mathbf{S}}_i$, $i = x, y, z$.

Nematic states ("rotations of $|m_F = 0\rangle$")

We now use the quadrupolar spin tensor to get a better understanding of the nature of the mean-field ground states we identified in the chapter 1. We first focus on the ground state at zero magnetization and zero field, where we found that the mean-field energy was minimized by a family of degenerate polar states. Transforming their expression (1.64) from the standard basis to the cartesian spin basis, the polar states are defined by the spin-1 state

$$|\mathbf{\Omega}\rangle = \begin{pmatrix} \sin\theta\cos\phi \\ \sin\theta\sin\phi \\ \cos\theta \end{pmatrix} \tag{3.29}$$

This corresponds to the expression of a real unit vector $\mathbf{\Omega}$ defined in real space by the polar angles θ and ϕ (respectively the colatitude and the azimuthal angle). As these angles describe respectively the intervals $[0;\pi] \times [0;2\pi]$, the vector $\mathbf{\Omega}$ describes the entire sphere of radius unity. We note $|N : \mathbf{\Omega}\rangle \equiv |\mathbf{\Omega}\rangle^{\otimes N}$. Since the cartesian basis verifies the property $\hat{S}_a|a\rangle = 0$, with $a = x, y, z$, the state $|\mathbf{\Omega}\rangle$ is the eigenstate with eigenvalue 0 of the operator $\mathbf{\Omega}.\hat{\mathbf{S}}$.

We now compute the associated quadrupolar tensor Q. From (3.29) we obtain $\mathbf{u} = \mathbf{\Omega}$ and $\mathbf{v} = 0$. The vector $\mathbf{u}$ is in this case unitary and $\underline{\mathbf{u}} = \mathbf{u}$. Using the relation (3.14) we find that these states have no net orientation: $\langle\hat{\mathbf{S}}\rangle = 0$. The tensor Q is then only defined by the vector $\mathbf{u}$:

$$Q = \mathbb{1} - \mathbf{u} \otimes \mathbf{u} \tag{3.30}$$

This result shows that in a polar state $|N : \mathbf{\Omega}\rangle$ the spin fluctuates isotropically in the plane perpendicular to the vector $\mathbf{\Omega}$. The polar states are completely characterized by one direction of space along which their spin projection is exactly zero. These states spontaneously break the rotational symmetry of the spinor gas at zero magnetization and zero magnetic field. They are called nematic states. The vector $\mathbf{\Omega}$ is called the nematic director.

Polarized states ("rotations of $|m_F = +1\rangle$")

We now consider a polarized (or oriented) state, which is defined by its maximal average spin: $|\langle\mathbf{S}\rangle| = 1$. Using the two relations (3.14) and (3.13) this implies $|\mathbf{u}| = |\mathbf{v}| = 1/\sqrt{2}$. Its quadrupolar tensor reads:

$$Q = \mathbb{1} - \frac{1}{2}\underline{\mathbf{u}} \otimes \underline{\mathbf{u}} - \frac{1}{2}\underline{\mathbf{v}} \otimes \underline{\mathbf{v}} - \underline{\mathbf{w}} \otimes \underline{\mathbf{w}} = \frac{1}{2}\begin{pmatrix} 1 & 0 & 0 \\ 0 & 1 & 0 \\ 0 & 0 & 0 \end{pmatrix} \tag{3.31}$$

The macroscopic spin fluctuates in the plane perpendicular to its polarization. The state exhibits some spin anisotropy associated to its polarization.

The anisotropy of a spin state has two origins: the orientation of the spin (a net magnetization) and its alignment. The first kind of anisotropy breaks the time reversal

symmetry while the second does not. The nematic states correspond to maximally aligned states, while polarized states represent maximally oriented states. For a generic state, alignment and orientation of the spin both contribute to the anisotropy of the spin state.

Generic states

The three eigenvalues of the tensor Q are related by (3.13) and (3.14), so that only one parameter is needed to define the anisotropy of a generic mean-field spin state. We consider the general form of the tensor Q and note $|\mathbf{u}|^2 = \chi$. We then also have $|\mathbf{v}|^2 = 1 - \chi$ and $|\langle \mathbf{S} \rangle|^2 = 4\chi(1-\chi)$. We introduce the parameter $\mathcal{N}$ defined by

$$\mathcal{N} = 2\chi - 1 \tag{3.32}$$

The tensor Q can then be written

$$Q = \mathbb{1} - \frac{\mathcal{N}+1}{2}\underline{\mathbf{u}} \otimes \underline{\mathbf{u}} - \frac{1-\mathcal{N}}{2}\underline{\mathbf{v}} \otimes \underline{\mathbf{v}} - (1-\mathcal{N}^2)\mathbf{w} \otimes \mathbf{w} \tag{3.33}$$

The anisotropy of a generic state is characterized by the quantity $|\mathcal{N}|$ which takes values between 0 and 1. The case $\mathcal{N} = 0$ describes a polarized state, whereas the case $|\mathcal{N}| = 1$ corresponds to a nematic state. We call $\mathcal{N}$ the nematic parameter.

In a mean-field state we have $\Delta S_i^2 \ll \langle S_i^2 \rangle$ and so

$$\langle \hat{S} \rangle^2 = \langle \hat{S}_z \rangle^2 + \langle \hat{S}_\perp \rangle^2 = 1 - \mathcal{N}^2 \tag{3.34}$$

where we introduced the transverse component of the average spin $\langle S_\perp \rangle^2 = \langle S_x \rangle^2 + \langle S_y \rangle^2$.

Other nematic states

The concept of nematicity originates from the physics of liquid crystals where it characterizes the tendency of rod-shaped molecules to align along a preferred axis which results in a long-range orientational order [77]. This orientation is non-polar, meaning that the molecules do not distinguish between the orientation along the directions $\mathbf{u}$ and $-\mathbf{u}$, where $\mathbf{u}$ is a unit vector in real space. This implies that, if we note $\mathbf{u}^{(\alpha)}$ the orientation of the molecule α, one has $\langle \mathbf{u} \rangle = \sum_\alpha \mathbf{u}^{(\alpha)} = 0$ by inversion symmetry but $\langle u_i u_j \rangle \neq 0$, where $i, j = x, y, z$. Thus, the system is aligned but has no net orientation. The direction of the preferred axis - called the nematic director - is determined by weak forces induced by external magnetic or electric fields. At high temperatures thermal fluctuations would prevail on these forces and prevent the formation of a nematic order. But below a certain temperature the system does experience a transition from an isotropic phase to a nematic phase. Since there is no average orientation, the order parameter associated to this phase transition has to be a second-rank tensor. A nematic tensor similar to Q is then defined to characterize the anisotropy of the ensemble of molecules, that plays the role of an order parameter.

The notion of nematic states has then be extended to spin systems [78] and applied to various magnetic models and to correlated electron systems [79]. It refers to a state that breaks the spin $SU(2)$ symmetry but preserves the translational and time-reversal symmetry. Since this last invariance implies that the local spin density vanishes, the spin order appears in two-spins correlation functions. In the context of strongly correlated electron systems for instance, nematic states originate from charge fluctuation in a spin

stripe phase. A spin stripe consists of antiferromagnetically ordered domains separated by walls at which the staggered magnetization flips sign but keeps a fixed direction. In a nematic state the position of the domain walls fluctuates on a large enough length scale so that for times long compared to these fluctuations, the average spin at each point vanishes and the translation symmetry is restored. Yet, there is a preferred axis of space in which the staggered magnetization points, and the $SU(2)$ symmetry is broken [80].

3.1.3 Nematic order of a mean-field ground-state

We consider now the general mean-field ground state (3.1) parametrized by the magnetization m_z, by $x = 1 - n_0$ and by the angles α and Θ. We take $\alpha = 0$ without loss of generality (the liberty in the choice of α derives from the invariance by rotation around the z axis). Additionally in the antiferromagnetic case one has $\Theta = \pi$. The expression (3.1) shows the expression of the ground-state in the standard basis. Transforming it into the cartesian basis, we find:

$$|\zeta\rangle = \begin{pmatrix} -iA_- \\ A_+ \\ B \end{pmatrix}_c = \begin{pmatrix} 0 \\ A_+ \\ B \end{pmatrix}_c - i \begin{pmatrix} A_- \\ 0 \\ 0 \end{pmatrix}_c \tag{3.35}$$

with $A_\pm = \frac{1}{2}(\sqrt{x + m_z} \pm \sqrt{x - m_z})$ and $B = \sqrt{1 - x}$ (where $x = 1 - n_0$). The vectors $\mathbf{u}$ and $\mathbf{v}$ appear immediately and we can calculate the nematic parameters:

$$\mathcal{N} = 1 - x + \sqrt{x^2 - m_z^2} \tag{3.36}$$

The value of x in the ground-state was given in section 1.4.3 as a function of the magnetization m_z and of the quadratic Zeeman effect q. We are then able to compute the nematic parameter $\mathcal{N}$ in the ground-state. The figure (3.2) shows its evolution when q increases at a fixed magnetization, for several values of the magnetization. If we first

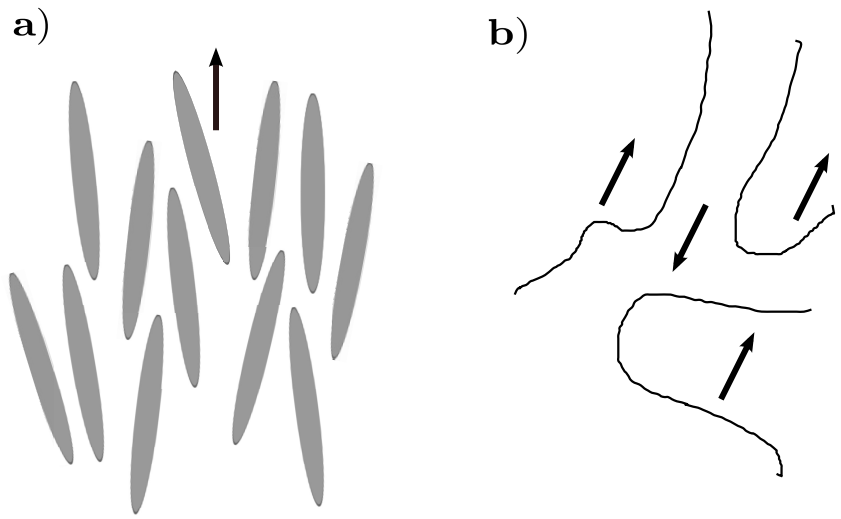

Figure 3.1: **a**): Rod-like molecules in a nematic phase, and the nematic director. **b**): A spin stripe: the staggered magnetization is well defined in each domain and flips sign at the domain walls. The fluctuations of the walls restore the translational symmetry, but there is still a preferred axis.

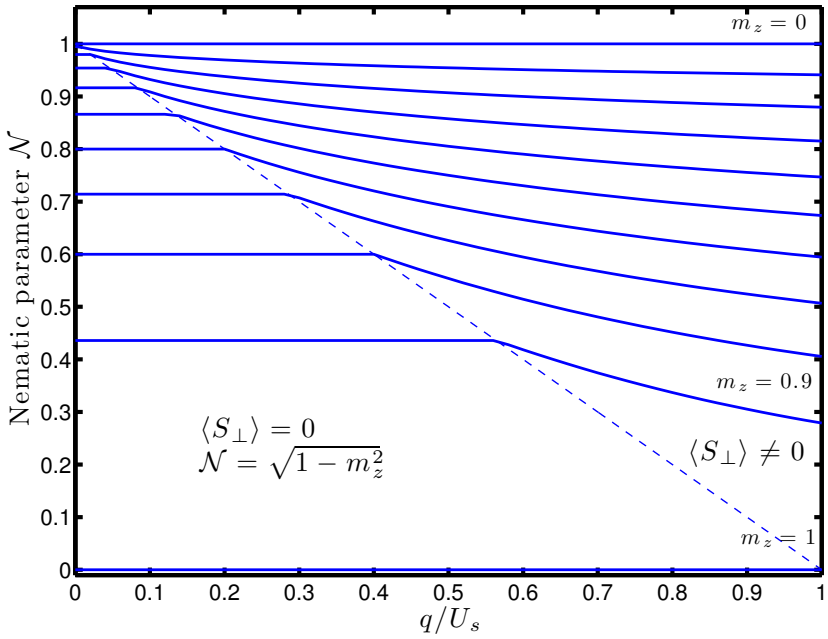

Figure 3.2: Nematic parameter $\mathcal{N}$ calculated as a function of q/U_s for magnetizations from 0 to 1 by 0.1 step. The top curve correspond to $m_z = 0$, the lower one to $m_z = 0.1$, etc... the lowest one to $m_z = 1$. For each magnetization m_z the parameter $\mathcal{N}$ is constant for $q \leq q_c$ and then decreases for $q > q_c$. The dashed line shows this transition for all magnetizations. One can identify the same two phases than in the first section.

look at the different curves at $q = 0$, we see that the nematic parameter decreases with the magnetization: $\mathcal{N}$ is equal to unity at $m_z = 0$ where the ground-state is a nematic state, and then goes down to zero at $m_z = 1$, where the the spin-state is fully polarized. This reflects the fact that when the magnetization rises the system exchanges alignment against orientation. Now for a given magnetization, $\mathcal{N}$ first stays constant as q increases until the critical value $q = q_c$ defined in (1.65), and then decreases for $q > q_c$. We here again identify the two same phases as in the first section when we looked at the population n_0.

We now consider the average spin $\langle \hat{\mathbf{S}} \rangle$. From (3.35) and using expression (3.14) we obtain :

$$\langle \mathbf{S} \rangle = \begin{pmatrix} 0 \\ -2A_- B \\ 2A_- A_+ \end{pmatrix} \tag{3.37}$$

The x component of the spin is zero because we chose $\alpha = 0$. The vector $\langle \mathbf{S} \rangle$ for an other choice of α is deduced from this one by a rotation around the z axis, leading to the cancellation of the spin in an other direction of the xy plane. We can check that we find the norm of the mean spin as in (1.63):

$$\begin{aligned} \langle \mathbf{S} \rangle^2 &= 4A_-^2 (A_+^2 + B^2) \\ &= m_z^2 + 2x(1-x)(x - \sqrt{x^2 - m_z^2}) \end{aligned} \tag{3.38}$$

This norm is the sum of the longitudinal spin $\langle S_z \rangle^2 = m_z^2$ and of the transverse spin $\langle S_\perp \rangle^2 = 2x(1-x)(x - \sqrt{x^2 - m_z^2})$. The longitudinal part is fixed by the conservation of the magnetization, so that the system can only change its transverse spin to minimize its energy. The figure (3.3) shows the phase diagram of the transverse spin calculated in the mean-field ground state. The two phases appear clearly: at a given magnetization m_z, the transverse spin vanishes below the critical QZE q_c, and then rises with q.

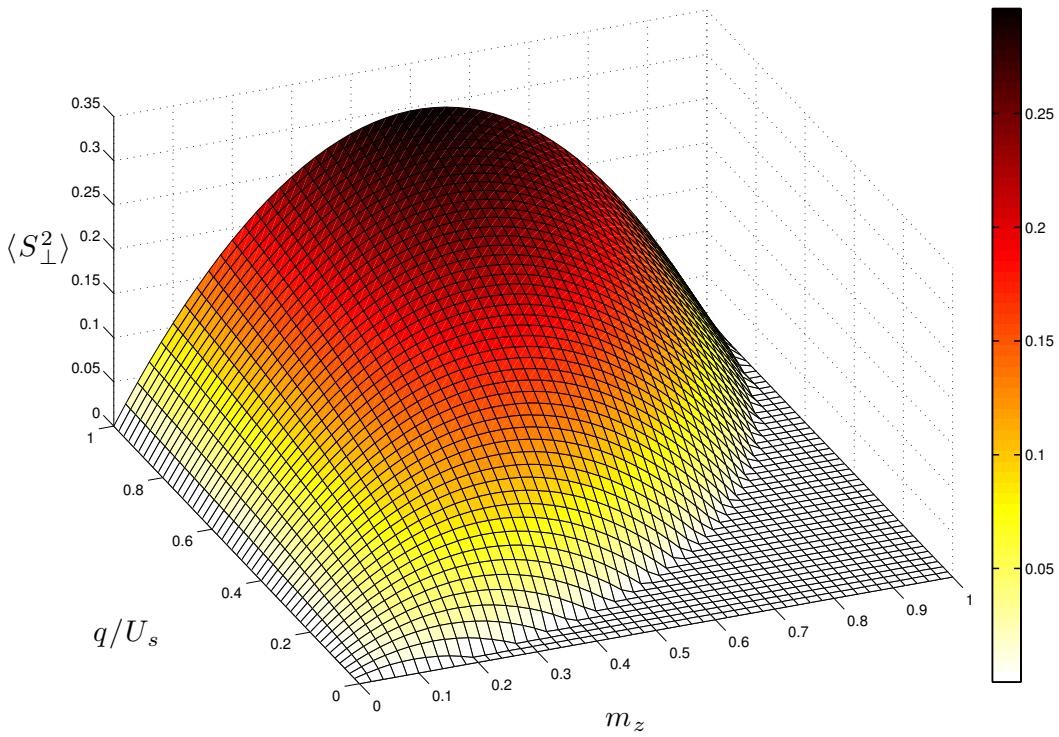

Figure 3.3: Transverse spin $\langle \hat{\mathbf{S}}_\perp \rangle^2$ as a function of the magnetization m and QZE q.The same two phases emerge: the first one for $q \leq q_c$ where the spin has no transverse component, and the second one for $q > q_c$ where the transverse spin increases with q.

By considering the nematic order parameter and the transverse spin, we identified the same two phases as in chapter 1 with the population n_0, but we can now interpret the phase diagram in terms of symmetry of the spin state. The two phases originate from the competition between the spin-dependent interactions and the quadratic Zeeman effect. This competition is expressed by the equation (3.34) that we reshape in

$$\langle S_\perp \rangle^2 + \mathcal{N}^2 = 1 - m_z^2 \tag{3.39}$$

The right hand side of this equation is fixed due to conservation of magnetization. The anisotropy of a spin state is then distributed between the nematic alignment of the spin (quantified by $\mathcal{N}$) and the transverse component of the total spin.The balance between nematic order and transverse spin is determined by the relative strength of interactions and Zeeman effect. Antiferromagnetic interactions favor the alignment of the spins (whereas ferromagnetic interactions would favor their orientation) and so tend to increase the nematic parameter $\mathcal{N}$. At $q = 0$ the ground-state is set by the interactions only, and so

consists of the maximally aligned state compatible with the magnetization. The effect of the magnetic field on the other hand is to favor the $|m_F = 0\rangle$ spin state. The transverse spin is created by spin coherences between the $|m_F = 0\rangle$ state and the two others, which are automatically non-zero in a condensate. Adding atoms in $|m_F = 0\rangle$ thus increases the transverse spin. The apparition of a transverse spin destroys the rotational symmetry around the z axis, and so lowers the nematic order. In the first phase that we denoted "antiferromagnetic" in the first section, the effect of the interactions is strong enough to overcome that of the magnetic field and to maintain the rotational symmetry around z. The spin state remains maximally aligned and the nematic parameter $\mathcal{N}$ stays constant at the maximum value allowed by the magnetization. Then, as q reaches the critical value q_c, the quadratic Zeeman effect starts to dominate over the interactions, and forces the accumulation of atoms in the $|m_F = 0\rangle$ state. A transverse spin appears that breaks the rotational symmetry and causes a loss of alignment (hence the denomination "broken axisymmetry"). As q increases, the population n_0 and the transverse spin increase, and the nematic order of the state decreases. The antiferromagnetic phase thus corresponds to a phase of maximal nematic ordering of the spins, while in the "broken axisymmetry" phase the quadratic Zeeman effect reduces this order by "forcing" the development of a transverse component of the average spin.

3.2 Experimental study of the phase diagram

The mean-field ground state of a spinor condensate of Sodium was studied experimentally in [51, 30] where the authors measured the magnetic phase diagram in terms of the population n_0. However these works did not reliably measure the region of low magnetic fields, presumably because of the long equilibration time required in this domain. We present in this section our experimental results on the mean-field phase diagram which include this low field region. We make sure equilibrium is reached by waiting several seconds before counting the three Zeeman populations.

3.2.1 Experimental sequence

The experiment consists in measuring the population in the $|m_F = 0\rangle$ spin state in the ground state as a function of the magnetization and of the quadratic Zeeman effect q. For this we prepare a cloud of desired magnetization using the rf-mixing or distillation process, as explained in chapter 2. We then perform the two-step evaporation. In the second step we use the exponential ramp described in chapter 2 to decrease the power of the dimple trap. At the beginning of this evaporation we ramp the magnetic field to a chosen value. The direction of the field does not matter but only its amplitude which determines the quadratic Zeeman effect. We decide to always apply this magnetic field in the x direction. At the end of the evaporation the condensed fraction is on the order 0.9. We now have to hold the cloud in the dimple trap while keeping the magnetic field at the same value, and wait long enough to allow the system to reach its equilibrium. We explain in the next paragraph how we choose this hold time. At the end of this waiting step we perform a Stern-Gerlach experiment to separate the three Zeeman states. We finally image the clouds, count the three populations and deduce the relative population n_0.

As suggested in [51] and [66], the long equilibration time could be an obstacle to the observation of the true ground-state at equilibrium. To evaluate this time we prepare

clouds of different magnetization with different values of the applied magnetic field, and starting from the end of the evaporation stromboscopically measure the three spin populations after a Stern-Gerlach separation. We can this way follow the equilibration of the spin populations as we hold the cloud. We find indeed that the equilibration is the slowest for low magnetic field and low magnetization. We observed equilibration on a typical time scale up to 1 s. Hopefully, the lifetime of our condensate in the dimple trap is much longer, on the order of 10 s. We finally decide to wait for 6 s before measuring the populations. This way, we make sure the equilibrium is reached while the total atom number is still sufficient to obtain a good signal.

3.2.2 Results

We repeat this experiment scanning the magnetization of the cloud and the amplitude of the magnetic field. For a given magnetization we measure the population n_0 as a function of the magnetic field. An example of these measurements is shown in figure (3.4) where the cloud was prepared with a magnetization close to 0.4. We observe the transition from a region where n_0 is constant and small at low magnetic field to a region where it progressively increases toward an asymptotic value. The transition between these two regions occurs at the critical field B_c.

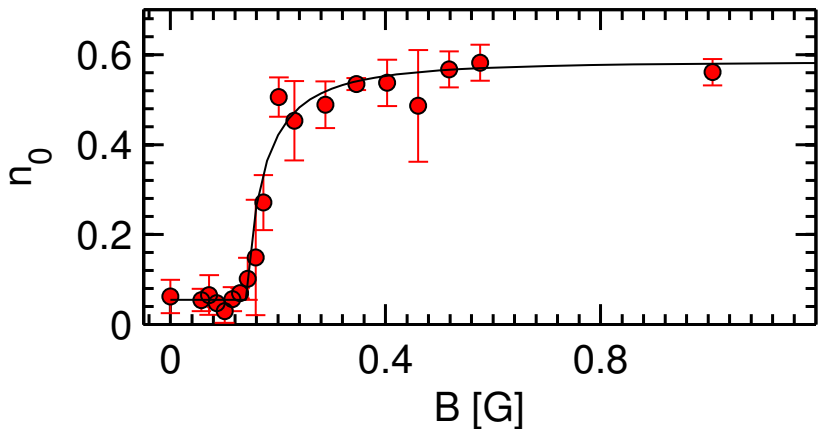

Figure 3.4: Measured population n_0 for a fixed magnetization $m_z \sim 0.4$ and for several values of the applied magnetic field B. We observe the transition from a region of constant and low n_0 at low B to a region of large n_0. The black solid line is a fit using the function (3.40) from which we extract the critical field B_c and the asymptotic value of n_0 at large B. The error bars correspond to the statistical uncertainties of one standard deviation.

The summary of these results for various magnetizations is shown in the phase diagram (3.5). To extract the critical magnetic field B_c from these measurements we fit them with the hyperbolic function:

$$f(B) = \alpha + \beta \max\left(\frac{B^2 - B_c^2}{B^2 - B_c^2 + \Delta B^2}, 0\right) \tag{3.40}$$

which reproduces well our data. In addition to the critical field, the parameters of this function give access to the offset of n_0 in the antiferromagnetic phase (α), to its asymptotic value at large field (β) and to the slope of n_0 at the transition (ΔB). The theoretical value

of the critical field is given by equation (1.65). It depends on the interaction energy U_s. To compare it with our fit results we evaluate U_s from the solution of the Gross-Pitaevskii equation using our trap frequencies. We obtain $U_s \approx h \times 40\,\mathrm{Hz}$. The measured values of the critical field are shown in figure (3.6) and compared to the theoretical prediction for this value of U_s. We find a very good quantitative agreement.

Effect of the thermal fraction

At non-zero temperature we expect that the presence of thermal atoms causes some deviation to the SMA prediction. Indeed, the thermal fraction is not captured by the single-mode mean-field theory, and its distribution among the three spin states may differ from that of the condensate. A first level of description of the thermal fraction is to suppose an isotropic distribution of the populations. This assumption is supported by a Hartree-Fock model of the partly condensed spin-1 Bose gas [81]. We denote by superscripts c and th the contributions of the condensed and thermal components respectively, and note f_c the condensed fraction. We have

$$n_0^{tot} = f_c n_0^c + (1 - f_c) n_0^{th} \tag{3.41}$$

$$m_z^{tot} = f_c m_z^c + (1 - f_c) m_z^{th} \tag{3.42}$$

where n_0^c and m_z^c are normalized to the number of condensed atoms and n_0^{th} and m_z^{th} are normalized to the number of thermal atoms. The supposed isotropy of the thermal fraction gives

$$n_0^{tot} = f_c n_0^c + \frac{1 - f_c}{3} \tag{3.43}$$

$$m_z^{tot} = f_c m_z^c \tag{3.44}$$

This modifies in particular the asymptotic value of n_0 at large field, which is predicted to be $1 - m_z$ in the SMA and becomes $(1 + 2f_c)/3 - m_z$. The value of n_0 in the antiferromagnetic phase is also modified (it becomes $(1 - f_c)/3$) as well as the value of the critical field B_c. In the figure (3.7) we show the effect of the thermal fraction on the asymptotic value of n_0. The left figure represents data from a first measurement of the phase diagram. We observe that the values of n_0 at high fields actually deviate from the $T = 0$ prediction. On the right figure we show data from a second measurement of the phase diagram, where we were able to further cool our clouds. The non-condensed fraction is only of a few percent and its effects are small: the asymptotic values of n_0 are compatible with the SMA prediction at $T = 0$. The presence of the thermal atoms also explains the measurement of a non-zero population n_0 in the antiferromagnetic phase, as appears in figure (3.4). In figure (3.6) we show the value of the critical field measured with our coldest clouds.

Our experimental data quantitatively reproduce the mean-field prediction of the phase boundary and the behavior of the population n_0 above the transition. We find a quantitative agreement between our measurement of the phase diagram and the theory over the whole range of parameter we explored (m_z varying from zero to 0.8 and the field B from zero to 1 G corresponding to $q/U_s \sim 6$). This confirms that the SMA holds in this regime of parameters.

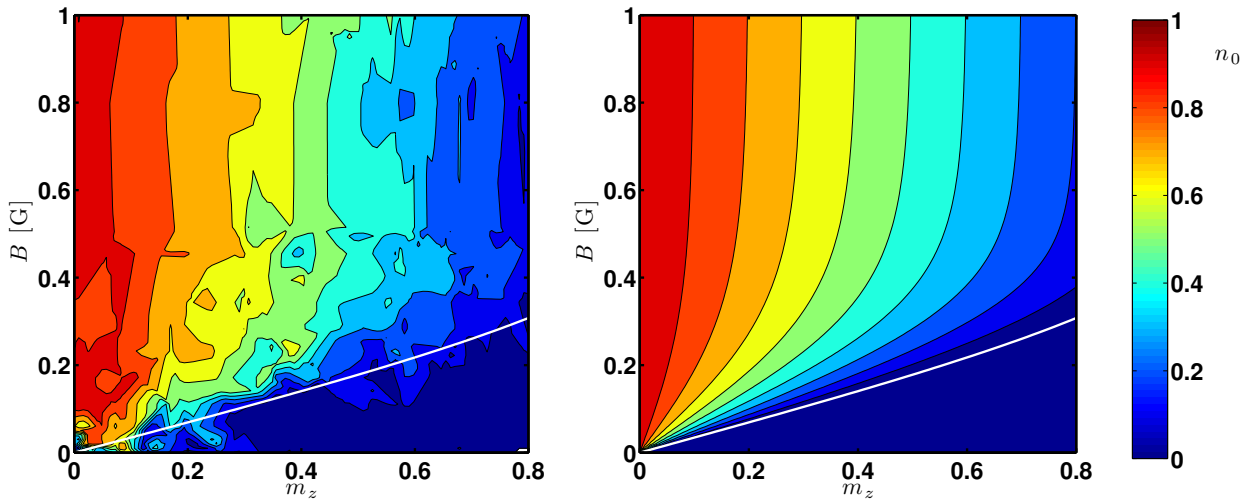

Figure 3.5: Measured phase diagram (left) and theoretical mean-field prediction in the SMA (right). We represent the population n_0 as a function of the magnetization m_z and of the applied magnetic field B. On each figure the white line shows the theoretical critical magnetic field.

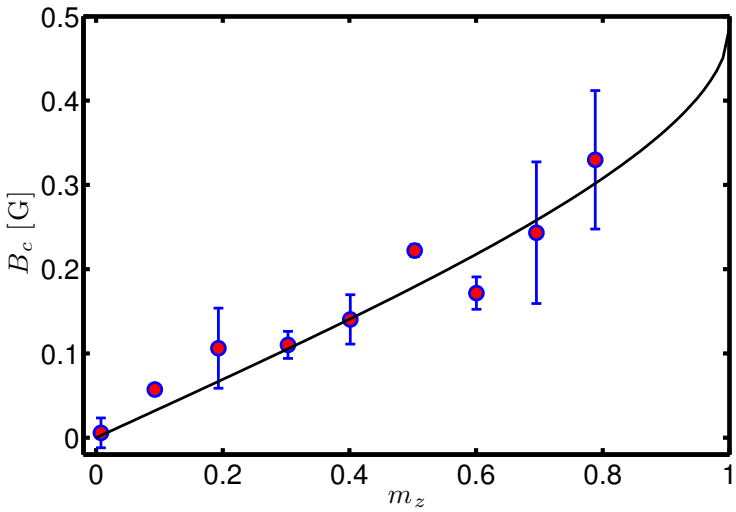

Figure 3.6: Critical field B_c fitted for different magnetizations. The error bars correspond to the one standard deviation confidence intervals. The solid black line gives the mean-field prediction in the SMA.

3.3 Detection of spin-nematic order

We have seen in the first section of this chapter that in an antiferromagnetic spin-1 Bose gas the spin-dependent interactions favor nematic ordering. A fully nematic state is however incompatible with a non-zero average magnetization. In this situation interactions tend to maximize the nematic order and consequently to minimize the transverse spin component. This results in particular in the locking of the relative phase Θ to π, independently of any other parameter. The measurement of Θ then represents a way to probe the nematic order. We report here on the method we used to measure this phase.

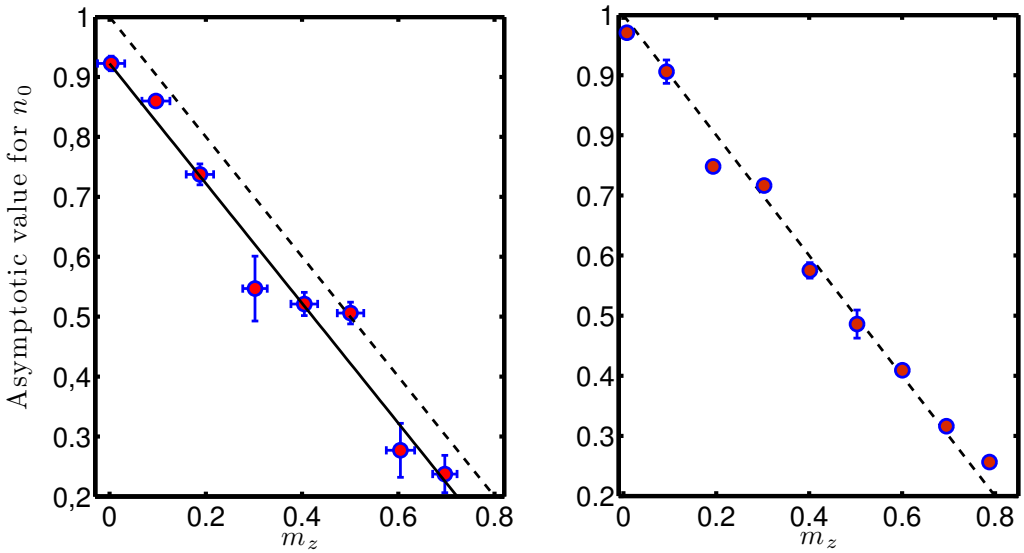

Figure 3.7: Asymptotic value for n_0. The dashed line corresponds to the mean-field prediction at $T = 0$, while the solid dashed line represents the expected asymptotic value in the presence of an isotropic thermal component. The two figures correspond to different temperatures, the right figure corresponding to colder clouds.

Imaging the three spin states at the end of our experimental sequence only give us access to their density, not to their relative phases. Measuring Θ then requires some more elaborate technique than merely preparing the system in its ground-state and probing it as we did for the phase diagram. When the Hilbert space is of dimension 2, the natural tool to measure the relative phase of a superposition of two internal eigenstates is Rabi oscillations. Indeed, by looking at how the relative populations of the two states oscillate during a spin rotation we can infer their relative phase before the rotation. Our idea is to extend this technique to our three level system to extract the relative phase Θ and compare it to π.

3.3.1 Rotation of the spinor wavefunction

We consider a spin-1 Bose-Einstein condensate described by the general mean-field state (3.1). For readability we keep the notation n_{+1}, n_0, n_{-1} for the three densities, so that we have

$$|\Psi\rangle = \begin{pmatrix} \sqrt{n_{+1}} e^{i(\Theta+\alpha)/2} \\ \sqrt{n_0} \\ \sqrt{n_{-1}} e^{i(\Theta-\alpha)/2} \end{pmatrix} \tag{3.45}$$

where the angles Θ and α are defined in (1.61). Since the angle α does not appear in the energy functional (1.63) it is in principle free to take any value at equilibrium. As this angle characterizes the direction of the average spin in the plane perpendicular to the direction of the magnetic field, it precesses at the Larmor frequency. Due to fluctuations of the ambient magnetic field, experimentally it is then very likely that α is actually random from shot to shot.

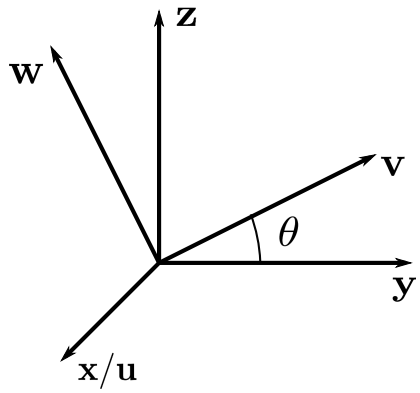

Figure 3.8: Initial and rotated basis.

We suppose that the degeneracy of the three spin states is lifted by an external static magnetic field $\mathbf{B} = B_0\mathbf{e}_z$, so that the splitting between the states $|m_F = +1\rangle$ and $|m_F = 0\rangle$ (equal to the splitting between the states $|m_F = 0\rangle$ and $|m_F = -1\rangle$) is equal to the Larmor frequency $\omega_L = \mu_B B_0/2\hbar$. We neglect the quadratic Zeeman effect. We now couple the spin states by adding at $t = 0$ a radio-frequency (rf) magnetic field polarized along the y axis $\mathbf{B}_{\rm rf} = \mathbf{e}_y(Be^{i\omega_{\rm rf}t} + \text{c.c})$ and quasi-resonant at the Larmor frequency. We note $\delta = \omega_L - \omega_{\rm rf}$ the detuning of the rf-field to the Larmor frequency. The rf-field couples to the $\hat{S}_y$ spin operator so that the total interaction Hamiltonian reads in the rotating-wave approximation

$$\hat{H} = \frac{\hbar\Omega_R}{2}\hat{S}_y + \frac{\hbar\delta}{2}\hat{S}_z \tag{3.46}$$

where we defined the Rabi frequency Ω_R. We note $\Omega = \sqrt{\Omega_R^2 + \delta^2}$ the generalized Rabi frequency and rewrite the Hamiltonian as

$$\hat{H} = \frac{\hbar\Omega}{2}\left(\cos(\theta)\hat{S}_y + \sin(\theta)\hat{S}_z\right) = \frac{\hbar\Omega}{2}\hat{\mathbf{S}}.\mathbf{v} \tag{3.47}$$

where we introduced $\cos(\theta) = \Omega_R/\Omega$ and $\sin(\theta) = \delta/\Omega$ and the rotated basis

$$\mathbf{u} = \mathbf{e}_x \tag{3.48}$$
$$\mathbf{v} = \cos(\theta)\mathbf{e}_y + \sin(\theta)\mathbf{e}_z \tag{3.49}$$
$$\mathbf{w} = \cos(\theta)\mathbf{e}_z - \sin(\theta)\mathbf{e}_y \tag{3.50}$$

In the presence of a non-zero detuning δ the state does not rotate around the y axis but around the tilted axis defined by the vector $\mathbf{v}$. We are now interested in the calculation of the spin state after a Rabi oscillation of duration t as a function of the initial state. We note the angle of the rotation $\beta = \Omega t$. We can in principle fully calculate the rotated state from the relation

$$|\Psi(t)\rangle = e^{-i\hat{H}t/\hbar}|\Psi_0\rangle \tag{3.51}$$

where $|\Psi_0\rangle = |\Psi(t = 0)\rangle$. However in the case of a non-zero detuning δ this calculation becomes quite cumbersome. We show in appendix D the results in the simple case $\delta = 0$, as it qualitatively describes our experimental measurement. A more easily accessible quantity is the magnetization of the rotated state. For this we have to rotate the total spin operator $\hat{S}_z$, which transforms as the single-particle spin operator $\hat{s}_z$. We define the rotation operator $\hat{\mathcal{R}}_{\mathbf{v}}(\beta) = e^{-i\beta\hat{\mathbf{S}}.\mathbf{v}}$. We note $\hat{S}'_z$ the rotated spin operator and $\hat{S}_z$ the

unrotated operator.. We have:

$$\begin{aligned}
\hat{S}'_z &= \hat{\mathcal{R}}^\dagger_{\mathbf{v}}(\beta)\hat{S}_z\hat{\mathcal{R}}_{\mathbf{v}}(\beta) && (3.52)\\
&= \hat{\mathcal{R}}^\dagger_{\mathbf{v}}(\beta)\left(\cos(\theta)\hat{S}_{\mathbf{w}} + \sin(\theta)\hat{S}_{\mathbf{v}}\right)\hat{\mathcal{R}}_{\mathbf{v}}(\beta) && (3.53)\\
&= \sin(\theta)\hat{S}_{\mathbf{v}} + \cos(\theta)\hat{\mathcal{R}}^\dagger_{\mathbf{v}}(\beta)\hat{S}_{\mathbf{w}}\hat{\mathcal{R}}_{\mathbf{v}}(\beta) && (3.54)
\end{aligned}$$

Transforming this last expression back into the (x, y, z) basis we obtain

$$\hat{S}'_z = A\hat{S}_z + B\hat{S}_y - C\hat{S}_x \tag{3.55}$$

where

$$\begin{aligned}
A &= 1 - \cos^2(\theta)\,(1 - \cos(\beta)) && (3.56)\\
B &= \sin(\theta)\cos(\theta)\,(1 - \cos(\beta)) && (3.57)\\
C &= \cos(\theta)\sin(\beta) && (3.58)
\end{aligned}$$

Experimentally we can prepare an initial state of well controlled spin populations. However we have no control on the phases, and in particular if we repeat several times the same preparation of the initial state, the phase α will be random from one realization to the next. If we experimentally perform several Rabi oscillations starting from initial states of identical populations, the measured mean magnetization after the rotation is averaged over the uniform distribution of the phase α, which leads to $\langle\hat{S}_x\rangle_\alpha = \langle\hat{S}_y\rangle_\alpha = 0$ (see expressions (3.2) and (3.3)). We then have

$$\langle\hat{S}'_z\rangle_\alpha = A\langle\hat{S}_z\rangle_\alpha = Am_z \tag{3.59}$$

The average magnetization oscillates during the rotation independently of the phases Θ or α. We now consider the operator $(\hat{S}'_z)^2$. We can calculate its expression from the result (3.55). Crossed terms of the form $\hat{S}_i\hat{S}_j, i \neq j$ appear. When averaged over the uniform distribution of α, their mean value actually vanishes for all of them, and we are left with:

$$\langle(\hat{S}'_z)^2\rangle_\alpha = A^2\langle\hat{S}^2_z\rangle_\alpha + B^2\langle\hat{S}^2_y\rangle_\alpha + C^2\langle\hat{S}^2_x\rangle_\alpha \tag{3.60}$$

As α is random, we have $\langle\hat{S}^2_x\rangle_\alpha = \langle\hat{S}^2_y\rangle_\alpha = \langle\hat{S}^2_\perp\rangle_\alpha/2$, where we noted $\hat{S}_\perp$ the transverse component in the $x - y$ plane of the total spin. The previous expression reduces to

$$\langle(\hat{S}'_z)^2\rangle_\alpha = A^2\langle\hat{S}^2_z\rangle_\alpha + \frac{B^2 + C^2}{2}\langle\hat{S}^2_\perp\rangle_\alpha \tag{3.61}$$

and so we have for the variance of the magnetization in the rotated state:

$$(\Delta\hat{S}'_z)^2 = \frac{B^2 + C^2}{2}\langle\hat{S}_\perp\rangle^2_\alpha + \frac{B^2 + C^2}{2}\Delta S^2_\perp + A^2\Delta\hat{S}^2_z \tag{3.62}$$

In a mean-field state, the quantum fluctuations ΔS^2_i are on the order of N. When it is not zero, the average transverse spin $\langle S^2_\perp\rangle$ is on the order on N^2. Only in the phase where $\langle S^2_\perp\rangle$ vanishes the quantum noise is important, but it is not within our experimental sensibility. We then neglect these quantum fluctuations. After averaging over α, the magnetization noise is actually dominated by classical fluctuations of S_z and $S_\perp$ due to preparation noise.

It appears that the variance of the magnetization oscillates during the rotation, with an amplitude fixed by $\langle\hat{S}_\perp\rangle^2$ and so which depends on the value of the phase Θ. Note that

even if the phase α is random from shot to shot, the transverse spin $\langle \hat{S}_\perp \rangle$ is not zero in a condensate, for in one given realisation all the atoms of the condensate are described by the same α and the "individual" transverse spins of all the atoms add constructively. This is in contrast with the situation in the thermal component of the gas where we can expect that the phase α takes random values from atom to atom, so that the transverse component of the total spin vanishes. The principle of our method to confirm the mean-field prediction is to measure the fluctuations of the magnetization during a Rabi oscillation and to check that the amplitude of these fluctuations is described by the relation $\Theta = \pi$.

3.3.2 Experimental implementation of three-level Rabi oscillations

Experimental configuration

To drive Rabi oscillations between the three Zeeman sublevels of the $F = 1$ hyperfine manifold we first split the degeneracy by applying a bias magnetic field. This field should be small enough to allow us to neglect the quadratic Zeeman effect compared to our Rabi coupling, but this is easily achievable within the range of magnetic field where we have a good control, as we will see in the following. The Rabi experiment then consists in applying a pulse of radio-frequency magnetic field of precise duration and immediately after, perform a Stern-Gerlach separation to measure the three spin populations. As we already mentioned for the measurement of the phase diagram, the Stern-Gerlach experiment requires before the actual separation a step of 10 ms where the bias magnetic field and the gradient are ramped up. The Rabi pulse obviously has to stop before this step, but 10 ms is then too short of a time for the three populations to redistribute because of the spin interaction, so that what we measure is to a good approximation the outcome of the Rabi rotation. Our experimental sequence is depicted in figure (3.9).

To produce the radio-frequency magnetic field we use a function generator and a radio-frequency power amplifier to send a current in an antenna placed close to the chamber and tilted by 45° with respect to the three axis x, y, z. Only the component of the rf field which is perpendicular to the bias magnetic field is able to couple the different Zeeman state. Given the configuration of the antenna we can then apply the bias field in any of the three directions (but with a loss in effective rf power). The amount of rf power radiated depends on the frequency of the signal. As we want the rf coupling to be resonant with the Larmor frequency, this implies that the effective rf power, and consequently the Rabi frequency, changes with the amplitude of the bias field. Yet these variations do not change the order of magnitude of the Rabi frequency which stays on the kHz level.

Optimization of the coherence time

We want to optimize the coherence time of the Rabi oscillations. First the magnetic bias field has to be controlled precisely, as fluctuations of the Larmor frequency would result in fluctuations of the detuning and then in a dephasing of the oscillations. At our level of control, the main source of noise in the Larmor frequency is the 50 Hz of the line which causes a modulation of the magnetic field at this frequency on the order of several mG. To cancel the dephasing effect due to the 50 Hz, we synchronize the experimental sequence to the line. Practically, when we activate the synchronization the card controlling the outputs of all the analog and digital channels hold them at their current values until it receives a trigger signal. At this moment the experimental sequence goes on. The trigger signal is generated by a Schmitt trigger that detects the rising flank of the voltage delivered by a 50 Hz power supply connected to the line. Thus, when the sequence starts

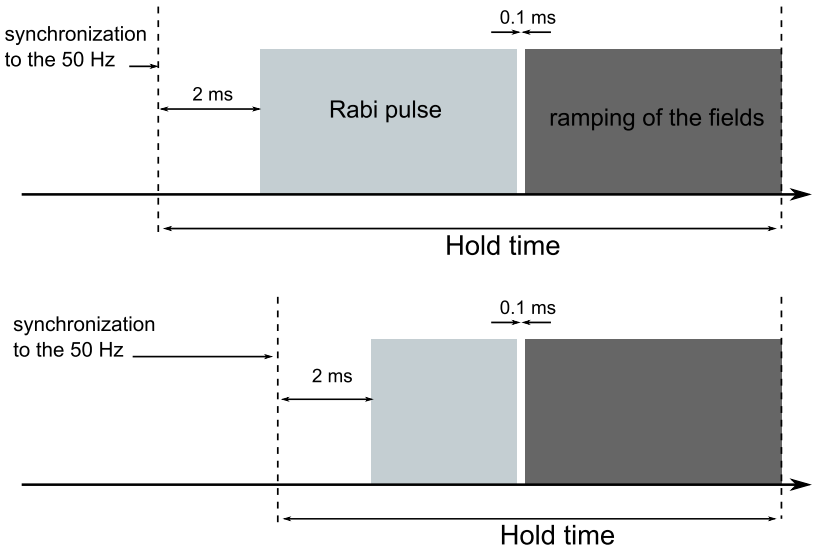

Figure 3.9: Time sequence of the Rabi pulse. The time between the synchronization to the line and the begining of the RF pulse is kept constant, and the time after the end of the pulse is made as short as possible to avoid any effect of the interactions.

again after the synchronization, the phase of the line is fixed while it was unknown and random before. The synchronization does not suppress 50 Hz field fluctuations, but as their phase is controlled they have the same effect from shot to shot and do not blur the oscillations.The time when the sequence is "frozen" waiting for the trigger can vary from zero to 20 ms. To minimize desynchronizing effects of drifts in the line or in the timing of the experimental sequence the synchronization should be realized shortly before the Rabi pulse. We do it 2 ms before the beginning of the Rabi pulse. The synchronization is of crucial importance: it increases the coherence time by almost two orders of magnitude. Without it we could only observe half an oscillation in approximately 0.2 ms, whereas as soon as we used it we were still able to measure clear oscillations after a Rabi pulse of 10 ms.

Preparation of the initial state

Another key factor to observe Rabi oscillations is the reproducibility of the initial spin state. This does not influence the coherence time but it can still cause some dephasing in the oscillations as the preparation noise of the initial state will be transferred to the rotated state. As seen before we can control to typically a few percents the relative populations in the three Zeeman states.

Preparing a spin state with all the atoms in the same Zeeman state is the best controlled situation. Indeed we can create polarized clouds with magnetizations very close to one using the spin distillation technique before. The conservation of the magnetization then ensures that the spin state remains the same till the beginning of the Rabi pulse (see figure 3.10). Similarly we can prepare all the atoms in the $m_F = 0$ state within one percent. To do this, we first depolarize the cloud using the rf spin-mixing technique to obtain a magnetization of zero (within three percent), and then add a large magnetic field during the evaporation to favor the $|m_F = 0\rangle$ state. After the evaporation we hold the atoms in the dimple to let them accumulate in the $|m_F = 0\rangle$ state (the equilibration

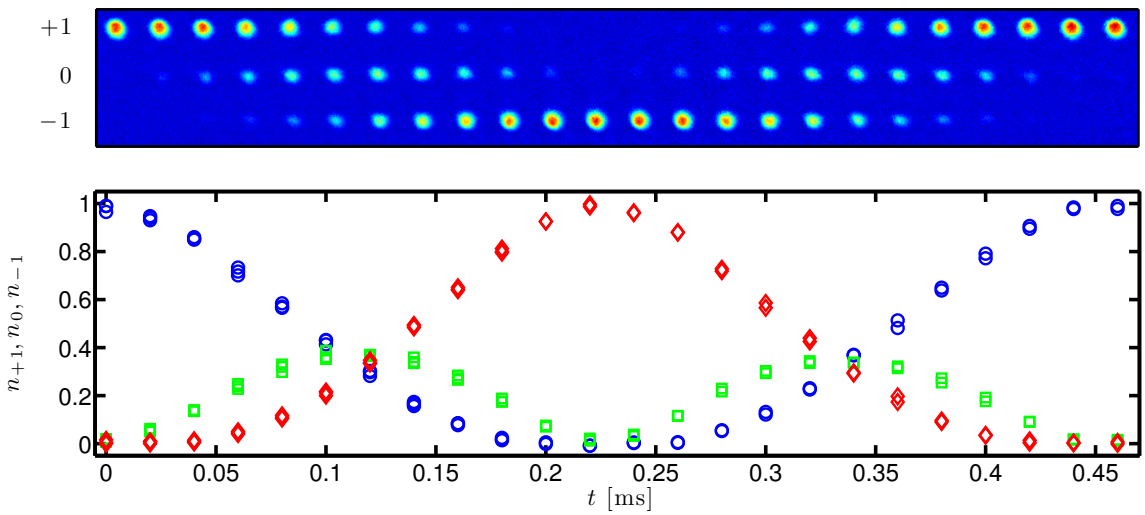

Figure 3.10: Rabi oscillations starting from a fully polarized state: $|\Psi\rangle = (1, 0, 0)^T$. The lower graph shows the three relative Zeeman populations as a function of the pulse duration. Blue circles correspond to the population in $m_F = +1$, red losanges to the population in $m_F = -1$ and green squares to the population in $m_F = 0$. The upper picture shows the corresponding absorption images of the three clouds at the same times t. At each time t the image shown is an averaged image over the few (typically three) that were taken at that time. The Larmor frequency in these data is 190 kHz. The population in the state $m_F = 0$ oscillates at twice the frequency of the two others, as we expect from expressions (C.8). We measure a Rabi frequency approximately equal to 2.2 kHz. We only show here one full oscillation, but we still observe clear oscillations after 10 ms.

time at large magnetic fields is quite short, shorter than 100 ms). We finally get rid of the remaining thermal atoms in the $|m_F = \pm 1\rangle$ states by performing two successive spin distillation steps in the condensate as described in chapter 2 (see figure (3.11)).

In the general case where the atoms are distributed among the three Zeeman states, we prepare the initial state in equilibrium. We set the magnetization using the rf spin-mixing or the spin distillation at high temperatures, evaporate and then hold the atoms in the trap to reach the mean-field ground-state. Due to fluctuations in the preparation of the magnetization, the Rabi oscillations in these situations look much more noisy as shown in figure (3.12). However the contrast stays good, and we can still observe population oscillations after averaging.

3.3.3 Evidence for phase-locking

We prepare the system in a given point of the phase diagram (by preparing a chosen magnetization and applying a given magnetic field) and from this point start to rotate the spin using a radio-frequency pulse. To sample the rotation we stop the pulse after different times and then image the atoms. For each rotation time we repeat the experiment several times. From the measured oscillation of the averaged magnetization which evolves as a cosine of the Rabi angle (expression (3.59)) we fit the angle θ and the generalized Rabi frequency Ω. Knowing this we deduce the Rabi frequency Ω_R, the detuning δ and the angle β of the rotation at each time t.

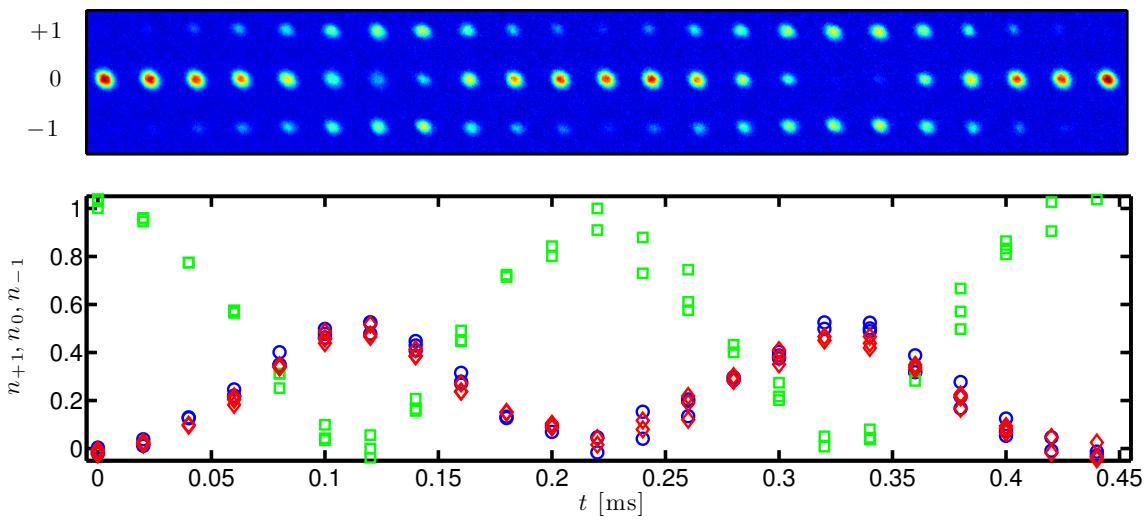

Figure 3.11: Rabi oscillations starting from the state $|\Psi\rangle = (0, 1, 0)^T$. As in figure (3.10) the lower graph shows the evolution of the three relative spin populations and the upper picture shows the corresponding (averaged) absorption images. The color code is the same as in figure (3.10). The Larmor frequency is also 190 kHz. According to expression (C.10), the three populations oscillate at twice the Rabi frequency, which we therefore evaluate at approximately 2.2 kHz, consistently with what we measure in figure (3.10).

Considering the data where no rotation was performed we determine the quantities $\langle m_z\rangle_\alpha(t = 0)$ and $\langle n_0\rangle_\alpha(t = 0)$. We deduce the value $\langle S_\perp\rangle^2_\alpha(t = 0)$ of the average transverse spin in the initial state. We are now able to calculate the variance of the magnetization at any time in the rotation and for different values of the relative phase Θ. In particular we consider the values $\Theta = \pi, \Theta = 0$ (expected for ferromagnetic interactions) and the case where Θ is random. We finally compare these different situations to the measured evolution of the variance. We repeat this procedure for three different preparations of the initial state, which are displayed in the magnetic phase diagram in figure (3.14).The results are shown in figure (3.13).

The first observation is that the average magnetization is very well described by the function (3.59). The fitted detunings are on the order of a few hundreds of Hz (corresponding to a few tens of mG). The fitted generalized Rabi frequency are close to 3 kHz for the two lower Larmor frequency (82.5 kHz and 103 kHz) and close to 2 kHz for the largest one (244 kHz). This difference can be explained by the frequency-dependent impedance matching of our antenna.

If we now look at the variance of the magnetization, it appears that the experimental points are much better described by $\Theta = \pi$ than by $\Theta = 0$ or a uniform distribution of Θ, which tends to confirm the mean-field prediction. This shows that, for a given population n_0 and magnetization m_z, the transverse spin in the condensate takes the minimal value allowed, and consequently that the nematic order is maximal for this n_0 and m_z. However, we point out two important effects.

First, the measured variance of the magnetization is consistently smaller than the calculated one for $\Theta = \pi$ (up to 40% smaller). In our analysis we calculated $\langle S_\perp\rangle$ using a

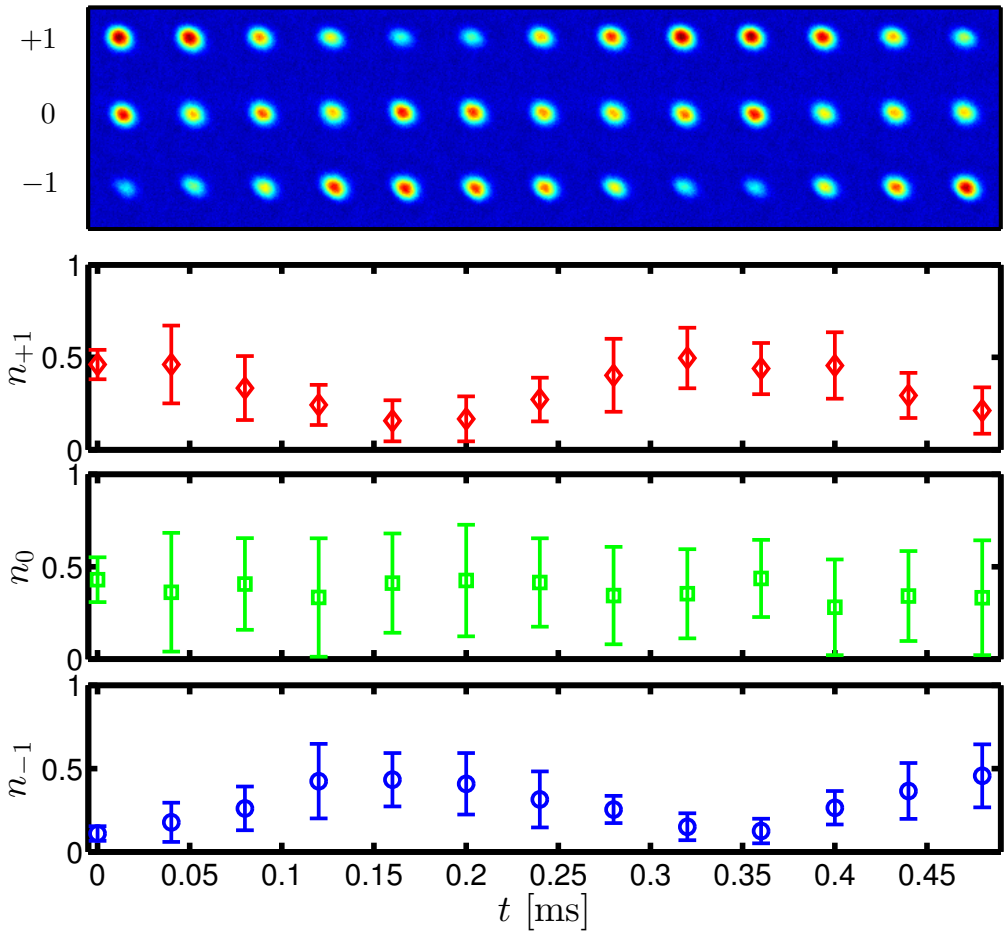

Figure 3.12: Rabi oscillations starting from the mean-field ground state prepared with a magnetic field of 150 mG and a magnetization of $0.35 \pm 0.0.4$. The lower three graphs show the evolution of the spin populations during the spin rotation, averaged at each time t over ten experimental realizations. The errorbars correspond to one standard deviation. The upper picture shows the corresponding averaged absorption images. The Larmor frequency is 103 kHz. We infer the Rabi frequency $\Omega_R/2\pi = 2.94 \pm 0.09\,\text{kHz}$.

$T = 0$ theory, i.e. all the atoms are assumed to be in the condensate. However in reality a thermal component is always present, as already discussed in the section 3.2. Let us consider the effect of a finite temperature. In a spin-1 Bose gas we expect the three spin components (if they are present) to condense at three different critical temperatures (two in the non-interacting case) [82]. At high enough temperatures, only one spin species will be condensed. In this case, the transverse spin component of the condensate is zero, for it is created by the coexistence of $m_F = 0$ with one of the two others species in the condensate. The total transverse spin is then zero. At $T = 0$ the transverse spin takes in the broken-axisymmetry phase a positive value. Between these two regimes we then expect that the presence of a thermal fraction reduces the transverse spin compared to the case $T = 0$. Still, we know from another analysis that the condensed fraction in these data is quite high, much higher than what would be required to explain that the variance Δm_z^2 we observe corresponds to the reduction of the signal calculated with $\Theta = 0$ or Θ uniformly distributed.

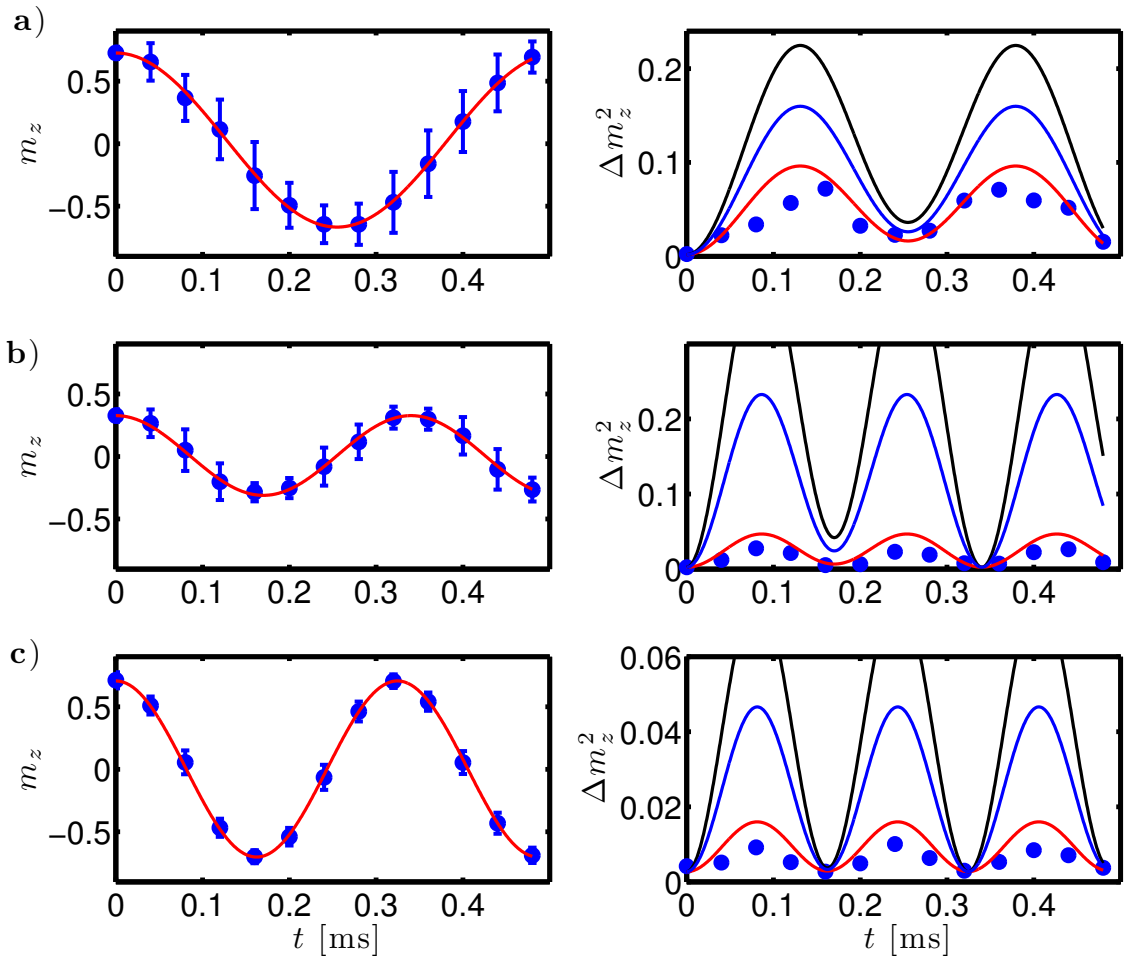

Figure 3.13: Measured average magnetization m_z (left) and variance of the magnetization Δm_z^2 (right) during three Rabi oscillations performed at three different points of the magnetic phase diagram. These points are characterized by the magnetization m_z^0 of the initial state and by the applied magnetic field (or equivalently by the associated Larmor frequency). **a**): $m_z^0 \approx 0.75, \omega_L = 244\,\text{kHz}$, **b**):$m_z^0 \approx 0.35, \omega_L = 103\,\text{kHz}$, **c**): $m_z^0 \approx 0.75, \omega_L = 82.5\,\text{kHz}$. The red curve on the left plots is a fit of the average magnetization using a function of the form (3.59). The detuning δ and the generalized Rabi frequency are extracted from this fit. These parameters are then used to calculate the variance of the magnetization during the rotation for different values of Θ. The blue points on the right plots correspond to the measured variance Δm_z^2 and the three solid lines correspond to: black: $\Theta = 0$, blue: Θ uniformly distributed and red: $\Theta = \pi$.

As a second remark, we note in figure (3.14) that two of the initial states we prepare (**a** and **b**) are located in the broken-axisymmetry phase while the last one (**c**) sits in the antiferromagnetic phase. According to our previous discussion of the phase diagram, a condensate prepared in conditions **c** has a vanishing population n_0 and a vanishing transverse spin $S_\perp$. Still we observe an oscillation of small amplitude (~ 0.01). We also do measure an average non-zero population n_0 in the initial state, which is explained by the presence of thermal atoms. The measurement of the variance Δm_z^2 during the rotation

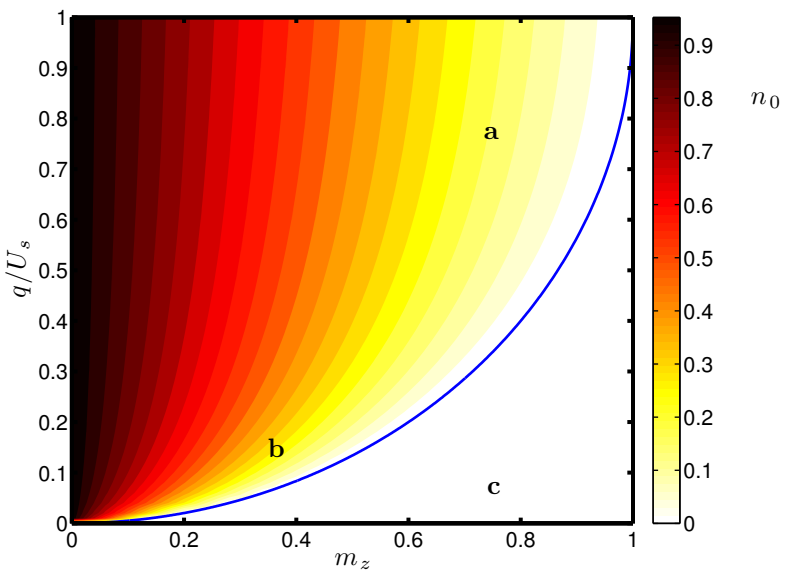

Figure 3.14: Position in the magnetic phase diagram of the three initial states considered in figure (3.13). We use $U_s = 45\,\text{Hz}$ which we calculated from the measured atom number and a numerical solution of the Gross-Pitaevskii equation. The blue line represents the critical field.

is actually a measurement of the transverse spin in the initial state. The observation of an oscillation of Δm_z^2 thus suggests that the thermal fraction does possess a non-zero average transverse spin component. This implies the existence of some amount of coherence between thermal atoms. In the presence of a condensate, the spin coherence of thermal atoms is actually expected to arise due to the coherent collisions between condensed and uncondensed atoms [83][65]. The coherence of the thermal fraction has been demonstrated experimentally in a two component pseudo-spin system [84].

3.4 Conclusion

In this chapter we revisited the magnetic phase diagram using a nematic order parameter that provides a more geometrical understanding of the mean-field ground-state. The two different phases are described here in terms of the possible existence of a transverse component of the total spin of the system, rather than the population of the $|m_F = 0\rangle$ state. We then presented an experimental measurement of the phase diagram. We found a very good agreement with the mean-field theory in the single-mode approximation in the whole range of magnetic field and magnetization. Finally we experimentally confirmed the locking of the relative phase Θ of the spinor wavefunction by measuring the variance of the magnetization during a Rabi oscillation. This experiment is actually a method to measure the transverse component of the total spin. We showed that a spin coherence exists between thermal atoms, due to the coupling with the condensate. This experiment was realized with clouds at low temperature, with a high condensed fraction. It would be interesting to perform the same kind of experiment at higher temperatures. This would allow one to study the evolution of the total transverse spin with temperature, and explore how the thermal atoms acquire their spin coherence. We plan to explore this direction in

future experiments.

Chapter 4

Spin fragmentation in a spin-1 Bose gas

In chapter 3 we investigated how well the mean-field theory of the spin-1 Bose gas compares to experiments. We found a good agreement between the theoretical predictions and our experimental observations in terms of the spin populations. However, as will be presented in chapter 5, while measuring the magnetic phase diagram in the region of zero magnetization and low magnetic fields we noted anomalously large spin fluctuations. These huge fluctuations are not explainable in a simple mean-field picture where all atoms condense in the same single-particle state and only poissonian fluctuations are expected. They are in fact a manifestation of the symmetry of the system at zero-magnetic field where the spinor condensate becomes fragmented. As this intrinsically quantum phenomenon is out of reach of our previous treatment, we need to develop a beyond mean-field theory of the spin-1 Bose gas. In a first part we will introduce the notion of fragmentation and show by a direct diagonalization of the Hamiltonian that it implies super-Poissonian spin fluctuations. We then construct an approximate but very efficient approach to describe this phenomenon at finite temperatures: the so-called broken-symmetry approach. In a last part we show how this theory is closely related to the more general concept of spontaneous symmetry-breaking.

4.1 Fragmentation of a spinor condensate at zero field

Fragmentation describes the situation where an assembly of particles Bose-condenses in several single particle states. We here give some general elements about fragmented condensates, before detailing the case of the spin-1 Bose gas.

4.1.1 Fragmented Bose-Einstein condensates

Definition of condensation and fragmentation

We consider a confined atomic gas of weakly interacting bosons at low temperature, with an internal degree of freedom. As recalled in chapter 1, Bose-Einstein condensation reveals itself by the macroscopic accumulation of atoms in the single-particle ground state of the system due to their bosonic statistics. This concept implicitly assumes that this ground-state is non-degenerate, as it is the case in a polarized gas trapped in a harmonic potential. However, this assumption may not be verified. Degenerate single-particle ground states are realized in several actual systems [85]. This degeneracy can be of orbital nature, for

example bosons in an optical lattice in the limit of zero tunneling. In other systems it follows from the existence of an internal degree of freedom. These systems include pseudo-spin systems and spinor gases. The degeneracy of the ground state is typically of order of unity in the case of internal degeneracies, but it can also be on the order of the size of the system (bosons in a lattice). In all these cases, the picture of the accumulation of the atoms in the single-particle state of lowest energy becomes inadequate: what happens to the atoms once the excited states have saturated? Do they accumulate in one of the degenerate states or do they distribute in several, or in all of them? What is the role of interactions?

To answer these questions we need to define more precisely the concept of Bose-Einstein condensation, following Penrose and Onsager [86]. Let us consider a system of N particles. The single-particle density matrix is defined by its components in position space $\hat{\rho}^{(1)}(\mathbf{r},\mathbf{r}') = \langle\hat{\Psi}^\dagger(\mathbf{r}')\hat{\Psi}(\mathbf{r})\rangle$ where $\hat{\Psi}^\dagger(\mathbf{r})$ creates a particle at position $\mathbf{r}$. This operator is hermitian and can be diagonalized. There exists an orthonormal basis of single-particle states (ψ_i) such that:

$$\hat{\rho}^{(1)} = \sum_i n_i |\psi_i\rangle\langle\psi_i| \tag{4.1}$$

where n_i is the eigenvalue associated to the eigenvector $|\psi_i\rangle$. In a non-interacting system the states $|\psi_i\rangle$ coincide with the eigenstates of the single-particle Hamiltonian, but in the interacting case this is generally not true. $\hat{\rho}^{(1)}$ verifies $\mathrm{Tr}(\hat{\rho}^{(1)}) = N$ so that one has $\sum_i n_i = N$. We choose to reorder the eigenstates such that $n_0 \geq n_1 \geq n_2 \geq ...$ Ordinary Bose-Einstein condensation corresponds to the situation where the largest eigenvalue n_0 is on the order of N while all the others are on the order of unity:

$$n_0 \sim \mathcal{O}(N) \tag{4.2}$$

$$n_i \sim \mathcal{O}(1) \quad \text{for } i = 1, ..., N-1 \tag{4.3}$$

The function $\psi_0(\mathbf{r})$ is then the mode of the condensate, or, as we called it in the first chapter, the macroscopic wavefunction.

In the situations where the single-particle ground-state is degenerate the number of macroscopic eigenvalues may not be exactly one. Two situations can then arise: either none of the eigenvalues is macroscopic, or several are. The latter situation is referred to as a fragmented condensate: the atoms condense in several single-particle states. This phenomenon typically arises when the degeneracy of the ground-state is of order of unity.

A simple example of fragmentation

The effect of the interactions in the process of fragmentation has to be considered carefully, as they will dramatically influence the way it manifests itself. Indeed, if the single-particle states are degenerate, the many-particle states will only differ by their interaction energy. Besides, in experimental situations, exact degeneracy is not achieved, because of small single particle terms that split the ground states. Only the interactions, if they dominate over the induced energy splittings, allows to actually observe the effect of degeneracy. We illustrate this idea with a simple example.

The Nozières model [87] considers N bosons that have two degenerate internal states $|1\rangle$ and $|2\rangle$. Particles in a different state interact with a coupling constant g. The interaction energy is then $E = (g/2)N_1N_2$. We first consider the case $g < 0$. The ground state

$|GS\rangle$ is a Fock state:

$$|GS\rangle = \frac{1}{N!}\hat{a}_1^{\dagger N/2}\hat{a}_2^{\dagger N/2}|0\rangle \tag{4.4}$$

where $\hat{a}_i^\dagger$ creates a particle in state $|i\rangle$ $(i = 1, 2)$. Its single particle density matrix is

$$\hat{\rho}^{(1)} = \frac{N}{2}\begin{pmatrix} 1 & 0 \\ 0 & 1 \end{pmatrix} \tag{4.5}$$

The two eigenvalues are equal to $N/2$: the condensate is fragmented.

If we have $g > 0$, the energy is minimized by having all the atoms in the same internal state. There are two degenerate many-particles ground-states: $|N_1 = N, N_2 = 0\rangle$ and $|N_1 = 0, N_2 = N\rangle$. The two associated single-particle density matrices have eigenvalues 0 and N. If we write the ground state as a statistical mixture with equal weights of these two states, we find that its density matrix also has $N/2$ as a double eigenvalue: it has the exact same expression as in the case $g < 0$. Here again the condensate is fragmented. This trivial example shows that the way fragmentation occurs is very sensitive to interaction parameters and that, in a given system, the ground state can take very different forms. It here appears that the Penrose-Onsager definition may be insufficient to fully characterize how fragmentation takes place, as the two fragmented condensates can not be distinguished by their single-particle density matrix only. Higher order correlation functions are then needed to characterize these fragmented states. For instance in our example, the difference between the two types of condensates is revealed by the number fluctuations: both verify $\langle N_i\rangle = N/2$ (i=1,2), but the Fock state has zero fluctuations when the mixture has $\Delta N_i^2 = N^2/4$.

4.1.2 Spin fragmentation in an antiferromagnetic spinor BEC at $T = 0$

Spin fragmentation at $q = 0$

We now consider a Bose-Einstein condensate of Sodium atoms in the $F = 1$ hyperfine manifold. We assume the single-mode approximation. As established in Chapter 1 in (1.51), at zero magnetic field the spin Hamiltonian reads $\hat{H}_s = (U_s/2N)\hat{\mathbf{S}}^2$ where $\hat{\mathbf{S}}$ is the total spin of the condensate and U_s is the spin interaction energy per particle and is positive for sodium. To investigate the fragmentation in this system we have to go beyond the simple mean-field solution developed in Chapter 3. The mean-field states $|\psi\rangle = (\hat{a}_\phi^\dagger)^N|\text{vac}\rangle$ (where $\hat{a}_\phi^\dagger$ creates a particle in the single-particle $|\phi\rangle$) are by definition singly condensed states: all the atoms occupy the same single-particle state, the single-particle density matrix has one eigenvalue equal to N and all the others equal to zero. We need to study the exact ground state, which is feasible for the simple case of spin-1 bosons in the single mode approximation. The eigenstates of the spin Hamiltonian are the total spin eigenstates $|N, S, M\rangle$, where N is the total atom number, S is the total spin and M its projection on the z axis, and where the bosonic symmetry imposes that $N - S$ is even. They have an energy $(U_s/2N)S(S+1)$. These states can actually be constructed in the Fock space as:

$$|N, S, M\rangle = \frac{1}{\sqrt{\mathcal{N}(N, S, M)}}(\hat{S}_-)^P(\hat{A}^\dagger)^Q(\hat{a}_{+1}^\dagger)^S|0\rangle \tag{4.6}$$

with

$$P = S - M \tag{4.7}$$

$$2Q = N - S \tag{4.8}$$

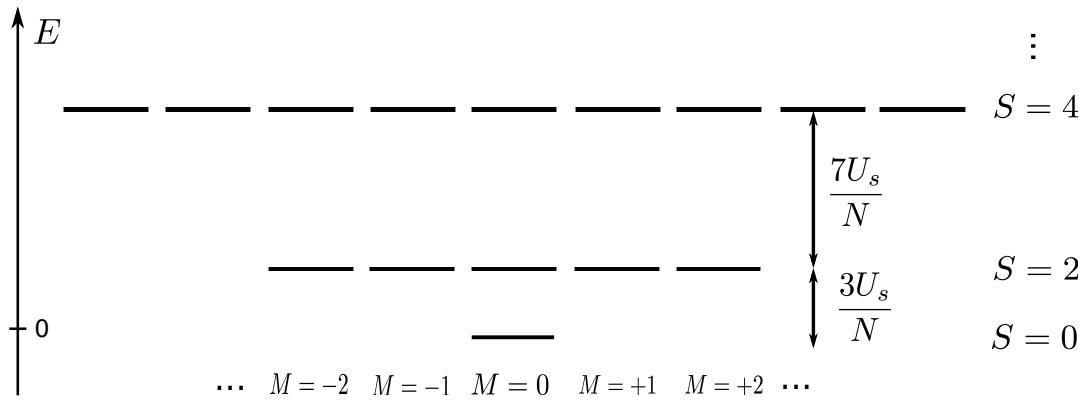

Figure 4.1: Spectrum of the spin Hamiltonian $\hat{H}_s$ at $q = 0$. The ground state is the unique $|N, S = 0, M = 0\rangle$ singlet state, the excited states have an energy $E(S) = U_s S(S+1)/2N$.

and where we introduced the operators:

$$\hat{A}^\dagger = (\hat{a}_0^\dagger)^2 - 2\hat{a}_{+1}^\dagger \hat{a}_{-1}^\dagger \tag{4.9}$$

$$\hat{S}_- = \sqrt{2}(\hat{a}_{-1}^\dagger \hat{a}_0 + \hat{a}_0^\dagger \hat{a}_{+1}) \tag{4.10}$$

$\hat{A}^\dagger$ creates a pair of atom with total spin 0, and $\hat{S}$ removes one quantum of angular momentum. $\mathcal{N}(N, S, M)$ is a normalization constant.

Since U_s is positive, the ground-state at zero magnetic field is the singlet state with zero total spin $|S = 0\rangle$. We consider even values of N for simplicity (odd values of N can be treated in a similar way without modifying the results to order $1/N$). As can be seen from expression (4.6), the singlet state consists of a product of singlet pairs:

$$|N, S = 0, M = 0\rangle \propto (\hat{A}^\dagger)^{N/2}|0\rangle \tag{4.11}$$

In the SMA this state is unique, and retains the rotational symmetry of the Hamiltonian. (On the contrary, the mean-field ground state is degenerate, and composed of the whole family of nematic states. Each of these states obviously break the rotational symmetry as they are defined by a direction of space along which they have exactly zero spin projection). Law, Pu and Bigelow demonstrated that the singlet state can be written in the Fock basis as a coherent superposition of all Fock states $|N_{+1} = k, N_0 = N - 2k, N_{-1} = k\rangle$, $k = 0, 1, ..., N/2$, with almost uniformly distributed coefficients [61]. This quasi-uniform superposition results in super-Poissonian fluctuations of the different spin states populations. Furthermore, due to its rotational symmetry, the singlet state has isotropic spin populations in average. Its single-particle density matrix in the standard basis reads:

$$\hat{\rho}^{(1)} = \frac{N}{3}\begin{pmatrix} 1 & 0 & 0 \\ 0 & 1 & 0 \\ 0 & 0 & 1 \end{pmatrix} \tag{4.12}$$

It has three equal macroscopic eigenvalues: the condensate is fragmented.

Comparing the singlet state to any nematic single condensate, super-poissonian spin fluctuations appear as a signature of fragmentation. To quantify the degree of fragmentation of our system we chose as figures of merit the two first moments (mean value and

variance) of the population $\hat{N}_0 = \hat{a}_0^\dagger \hat{a}_0$ in the $|m_F = 0\rangle$ spin state. For the singlet state it can be calculated from the expression (4.11). We find:

$$\langle \hat{N}_0 \rangle = \frac{N}{3} \tag{4.13}$$

$$\Delta N_0^2 = \frac{4N^2 + 12N}{45} \tag{4.14}$$

The fluctuations of N_0 are indeed super-poissonian (to leading order in N, $\Delta N_0^2 \propto N^2$). Numerically $\Delta N_0/N \approx \sqrt{4/45} \simeq 0.298$.

Spin fragmentation for $q > 0$

For non-zero values of q, the ground state is no longer the singlet state. Considering the high q limit we expect the system to condense in the $|m_F = 0\rangle$ spin state with negligible fluctuations, a situation much different from the $q = 0$ case. Continuously increasing the field the ground state of the system evolves from a fragmented singlet condensate to a mean-field nematic one. We can track this evolution by looking at the behavior of $\langle N_0 \rangle$ and ΔN_0 as q is increased. This problem was treated extensively in [88], which we reproduce in Appendix E. However to describe our experiments we have to consider finite temperature effects and we will not treat here the case $T = 0$.

4.1.3 Spin fragmentation at finite temperatures

At zero magnetic field, the energy splitting between the lowest eigenstates of the spin Hamiltonian (1.51) is on the order of U_s/N. A typical value for U_s in an harmonic trap is around 5 nK, which gives for atom numbers of a few thousands an energy scale on the order of a few pK, much lower than the temperature that can be achieved in an experiment (which at the lowest is on the order of a few tens of nK, see chapter 5). Hence, an experimental realization of a spinor condensate will not be found in the singlet ground state, but instead several excited states will be populated. Can we still observe spin fragmentation?

Spin fragmentation at $q = 0$

As we said before, fragmentation in a spinor gas is revealed by the mean value and fluctuations of the N_0 population. We will then focus on calculating these quantities. Using the expression (4.6) we can calculate the action of $\hat{N}_0$ on the $|N, S, M\rangle$ states. We consider a regime of temperature where the highest populated excited states verify $1 \ll S \ll N$ (we will discuss these conditions later). For these states we find to leading order in N and S:

$$\langle \hat{N}_0 \rangle_{S,M} \simeq \frac{N(S^2 - M^2)}{2S^2} \tag{4.15}$$

$$(\Delta N_0)^2_{S,M} \simeq \frac{(N^2 - S^2)(S^2 - M^2)^2}{8S^4} \tag{4.16}$$

It appears that all low-energy eigenstates with $M \ll S \ll N$ display super-Poissonian fluctuations ($(\Delta N_0)^2_{S,M} \propto N^2$).

To calculate the mean value of N_0 in a thermal state we work in the canonical ensemble. We define a temperature T_s that we call spin temperature and write:

$$\langle N_0 \rangle_T = \frac{1}{\mathcal{Z}} \sum_{S,M} e^{-\beta U_s S(S+1)/2N} \langle N_0 \rangle_{S,M} \tag{4.17}$$

where $\beta = 1/k_\mathrm{B} T_s$ and $\mathcal{Z}$ is the partition function. We replace the sum by an integral over S and M, which is justified in the limit $\beta U_s/N \ll 1$ where many excited states are occupied. In this case the sum (4.17) is dominated by states with $S \gg 1$. For intermediate temperatures the contributing states also verify $S \ll N$ and one can set the upper bound of the integral over S to $+\infty$,

$$\langle N_0 \rangle_T \simeq \frac{1}{\mathcal{Z}} \int_0^{+\infty} \mathrm{d}S \int_{-S}^{S} \mathrm{d}M e^{-\beta S(S+1)} \langle N_0 \rangle_{S,M} \tag{4.18}$$

The fluctuations are calculated in a similar way and one finds:

$$\langle N_0 \rangle_T \simeq \frac{N}{3} \tag{4.19}$$

$$(\Delta N_0)_T^2 = \langle N_0^2 \rangle_T - \langle N_0 \rangle_T^2 \simeq \frac{4N^2}{45} \tag{4.20}$$

To leading order in N the mean value and variance of N_0 are the same as at $T = 0$. Low-lying $|N, S, M\rangle$ states share with the singlet state the same property of (quasi) isotropic populations and super-poissonian fluctuations. Estimating the temperature by $U_s S^2/2N \simeq k_B T/2$, the condition $1 \ll S \ll N$ gives a regime of temperature:

$$\frac{U_s}{N} \ll k_\mathrm{B} T \ll N U_s \tag{4.21}$$

In the regime $k_\mathrm{B} T \gg N U_s$ all spin states are equally occupied and the upper bound of the integral over S cannot be sent to $+\infty$. Setting the Boltzmann weights to 1, the sums can still be estimated analytically. One obtains:

$$(\Delta N_0^2)_{T \gg N U_s} \simeq \frac{N^2}{18} \tag{4.22}$$

Thus we find that at zero magnetic field, irrespective of the temperature the variance of N_0 is always Super-Poissonian ($\Delta N_0^2 \propto N^2$), and that the depletion of the population N_0 is large. We conclude that at $q = 0$, fragmentation should be observable experimentally.

Spin fragmentation for $q > 0$

As in the previous section for $T = 0$ we do not develop the case $q > 0$, as a complete analysis can be found in [88]. Rather, for completeness we just give here the main result.

We have seen that the fragmentation survives at finite temperatures. Thus, similarly to the case $T = 0$, while q is increased the system evolves from a fragmented condensate to a mean-field state, and this evolution can be seen from the behavior of the moments of the population N_0 with q. We present in figure (4.2) the results of an exact numerical diagonalization of the spin Hamiltonian where no constraint was imposed on the distribution of the magnetization. At zero magnetic field we observe a large depletion of the $m_F = 0$ spin state and super-Poissonian spin fluctuations. As the field increases, the Zeeman effect

favors more and more the $m_F = 0$. The atoms progressively accumulate in this state and the fluctuations are suppressed. The system evolves from a fragmented state at zero field to a mean-field state at large field. For a magnetization of zero average the asymptotic mean-field state corresponds to the nematic state with all the atoms in $m_F = 0$. Both $\langle N_0 \rangle$ and ΔN_0 appear to be almost universal functions of the only variable $Nq/k_{\mathrm{B}}T_s$. The typical width of the transition is then given by $q \sim k_B T/N$.

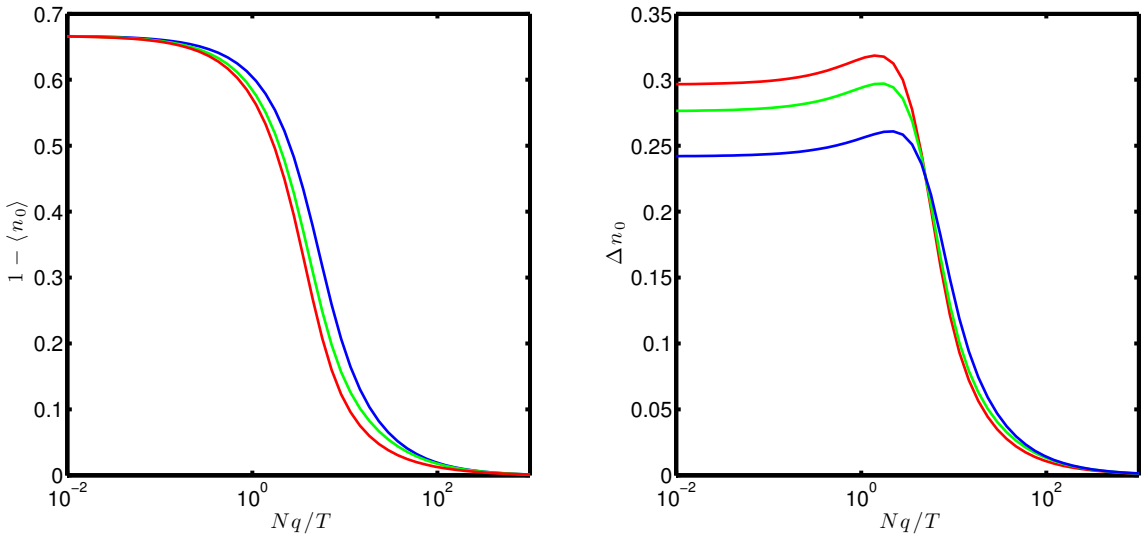

Figure 4.2: Mean value and variance of $n_0 = N_0/N$ calculated by an exact diagonalization in the canonical ensemble, for $N = 1000$ and for different spin temperatures. The red curve corresponds to $T = 10U_s$, the green one to $T = 100U_s$ and the blue one to $T = 1000U_s$. The value of the fluctuations at $q = 0$ evolves from approximately $\sqrt{4/45} \approx 0.3$ for low values of NU_s/k_BT (red curve) to approximately $\sqrt{1/18} \approx 0.24$ for large values of NU_s/k_BT (blue curve). The left figure corresponds to the line $m_z = 0$ of the magnetic phase diagram presented in chapter 3 (note that here we represent $1 - \langle n_0 \rangle$)

4.2 The broken-symmetry picture

In the previous section we calculated the moments of N_0 by the most natural method, by looking at the exact eigenstates of the Hamiltonian. However, for an atom number $N = 5000$ as we have in our experiments, the Hilbert space becomes too large to allow for an efficient numerical treatment of the problem with this method. In this section we introduce a powerful approach to describe a spinor gas at low temperatures, based on the concept of symmetry breaking states [89]. The principle of this general method is to construct states that obey a particular symmetry by properly mixing states that individually break this symmetry.

4.2.1 Broken-symmetry picture at $T = 0$

In the case of a spinor gas of zero magnetization and in the absence of magnetic field, the true ground state is the rotationally invariant singlet state. The broken-symmetry approach consists in approximating this state by an isotropic mixture of all the nematic

states $|N:\mathbf{\Omega}\rangle \propto (\mathbf{\Omega}.\hat{\mathbf{a}}^\dagger)^N|\text{vac}\rangle$ where $\hat{\mathbf{a}}^\dagger = (\hat{a}^\dagger_{+1}, \hat{a}^\dagger_0, \hat{a}^\dagger_{-1})^T$ and the vector $\mathbf{\Omega}$ is defined by

$$\mathbf{\Omega} = \begin{pmatrix} -\frac{1}{\sqrt{2}}\sin(\theta)e^{-i\phi} \\ \cos\theta \\ \frac{1}{\sqrt{2}}\sin(\theta)e^{i\phi} \end{pmatrix} \tag{4.23}$$

in the standard basis. This mixture is described by the density operator

$$\hat{\rho}_{BS} \propto \int \mathrm{d}\mathbf{\Omega}|N:\mathbf{\Omega}\rangle\langle N:\mathbf{\Omega}| \tag{4.24}$$

The validity of this description follows from the remarkable properties of nematic states in the limit $N \to +\infty$. These states form an overcomplete basis of the spin space, meaning that the family of nematic states has more states than needed to span the Hilbert space. They verify the resolution of unity

$$\frac{4\pi}{2N+1}\int \mathrm{d}\mathbf{\Omega}|N:\mathbf{\Omega}\rangle\langle N:\mathbf{\Omega}| = \mathbb{1} \tag{4.25}$$

Because of its over completeness the family of nematic states is not orthogonal. The overlap of two nematic states is given by

$$\langle N:\mathbf{\Omega}|N:\mathbf{\Omega}'\rangle = \left(\mathbf{\Omega}.\mathbf{\Omega}'\right)^N \tag{4.26}$$

When the atom number becomes large, this scalar product becomes very peaked around $\mathbf{\Omega} = \mathbf{\Omega}'$ and can be approximated by[1]

$$\langle N:\mathbf{\Omega}|N:\mathbf{\Omega}'\rangle = \mathcal{N}\delta(\mathbf{\Omega}-\mathbf{\Omega}') + \mathcal{O}(\frac{1}{N^2}) \tag{4.27}$$

where $\mathcal{N}$ is a normalization factor. Thus, in the limit of large atom number, the nematic states become quasi-orthogonal.

Another important property of nematic states is given by the action of annihilation operators $\hat{a}_i$ on these states:

$$\hat{a}_i|N:\mathbf{\Omega}\rangle = \sqrt{N}\,\Omega_i|N-1:\mathbf{\Omega}\rangle \tag{4.28}$$

where $i = 0, \pm 1$. The operator $\hat{a}_i$ removes one particle but does not change the state of the $N-1$ others. The precision of the broken-symmetry approach results from the combination of these two properties as we explain now.

The singlet state actually accepts the decomposition in the basis of nematic states[2] [89]:

$$|S=0\rangle \propto \frac{1}{\sqrt{4\pi}}\int \mathrm{d}\mathbf{\Omega}|N:\mathbf{\Omega}\rangle \tag{4.30}$$

[1] Since we consider even values of N the scalar product is also peaked around $\mathbf{\Omega} = -\mathbf{\Omega}'$. However, the states $\mathbf{\Omega}$ and $-\mathbf{\Omega}$ actually represent the same physical state. To avoid this ambiguity we can chose to only consider nematic states with $\Omega_z \geq 0$ for instance, taking care of correctly normalizing the integrals.

[2] More generally such a decomposition exists for all the total spin eigenstates:

$$|S,M\rangle \propto \int \mathrm{d}\mathbf{\Omega}Y_{S,M}(\mathbf{\Omega})|N:\mathbf{\Omega}\rangle \tag{4.29}$$

where $Y_{S,M}$ are the usual spherical harmonics.

Let us now consider a k-body operator $\hat{O}^{(k)}$ acting in the Fock space of N spin-1 bosons, with $k \ll N$. We suppose this operator is in normal order. The expectation value of this operator in the singlet state is:

$$\langle \hat{O}_k \rangle_{\text{singlet}} = \frac{1}{4\pi} \int \mathrm{d}\mathbf{\Omega} \int \mathrm{d}\mathbf{\Omega}' \langle N : \mathbf{\Omega} | \hat{O}_k | N : \mathbf{\Omega}' \rangle \tag{4.31}$$

We need to evaluate the matrix elements of $\hat{O}^{(k)}$ in the nematic basis. Using expressions (4.28) and (4.26) we find that actually only the diagonal elements of $\hat{O}^{(k)}$ matter and one has to leading order in N:

$$\langle \hat{O}_k \rangle_{\text{singlet}} \approx \frac{\mathcal{N}}{4\pi} \int \mathrm{d}\mathbf{\Omega} \langle N : \mathbf{\Omega} | \hat{O}_k | N : \mathbf{\Omega} \rangle \tag{4.32}$$

The right-hand term is equal to the expectation value calculated in the broken-symmetry description[3] $\langle \hat{O}^{(k)} \rangle_{BS} = \mathrm{Tr}\left(\hat{\rho}_{BS} \hat{O}^{(k)}\right)$, so that one has

$$\langle \hat{O}_k \rangle_{\text{BS}} = \langle \hat{O}_k \rangle_{\text{singlet}} \left(1 + \mathcal{O}\left(\frac{1}{N}\right)\right) \tag{4.34}$$

The two descriptions coincide in the thermodynamic limit where measurements of few-body observables cannot distinguish between the singlet state and the broken-symmetry one. As explained in [89], the description of the state of the condensate by the broken-symmetry mixture allows to imagine that all the atoms condense in the same nematic state for one particular experimental realization, thus breaking the rotational symmetry, but that the realized nematic state fluctuates from one shot to the next. This decomposition provides an intuitive understanding of the spin fluctuations: to conserve the rotational symmetry, the system equally spreads within the whole family of degenerate nematic states, thus uniformly mapping all directions of the spin space. This 'delocalization' in spin space directly implies the huge spin fluctuations and the equality of the averaged spin populations. The effect of this delocalization is to reduce the energy from U_s for a nematic state to zero for the singlet state.

Due to the relation (4.28), the description of the condensate by $\hat{\rho}_{BS}$ allows one to conveniently compute expectation values of few-body operators, for instance of $\hat{N}_0$, and the signatures of fragmentation we found previously are easily recovered. However, if this approach is well adapted to the case $T = 0$, it is not easily extended to the case of finite temperatures. At finite temperature we indeed expect to populate $|N, S, M\rangle$ states with $S, M > 0$, and experimentally this distribution is constrained by the conservation of the magnetization. Yet nematic states verify $\langle \hat{\mathbf{S}} \rangle = 0$, and it is not possible to describe for instance a condensate with a non-zero magnetization by a mixture of nematic states. As the distribution of the magnetization does affect the expectation value of $\hat{N}_0$, the set of nematic states is not adapted to study the occurrence of spin fragmentation in our experimental system. The properties of the nematic states actually originates from their similarity with coherent states. To benefit from these properties while being able

[3] If the few-body operator $\hat{O}^{(k)}$ is not normally ordered, one can always write

$$\hat{O}^{(k)} =: \hat{O}^{(k)} : + \hat{R}^{(k)} \tag{4.33}$$

where : : stands for normal ordering. The residual operator $\hat{R}^{(k)}$ results from the commutation of the $\hat{a}_i^\dagger$ and $\hat{a}_i$ operators. As a consequence, the expectation value of $: \hat{O}^{(k)} :$ is of order N^k while the one of $\hat{R}^{(k)}$ is of order N^{k-1}. It can usually be neglected in the limit $N \to +\infty$ that we consider here.

to completely describe the Hilbert space of our problem we develop a broken-symmetry approach based on another family of mean-field spin states, the so-called $SU(3)$ coherent states.

4.2.2 Broken-symmetry approach at finite temperatures

The notion of coherent state, originally introduced in the context of quantum optics, can indeed be extended to atomic systems [90, 91]. Each set of generalized coherent states is closely related to one particular symmetry group. All these sets of states share important properties that make them well-suited to describe large ensembles of particles that possess this particular symmetry [92]. We use $SU(3)$ coherent states to accurately describe our atomic samples at finite temperature.

The notion of generalized coherent states and the construction of $SU(3)$ coherent states are the object of Appendix D. We here present their major properties that will be used to simplify calculations. Finally we derive expressions for the two first moments and the distribution of the population n_0 at finite temperatures. These results will be used in chapter 5 to analyze our experimental observations of spin fragmentation.

4.2.3 $SU(3)$ coherent states

A $SU(3)$ coherent state is a mean-field many-body spin state defined by

$$|N:\boldsymbol{\zeta}\rangle = \frac{1}{\sqrt{N!}}\left(\boldsymbol{\zeta}.\hat{\mathbf{a}}^\dagger\right)^N |\text{vac}\rangle \tag{4.35}$$

where $\boldsymbol{\zeta}$ is a normalized complex vector. The operator $\boldsymbol{\zeta}.\hat{a}^\dagger$ creates one particle in the spin-1 state

$$|\boldsymbol{\zeta}\rangle = e^{i\phi_0}\begin{pmatrix} \sin(\theta)\cos(\nu)e^{i\phi_{+1}} \\ \cos(\theta) \\ \sin(\theta)\sin(\nu)e^{i\phi_{-1}} \end{pmatrix} \tag{4.36}$$

As well as nematic states, the $SU(3)$ coherent states form an overcomplete basis of the Hilbert spin space. They verify the resolution of unity

$$\int \mathrm{d}\boldsymbol{\zeta}|N:\boldsymbol{\zeta}\rangle\langle N:\boldsymbol{\zeta}| = \mathbb{1} \tag{4.37}$$

where the measure is given by

$$\mathrm{d}\boldsymbol{\zeta} = \frac{(N+2)(N+1)}{\pi^2}\sin^3(\theta)\cos(\theta)\cos(\nu)\sin(\nu)\mathrm{d}\theta\mathrm{d}\nu\mathrm{d}\phi_{+1}\mathrm{d}\phi_{-1} \tag{4.38}$$

with $\theta, \nu \in [0, \pi/2]$ and $\phi_{\pm 1} \in [0, 2\pi]$. Any state of the Fock space of N spin-1 can be represented in the basis of $SU(3)$ coherent states:

$$|\Psi\rangle = \int \mathrm{d}\boldsymbol{\zeta}\tilde{\Psi}(\boldsymbol{\zeta})|N:\boldsymbol{\zeta}\rangle \tag{4.39}$$

but the decomposition $\tilde{\Psi}(\boldsymbol{\zeta})$ is not unique.

The coherent states are also not orthogonal and we have:

$$\langle N:\boldsymbol{\zeta}|N:\boldsymbol{\zeta}'\rangle = \left(\boldsymbol{\zeta}.\boldsymbol{\zeta}'\right)^N \tag{4.40}$$

Again, because of the large power N, the scalar product is very peaked around $\boldsymbol{\zeta} = \boldsymbol{\zeta}'$. In the limit $N \to +\infty$ it can be approximated by a Dirac distribution:

$$\langle N : \boldsymbol{\zeta} | N : \boldsymbol{\zeta}' \rangle = \mathcal{A}\delta\left(\boldsymbol{\zeta} - \boldsymbol{\zeta}'\right) + \mathcal{O}\left(\frac{1}{N^2}\right) \tag{4.41}$$

where $\mathcal{A}$ is a normalization factor and the coherent states become quasi-orthogonal in this limit.

An other major property is that zero is the only operator for which the expectation value vanishes for all coherent states. This property is actually required to ensure that any operator $\hat{O}$ acting in the Fock space can be represented as a diagonal operator in the coherent state basis:

$$\hat{O} = \int \mathrm{d}\boldsymbol{\zeta} \tilde{O}(\boldsymbol{\zeta}) | N : \boldsymbol{\zeta} \rangle \langle N : \boldsymbol{\zeta} | \tag{4.42}$$

As for the decomposition of states, the decomposition $\tilde{O}(\boldsymbol{\zeta})$ is not unique. In particular we note that $\tilde{O}(\boldsymbol{\zeta}) \neq \langle N : \boldsymbol{\zeta} | \hat{O} | N : \boldsymbol{\zeta} \rangle$. These two quantities are called upper and lower symbols respectively.

We point out that the existence of such a diagonal representation of operators in the nematic basis is not guaranteed, and that this is the reason why the nematic states are not adapted to describe our experiments. In particular, the expectation value of the spin operator $\hat{S}$ vanishes for all nematic states. In this case, off-diagonal elements are needed to determine these operators, which makes calculations much more difficult.

The use of coherent states allows for simple calculations in the classical limit $N \to \infty$. First we note that the annihilation operators $\hat{a}_{+1}, \hat{a}_0, \hat{a}_{-1}$ act on these states in the same way as on the nematic states:

$$\hat{a}_i | N : \boldsymbol{\zeta} \rangle = \sqrt{N} \zeta_i | N - 1 : \boldsymbol{\zeta} \rangle \tag{4.43}$$

where $i = \pm 1, 0$.

As previously we consider a k-body operator $\hat{O}^{(k)}$ (in normal order) acting in the Fock space of N spin-1 bosons, with $k \ll N$. Using expressions (4.37), (4.43) and (4.40) one finds (see Appendix D) that the operator $\hat{O}^{(k)}$ accepts the decomposition

$$\hat{O}^{(k)} \approx \int \mathrm{d}\boldsymbol{\zeta} \langle N : \boldsymbol{\zeta} | \hat{O}^{(k)} | N : \boldsymbol{\zeta} \rangle | N : \boldsymbol{\zeta} \rangle \langle N : \boldsymbol{\zeta} | \tag{4.44}$$

In this limit $N \to +\infty$ the distinction between lower and upper symbols vanishes

We also easily find that the expectation value of a product of two operators in a coherent state obey the simple rule:

$$\langle \hat{O} \hat{P} \rangle \approx \langle \hat{O} \rangle \langle \hat{P} \rangle \tag{4.45}$$

Using this property we can calculate the density operator $\hat{\rho}$ describing a thermal state in the canonical ensemble. According to (4.44) only the diagonal elements matter and one

finds:

$$\langle N:\boldsymbol{\zeta}|\hat{\rho}|N:\boldsymbol{\zeta}\rangle = \frac{1}{\mathcal{Z}}\int \mathrm{d}\boldsymbol{\zeta}\langle N:\boldsymbol{\zeta}|\left(\sum_{n=0}^{+\infty}\frac{\beta^n\hat{H}^n}{n!}\right)|N:\boldsymbol{\zeta}\rangle \tag{4.46}$$

$$\approx \frac{1}{\mathcal{Z}}\int \mathrm{d}\boldsymbol{\zeta}\left(\sum_{n=0}^{+\infty}\frac{\beta^n\langle N:\boldsymbol{\zeta}|\hat{H}|N:\boldsymbol{\zeta}\rangle^n}{n!}\right) \tag{4.47}$$

$$= \frac{1}{\mathcal{Z}}e^{-\beta\langle N:\boldsymbol{\zeta}|\hat{H}|N:\boldsymbol{\zeta}\rangle} \tag{4.48}$$

where $\mathcal{Z}$ is the partition function and $\beta = 1/k_BT$. We can now compute thermodynamic averages:

$$\langle\hat{O}\rangle = \mathrm{Tr}\left(\hat{O}\hat{\rho}\right) \tag{4.49}$$

$$\approx \int \mathrm{d}\boldsymbol{\zeta}\langle N:\boldsymbol{\zeta}|\hat{O}|N:\boldsymbol{\zeta}\rangle\langle N:\boldsymbol{\zeta}|\hat{\rho}|N:\boldsymbol{\zeta}\rangle \tag{4.50}$$

$$\approx \frac{1}{\mathcal{Z}}\int \mathrm{d}\boldsymbol{\zeta}\langle N:\boldsymbol{\zeta}|\hat{O}|N:\boldsymbol{\zeta}\rangle e^{-\beta\langle N:\boldsymbol{\zeta}|\hat{H}|N:\boldsymbol{\zeta}\rangle} \tag{4.51}$$

This expression corresponds to the expectation value calculated in a statistical mixture of coherent states, weighted by the factor $\frac{1}{\mathcal{Z}}e^{-\beta\langle N:\boldsymbol{\zeta}|\hat{H}|N:\boldsymbol{\zeta}\rangle}$.

4.2.4 Broken symmetry description of a spin-1 gas with constrained magnetization

We now apply the results we just derived to calculate the thermodynamic averages of observables that express the spin fragmentation of our system, namely the population $\hat{n}_0 = \hat{N}_0/N$ and its square. First, for physical clarity we prefer to perform a change of variable in the definition (4.36) of $SU(3)$ coherent states. We introduce the new variables:

$$n_0 = \cos^2(\theta) \tag{4.52}$$

$$m_z = \sin^2(\theta)\cos(2\nu) \tag{4.53}$$

$$\Theta = \phi_{+1} + \phi_{-1} - 2\phi_0 \tag{4.54}$$

$$\alpha = \phi_{+1} - \phi_{-1} \tag{4.55}$$

which gives the familiar form of mean-field states introduced in chapter 1:

$$|\boldsymbol{\zeta}\rangle = \begin{pmatrix} \sqrt{\frac{1-n_0+m_z}{2}}e^{i(\Theta+\alpha)/2} \\ \sqrt{n_0} \\ \sqrt{\frac{1-n_0-m_z}{2}}e^{i(\Theta-\alpha)/2} \end{pmatrix} \tag{4.56}$$

The new measure is $\mathrm{d}\boldsymbol{\zeta} = \frac{(N+1)(N+2)}{(2\pi)^2}\mathrm{d}n_0\mathrm{d}m_z\mathrm{d}\Theta\mathrm{d}\alpha$, where $\Theta \in [0, 2\pi], \alpha \in [0, 4\pi], m_z \in [-1, 1]$ and $0 < n_0 < 1 - |m_z|$.

Density operator

Before calculating thermodynamic averages, we need to determine which ensemble we have to consider, since our system is constrained. We first point out that $[\hat{H}_s, \hat{S}_z] = 0$, where $\hat{H}_s$ is the spin Hamiltonian. The azimuthal quantum number M remains a good quantum number even in the presence of an external magnetic field. This also implies $[\hat{P}_M, \hat{H}_s] = 0$,

where $\hat{P}_M$ is the projector on the subspace characterized by the spin projection M, so that the decomposition of a state in all these subspaces is conserved. The most general ensemble we can consider is then a canonical ensemble where the population in each subspace of well-defined M (eigenvalue of $\hat{S}_z$) is fixed in average. This leads to the density matrix

$$\hat{\rho} = \frac{1}{\mathcal{Z}} e^{-\beta \hat{H} - \sum_{M=-N}^{N=N} \lambda_M \hat{P}_M} \tag{4.57}$$

where λ_M is the Lagrange factor associated to the conservation of its population. Using the relations $[\hat{H}, \hat{P}_M] = 0$ and $[\hat{P}_M, \hat{P}_{M'}] = 0$ we can disentangle the different parts of the exponential. Considering the part that involves the $\hat{P}_M$'s only we decompose the exponentials in sums and using $\hat{P}_M^k = \hat{P}_M$ for $k > 0$ and $\hat{P}_M \hat{P}_{M'} = 0$ for $M \neq M'$ we finally obtain the expression

$$\hat{\rho} = \frac{1}{\mathcal{Z}} \sum_{M=-N}^{M=N} e^{-\lambda_M} \hat{P}_M e^{-\beta \hat{H}} \hat{P}_M. \tag{4.58}$$

To calculate the diagonal elements of this density operator in the coherent state basis one has to decompose these states in the basis of total angular momentum eigenstates. This decomposition exists and is known. It involves a generalization of spherical harmonics (called hyper spherical harmonics), whose mathematical manipulation would be very cumbersome in this context, and would remove the advantage of working with these coherent states.

Constraining the whole distribution of the magnetization is equivalent to constraining all the moments of $\hat{S}_z$. Rather we decide to only constrain the two first moments. In the case of a gaussian distribution of the magnetization this is enough to fully characterize it. As the experimental distributions we measure seem roughly gaussian, we expect that this choice allows us to correctly describe our observations. We then consider the density matrix

$$\hat{\rho}_{BS} = \frac{1}{\mathcal{Z}} e^{-\beta \hat{H} - \lambda_1 \hat{S}_z - \lambda_2 \hat{S}_z^2} = \frac{1}{\mathcal{Z}} e^{-\beta \hat{K}} \tag{4.59}$$

We now calculate thermodynamic averages. We suppose the validity of the single mode approximation. We first calculate the expectation value of the Hamiltonian in a $SU(3)$ coherent state. To leading order in N we find:

$$E_s(\boldsymbol{\zeta}) = \frac{NU_s}{2} \left(m_z^2 + 2n_0(1-n_0) + 2n_0 \sqrt{(1-n_0)^2 - m_z^2} \cos(\Theta) \right) - qNn_0 \tag{4.60}$$

where q is the quadratic Zeeman energy. We introduce the two dimensionless parameters

$$\eta = \frac{Nq}{k_B T} \tag{4.61}$$

$$\beta' = \frac{NU_s}{k_B T} \tag{4.62}$$

and define two new factors $\gamma_1 = \lambda_1/\beta$ and $\gamma_2 = \lambda_2/\beta$. We then have

$$\beta K = \beta \langle N : \boldsymbol{\zeta} | \hat{K} | N : \boldsymbol{\zeta} \rangle \tag{4.63}$$

$$= \frac{\beta'}{2} \left((1 + 2\gamma_2) m_z^2 + 2\gamma_1 m_z + 2n_0 \left(1 - n_0 + \sqrt{(1-n_0)^2 - m_z^2} \cos(\Theta) \right) \right) - \eta n_0 \tag{4.64}$$

The values of the two multipliers are fixed by the conditions

$$\langle m_z \rangle = \frac{1}{\mathcal{Z}} \int \mathrm{d}\boldsymbol{\zeta} m_z e^{-\beta K} \tag{4.65}$$

$$\langle m_z^2 \rangle = \frac{1}{\mathcal{Z}} \int \mathrm{d}\boldsymbol{\zeta} m_z^2 e^{-\beta K} \tag{4.66}$$

The partition function is found by integration over the four variables:

$$\mathcal{Z} = \frac{N^2}{2\pi} \int_0^1 \mathrm{d}n_0 \int_{n_0-1}^{1-n_0} \mathrm{d}m_z I_0 \left(\beta' n_0 \sqrt{(1-n_0)^2 - m_z^2}\right) e^{-\frac{\beta'}{2}\left((1+2\gamma_2)m_z^2 + 2n_0(1-n_0)\right) + \eta n_0 - \beta'\gamma_1 m_z} \tag{4.67}$$

where I_0 is the modified Bessel function of the first kind. The average values $\langle n_0 \rangle$ and $\langle n_0^2 \rangle$ are calculated similarly to (4.65) and (4.66). They only depend on the two dimensionless parameters η and β', and not on the three energy scales $U_s, q.$ and $k_B T$ independently.

Quasi spin-nematic states

From expression (4.64) we see that in equilibrium the fluctuations of the phase Θ around the value $\Theta = \pi$ that minimizes the energy have a typical width $1/\sqrt{\beta'}$. In practice we are interested in the regime of low temperatures, defined by the condition [88]

$$k_B T \ll N U_s, \text{ or } \beta' \gg 1 \tag{4.68}$$

In this regime, we thus expect the fluctuations of Θ to be very small. The theory can be simplified by expanding Θ around π and m_z around zero, which is the situation realized in our experiments. We write $\Theta = \pi + \delta\Theta$ and assume $m_z \ll 1 - n_0$. We obtain

$$|N:\boldsymbol{\zeta}\rangle \approx \begin{pmatrix} \sqrt{\frac{1-n_0}{2}} \left(1 + \frac{m_z}{2(1-n_0)}\right) e^{i(\pi+\delta\Theta+\alpha)/2} \\ \sqrt{n_0} \\ \sqrt{\frac{1-n_0}{2}} \left(1 - \frac{m_z}{2(1-n_0)}\right) e^{i(\pi+\delta\Theta-\alpha)/2} \end{pmatrix} = \begin{pmatrix} i\frac{\sin\theta}{\sqrt{2}} \left(1 + \frac{m_z}{2\sin^2\theta}\right) e^{i(\delta\Theta+\alpha)/2} \\ \cos\theta \\ i\frac{\sin\theta}{\sqrt{2}} \left(1 - \frac{m_z}{2\sin^2\theta}\right) e^{i(\delta\Theta-\alpha)/2} \end{pmatrix} \tag{4.69}$$

where we defined $\cos\theta = \sqrt{n_0}$. These states approach nematic states. In this case the integrals over these variables become gaussian and can be easily calculated. The moments of n_0 can then be expressed as integrals of the variable n_0 alone, that can be efficiently calculated numerically. We show in figure (4.3) a comparison of the exact and approximate theories for different average magnetizations. We find that the approximate theory works well even for quite large magnetizations ($\langle m_z \rangle = 0.2$). We find the same qualitative behavior as evidenced in the first section by an exact diagonalization. At large η the limit $\langle n_0 \rangle = 1 - \langle m_z \rangle$ is reached.

It is interesting to calculate the effect of the constraint on m_z^2 on the average value and standard deviation of n_0. This constraint is carried by the Lagrange multiplier γ_2. We can define a pseudo inverse temperature $\beta_z = NU_s/k_B T_z$ to describe the distribution of m_z:

$$\beta_z = \beta'(1 + 2\gamma_2) \tag{4.70}$$

A purely thermal distribution of m_z corresponds to $\gamma_2 = 0$ and so to $\beta_z = \beta'$. A narrow distribution is characterized by $\gamma_2 \gg 1$ ($\beta_z \gg \beta'$) and a broad one is characterized by $2\gamma_2 \to -1$ ($\beta_z \ll \beta'$). The dependence of $\langle n_0 \rangle, \Delta n_0$ and Δm_z on the ratio β_z/β', calculated

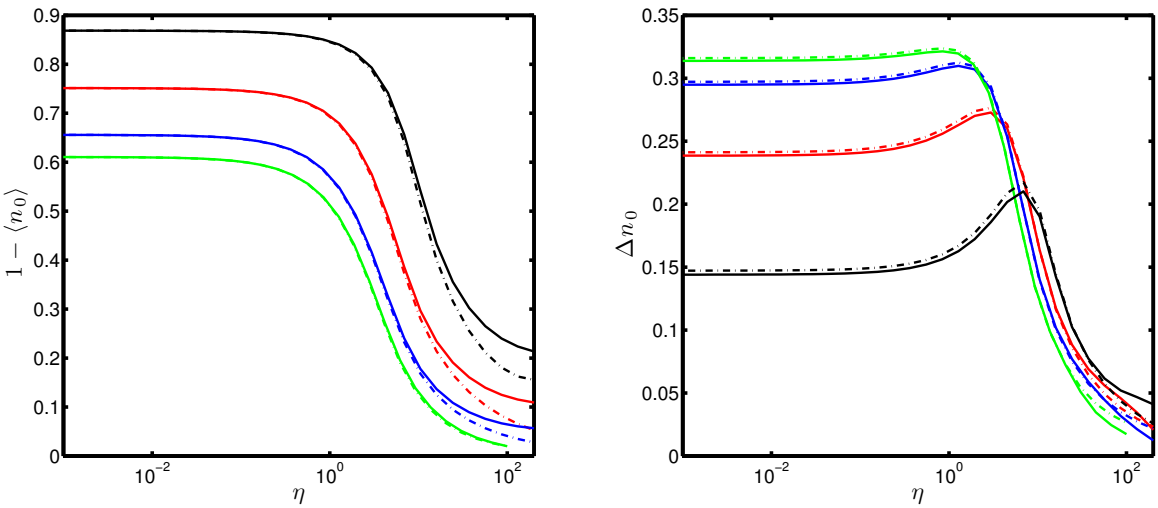

Figure 4.3: Average depletion and standard deviation of the population n_0 as functions of η calculated with the exact theory (solid lines) and with the approximate one (dashed lines), for various average magnetization. The parameters are $\beta' = 100$, $\Delta m_z = 0.04$. Black: $\langle m_z \rangle = 0.2$, red: $\langle m_z \rangle = 0.1$, blue: $\langle m_z \rangle = 0.05$, green: $\langle m_z \rangle = 0.02$. The deviation at high η are explained by the approximation $m_z \ll 1 - n_0$ that fails in this region.

within the approximate theory for $\eta = 0$ and $\langle m_z \rangle = 0$, is shown in figure (4.4). We recover the results (4.19) and (4.20) of the first section of this chapter: if the magnetization is only fixed in average, we obtain at $q = 0$ $\langle n_0 \rangle \approx 1/3$ and $\Delta n_0 \approx 0.3$. As the distribution then gets narrower the average value of n_0 goes from 1/3 to 1/2.

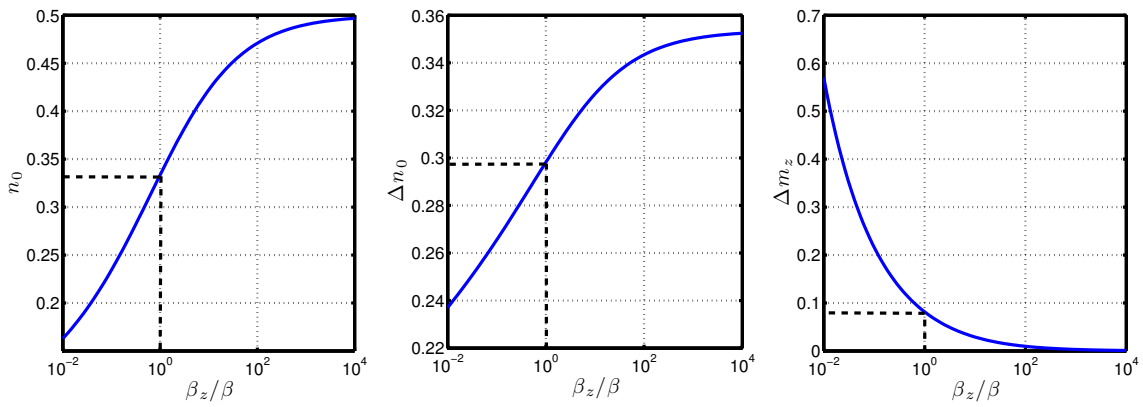

Figure 4.4: Average value and standard deviation of n_0 and standard deviation of m_z as functions of $\beta_z/\beta' = 1 + 2\gamma_2$, for $\langle m_z \rangle = 0$ and $\eta = 0$, calculated using the approximate theory obtained by the development of Θ around π.

The distribution of the variable n_0 for a given value of η can be obtained by integrating the phase-space distribution $e^{-\beta K}/\mathcal{Z}$ over the other variables. For $\langle m_z \rangle = 0$ the

approximate development of K gives

$$P(n_0) \approx \frac{1}{\mathcal{Z}} \frac{e^{\eta n_0}}{\sqrt{n_0\,(1+2\gamma_2(1-n_0))}} \tag{4.71}$$

In the case of a very narrow distribution of magnetization (corresponding to $\gamma_2 \gg 1$) the distribution at $\eta = 0$ is symmetric around $n_0 = 1/2$. As the distribution of m_z gets broader the distribution of n_0 at $\eta = 0$ becomes peaked at $n_0 = 0$. Figure (4.5) shows the distribution for various values of η calculated for $\gamma_1 = \gamma_2 = 0$. For $\eta = 0$ the distribution varies as $1/\sqrt{n_0}$. For large values of η the distribution goes as $e^{\eta n_0}/\sqrt{n_0}$ and is peaked at $n_0 = 1$.

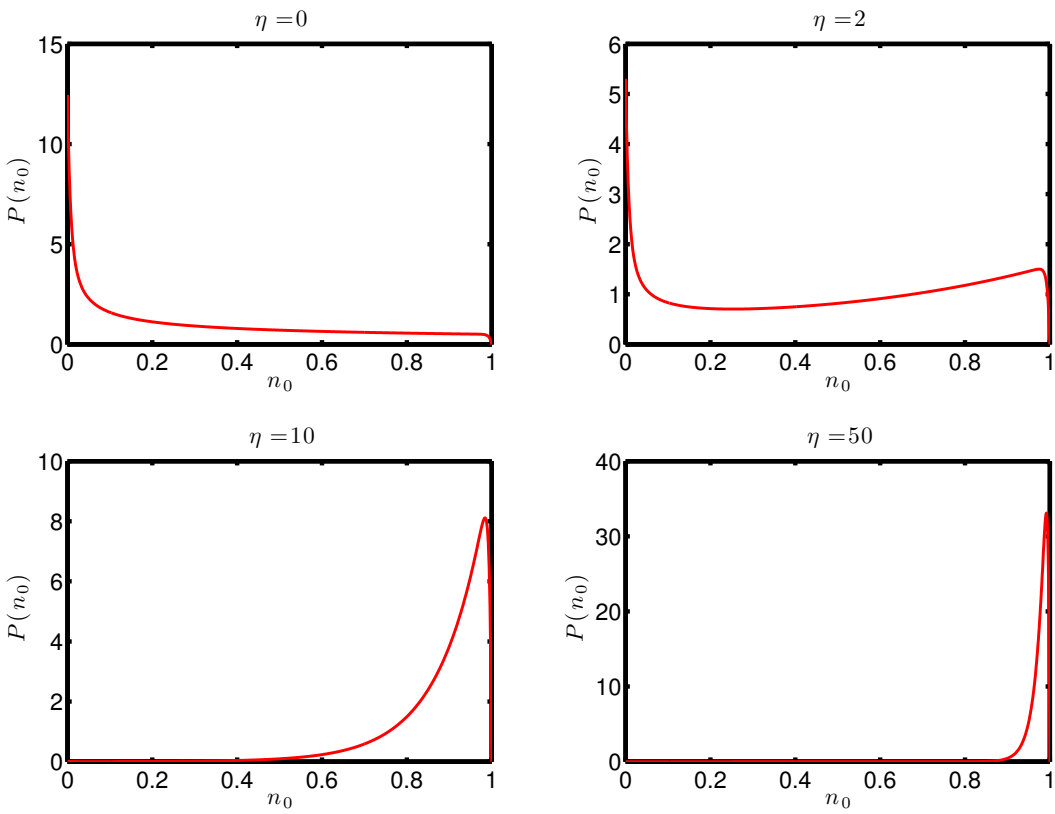

Figure 4.5: Distribution of the population n_0 for $\beta' = 100$ and $\gamma_1 = \gamma_2 = 0$. For $\eta = 0$ one observes the $1/\sqrt{n_0}$ distribution predicted by the expression (4.71). For large a values of η the distribution becomes very peaked close to $n_0 = 1$, with a width of order $1/\eta$.

Similarly one can calculate the distribution of m_z. Figure (4.6) shows numerical calculations for $\gamma_1 = \gamma_2 = 0$ for different values of η and β'. As one expects, increasing these parameters results in a narrower distribution of m_z.

Limiting case of nematic states

If $\gamma_1 = \gamma_2 = 0$ the magnetization is unconstrained and vanishes in average. The description in terms of $SU(3)$ coherent states is then equivalent to that using nematic states $|N : \mathbf{\Omega}\rangle$ defined in (4.23). To leading order in N, nematic states have no spin interaction energy

and the density operator then reduces to

$$\hat{\rho}_{BS} = \frac{1}{\mathcal{Z}} \int \mathrm{d}\mathbf{\Omega} |N : \mathbf{\Omega}\rangle\langle N : \mathbf{\Omega}| e^{N\beta q \cos^2\theta} \tag{4.72}$$

with

$$\mathcal{Z} = \int_0^{2\pi} \mathrm{d}\phi \int_0^{\pi} \sin\theta \mathrm{d}\theta e^{N\beta q \cos^2\theta} \tag{4.73}$$

In the absence of magnetic field, all the Boltzmann weights are equal to 1 and the mixture is isotropic. In the other limit of very large q, only the nematic state directed along the z axis contributes to the density matrix. We can visualize the evolution of this distribution by calculating the diagonal elements of the density matrix, similarly to what is commonly done with coherent states with the Q function. For each nematic state $|N : \mathbf{\Omega}\rangle$ we compute the quantity $\langle N : \mathbf{\Omega}|\hat{\rho}_{BS}|N : \mathbf{\Omega}\rangle$, and then plot it as a function of $\mathbf{\Omega}$ on a sphere. Figure (4.7) shows the progressive localization of the trace around the north pole. In the limit of large magnetic field only the nematic state $|N : e_z\rangle$ remains in the mixture, but the distribution on the sphere still has some width for the nematic states are not orthogonal and the atom number is finite (1000 in the figure).

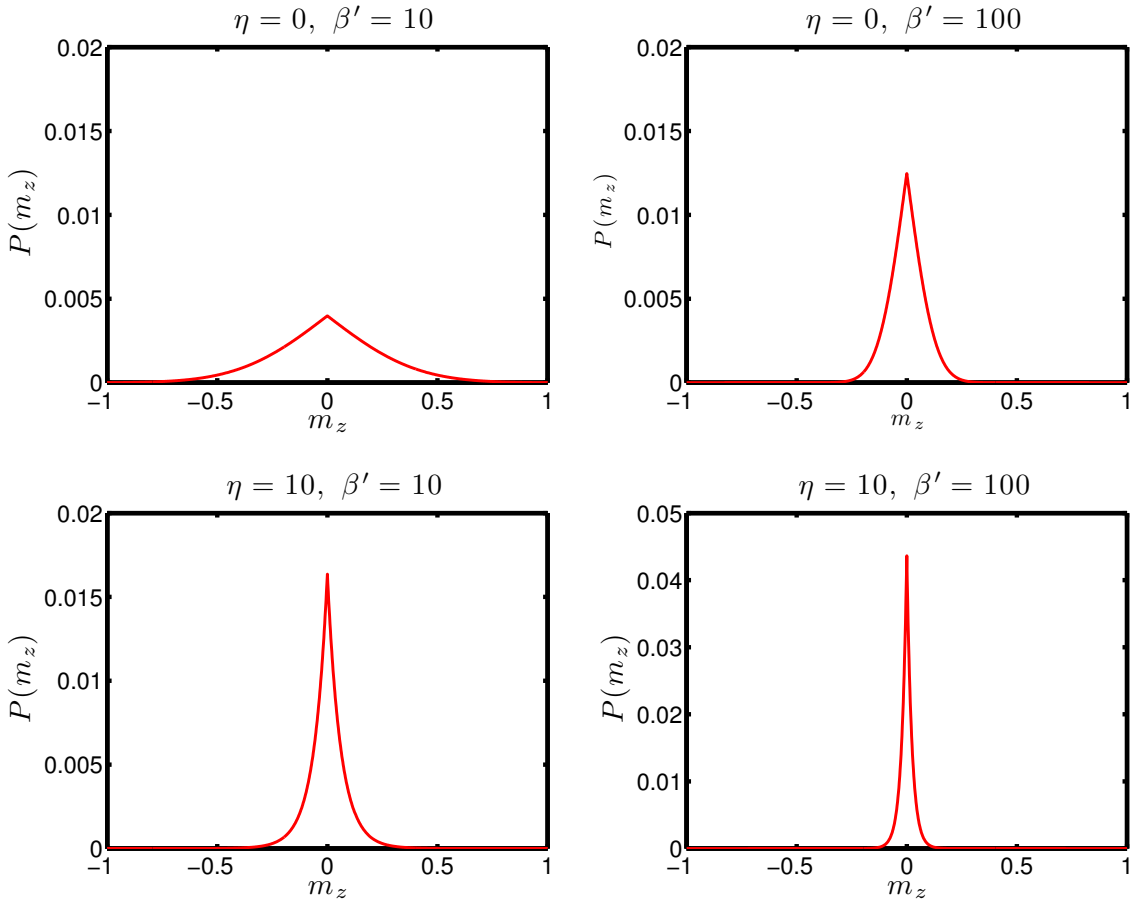

Figure 4.6: Distribution of the magnetization m_z for $\beta' = 10, 100$ and $\eta = 0, 10$. For all curves $\gamma_1 = \gamma_2 = 0$).

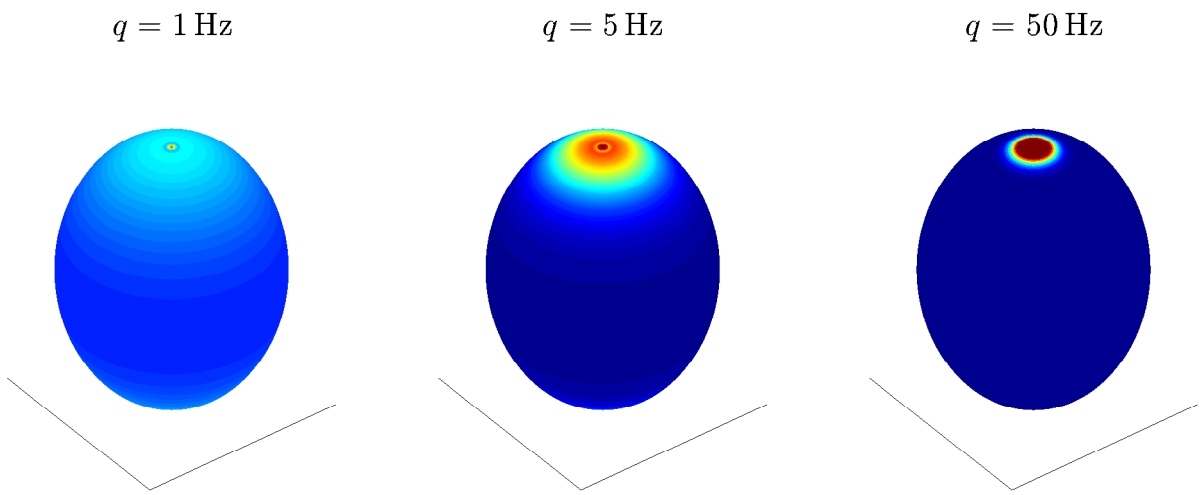

Figure 4.7: Q function associated to the matrix $\hat{\rho}_{BS}$ for different values of the quadratic Zeeman effect q. In the point of the sphere defined by the vector $\mathbf{\Omega}$ the function Q takes the value $Q(\mathbf{\Omega}) = \langle N : \mathbf{\Omega}|\hat{\rho}_{BS}|N : \mathbf{\Omega}\rangle$. Calculations are done with $N = 1000$ and $T_s = 50$nK. The color scale is the same for the different plots. We clearly observe the progressive localization of the mixture of nematic states around the north pole corresponding to the $|m_F = 0\rangle^{\otimes N}$ many-body spin state. Even for very high q the Q function keeps a finite width around this point, due to the finite atom number and the consequent non-orthogonality of the nematic states.

We confirm the precision of the broken symmetry approach in this limiting case of unconstrained magnetization by comparing its prediction to the results of an exact diagonalization. Figure (4.8) shows the two first moments of n_0. We find a very good agreement.

We can also compute the probability distribution of N_0. We define $\hat{P}(N_0)$ the projector on the subspace of states with exactly N_0 atoms in the $m_F = 0$ spin state:

$$\hat{P}(N_0) = \sum_M |N_{+1}, N_0, N_{-1}\rangle\langle N_{+1}, N_0, N_{-1}| \tag{4.74}$$

$$N_{\pm 1} = \frac{N - N_0 \pm M}{2} \tag{4.75}$$

The probability to have N_0 atoms is given by:

$$P(N_0) = \frac{1}{\mathcal{Z}} \int \mathrm{d}\mathbf{\Omega} |\langle N : \mathbf{\Omega}|\hat{P}(N_0)|N : \mathbf{\Omega}\rangle|^2 e^{N\beta q \cos^2\theta} \tag{4.76}$$

The average value of $\hat{P}(N_0)$ is calculated using the explicit decomposition of nematic states in the Fock basis. The calculation of the integral for $q > 0$ is quite involved but can be efficiently approximated. We obtain

$$P(N_0) = \frac{1}{NF_{-1/2}(\eta)} \frac{e^{\eta N_0/N}}{\sqrt{N_0/N + 1/2N}} \tag{4.77}$$

where we defined the function $F_{-1/2}(x) = \int_0^1 t^{-1/2} e^{xt} \mathrm{d}t$. We finally convert the distribution of N_0 in a distribution of $n_0 = N_0/N$:

$$p(n_0) = \frac{1}{F_{-1/2}(\eta)} \frac{e^{n_0\eta}}{\sqrt{n_0}} \tag{4.78}$$

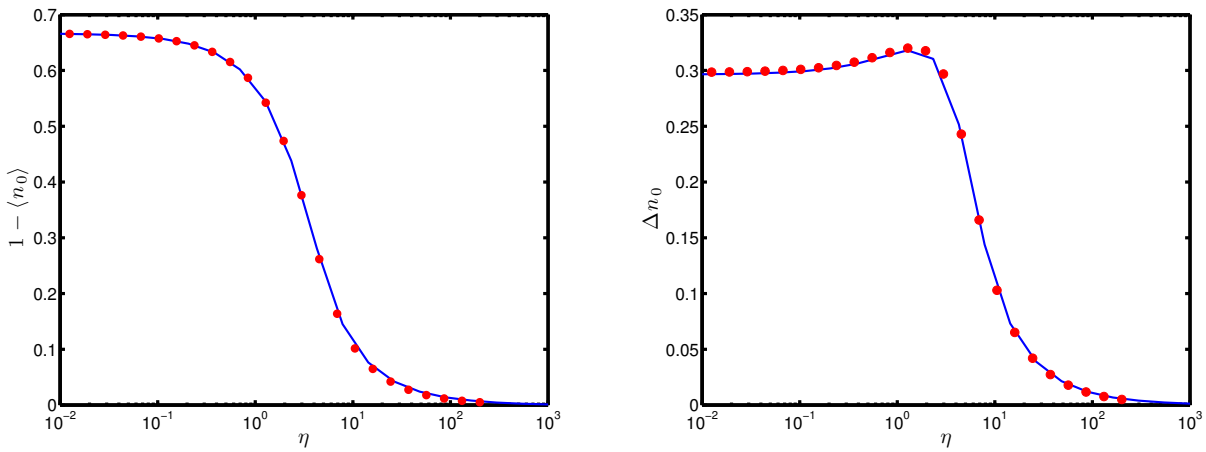

Figure 4.8: Average depletion of the population $\langle n_0 \rangle$ (left) and its standard deviation (right) as functions of η calculated via an exact diagonalization (blue curve) and using the broken symmetry description (red points). Calculations are done with $N = 1000, \beta' = 100$ and $\gamma_1 = \gamma_2 = 0$. The average of the magnetization is then zero and its distribution is purely thermal (unconstrained).

When $\eta \to \infty$, $F_{-1/2}(\eta) \sim e^{\eta}/\eta$. The distribution for large values of η becomes quasi exponential, centered at $n_0 = 1$ with a width $1/\eta$:

$$p(n_0|\eta) \underset{\eta\to\infty}{\sim} \frac{\eta e^{(n_0-1)\eta}}{\sqrt{n_0}} \tag{4.79}$$

One recovers the result (4.71) for $\gamma_2 = 0$. However, the treatment using $SU(3)$ coherent states is much more powerful, as it accounts for the complete Hilbert space and for instance allows to compute the distribution of m_z, which is out of reach of the treatment with nematic states only.

4.3 Connection to spontaneous symmetry breaking

The spin Hamiltonian at zero magnetic field is rotationally symmetric. Its exact ground state then has to share this symmetry, which implies huge spin fluctuations. As the magnetic field increases, the system continuously evolves to a symmetry-breaking nematic state. As we have seen, this transition is illustrated by the collapse of the spin fluctuations. We calculated the variance of the population in the $m_F = 0$ spin state in the broken symmetry picture and found that it depended only on the variable $Nq/k_{\mathrm{B}}T$. At fixed temperature, the collapse of the spin fluctuations then happens on a typical scale $q_c \sim 1/N$ of quadratic Zeeman effect, or equivalently on a scale $B_c \sim 1/\sqrt{N}$ of magnetic field. In the thermodynamic limit B_c goes to 0, and an infinitesimally small magnetic field is enough to destroy the spin fluctuations and to project the system in a mean-field state. This behavior has a close connection to the phenomenon of spontaneous symmetry breaking.

4.3.1 Spontaneous symmetry breaking in the thermodynamic limit

Introduction to spontaneous symmetry breaking

Symmetry plays a crucial role in quantum mechanics. For instance translational symmetry of a system imposes that its eigenstates are fully delocalized over space. This is obviously not observed in classical mechanics where, even in the presence of translational invariance, objects are very well localized. In a classical phase transition, for instance when a crystal is formed out of a fluid, translational symmetry of laws of physics is broken. The same observation holds for rotational symmetry. In quantum mechanics, states that can be deduced one from the other by a transformation keeping the system invariant should have the same status. On the contrary, in the classical limit one of these states is singled out. The system chooses 'arbitrarily' one particular solution out of a set of equivalent ones. The symmetry is said to be spontaneously broken.

One of the major achievements of condensed matter physics was to understand the mechanism of spontaneous symmetry breaking and to develop the underlying mathematical formalism. We will here only briefly recall simple elements of this formalism. Still this will be enough to then apply it to the case of the spin-1 Bose gas.

We consider a system of N particles described by a Hamiltonian $\hat{H}$ which is invariant under some transformation. The ground state then retains the symmetry of $\hat{H}$. Now we add to $\hat{H}$ some external field which breaks the original symmetry of the system. The table shows some examples taken from condensed matter physics [93, 94]. The new ground state of the system also loses its symmetry. For finite values of N, if we send the amplitude of this symmetry-breaking field to zero, the ground state evolves back to the symmetric state. Afterwards taking the thermodynamic limit does not affect this property. If we now first take the thermodynamic limit and send N to infinity while keeping some finite symmetry-breaking part in the Hamiltonian, the system converges to some non-symmetric state. At this point the symmetry is explicitly broken by the presence of the perturbation. We finally reduce the amplitude of this perturbation to zero. It turns out that the symmetry breaking survives this limit: the system picks up one non-symmetric ground-state whereas it should be isotropic. The phenomenon of spontaneous symmetry breaking originates from this non commutation of the two limits.

physical system	**broken symmetry**	**symmetry breaking field**
crystal	translation of the center of mass	pinning potential
nematic liquid crystal	rotation in real space	electric or magnetic field
antiferromagnet	rotation in spin space	staggered magnetic field

Table 4.1: Examples of systems experiencing spontaneous symmetry breaking, with the associated symmetry breaking field.

Case of a spin-1 Bose gas

We now describe this mechanism in a more formal way. We consider a system of N spin-1 particles, and for simplicity assume a uniform trapping potential. We first suppose that

no external magnetic field is present. In chapter 1 we developed a simplified Bogoliubov theory of this system. We decomposed the state of the condensate in plane waves of momentum $\mathbf{k}$ and obtained the Hamiltonian

$$\hat{H} = \frac{U_s}{2N}\hat{\mathbf{S}}^2_{\text{tot}} + \sum_{k\neq 0} E_\alpha(k)\hat{\alpha}^\dagger_k\hat{\alpha}_k + E_0 \tag{4.80}$$

where E_0 is constant and $\hat{\alpha}^\dagger_k$ creates an elementary excitations of energy $E_\alpha(k)$. In this expression we do not distinguish between the different elementary excitations (density and spin waves) for it is not necessary here. The $k = 0$ part of the Hamiltonian corresponds to the SMA Hamiltonian $\hat{H}_0 = (U_s/2N)\hat{\mathbf{S}}^2$. It describes the "center of mass" of the system in spin space and so is the part we should consider to track the symmetry breaking. We isolate it from the $k \neq 0$ part. $\hat{H}_0$ is rotationally symmetric and its eigenstates are the total angular momentum eigenstates $|N, S, M\rangle$ with an even value of the total spin S. They have an energy $E(S) = (U_s/2N)S(S+1)$.

The profound cause of spontaneous symmetry breaking lies in the structure of the spectrum of the collective Hamiltonian. In systems exhibiting symmetry breaking, this spectrum is made of a family of states whose energy scales down with the particle number, and eventually collapses onto that of the ground state in the thermodynamic limit. Such a spectrum is denoted as an Anderson tower of states, as P.W. Anderson was the first to identify its key role [95]. Does the spectrum of $\hat{H}_0$ have the shape of an Anderson tower of states? We here have to check the behavior of U_s in the thermodynamic limit.

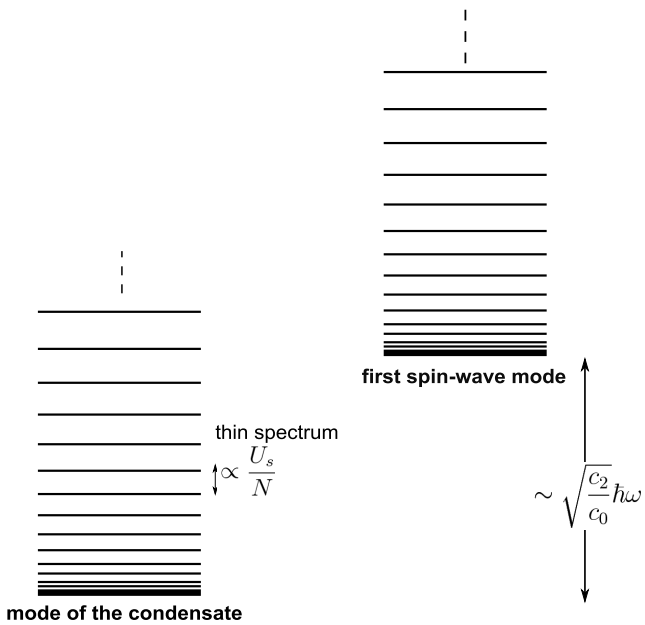

Figure 4.9: Energy spectrum with the mode of the condensate and the first spatial excitation which is a spin-wave mode. Above each mode are the collective spin excitations forming the thin spectrum. A typical value for U_s is 100 Hz, which gives an energy scale for the thin spectrum of 0.1 Hz. The first spin wave excitation has an energy of order $\sqrt{c_2/c_0}\hbar\omega$ where ω is the trapping frequency (see chapter 1). The ratio $c_2/c_0 = 0.035$ gives for a frequency of $2\pi \times 600$Hz an energy $\sqrt{c_0/c_2}\hbar\omega \sim 100\,$Hz.

The energy U_s was defined in the first chapter by $U_s = c_2 N \int |\phi|^4$, where ϕ is the

spatial mode of the condensate in the SMA and is normalized to unity. We note V the volume of the system. $|\phi|^4$ is then of order $1/V^2$, so that U_s is of order N/V. Yet, in the thermodynamic limit, N goes to infinity but the ratio N/V is kept constant, so that U_s keeps the same order of magnitude while taking this limit. The energies $E(S)$ effectively collapse to zero in the thermodynamic limit like $1/N$. Let us now look at the partition function

$$\mathcal{Z}_{\text{thin}} = \sum_{S,M} e^{-\beta U_s S(S+1)/2N} \simeq \frac{2N}{\beta U_s} \tag{4.81}$$

from which we deduce the contribution of the spectrum of $\hat{H}_0$ to the free energy:

$$F_{\text{thin}} = -k_B T \ln(\mathcal{Z}_{\text{thin}}) \propto \ln(N) \tag{4.82}$$

The total free energy of the system is an extensive quantity: it scales like N, and so the relative contribution of the spectrum of $\hat{H}_0$ scales like $\ln(N)/N$: it is negligible in the thermodynamic limit. For this reason this spectrum is also often referred to as the 'thin spectrum'. However its existence has far-reaching consequences.

We now consider the situation where a symmetry breaking field is added to the collective Hamiltonian $\hat{H}_0$. In our case this role is played by the magnetic field through the quadratic Zeeman effect and adds a term $-q\hat{N}_0$ to the Hamiltonian $\hat{H}_0$. If $q = 0$, the ground state is the rotationally symmetric singlet state. If now $q > 0$, its effect is to admix the low-lying $|S\rangle$ states of the thin spectrum to the symmetric ground-state to form the new non-symmetric ground state. If we increase q while keeping N fixed, this superposition involves states of larger total spin S. When the number of contributing states gets on the order of $\sqrt{N}$, the system has evolved to a nematic state (which can be constructed as a superposition of $|S\rangle$ states with non-negligible contribution up to $S \sim \mathcal{O}(\sqrt{N})$, as shown in [88] and [96] and in figure (4.10)). We now adopt the opposite approach: we apply some fixed magnetic field and increase the number of atoms. The energies of the thin spectrum decrease and the levels get closer to each other, so that at fixed q more and more $|S\rangle$ states are admixed to the ground state. In the thermodynamic limit all the $|S\rangle$ states collapse on the singlet state, and any infinitesimally small q is enough to form a nematic state as a combination of these degenerate states. The symmetry is spontaneously broken. The first picture (increase q at fixed N) describes our experimental approach that we will develop in the next chapter, while the second one (increase N at fixed q) is closer to the spirit of spontaneous symmetry breaking.

In the thermodynamic limit, the spinor condensate spontaneously collapses to a nematic state which breaks the rotational symmetry of the Hamiltonian. However in our system, because of the finite atom number, there exists a range of values of q where the number of states from the thin spectrum contributing to the ground state is smaller than $\sqrt{N}$. Equivalently, the system has not yet collapsed to the nematic state. This means that, starting from a high magnetic field and then progressively decreasing it, we can observe in this region of q the transition from a nematic symmetry-breaking state back to a fragmented, rotationally symmetric state, and observe the rise of the spin fluctuations that progressively restore the symmetry broken by the magnetic field. We showed in the previous section that the spin fluctuations are a quasi-universal function of the single variable $Nq/k_{\text{B}}T$. This is consistent with the fact that the amplitude of q necessary for the symmetry to be broken scales as $1/N$.

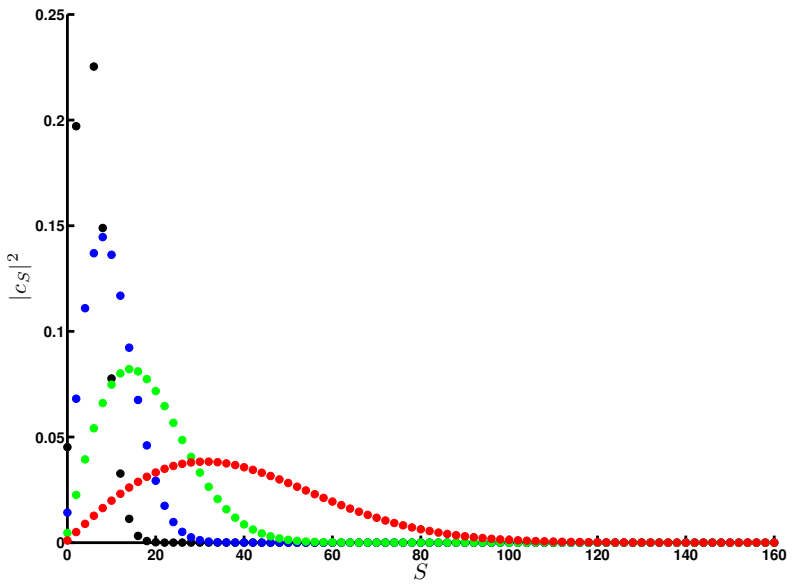

Figure 4.10: Decomposition of the ground state $|GS\rangle$ of the spin-1 Bose gas in the total spin basis (here $M = 0$) for different values of the QZE q, calculated by exact diagonalization of the total Hamiltonian. We noted $c_S = \langle N, S, 0|GS\rangle$. The color code is the following: black: $q = U_s/N$, blue: $q = 10U_s/N$, green: $q = 100U_s/N$. The red points correspond to the decomposition of the nematic state $|0, N, 0\rangle$ in Fock basis. In all cases $N = 1000$. At maximum the number of contributing states is on the order of $\sqrt{N}$, then forming the nematic state.

At $T = 0$, the range of q where the quantum fluctuations beat the symmetry-breaking effect and restore the symmetry is very small, of order U_s/N. At finite temperature, the symmetry breaking effect competes with the thermal fluctuations, which gives a range of q of order k_BT/N where the symmetry is restored. In previous experimental realizations of spin-1 Bose-Einstein condensates, the atom number was on the order of 10^6. For typical temperatures of a few tens of nK, the collapse to a nematic state happens for a field of a few mG, which makes the spin fluctuations very hard to observe just because of the ambient magnetic field noise. In this case, the symmetry is effectively spontaneously broken. In our experiment we take advantage of our quite small atom number (around 5.10^3) which shifts the transition between 30 and 100 mG (depending on the temperature). This level of magnetic field can be achieved experimentally with a reasonable control (of a few mG) without any active stabilization. The experimental observation of the transition is presented in the next chapter.

4.4 Conclusion

In this chapter we introduced the notion of fragmentation in Bose-Einstein condensates and studied its occurrence in a single-mode spin-1 Bose gas. We showed that the spin fragmentation of a spinor condensates is a direct consequence of the rotational symmetry of the Hamiltonian that manifests itself in anomalously large fluctuations of the spin populations. The fragmentation actually survives at finite temperatures and in the presence

of a small enough magnetic field, although the rotational symmetry is in this case broken. We demonstrated these results using first a diagonalization of the spin Hamiltonian. We then introduced the numerically much more convenient broken-symmetry approach that describes the spinor gas at low temperature by a thermal mixture of mean-field states: the $SU(3)$ coherent states. These generalized coherent states have remarkable properties in the limit of large particle number, which makes the method very efficient. It also provides an intuitive picture for the survival of the spin fluctuations at finite magnetic field in terms of a finite size effect in a symmetry breaking phenomenon.

In the next chapter we will present the observation of spin fragmentation in our experimental system. We will then use the results that we derived here for the moments and the distribution of the population n_0 within the broken-symmetry theory to analyze these observations.

Chapter 5

Observation of spin fragmentation and spin thermometry

In chapter 3 we presented a measurement of the equilibrium spin state of spin-1 condensates of Sodium as a function of the applied magnetic field and of the magnetization of the atomic sample. We concluded that our experimental data were reproducing well the mean-field prediction. Actually, in the region of low magnetic field and zero magnetization we observed anomalous spin fluctuations: when we prepared clouds under these conditions, the spin distribution seemed to take all possible configurations between having all the atoms in the $|m_F = 0\rangle$ state (and none in the $|m_F = \pm 1\rangle$ states) and having all the atoms in the $|m_F = +1\rangle$ and $|m_F = -1\rangle$ states, as illustrated by figure (5.1). These fluctuations were associated with a significant depletion of the average spin population n_0. On the contrary, for larger values of the magnetic field we consistently measured that almost all the atoms accumulated in the $|m_F = 0\rangle$ state (see figure (5.2)), as expected from the mean-field theory.

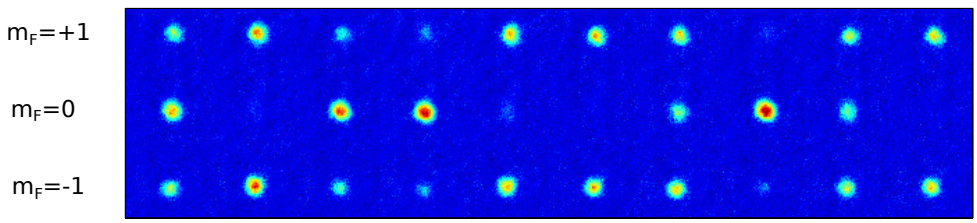

Figure 5.1: A serie of 10 experimental images after a Stern-Gerlach separation of the three spin states and absorption imaging when the applied magnetic field during the hold time is zero ($q = 0\,\mathrm{Hz}$). In each case the experimental sequence is exactly the same. The magnetization is zero (within 2%) in each realization (as many atoms in the $|m_F = +1\rangle$ and$|m_F = -1\rangle$ states) but the distribution of the population within the three spin states fluctuates strongly.

As we explained in chapter 4, the fluctuations at low magnetic field and zero magnetization express the spin fragmentation of the condensate. As the naive mean-field theory is not able to describe them, we developed a theory based on $SU(3)$ coherent states to

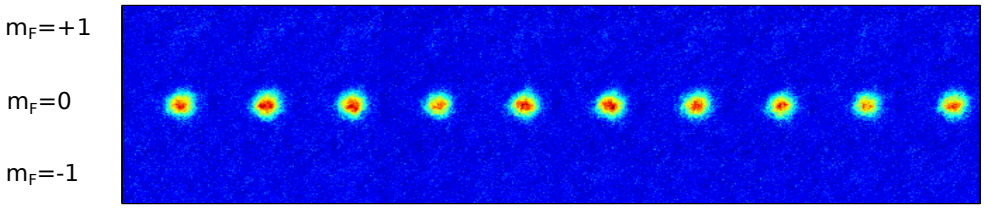

Figure 5.2: A serie of 10 experimental images after a Stern-Gerlach separation of the three spin states and absorption imaging when the applied magnetic field is 850 mG ($q = 200\,\mathrm{Hz}$). Almost all the atoms are in the $|m_F = 0\rangle$ spin state, the fluctuations are extremely reduced.

describe the spin state of the condensate at low temperature (low meaning here that the effect of the non-condensed atoms is negligible). The temperature we introduced in this theory characterises the distribution of the spin state of the condensate in the spectrum of collective spin excitations. We call it the spin temperature. However, experimentally a sizeable fraction of the atoms occupy uncondensed modes, and their effect cannot be neglected. The distribution of these atoms in the spectrum of spatial excitations is characterised by temperature that we denote as kinetic temperature. We expect that in complete thermal equilibrium, the spin and kinetic temperatures equalize. Yet we have found that our observations could not be described by a single temperature characterising both the condensate and the thermal fraction. Rather, we have to consider two different temperatures.

We present in this chapter a detailed experimental investigation of the phenomenon of fragmentation in a spin-1 Bose gas in this framework. We observe the transition from a fragmented condensate to a mean-field state as the magnetic field is increased and analyze these experimental results using the broken-symmetry theory presented in chapter 4. From the study of the measured distributions of n_0 and m_z we are able to extract the spin temperature. In the last part of this chapter we compare it to the kinetic temperature obtained from another method and discuss the observed differences.

5.1 Observation of spin fluctuations

5.1.1 Experimental sequence

The anomalous spin fluctuations are a consequence of the rotational symmetry of the system, which implies that they arise for very low magnetizations. The first step of our experimental sequence is to prepare a zero-magnetized atomic cloud using the spin mixing technique at high temperature described in chapter 2. This way we produce clouds with an average magnetization equal to zero within 2% (the average value of the magnetization varies between different sets of data due to fluctuations in the preparation step). The typical width of the magnetization distribution is 2 to 3%. This width is determined by the experimental preparation (in particular the evaporation could be responsible for some broadening of the magnetization distribution, as atoms are almost equally removed from the three spin states)[1].

[1]We cannot use the two-step spin filtering described in section 2.3.3 to purify the magnetization of the cloud: it would bring the system far from its equilibrium, whereas this it what we aim at. This is not

After the depolarization we perform the two-step evaporation. We stop the evaporation at a chosen point in the second ramp, thus varying the kinetic temperature of the cloud. We explore the regime from a trap depth where the condensed fraction is around 0.4 until full evaporation, where the condensed fraction is around 0.9. At the beginning of the evaporation the magnetic field is ramped to some chosen value that determines the quadratic Zeeman effect q. The field enters the Hamiltonian through its amplitude only. We experimentally confirmed after a full evaporation that the observed fluctuations and depletion were independent on the direction of the field. For each axis we applied the field in the two directions and checked the symmetry of the fluctuations relatively to the point of zero field. We then chose to always set the magnetic field on the x axis in one direction. All the results presented in the following were obtained in this configuration. To explore entirely the transition from a fragmented state to a mean-field state, we need to scan the parameter $\eta = N_c q/k_B T_s$ (N_c being the number of condensed atoms) from 0 to approximately 100 (where for small average magnetizations the fluctuations are expected to vanish and the atoms to accumulate in the spin state $m_F = 0$, as shown in figure (4.3)). For our atom number $N \sim 7000$ and a spin temperature $T_s \sim 100\,\mathrm{nK}$ (order of magnitude of the kinetic temperature T_k) the transition is expected to happen for a magnetic field of a few mG, a regime where we have a good control of the applied field.

At the end of the evaporation we hold the atoms in the trap for 6 s, to make sure the equilibrium state is reached. This equilibration time was determined in the same way as explained in section 3.2.1 for the measurement of the phase diagram. During the hold time, the depth of the trap is kept constant and equal to its value when the evaporation was stopped. At the end of this period, we perform the Stern-Gerlach separation[2] and image the three clouds. By repeating the experiment we can measure the mean value of the population in the $m_F = 0$ state and its variance, which illustrate the fragmentation of the system. The results are presented in the next section.

5.1.2 Data acquisition

To study the evolution of our spinor condensates from a fragmented condensate to a singly condensed mean-field state we measure the mean value and variance of the population n_0 for different values of the applied magnetic field. To correctly estimate these quantities, we have to accumulate large sets of data. However the measured values may change if we accumulate data over a long time, because of drifts of experimental conditions (of ambient magnetic field in particular). We thus have to determine how many realizations are required for the estimation of the moments of n_0 to converge, and restrict to these numbers to avoid drift issues. For large magnetic fields we expect that the estimators converge fast, for the system is close to a mean-field state: almost all the atoms are in the $|m_F = 0\rangle$ state and the fluctuations are small. For values of the field closer to zero the number of needed observations is much larger. To determine the number of observation we need, when taking the data we monitor the evolution of the mean and variance of n_0

a very serious concern: as we have seen previously, the non-zero average of the magnetization and the finite-size of its distribution are taken into account by the broken-symmetry analysis with $SU(3)$ coherent states and the spin fragmentation survives at the small average magnetization we consider.

[2]During this step, the magnetic field (and so the quadratic Zeeman effect) at the position of the atoms is changed while the three clouds still overlap (gradient and bias field needed to perform the Stern-Gerlach separation). However this happens on a much to short time scale (7 ms) for the atoms to respond to this change.

as a function of the number of points. We decide to stop the acquisition when they do not vary by more than 5% in the 10 last realizations. This procedure is shown in figure (5.3).

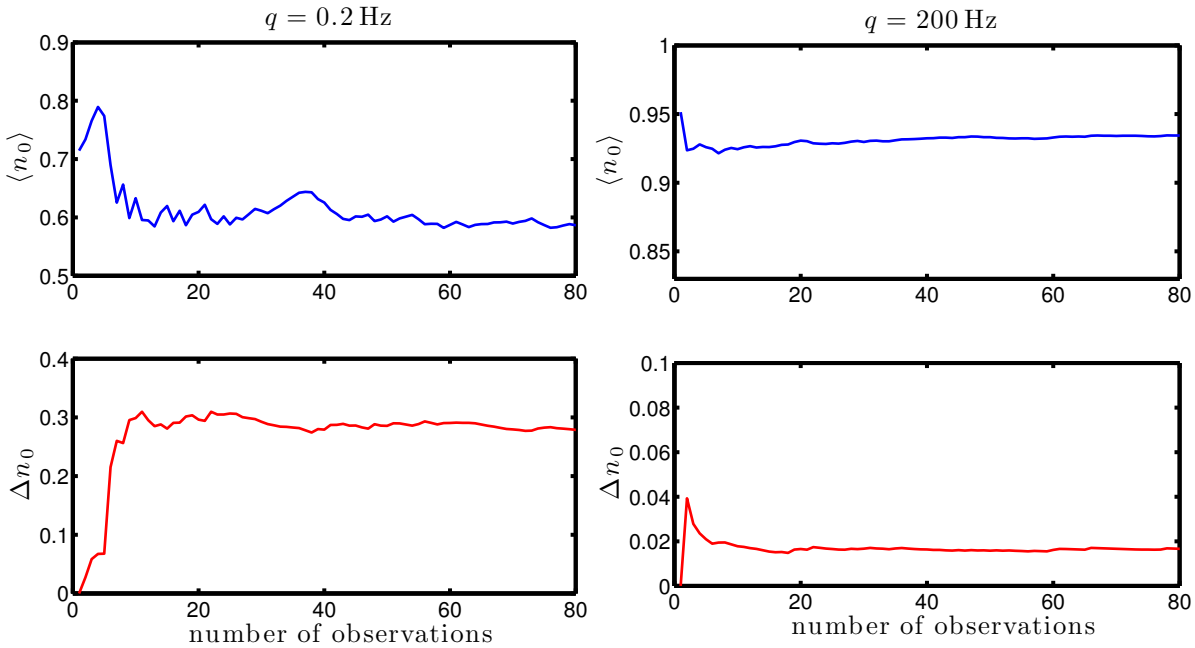

Figure 5.3: Evolution of the estimated mean value (blue) and standard deviation (red) of n_0 for two different values of the QZE q as we accumulate data. The x axis is the number of experimental realizations considered to compute the two moments. The moments of n_0 reach a steady regime faster for larger values of q. In the case $q = 200$ Hz, about 20 runs are enough to reach a steady-state, whereas for $q = 0.2$ Hz about 50 are required.

5.1.3 Measured moments of n_0

We measure the evolution of the moments of the population n_0 at various kinetic temperatures by stopping the evaporation at different points. The results at two evaporation times (975 ms and 700 ms) are shown in figures (5.4) and (5.5). At both times we observe when q increases the drop of the depletion and of the fluctuations of n_0 which reveal the transition from a fragmented to a mean-field spin state. We show in figures (5.4) and (5.5) the complete measured distributions of n_0 for a low value of q ("before" the transition) and for a large value of q ("after" the transition). The qualitative behavior we describe here is observed at all evaporation times.

Using the broken-symmetry approach we calculated in chapter 4 the behavior of the moments of n_0 for a vanishing average magnetization (which is the situation we try to reproduce) and for an unconstrained distribution of the magnetization (see figure (4.8)). We found in particular the values at zero field: $1 - \langle n_0 \rangle = 0.66$, $\Delta n_0 \approx 0.3$ and at large field: $1 - \langle n_0 \rangle = \Delta n_0 = 0$.

However, two main additional effects result in a deviation of our data from these

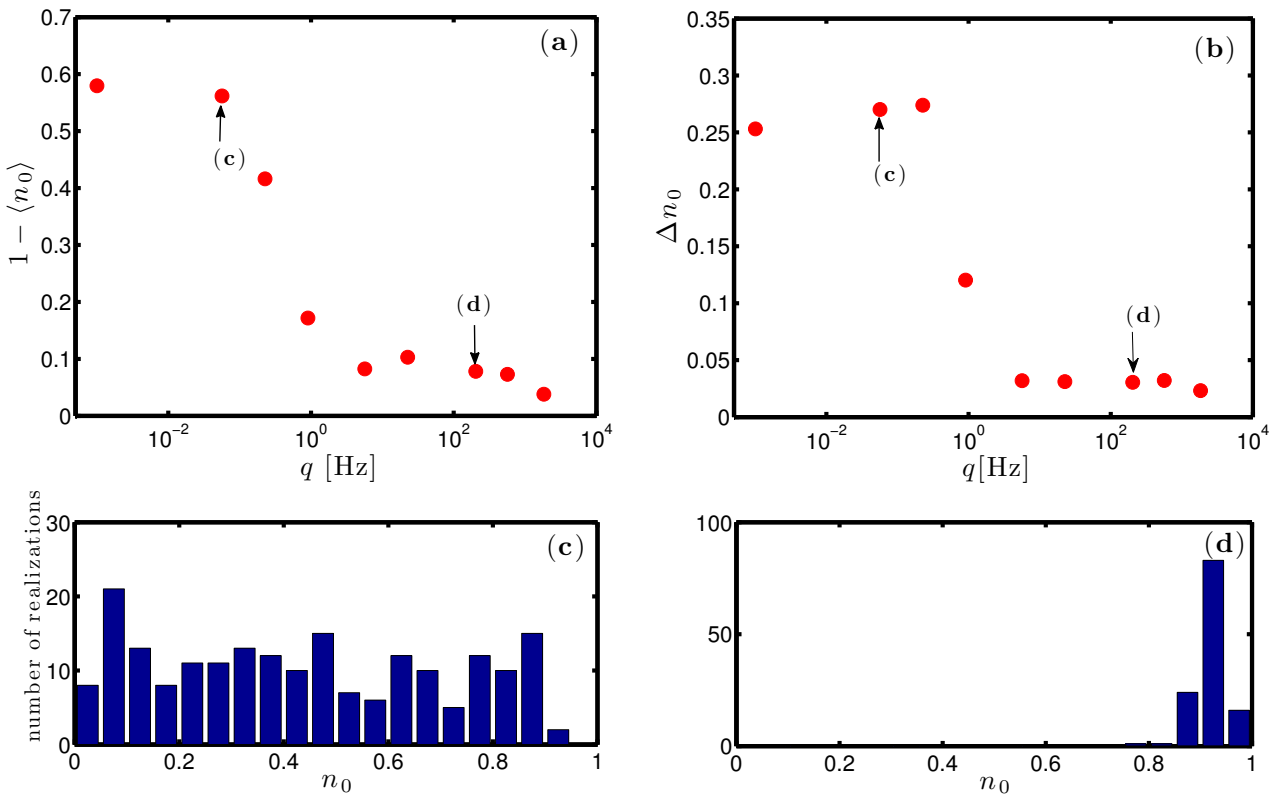

Figure 5.4: Measured average depletion (figure (**a**)) and standard deviation (figure (**b**)) of the population n_0 as a function of the QZE q, after 975 ms of evaporation. The complete distributions of the population n_0 measured at $q = 6\,\text{mHz}$ and $q = 200\,\text{Hz}$ are shown in histograms (**c**) and (**d**) respectively. We use 20 bins.

predictions. First, not all the atoms are condensed (which is the situation described by the broken symmetry theory). The thermal component is expected to display a "standard" statistical behaviour with small fluctuations. Second, our preparation of the magnetization is not perfect, meaning that the average magnetization of our samples is not zero but a few percent (up to 3%). Finally, the distribution of the magnetization is constrained: its conservation by the spin exchange collisions indeed prevents the magnetization to relax to a thermal equilibrium. We now identify the effects of these experimental conditions on the moments of n_0.

Measured depletion of n_0

We first focus on the depletion of n_0. As q increases it drops from a high value, always close to 0.60, to a lower finite value which depends on the evaporation time. We discuss the case $q = 0$ and the asymptotic regime.

We consider the effect of the thermal atoms. We note n_0^c and n_0^{th} the relative populations of the $|m_F = 0\rangle$ state in the condensate and in the thermal fraction. n_0^c is normalized to the number of condensed atoms and n_0^{th} to the number of thermal atoms. We note f_c the condensed fraction. We have

$$n_0 = f_c n_0^c + (1 - f_c) n_0^{th} \tag{5.1}$$

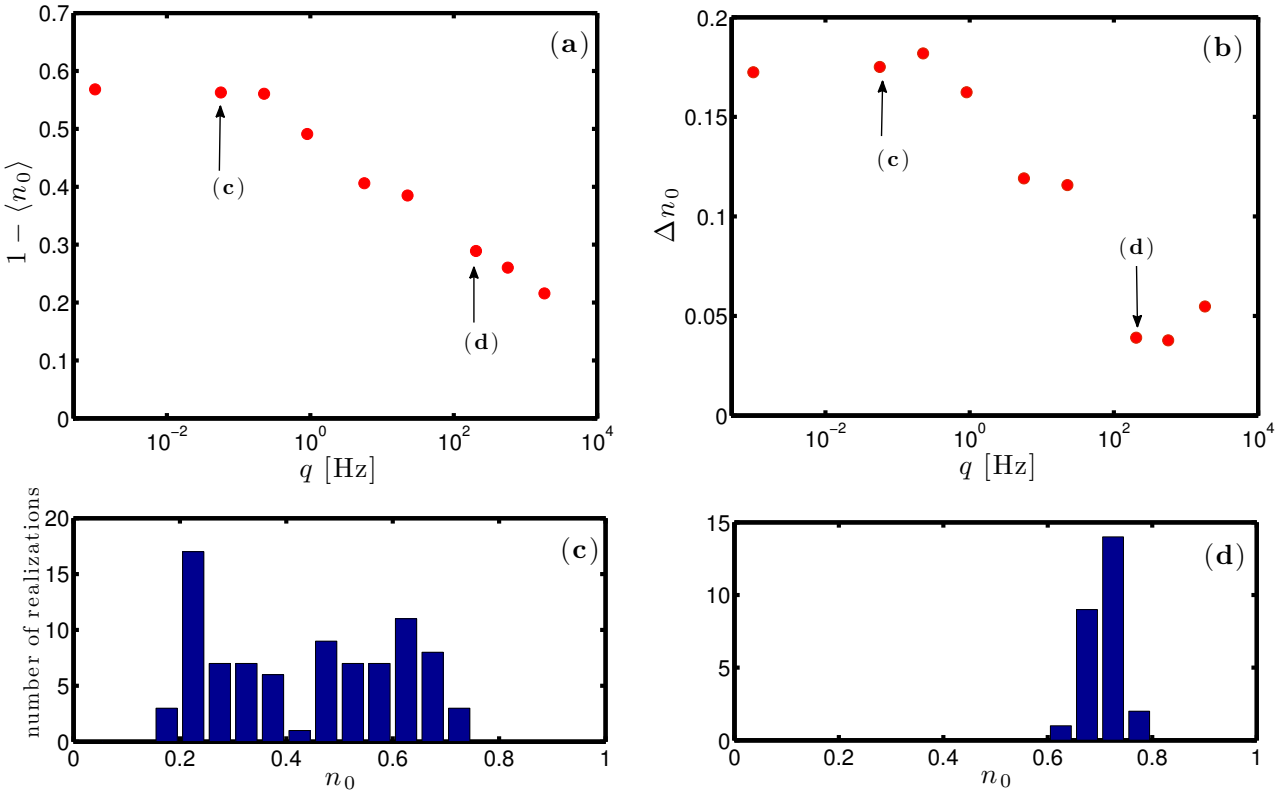

Figure 5.5: Measured average depletion (figure (**a**)) and standard deviation (figure (**b**)) of the population n_0 as a function of the QZE q after 750 ms of evaporation. As in figure (5.4), the complete distributions of the population n_0 measured at $q = 6\,\text{mHz}$ and $q = 200\,\text{Hz}$ are shown in histograms (**c**) and (**d**) respectively. The presence of the thermal fraction is revealed by the reduced number of values the population n_0 can actually take.

In the following we make the simplifying assumption that the distribution of the non-condensed atoms is independent of q and isotropic: we then have $n_0^{th} = 1/3$. This assumption is supported by an Hartree-Fock model that shows that in the range of q we consider, the thermal fraction is to a good approximation isotropic. Only at large q does the quadratic Zeeman effect force the thermal atoms in the $|m_F = \pm 1\rangle$ states to condense in the $|m_F = 0\rangle$ state.

At $q = 0$, in the case where the magnetization is unconstrained and vanishes in average, the condensed fraction is also isotropic and even in the presence of the thermal fraction we expect $1 - \langle n_0\rangle = 0.66$. The lower value we observed is actually mainly explained by the distribution of the magnetization. Indeed, the reduction of $1 - \langle n_0\rangle$ at $q = 0$ is consistent with an average magnetization of 2 to 3% (see figure (4.3)).

At large q the condensed atoms accumulate in $|m_F = 0\rangle$ and $n_0^c \to 1$. Due to the presence of the thermal atoms, a plateau then appears in the depletion of n_0 at large q, at a value:

$$1 - n_0 \underset{q\to+\infty}{\longrightarrow} \frac{2}{3}(1 - f_c) \tag{5.2}$$

The non-zero average of the magnetization also results in a finite asymptotic value of the depletion (see figure (4.3)) but given the magnetizations we measure we expect this effect to be negligible compared to the offset due to the thermal fraction. The non-zero value of the depletion of n_0 at large q and its dependence on the evaporation time is then mainly explained by the presence of thermal atoms. In the case of the two evaporation times presented in figures (5.4) and (5.5) we observe a plateau at $1 - \langle n_0 \rangle \simeq 0.1$ and 0.2 respectively, corresponding to condensed fractions $f_c = 0.85$ and $f_c = 0.7$.

After the first plateau we just mentioned, we observe in figure (5.4) that the measured depletion decreases again. This is explained by the fact that at very high q ($\sim 10^3$ Hz) the quadratic Zeeman effect forces thermal atoms in the $|m_F = \pm 1\rangle$ states to condense in the $|m_F = 0\rangle$ state [81]. The thermal fraction is then not isotropic any more.

Measured fluctuations of n_0

We now turn to the standard deviation of n_0. As a function of q, the observed behavior of the standard deviation is the following: first a region at low q where it stays almost constant, then it drops to a lower value and stay constant there for higher values of q (see figures (5.4) and (5.5)). This evolution is qualitatively expected in the SMA theory.

Let us consider the effect of the thermal fraction. The fluctuations of the thermal atoms are Poissonian. Their contribution is then on the order of $\sqrt{(1 - f_c)/3N} < 1\%$, and is negligible compared to the fluctuations of the condensate (and anyway below our sensitivity). From expression (5.1) we then obtain

$$\Delta n_0 \approx f_c \Delta n_0^c \tag{5.3}$$

The presence of the thermal fraction thus reduces the observed fluctuations at $q = 0$.

Looking at figure (4.3) we note that the distribution of the magnetization also has a significant effect on the value of the fluctuations at $q = 0$. For the two evaporation times presented in figures (5.4) and (5.5) we measure $\Delta n_0 = 0.26$ (evaporation time of 975 ms) and $\Delta n_0 = 0.17$ (evaporation time of 750 ms). Assuming that the deviation of the measured value of Δn_0 at $q = 0$ to the SMA prediction is due to the presence of thermal atoms only, and using the condensed fractions deduced previously from the analysis of the depletion of n_0, we calculate from the relation (5.3) $\Delta n_0 \approx 0.25$ and $\Delta n_0 \approx 0.21$. The first value seems to be compatible with the measurement, but not the second one. The data at 975 ms can then be explained by the presence of the thermal atoms only, but for the data at 750 ms we need to take the distribution of the magnetization into account.

At large q, the fluctuations of n_0 are expected to collapse to zero. This is not what we observe. The measured values of a few percent can be explained by our imaging noise (see section 2.2.5).

5.2 Statistical analysis of the distributions of n_0 and m_z

At each evaporation time and each value of the magnetic field we accumulated a large enough set of observations to obtain a reasonable estimation of the probability distribution of the population n_0 and of the magnetization m_z. The broken-symmetry theory gives us an expression of the joint distribution of these two variables that depends on the spin

temperature T_s, the interaction energy U_s and the quadratic Zeeman energy q. We present here a model based on this theory that accounts for the thermal fraction. By fitting our experimental data with this model we are able to extract values for the spin temperature and the condensed fraction.

5.2.1 Model and method

Joint distribution in the broken-symmetry theory

We recall some results of chapter 4. The $SU(3)$ coherent states we use to describe the spin state of the condensate are parametrized by their average population n_0 and magnetization m_z and by two phases Θ and α:

$$|\boldsymbol{\zeta}\rangle = \begin{pmatrix} \sqrt{\frac{1-n_0+m_z}{2}}e^{i(\Theta+\alpha)/2} \\ \sqrt{n_0} \\ \sqrt{\frac{1-n_0-m_z}{2}}e^{i(\Theta-\alpha)/2} \end{pmatrix} \tag{5.4}$$

We consider the statistical ensemble of coherent states whose two first moments of m_z are fixed. The "phase-space" density is given by

$$P(\boldsymbol{\zeta}) = \frac{1}{\mathcal{Z}}e^{-\beta\left(\langle\boldsymbol{\zeta}|\hat{H}_s|\boldsymbol{\zeta}\rangle-\gamma_1 m_z+\gamma_2 m_z^2\right)} \tag{5.5}$$

where $\mathcal{Z}$ is the partition function and $\beta = 1/k_B T_s$. We recall the definitions

$$\begin{aligned} \eta &= \frac{N_c q}{k_B T_s} \\ \beta' &= \frac{N_c U_s}{k_B T_s} \end{aligned} \tag{5.6}$$

where N_c is the number of atom in the condensate. The joint probability density distribution of n_0 and m_z in the condensate is found by integrating over the variables Θ and α. We obtain

$$P^c(n_0, m_z) = \frac{1}{\mathcal{Z}}I_0\left(\beta' n_0\sqrt{(1-n_0)^2 - m_z^2}\right)e^{-\frac{\beta'}{2}\left((1+\gamma_2)m_z^2+2n_0(1-n_0)\right)+\eta n_0+\beta'\gamma_1 m_z} \tag{5.7}$$

This distribution has four dimensionless parameters: η, β' and the Lagrange factors γ_1 and γ_2. The Lagrange factors are used to correctly account for the distribution of the magnetization. The parameters we are interested in are η and β'. In each run we know the quadratic Zeeman effect q and the total atom number N. Provided we can infer the condensed fraction, the knowledge of η and β allows one to deduce the physical quantities T_s and U_s.

Joint distribution at finite kinetic temperatures

We now consider the presence of thermal atoms, and we make as before the assumption that they are equally distributed among the three spin states. As discussed already, the spin fluctuations of the thermal atoms (scaling as $\sqrt{N}$ for an ideal gas) are expected to be much smaller than the ones in the condensate. The joint distribution of n_0 and m_z in the thermal fraction can then be approximated by a Dirac distribution:

$$P^{th}(n_0, m_z) = \delta(n_0 - 1/3)\delta(m_z) \tag{5.8}$$

This implies that the magnetization of the atomic cloud entirely come from the condensate. We know the joint distributions in the condensate and in the thermal fraction. We have the relations:

$$\begin{aligned} n_0^{tot} &= f_c n_0^c + (1-f_c) n_0^{th} \\ m_z^{tot} &= f_c m_z^c + (1-f_c) m_z^{th} \end{aligned}$$

The distribution in the total cloud is obtained by convoluting the two distributions of the condensate and of the thermal fraction. One obtains

$$P^{tot}(n_0^{tot}, m_z^{tot}) = P^c\left(\frac{1}{f_c}(n_0^{tot} - (1-f_c)/3), \frac{1}{f_c} m_z^{tot}\right) \tag{5.9}$$

Because we make the simple assumption of an isotropic thermal fraction, its inclusion in the model only adds one parameter: the condensed fraction f_c. In our experimental data we know the quadratic Zeeman energy q and the total atom number N. We then parametrize the joint distribution by the five independent parameters $T_s, \beta', \gamma_1, \gamma_2$ and f_c. We can thus fit the measured distribution at a given evaporation time and extract a spin temperature T_s and a condensed fraction f_c.

We use the maximum likelihood method to determine the temperature that best describes our data in the model we detail in the following. From this method we are also able to get confidence intervals for the fitted temperature.

Sources of noise

Because the thermal distribution P^{th} is a Dirac distribution, the convolution with the SMA distribution gives a "contracted" SMA distribution: similar to the SMA distribution but defined on a support $[(1-f_c)/3; (1+2f_c)/3] \times [-f_c; f_c]$. The resulting distribution $P(n_0)$ of n_0 alone (deduced by integrating over m_z) vanishes for n_0 close to 0 or 1, and is supposed to rise with sharp edges (see 5.6). This prediction is not verified for our measured distributions of n_0, which exhibit smooth wings. This smoothening of the distribution can be explained by various effects.

First the condensed fraction is not fixed but fluctuates from shot to shot due to fluctuations of the temperature and of the atom number. For an ideal gas at temperature T one has $f_c = 1-(T/T_c)^3$ with $T_c^3 \sim N$. Second, we know that the imaging has some noise: the atom numbers we count in each of the three spin states are not the 'true' atom numbers but are distributed around it with some variance, which modifies the distribution of the relative populations we measure. Third, the thermal fraction is not perfectly isotropic: the populations of the three spin states in the thermal fraction fluctuates around isotropic mean values (even if we expect these fluctuations to be small), and its true joint distribution is not a Dirac distribution.

Considering these three different effects altogether would add many parameters and would lead to a very complex fitting procedure. To evaluate their relative significance we look how they individually affect the distribution of n_0. We suppose successively gaussian fluctuations of the condensed fraction, a gaussian noise of the imaging and a thermal fraction which follows a multinomial law of mean (1/3,1/3,1/3). We consider the effect on the distribution of n_0 in the case $q = 0$ and $\langle m_z \rangle = 0$. The results are shown in figure (5.6). The three effects cause a broadening and a smoothening of the distribution of n_0.

For realistic experimental conditions (typical fluctuations of f_c of 5% and imaging noise of 50 atoms per component), the strongest effect is due to the fluctuations of the condensed fraction. Practically, the measured distributions of n_0 are displayed in histograms. For a typical number of bins of 20, the other effects will no be visible, because the resulting broadening is smaller than the bin size. Therefore we restrict our model to gaussian fluctuations of the condensed fraction

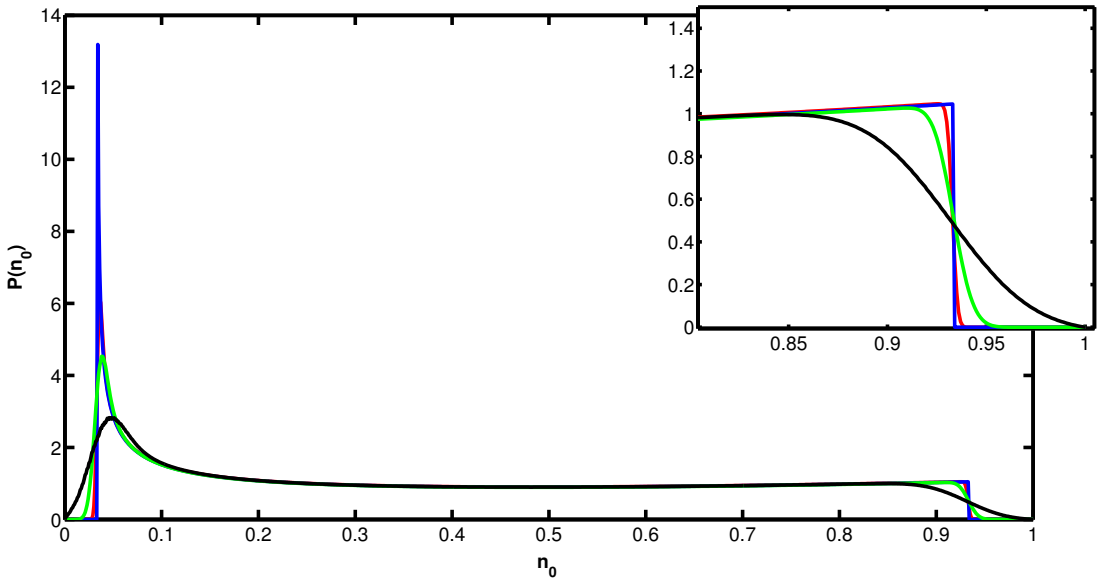

Figure 5.6: Probability densities of n_0 calculated for $\eta = 1$ in the following cases: in blue: fixed condensed fraction of 0.9, isotropic thermal fraction and no imaging noise; in red: fixed condensed fraction of 0.9 and a gaussian-distributed thermal fraction with central value 1/3 and variance $\sigma^2 = 2/9N_{th}$ (limit of the multinomial law for large number of variables); in green: fixed condensed fraction of 0.9, isotropic thermal fraction and gaussian imaging noise of standard deviation 50 atoms; in black: isotropic thermal fraction but gaussian-distributed condensed fraction, centered at 0.9 with $\sigma = 0.05$. In all cases, the total atom number is $N = 5000$.

The maximum likelihood method

In our model, the joint probability density of n_0 and m_z now depends on six parameters:

- the average condensed fraction $\bar{f}_c$
- the standard deviation of the condensed fraction σ_{f_c}
- the spin temperature T_s
- the dimensionless parameter β'
- the two Lagrange factors γ_1 and γ_2

We define $\boldsymbol{\theta} = (T_s, \beta', \gamma_1, \gamma_2, \bar{f}_c, \sigma_{f_c})$ the parameters vector. We note the joint probability density $P(n_0, m_z|\boldsymbol{\theta})$. To infer the values of the parameters that best describe our data within our model and their confidence intervals we resort to the maximum likelihood

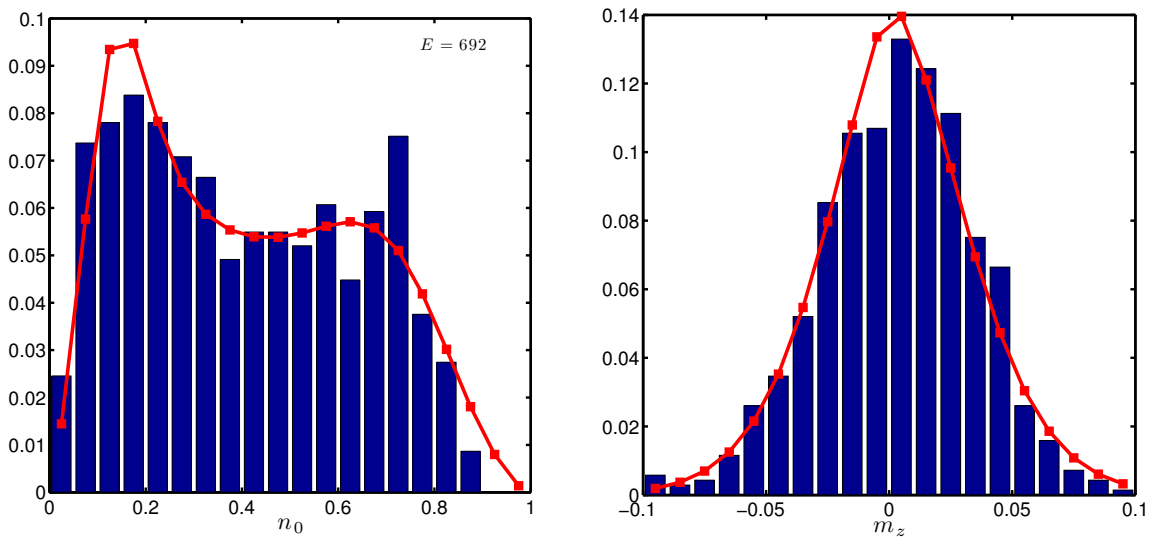

Figure 5.7: Distribution of n_0 (left) and m_z (right) for $q = 0$. The blue histograms are experimental observations, the red curves are the result of the fit using the maximum likelihood method. The fit is done on the joint distribution of n_0 and m_z. The fitted joint distribution is integrated over one variable to get the marginal distribution of the second one. For the particular value $q = 0$, since then $\eta = 0$ independent of T_s, the fit procedure does not allow us to extract the spin temperature (the log-likelihood is independent of the value of T_s). That is the reason why in the results we present in the following we only consider $q > 0$. Still in this case we can extract the other parameters. The result of the fit are: $\beta' = 27.7, \gamma_1 = 0.07, \gamma_2 = 7.7, \bar{f}_c = 0.75$ and $\sigma_{f_c} = 0.17$. The quantity E indicates the number of experimental realizations represented in the two histograms.

method.

At a given value of the evaporation time and of the quadratic Zeeman effect q the experiment provide us a set of N_E independent realizations $(n_{0,i}, m_{z,i})$ of the random variable (n_0, m_z). All these observation obey the parametrized probability distribution $P(n_0, m_z|\boldsymbol{\theta})$. To each value of the vector $\boldsymbol{\theta}$ we can associate a quantity called the likelihood $L(\boldsymbol{\theta})$ [97] that is defined by the conditional probability for observing the set $(n_{0,i}, m_{z,i})_{1<i<N_E}$ if the random variables (n_0, m_z) follows the probability density $P(n_0, m_z|\boldsymbol{\theta})$. In the case of independents events, this probability is the product of all the probabilities to observe each of these events:

$$L(\boldsymbol{\theta}) = \prod_{i=1}^{N_E} P(n_{0,i}, m_{z,i}|\boldsymbol{\theta}) \tag{5.10}$$

Given a set of observations, the likelihood measures the validity of the hypothesis that these data follow the probability distribution defined by some parameters $\boldsymbol{\theta}$. If the observed data are probable within this hypothesis, the likelihood will be large, whereas if the hypothesis is doubtful, it will be small. It should be stressed that, unlike a probability density that supposes fixed parameters to describe the chances to observe a set of particular realizations, the likelihood takes the observations as fixed and associate a "probability score" to the various distributions that could have led to them. The likelihood is a mean to compare different hypotheses: only the difference in likelihoods between two events is

meaningful, the absolute value is not. The likelihood is not a probability density of the parameters: in particular it is not normalized.

In the case of independent variables it is actually more convenient to work with the logarithm of the likelihood, which we denote as log-likelihood.

$$\ln[L(\boldsymbol{\theta})] = \sum_{i=1}^{N_E} \ln[P(n_{0,i}, m_{z,i}|\boldsymbol{\theta})] \tag{5.11}$$

The logarithm is monotonically increasing so that the same ordering of log-likelihoods holds that exists for likelihoods.
To speed up the analysis, the experimental data are binned in 2D histograms such that all the events in the same bin have approximately the same likelihood. For the bin (j, k) we note $d_{j,k}$ the number of observed entries in the bin, $t_{j,k}$ the number of expected entries and $\bar{n}_{0j}$ and $\bar{m}_{zk}$ the central values of n_0 and m_z. The bins all have the same size Δ. We have:

$$t_{j,k}(\boldsymbol{\theta}) = N_E P(\bar{n}_{0j}, \bar{m}_{zk}|\boldsymbol{\theta})\Delta \tag{5.12}$$

If the number of bins is large enough, then the number of entries in each bin is small compared to the total number of entries, and the distribution of entries in one bin can be described by a Poisson law. The probability of observing $d_{j,k}$ events where the mean is $t_{j,k}$ is given by:

$$L_{j,k} = \frac{t_{j,k}^{d_{j,k}}}{d_{j,k}!} e^{-t_{j,k}} \tag{5.13}$$

so that the log-likelihood reads:

$$\ln[L(\boldsymbol{\theta})] = \sum_{j,k} \ln L_{j,k} \tag{5.14}$$

$$= \sum_{j,k} (-t_{j,k} + d_{j,k} \ln t_{j,k} - \ln(d_{j,k}!)) \tag{5.15}$$

The dependence in $\boldsymbol{\theta}$ is carried by $t_{j,k}$, and we can drop the terms $\ln(d_{j,k}!)$ that only act as on offset. In our case, the vector $\boldsymbol{\theta}$ is allowed to vary continuously in a three-dimensional space, meaning we have to consider an infinite number of possible probability densities of n_0. The log-likelihood is a continuous function of $\boldsymbol{\theta}$ and in almost all cases it admits a single maximum. It is then possible, using numerical methods, to find the point in parameters space $\boldsymbol{\theta}_{max}$ where the likelihood reaches this maximum.

Confidence intervals

When the number of observations is large, the likelihood function approaches a gaussian and becomes proportional to the probability density function of the parameters (with an unknown normalization factor). The boundaries of the one-standard deviation confidence interval are then defined by a reduction of the likelihood function by a factor $e^{1/2}$ compared to its maximum value, corresponding to one sigma of the gaussian (and by factors e^2 and $e^{9/2}$ for two and three standard deviations respectively). This is equivalent to a drop of one half of the log-likelihood compared to its maximum value. In the case of a n-dimensional

parameter $\boldsymbol{\theta}$ the confidence interval is a n-dimensional volume defined by the points $\boldsymbol{\theta}$ such that

$$\ln[L(\boldsymbol{\theta})] \leq \ln[L(\boldsymbol{\theta}_{max})] - \frac{1}{2} \tag{5.16}$$

The error interval for one single fit parameter corresponds to the projection of the n-dimensional volume on the relevant dimension. We keep this definition of the error interval for finite number of observations, when the likelihood function is not necessarily Gaussian. This leads to asymmetric error limits.

In the following we present the results of our fit procedure. We checked that these results do not depend on the number of bins we use. We fitted the data using 40, 20 and 10 bins and concluded that the results are compatible within the fit confidence interval.

5.3 Spin temperature and condensed fraction during the evaporation

We fit the measured joint distribution of n_0 and m_z at various evaporation times and various quadratic Zeeman energies q. We are actually limited in the evaporation times we can use by the requirement that the three spin states are spatially well separated after the Stern-Gerlach experiment. For evaporation times shorter than 700 ms, the ballistic expansion of the clouds due to their kinetic temperature is too fast and leads to an overlap of the three clouds. The figures (5.8) and (5.9) show the fitted distributions $P(n_0, m_z)$ for 975 ms and 700 ms of evaporation respectively. The joint distribution is integrated over one of the two variables to obtain the marginal distribution of the other one. We find that our experimental data are well described by our model, which generally supports the idea that the spin of the condensate has reached an equilibrium. In both figures we observe the progressive accumulation of the atoms in $|m_F = 0\rangle$ as q is increased. The fact that at large q the distribution of n_0 becomes peaked at a value lower than $n_0 = 1$ reveals the presence of the thermal fraction. This effect is clearly visible after 750 ms of evaporation where n_0 takes its values in a reduced interval. These figures also confirm that it is important to account for the distributions of m_z, as they vary both in average value and in width between different sets of data (due to uncontrolled fluctuations in the preparation). The figure (5.10) summarizes the results for the spin temperature T_s for all the evaporation times we considered and for various values of q.

We point out that in figure (5.10) we did not represent all the values of q we used. Large values ($\gtrsim 50$ Hz) actually lead to large fitted temperatures (several μK) with huge error bars. The same phenomenon is also sometimes observed for very small values of q ($\lesssim 0.1$ Hz). To justify the choice of discarding these points we note that for large values of $\eta = Nq/k_B T_s$ the distribution of n_0 becomes very peaked close to $n_0 = 1$ (see figure (4.5)), with a typical width in n_0 given by $1/\eta$. At some point this width becomes on the order of the broadening due to the fluctuations of the condensed fraction, which are of a few percents, and the dependence of the distribution in the temperature T_s is blurred. On the other hand the large error bars at low q can be explained by the weak dependence of the distribution of $P(n_0, m_z)$ in η for small values of this parameter. This can be seen for instance in figure (4.3): the two first moments of n_0 vary very slowly in the region $\eta \ll 1$ and are independent of T_s in the limit $q \to 0$ (this is true as long as $T_s \ll NU_s$, which is always the case for us [88]). Small values of q bring the system in this region, where large

changes in T_s then have little effect on the distribution.

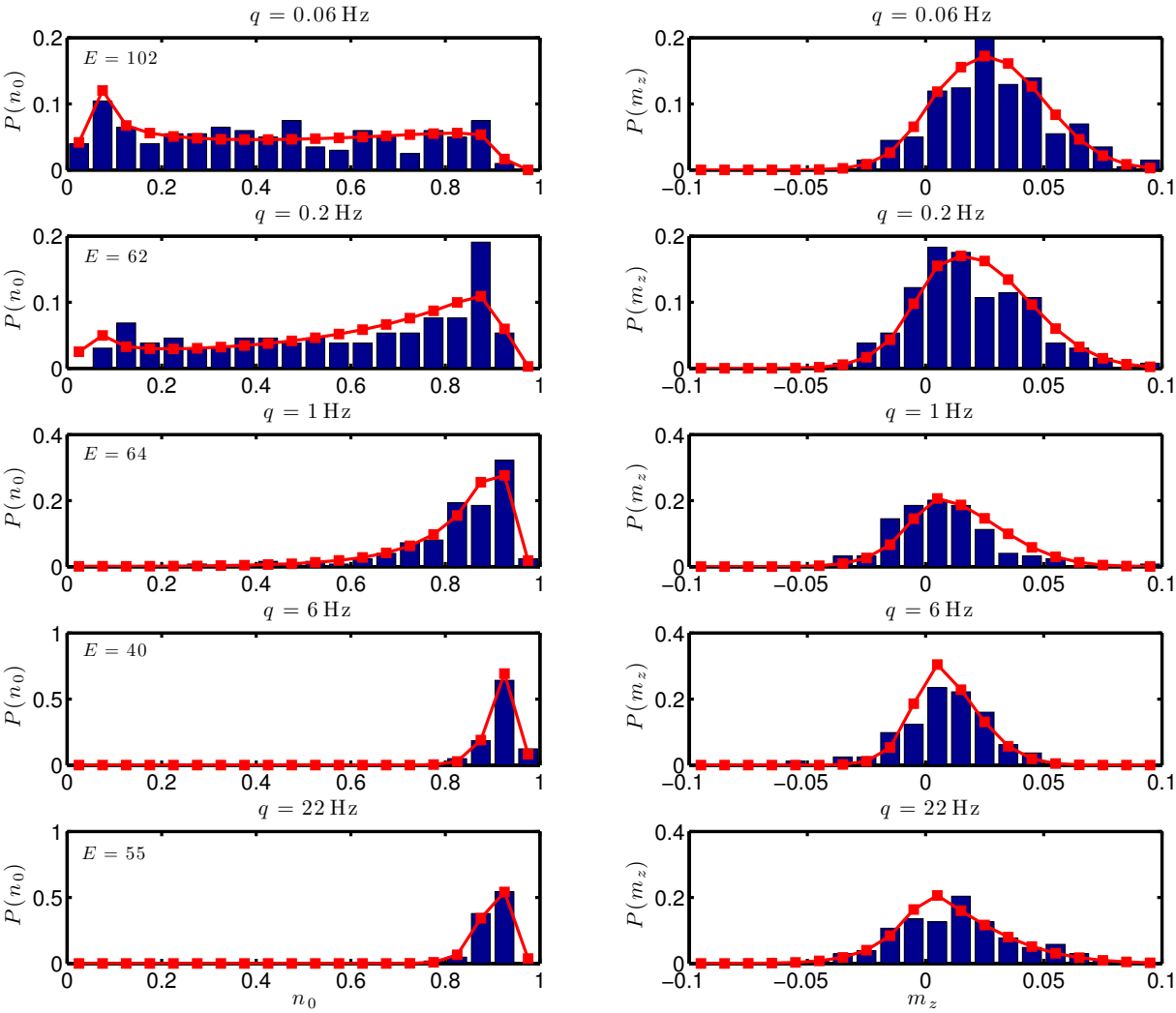

Figure 5.8: Distributions of n_0 (left) and of m_z (right) for an evaporation time of 975 ms and different applied magnetic fields indicated by the value of q. The blue histograms show the experimental data, the red curves show the fitted distribution integrated over m_z to obtain the marginal distribution of n_0 (left) and the fitted distribution integrated over n_0 to obtain the marginal distribution of m_z (right). Two figures on the same line describe the same set of observations. The number of observations E in each set is indicated in the histogram of n_0. We observe the progressive accumulation of the atoms in the $m_F = 0$ state and the narrowing of the distribution of n_0 when q increases. To each value of q corresponds a fitted spin temperature T_s that appears in figure (5.10).

Considering all the evaporation times, we can identify two regimes for the different values of q. First for q less than a few Hz we consistently find spin temperatures ranging from 30 to 100 nK. Then at larger q ($\gtrsim$ 10 Hz) the fitted temperatures increase. This

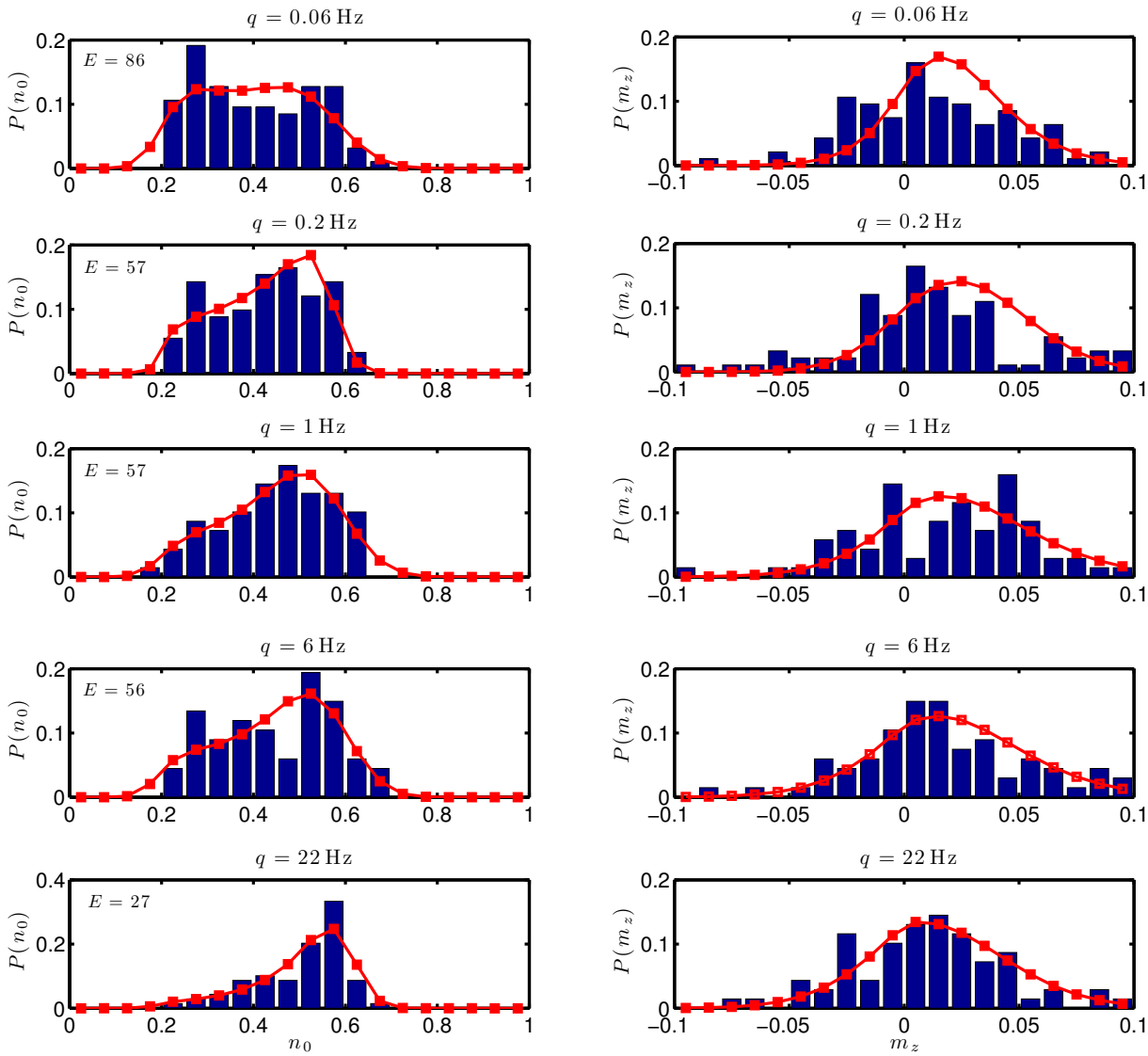

Figure 5.9: Distributions of n_0 (left) and of m_z (right) for an evaporation time of 700 ms and different applied magnetic fields indicated by the value of q. As in figure (5.8) blue histograms are experimental data and red curves are fitted marginal distributions. Two figures on the same line describe the same set of observations. The number of observations E in each set is indicated in the histogram of n_0. The effect of the finite temperature clearly appears in the smaller domain where the distribution of n_0 is not zero. To each value of q corresponds a fitted spin temperature T_s that appears in figure (5.10).

behavior is highlighted in figure (5.11) where the spin temperature is represented as a function of the evaporation time for four values of q (0.2 Hz, 1 Hz, 6 Hz and 22 Hz). For low q (0.2 Hz and 1 Hz) the spin temperature does not change with the evaporation time (in the part of the evaporation ramp we investigate) and is already as low as 50 nK after 700 ms of evaporation. For larger values of q we find larger spin temperatures, which now do decrease during the evaporation. This different behaviour of T_s for different values of q is revealed by figure (5.12) (which shows the same data as figure (5.11)). We note that the

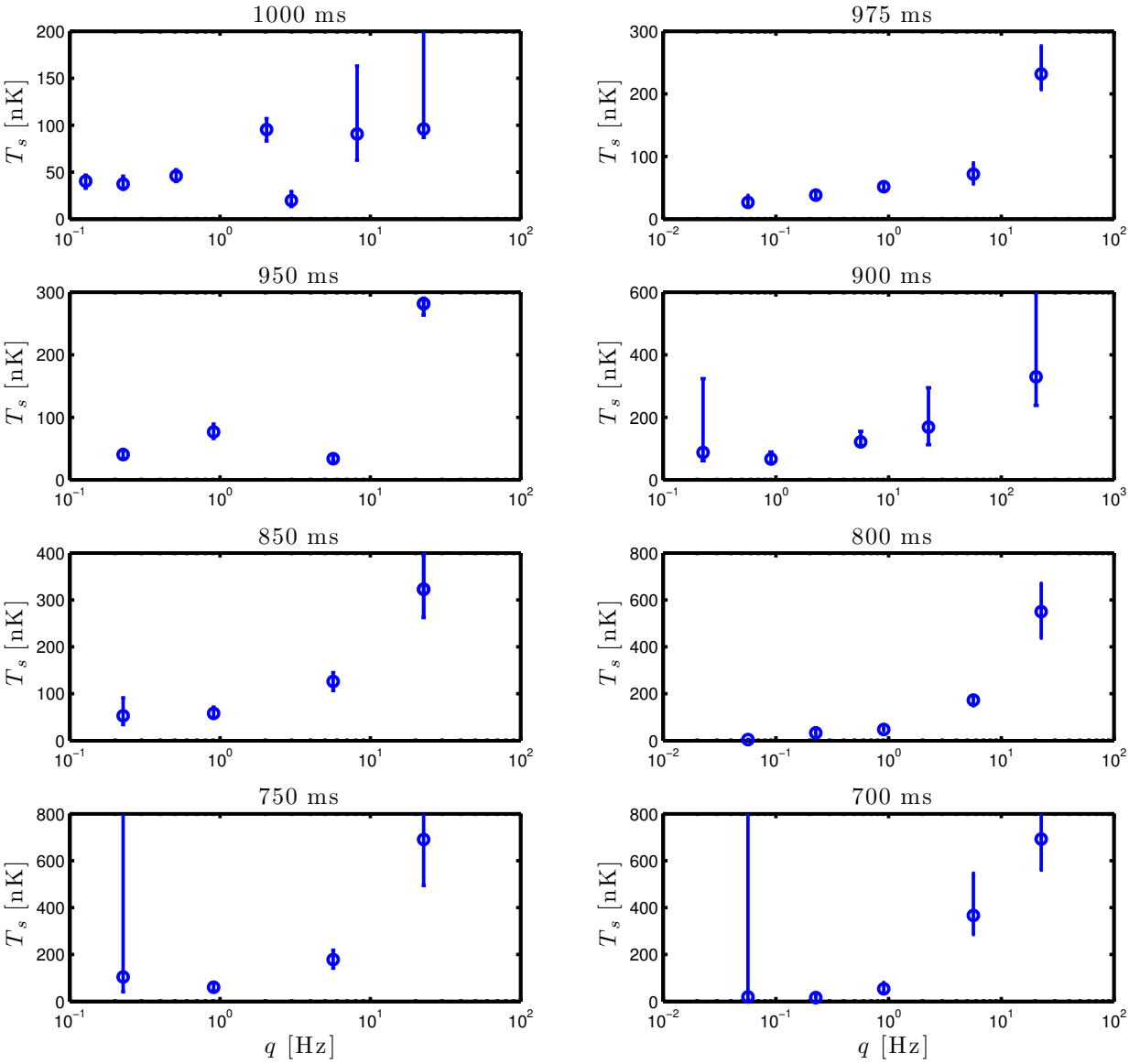

Figure 5.10: Results of the fit for the temperature, at different evaporation time and different quadratic Zeeman energies q. The error bars correspond to one standard deviation.

temperatures fitted at $q = 22\,\mathrm{Hz}$ should be considered carefully for the parameter η fitted at long evaporation times is on the order of the fluctuations of the condensed fraction and our analysis may interpret as fluctuations of the spin of the condensate what is actually preparation noise.

From our fit we also extract a condensed fraction. The figure (5.11 **b**) shows the fitted condensed fraction $\bar{f}_c$ for the different evaporation times and different values of q. The error bar shows the fitted width σ_{f_c} of the distribution of condensed fraction. (It is not the error bar on the fit parameter $\bar{f}_c$ of the fit function). We find values of $\bar{f}_c$ on the order of 0.9

or even more for the longest evaporation times (950, 975 and 1000 ms), and then lower and lower condensed fractions as we reduce the evaporation time, until $\bar{f}_c \approx 0.45$ for 700 ms of evaporation. Thus, the analysis of the distributions of n_0 and m_z gives us access to condensed fractions that we cannot measure with standard techniques (see chapter 2). For a given evaporation time and $q \lesssim 20$ Hz the condensed fraction does not seem to depend on q.

The increase of the condensed fraction with the evaporation time is associated to the

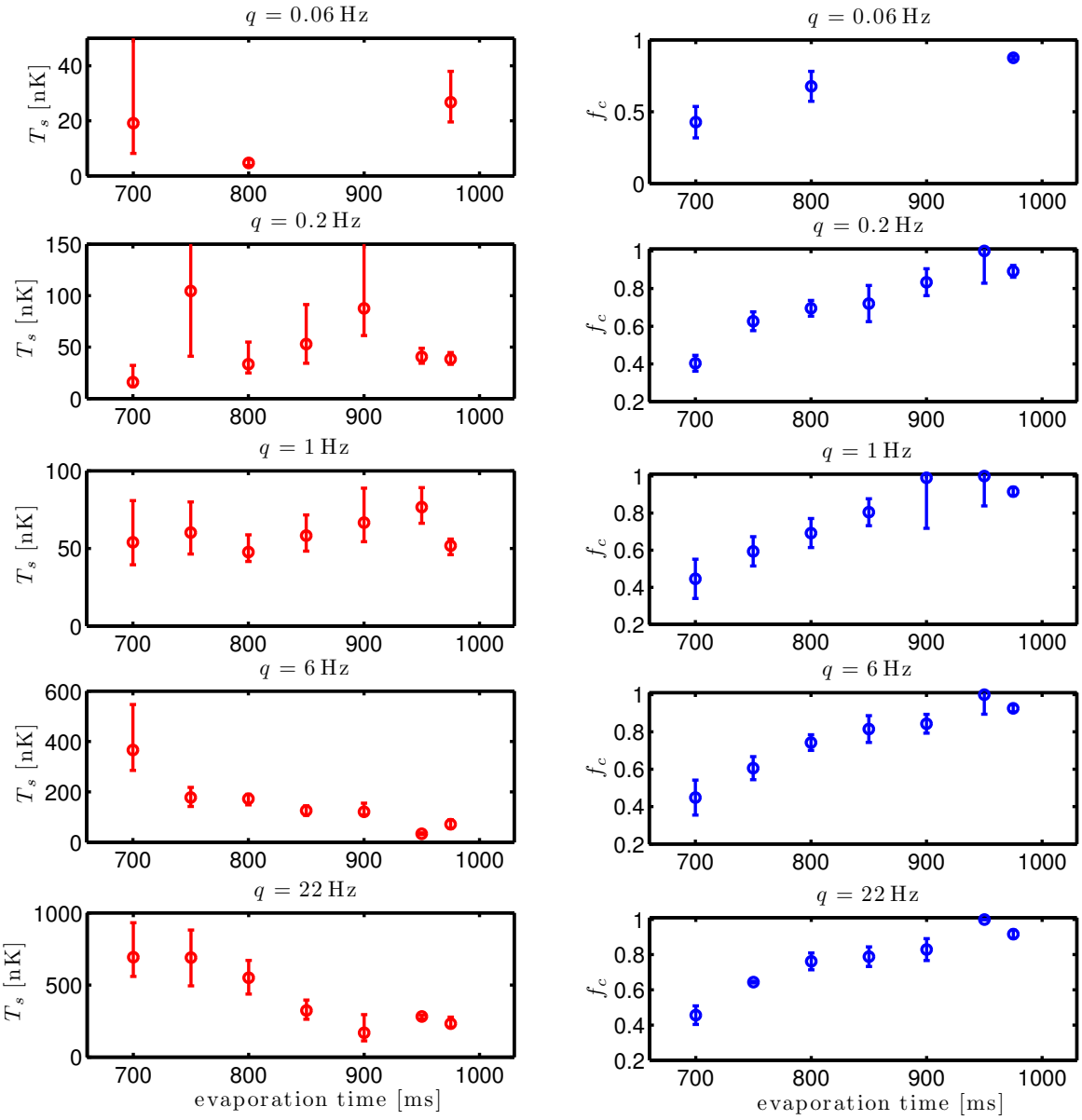

Figure 5.11: Spin temperature T_s (right) and condensed fraction f_c (left) during the evaporation ramp for four values of q. For $q = 0.2$ Hz and $q = 1$ Hz we observe that the spin temperature does not vary during the evaporation and is on the order of 50 nK. For $q = 6$ Hz and $q = 22$ Hz the spin temperature decreases during the evaporation. The condensed fraction always increases during the evaporation, independently of q.

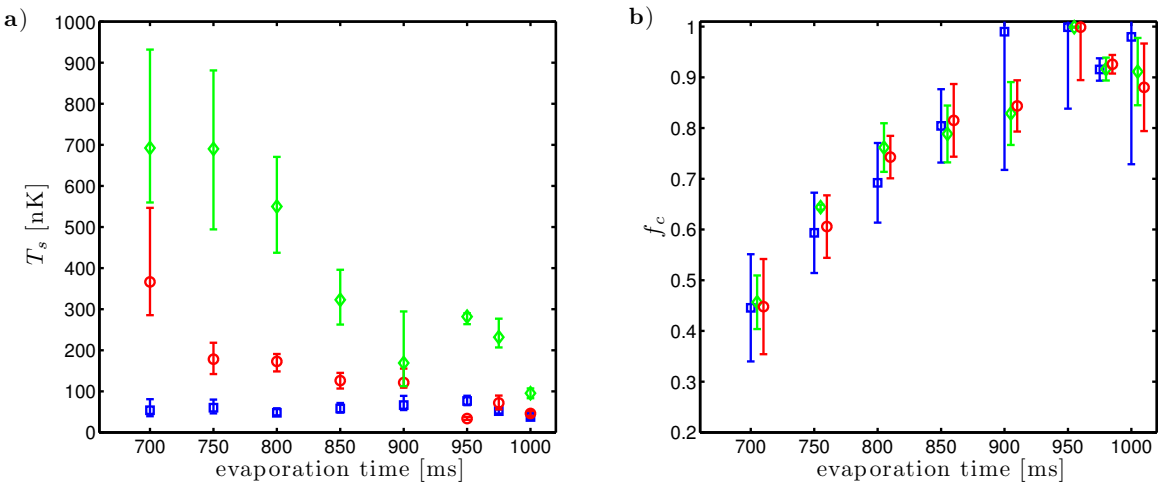

Figure 5.12: **a**): Spin temperature T_s during the evaporation ramp for three values of q: blue: $q = 1\,\text{Hz}$, red: $q = 6\,\text{Hz}$, green: $q = 22\,\text{Hz}$. The different behavior during the evaporation of the spin temperature for different q appears: at low q it is constant and quite low ($\sim 50\,\text{nK}$), while at higher q it decreases and is significantly larger. **b**): Condensed fraction f_c during the evaporation ramp for the same values of q and with the same colour code. The condensed fraction always increases during the evaporation and seems independent of q. The results at different q have been shifted along the time axis for clarity. The evaporation times used were the same for all values of q.

(expected) decrease of the kinetic temperature during the evaporation. However, the spin temperature - at least at low q - behaves differently: it remains constant and takes significantly lower values than the kinetic temperature.

5.3.1 Temperatures at fixed trap depth

To confirm these different behaviors we performed a different experiment. We now consider different runs where the evaporation time is fixed to 1000 ms (corresponding to full evaporation) and where we vary the time during which we hold the atoms in the trap before imaging, and the amplitude of the applied magnetic field. We recall that in the first series of experiments that we described previously, the hold time was set to 6 s to make sure that equilibrium was reached. In this serie of experiments we change it from 1 s to 15 s [3]. For each value of the hold time and of the applied magnetic field, we repeat the experiment a large number of times to obtain estimations of the distributions of n_0 and m_z. We then perform the same analysis of the distribution $P(n_0, m_z)$ as before. The fitted spin temperatures and condensed fractions are shown in figure (5.13) for three values of q (0.2 Hz, 1 Hz and 6 Hz).

We observe that, within error bars, the spin temperatures remain the same during the hold time, while the condensed fraction increases. This suggests:

- that the evaporative cooling goes on during the hold time, and that the kinetic temperature still decreases.

[3] The lifetime of our clouds is long enough to still keep around 5000 atoms after 15 s

- that the spin temperature on the other hand settles very quickly to the value it assumes after many seconds of hold.

From this we conclude that the spin and kinetic temperatures are set independently, or in other words that the two systems that they describe are not coupled.

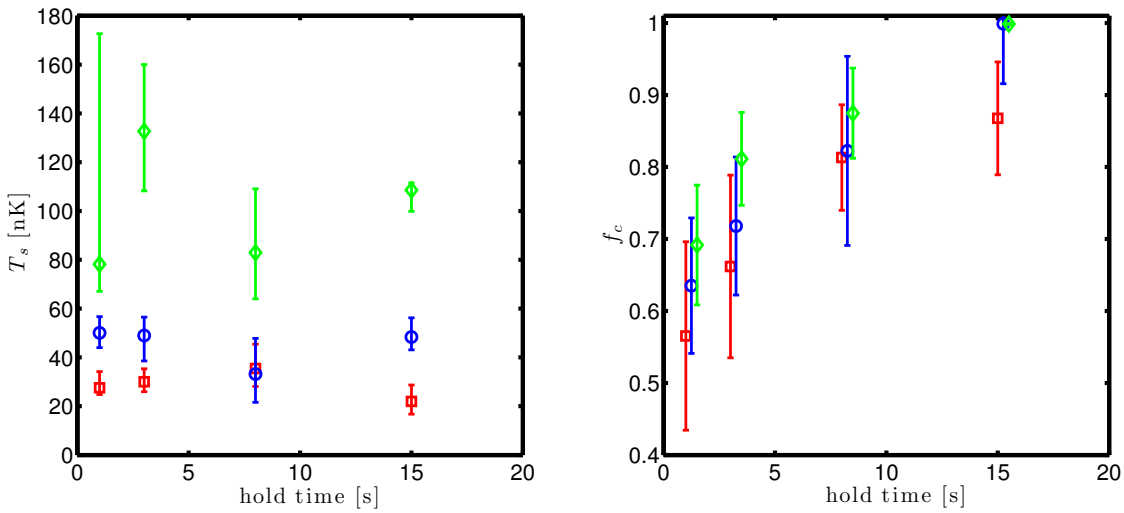

Figure 5.13: **a**): Fitted temperature T_s as a function of the hold time for three values of q: blue: $q = 0.2\,\mathrm{Hz}$, red: $q = 1\,\mathrm{Hz}$, green: $q = 6\,\mathrm{Hz}$. **b**): Fitted condensed fraction as a function of the hold time with the same color code. The set of evaporation times is the same for the different values of q, the points are shifted along the x axis for clarity.

To confirm the independence of these two systems we would like to compare directly the spin and the kinetic temperatures. This is the object of the next section.

5.4 Two spinor fluids isolated from each other

5.4.1 Comparison of spin and kinetic temperatures

As explained in chapter 2 we can deduce the kinetic temperature of our clouds by time-of-flight experiments. However, this method, based on the fit of the density distribution of the thermal atoms, fails at very low temperature, when thermal and condensed atoms become hardly distinguishable even after a time-of-flight expansion. It can provide a reliable measurement of the kinetic temperature only for evaporation times shorter than 800 ms. The determination of the kinetic temperature for longer evaporation times requires an other method.

For large values of q, all the atoms of the condensate accumulate in the $|m_F = 0\rangle$ state and the fluctuations are negligible. The total population n_0 takes the asymptotic value $n_0 = f_c + (1 - f_c)n_0^{th}$. Using a Hartree-Fock model it is possible to fit the condensed fraction from the observed n_0, and then from this value find the kinetic temperature. This analysis is detailed in the thesis of L.Shao [81]. The results are shown in figure (5.14) where we also represented the temperature obtained from time-of-flight experiment after 700 ms and 800 ms of evaporation.

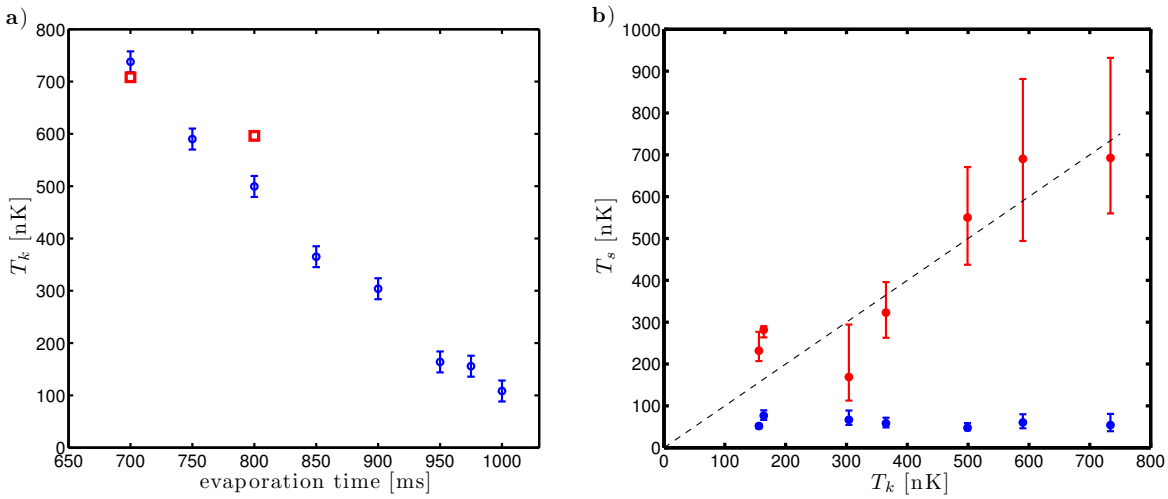

Figure 5.14: **a**): Kinetic temperatures during the evaporation ramp. The blue circles show the temperatures obtained from the analysis of the moments of n_0. The two red squares represent the kinetic temperatures deduced from a time-of-flight experiment. The time-of-flight method does not allow us to reliably determine the temperature for evaporation time longer than 800 ms. **b**): Spin temperature T_s as a function of the kinetic temperature T_k for two values of q: blue: $q = 1\,\mathrm{Hz}$, red: $q = 22\,\mathrm{Hz}$. The dashed line has slope unity.

If we compare these kinetic temperatures to the spin temperatures represented in figure (5.11) we identify two regimes. At low q we find that the spin temperature is significantly lower ($\sim 50\,\mathrm{nK}$), and that the behavior of the two temperatures during the evaporation also is different, the spin temperature staying constant. On the contrary, for larger values of q, the spin temperature is comparable to the kinetic temperature during the whole evaporation.

5.4.2 Large q: the condensate and the thermal gas are coupled

From the analysis of the joint distribution of n_0 and m_z, we concluded that in our experimental system the condensate has reached a quasi-equilibrium characterized by a spin temperature T_s. In addition to the condensate, thermal atoms are present which are characterized by a kinetic temperature T_k. These two temperatures describe two different systems: the collective spin of the condensate on one side, and the non-condensed modes on the other one. These two systems reach their equilibrium via different mechanisms. The thermal gas thermalizes through elastic collisions and evaporative cooling. The spin of the condensate on the other side thermalizes through spin-exchange collisions where two atoms in $|m_F = 0\rangle$ give a pair $|m_F = +1\rangle + |m_F = -1\rangle$.

For large values of q, only the $|m_F = 0\rangle$ state is condensed, and the redistribution of the spin energy via spin exchange collisions implies the coupling of the condensed $m_F = 0$ atoms to the thermal fraction in $|m_F = \pm 1\rangle$. In this case, the condensate and the thermal gas couple, and they are described by a single temperature. We then measure that the spin and kinetic temperatures coincide. Consistently, we note that the value of q for which we observe these similar two temperatures ($q = 22\,\mathrm{Hz}$) corresponds to the region of low spin fluctuations in the figures (5.4) and (5.5).

5.4.3 Low q: condensate at equilibrium but decoupled from the thermal gas

For low values of q (and given our low magnetization), the three spin species are condensed. In this case, spin exchange collisions can take place inside the condensate, and do not involve thermal atoms. The condensate is able to thermalize on its own. The two systems then equilibrate independently (on the time scale of one experiment) which results in the large difference between T_s and T_k. We note that the values of q for which we observe a decoupling of the two temperatures correspond to the region of strong spin fluctuations in the figures (5.4) and (5.5). The transition from a fragmented to a mean-field state typically occurs in our data for values of q of a few Hz. Indeed we see that at $q = 6\,\mathrm{Hz}$, the spin temperature is closer to the kinetic temperature than for lower values of q. Still, even at low q one could expect that at infinite time, due to a residual coupling of the two systems, the spin and kinetic temperatures converge to the same value.

The weakness of this coupling can also be understood by the large difference between the energy scales of the orbital and spin systems. At low magnetic field, the collective spin excitations of the condensate form a thin spectrum that we already discussed in chapter 4. The typical energy scale for these excitations is U_s/N, which in our experiment is on the order of 1 pK. On the other hand the spatial excitations are spaced by energies on the order of the trapping frequency. In our case ($\omega \approx 2\pi \times 600\,\mathrm{Hz}$) the first spatial excitation is a spin-wave mode with an energy $\epsilon \approx \sqrt{c_2/c_0}\hbar\omega \approx 6\,\mathrm{nK}$ (see chapter 1). Let us consider a process where energy is transferred from one system to the other, by example by adding one quantum of spatial excitation and consequently changing the collective spin state to conserve the total energy. This corresponds to a transition of the type $|k_0 : 1, k_1 : 0\rangle \otimes |\phi\rangle \to |k_0 : 0, k_1 : 1\rangle \otimes |\phi'\rangle$, where $|\phi\rangle$ and $|\phi'\rangle$ denote collective spin states of the condensate, and k_0 and k_1 label two spatial excitations. To happen, this transition has to be resonant. As illustrated by the figure (5.15), the difference in energy scales implies that $|\phi\rangle$ and $|\phi\rangle'$ are very distant in the collective spin spectrum. The transition from one to the other is then a very high order process, which is very unlikely. It follows that the whole transition probability is very small.

The spin of the condensate is thus a quasi-isolated system which equilibrates on its own. The equilibration process involves the dephasing of spin oscillations triggered by spin exchange collisions, which results in the thermal distribution of some few-body observables, in particular the spin populations. This mechanism is suggested by [98], where the authors study the long time dynamics of a spin-1 condensate initially in the $|m_F = 0\rangle$ spin state only, in the absence of magnetic field. They demonstrate that, even starting from this very ordered and out-of-equilibrium state, after a time $t \sim \sqrt{N}\,\hbar/U_s$, the individual spin populations present thermal-like distributions. In our system we find $t \sim 0.4\,\mathrm{s}$.

The spin of the condensate reaches its own equilibrium. What then sets the temperature characterizing this equilibrium? To answer this question we should estimate the amount of energy in the spin degree of freedom. This quantity is easier to determine at zero field, where the spin Hamiltonian restricts to the spin-dependent interaction. The spin energy is then given by $\langle \mathbf{S}^2 \rangle = \langle S_\perp^2 \rangle + \langle S_z^2 \rangle$. The fluctuations of the transverse spin in the condensate (and consequently the spin energy) are determined by the way the condensate builds up from the thermal fraction (the energy U_s depends very smoothly on the atom number). If we imagine an experiment where we quench the temperature of thermal gas through the critical temperature, the condensate would inherit the spin fluctuations

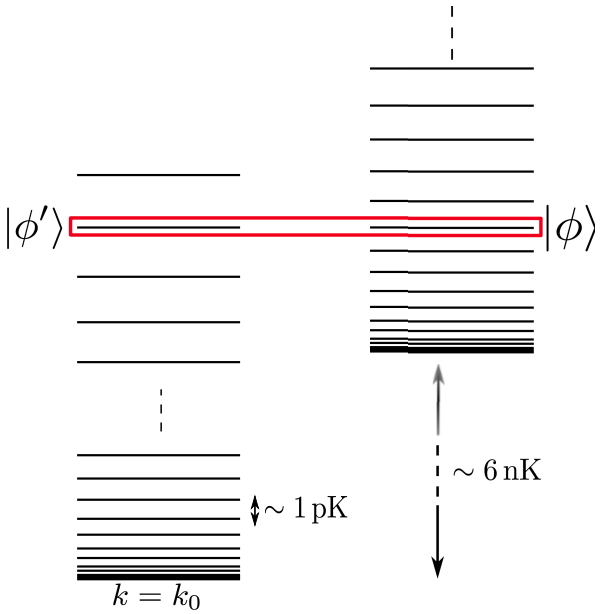

Figure 5.15: Detail of the spectrum. The vast difference in the energy scales of the collective spin excitations and of the spatial ones results in a weak coupling of the two systems.

of the thermal gas. Since the spin distribution of the thermal gas is isotropic, it is reasonable to assume that one has $\langle S_\perp^2 \rangle \sim \langle S_z^2 \rangle$. Under these conditions and assuming that the magnetization averages to zero we obtain for the spin energy:

$$E_s = \frac{U_s}{2N} \langle \hat{\mathbf{S}}^2 \rangle \sim \frac{U_s}{N} \Delta S_z^2 \tag{5.17}$$

The fluctuations of the magnetization ΔS_z^2 are directly accessible experimentally. From our data at $q = 0$ we can then estimate the spin energy. We find $(U_s/N_c)\langle S_z^2 \rangle \approx 35\,\mathrm{nK}$ for all evaporation times, which is on the same order as the spin temperatures we measure for very low values of q, as shown in figure (5.16), supporting the idea that at low q the spin temperature is correlated with the fluctuations of the magnetization.

5.5 Conclusion

In this chapter we presented an experimental investigation of the phenomenon of spin fragmentation in an antiferromagnetic spin-1 Bose gas. We measured the anomalous spin fluctuations and the depletion of the $m_F = 0$ spin state at low magnetic field and low magnetization for different trap depths. We analyzed these observations using the broken symmetry theory that we developed in chapter 4. We found that the distributions of the population n_0 and of the magnetization m_z are well described by a condensate in a broken symmetry state characterized by a spin temperature T_s and in equilibrium with a thermal fraction. Using a maximum likelihood method we extracted the spin temperature at different values of the quadratic Zeeman effect and for different evaporation times. We compared these results to the kinetic temperatures obtained from an analysis of the two first moments of n_0. We find that at low q (a few Hz) the kinetic and spin temperatures exhibit different behaviors during the evaporative cooling. The first one decreases during the evaporation while the second one stays constant. Additionally, we find that the

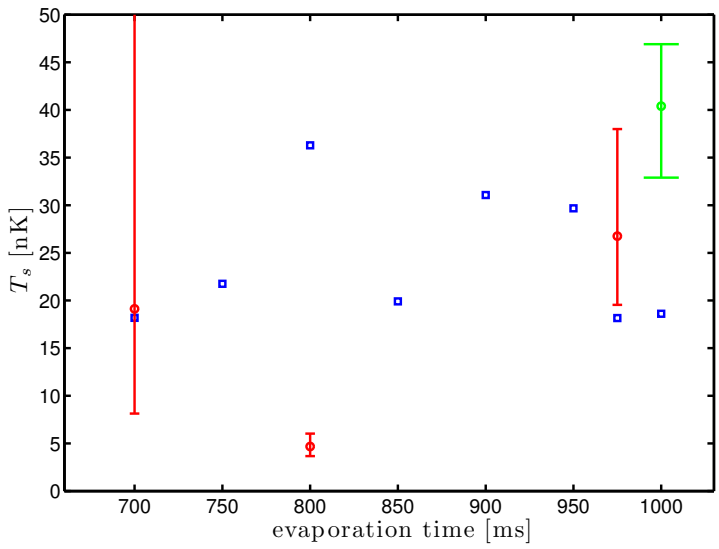

Figure 5.16: Comparison of the estimated energy in the spin degree of freedom $E_s/k_B = (U_s/2Nk_B)\Delta S_z^2$ (blue squares) and of the spin temperature for $q = 0.06\,\mathrm{Hz}$ (red circles) and $q = 0.12\,\mathrm{Hz}$ (green circle). We cannot use our analysis to deduce the spin temperature at $q = 0$ since then $\eta = 0$ and our algorithm becomes insensitive to T_s. The energy E_s is calculated from the measured fluctuations of the magnetization at $q = 0$.

spin temperature is lower than the kinetic one. We concluded that the two temperatures describe two systems - the collective spin excitations of the condensate on one side and all the non-condensed modes on the other side - that are quasi decoupled. We gave an estimate of the energy available in the spin degree of freedom at low q and found that it gives the correct order of magnitude for the spin temperature.

We were not able to repeat the experiments we presented in this chapter at shorter evaporation times, due to technical limitations in the Stern-Gerlach separation. It would be interesting to measure a spin temperature earlier in the evaporation ramp and explore further the link between the spin and kinetic temperatures. However, our model might then be questioned, as it supposes that the condensate is isolated from the thermal fraction, which is itself taken isotropic. These two assumptions are expected to fail for large enough kinetic temperatures.

An other interesting direction would be to study the dynamics of the thermalization of the spin degree of freedom. We plan to do this by quenching the magnetic field from a large value (where the condensate is in the $|m_F = 0\rangle$ state only) to a low value (where it is fragmented) and by measuring how the distribution of the population n_0 evolves after the quench.

Conclusion and perspectives

In this thesis we studied experimentally the magnetic properties of a spin-1 BEC of Sodium at equilibrium. We measured the mean-field magnetic phase diagram. We then focused on the behavior of the system at low magnetization and low magnetic field, where we revealed the fragmentation of the equilibrium spin state. We showed that this equilibrium state is characterized by a temperature that can be different from that of the orbital degrees of freedom, and interpret this situation in terms of a general formalism initially proposed by P.W. Anderson.

Summary

In chapter 1 we introduced the basic ingredients of the theory of spinor condensates. We obtained the expression of the spin dependent interactions in these gases and found that they conserve the magnetization. This quantity plays a major role in the thermodynamic properties of the system as we show by studying its ground-state. For this we developed a mean-field description of spinor condensates and made the important assumption that all the spin states share the same spatial mode. In this context we derived an expression for the ground-state of a spinor condensate with antiferromagnetic interactions (which is the case of Sodium) as a function of its magnetization and of the external magnetic field. We identified two phases. For a given magnetization, under a critical magnetic field only the spin states $|m_F = \pm 1\rangle$ are present. We called this phase antiferromagnetic. When the magnetic field is increased above this critical value, the atoms start to populate the $|m_F = 0\rangle$ state until an asymptotic value fixed by the magnetization. We called this phase broken-axisymmetry. We then checked the underlying single mode approximation by numerically solving the set of coupled Gross-Pitaevskii equations that the spinor wavefunction obeys. We found that under our experimental conditions (an atom number $N \approx 5000$ and an almost spherical trap of frequency $\omega = 2\pi \times 600\,\mathrm{Hz}$) this approximation gives a very good agreement with the exact solution. Finally we discussed elementary excitations of a condensate with internal degree of freedom. We made a Bogoliubov approximation and found, additionally to the density mode present in scalar gases, two spin-wave modes.

In chapter 2 we first described our experimental set-up and our sequence to produce spinor condensates of Sodium. We first create a background pressure of Sodium in the vacuum chamber using light-induced desorption and from it we load a magneto-optical trap. The atomic cloud is then transferred into a large volume crossed dipole trap where we start the evaporative cooling. The reduction of the trap frequencies associated to the lowering of the laser power does not allow to reach the degeneracy threshold in this trap. We consequently load the atoms in a second dipole trap of smaller volume where we pursue and complete the evaporative cooling. We obtain quasi-pure Bose-Einstein condensates of a few thousand atoms. In a second part of the chapter we detailed the techniques

we use to probe our spinor gases. To be able to measure the spin distribution of the atomic cloud we perform a Stern-Gerlach experiment to spatially separate the three spin states. We then image them using absorption imaging. We presented an empirical model of the atom-light interaction and calibrated the scattering cross sections of the three spin states. The sources of imaging noise were then analyzed and a noise-reduction algorithm was described. In the last part we explained how we can control the internal degree of freedom of our clouds, more precisely to prepare a cloud of chosen magnetization. We described two techniques to either increase or decrease the magnetization. Applying a resonant rf magnetic field, we can take advantage of the dephasing of Rabi oscillations to depolarize the cloud. On the opposite, by applying a gradient of magnetic field, we use the different couplings of the spin states to the field to purify the spin distribution of the cloud.

Chapter 3 presents a mean-field study of the ground state of an antiferromagnetic spin 1 condensate. We showed that the antiferromagnetic spin interactions favor the alignment of individual spins and lead to the existence in the many-body states of a spin nematic order. We defined a nematic order parameter and interpreted the magnetic phase diagram identified in chapter 1 in terms of this parameter. We then presented an experimental measurement of this phase diagram. We prepared the system at equilibrium in different conditions of magnetization and magnetic field and we measured the spin populations. We identified a critical magnetic field where the phase transition between the antiferromagnetic and broken-axisymmetry phases occurs. We found a very good agreement with the prediction of the single-mode approximation. In the last part we described a method to probe directly the spin nematic order of the system. This order is actually associated to the minimization of the transverse component of the total spin, which can be measured by analyzing the fluctuations of the magnetization during a rotation of the spin state. This rotation is performed by applying a resonant rf magnetic field. Using this technique we provided a direct evidence of the spin nematic order in condensates. We also showed with this technique the existence of a non-zero average of the transverse component of the spin in the antiferromagnetic phase. In this phase the transverse spin is expected to vanish in the condensate. We then attributed this transverse spin to the thermal atoms surrounding the condensate. As the transverse spin is directly linked to the existence of coherences between the component $m_F = 0$ and $m_F = \pm 1$ of the spin state, we deduced the existence of such spin coherences in the thermal fraction.

Chapter 4 focuses on the properties of the antiferromagnetic spin-1 Bose gas at low magnetization and low magnetic fields. This study was motivated by the observation of large spin fluctuations under these conditions. Such fluctuations are actually present even in the ground state which, due to the symmetry of the system, becomes fragmented. We introduced the notion of fragmentation and showed by an exact diagonalization that it manifests itself in the distribution of the population of the $|m_F = 0\rangle$ spin state. An exact resolution for a number of atoms of a few thousands is feasible, but computationally very long and is not suitable for an analysis of experimental data. We then developed an approximative theory in which the spin state of the condensate is described by a statistical mixture of mean-field states characterized by a spin temperature T_s. In this description, the symmetry of the spin state (that is broken in the naive mean-field treatment) is recovered. This approach also has the advantage to allow an efficient calculation of the spin distributions. We were then able to compute how the spin state of condensate evolves from a fragmented state at low magnetic field, to a mean-field state at larger fields. The use of the $SU(3)$ coherent states as a basis of mean-field states also made it possible to account

for experimental realities such as the distribution of the magnetization which is imposed by our preparation and then frozen. Finally we connected this transition from a symmetric fragmented state to a symmetry-breaking mean-field state to the phenomenon of spontaneous symmetry breaking. We identified the spectrum of collective spin excitations to an Anderson tower of states and showed that the existence of this "thin spectrum" involves that the width of the transition decreases with the number of particles. The rather small atom number of the samples we produce (smaller than in other experiments) allows us to observe these spin fluctuations.

Finally, chapter 5 presents an experimental investigation of the phenomenon of spin fragmentation. We prepared spinor gases with vanishing magnetization at equilibrium and under low magnetic fields. As suggested by the theoretical study of chapter 4 we measured the average value and fluctuations of the population n_0 in the $|m_F = 0\rangle$ spin state. We repeated this experiment at different kinetic temperatures by stopping the evaporative cooling at different times. For each evaporation time we observed the drop of the spin fluctuations with magnetic field and the progressive accumulation of the atoms in the $|m_F = 0\rangle$ state. We analyzed the measured distributions of the population n_0 and of the magnetization using the broken-symmetry theory developed in chapter 4. From this analysis we were able to extract the spin temperature of the system. We then compared these temperatures with the kinetic temperatures obtained from an analysis of the moments of n_0 only. We found that for low magnetic fields, the spin temperatures are lower than the kinetic ones and that their qualitative behavior during the evaporative cooling also differ. The kinetic temperature decreases (as expected) during the evaporation while the spin temperatures stay constant. We interpreted this differences as a signature of the weak coupling of the systems described by these two temperatures. We estimated the energy available in the spin degree of freedom and found it gives the correct order of magnitude for the spin temperature.

Perspectives

The evidence of the decoupling of the collective spin excitations of the condensate from the thermal excitations suggests several further experiments to investigate the behavior of isolated quantum systems, which is still a very debated topic [98][99][100][101]. In particular it would be interesting to study how the spin degree of freedom thermalizes by looking at the evolution of the spin distribution starting from a well defined out-of-equilibrium situation. One can for instance consider an experiment where the condensate would be prepared at a large magnetic field (the distribution of n_0 at equilibrium is then peaked at $n_0 = 1$) and where we would then quench the field to a very low value thus placing the spin of the condensate in a very excited state. The measurement of the distribution of n_0 in the time following the quench would provide information about the dynamics and the time scale of the equilibration of the spin degree of freedom.
One related direction we want to explore is to study the coupling of the spin state of the condensate to the thermal fraction. As we already pointed out in the thesis, the results of chapter 3 indeed suggests that the thermal fraction acquires some spin coherence through collisions with condensed atoms. This coherence was revealed by the measurement of a non-zero average transverse spin component in the antiferromagnetic phase. We plan to repeat the same kind of spin rotation experiment at shorter evaporation times to track the evolution of the transverse spin component with temperature.
Another on-going project is to measure the different critical temperatures of the three spin

species. Indeed, in the presence of a non-zero magnetic field or at non-zero magnetization, the three spin states are expected to condense at different temperatures [102][82]. In an ideal gas, two critical temperatures are predicted, the condensation occurring at the same time for two of the three species. This coincidence of the condensation is expected to be lifted by the interactions, and we should then measure three different critical temperatures. So far we have been able to observe that, depending on the conditions of magnetic field and magnetization, the first species that condenses changes. These first results are promising in order to quantitatively measure the effect of the interactions on the critical temperatures. In the long term, we will install an additional dipole trap of even smaller volume ($\sim 2\,\mu\mathrm{m}^3$) to be able to create condensates with a small and controlled atom number (on the order of hundred atoms). These systems are suited to produce strongly correlated states such as Schrödinger cats or twin states [42], one of the long term goal of our team.

Appendix A

Numerical methods for the spinor Gross-Pitaevskii equations

A.1 Gross-Pitaevskii equations in imaginary time

The imaginary time propagation method is a widely used method to compute the ground state of a quantum mechanical system. We first describe its principle and then apply it to our system of coupled Gross-Pitaevskii equations.

A.1.1 The imaginary time propagation method

We consider a quantum mechanical system described by a wavefunction $|\phi(t,\mathbf{r})\rangle$ whose time evolution obeys the Schrődinger equation

$$i\hbar\frac{\partial|\phi(t,\mathbf{r})\rangle}{\partial t} = \hat{H}|\phi(t,\mathbf{r})\rangle \tag{A.1}$$

where $\hat{H}$ is the Hamiltonian of the system. We note $|\phi_n(\mathbf{r})\rangle$ its eigenstates, E_n the corresponding energies and c_n the coefficients of the decomposition in this basis of the wavefunction at time $t = 0$. We choose E_0 as the energy reference. The wavefunction $|\phi(t,\mathbf{r})\rangle$ at any time $t > 0$ is then expressed by

$$|\phi(t,\mathbf{r})\rangle = \sum_n c_n e^{-iE_n t/\hbar}|\phi_n(\mathbf{r})\rangle \tag{A.2}$$

Although the explicit determination of all eigenstates $|\phi_n(\mathbf{r})\rangle$ can be quite complicated, there exists a mathematical method to compute the wavefunction of the ground state. The wavefunctions $|\phi(t,\mathbf{r})\rangle$ are formally extended to imaginary values of time t and one then make the change of variable

$$t \to -i\tau \tag{A.3}$$

where $\tau > 0$. The equation (A.2) becomes

$$|\phi(-i\tau,\mathbf{r})\rangle = \sum_n c_n e^{-E_n\tau/\hbar}|\phi_n(\mathbf{r})\rangle \tag{A.4}$$

We see that when we propagate this expression along the imaginary axis, all the terms of the sum but the first one are exponentially suppressed. Independent of the initial wavefunction, as τ increases the wavefunction $|\phi(-i\tau,\mathbf{r})\rangle$ thus converges to $|\phi_0(\mathbf{r})\rangle$, the ground-state of the system. The imaginary time propagation algorithm consists in choosing some initial wavefunction $|\phi_0\rangle$ and in discretely propagating the differential equation

governing the time evolution of $|\phi\rangle$. This propagation does not conserve the norm of $|\phi\rangle$, which has to be renormalized after each time step.. The initial choice of $|\phi_0\rangle$ does not influence the final result (but can influence the time needed to reach it).

A.1.2 Dimensionless coupled Gross-Pitaevskii equations

We now consider a spinor Bose-Einstein condensate of N atoms and of normalized magnetization m_z, trapped in a spherical potential $V(r)$. In the mean-field approximation the many-body wavefunction of the system is characterized by a single-particle wavefunction $\phi(t,\mathbf{r})$, which has three components: $\phi(t,\mathbf{r}) = (\phi_{+1}(t,\mathbf{r}), \phi_0(t,\mathbf{r}), \phi_{-1}(t,\mathbf{r}))^T$. Similarly to the Gross-Pitaevskii theory of the scalar Bose gas [52], the time evolution of these three components obey the set of coupled Gross-Pitaevskii equations [62]

$$i\hbar\frac{\partial}{\partial t}\phi_{+1} = (\mathcal{H} + E_{+1} - \eta + c_2(n_{+1} + n_0 - n_{-1}))\,\phi_{+1} + c_2\phi_0^2\phi_{-1}^* \tag{A.5}$$

$$i\hbar\frac{\partial}{\partial t}\phi_{0} = (\mathcal{H} + E_{0} + c_2(n_{+1} + n_{-1}))\,\phi_{0} + 2c_2\phi_0^*\phi_{+1}\phi_{-1} \tag{A.6}$$

$$i\hbar\frac{\partial}{\partial t}\phi_{-1} = (\mathcal{H} + E_{-1} + \eta + c_2(n_{-1} + n_0 - n_{+1}))\,\phi_{-1} + c_2\phi_0^2\phi_{+1}^* \tag{A.7}$$

To compute the wavefunctions of the three spin components in the condensate we choose some initial wavefunctions $\phi_{+1}^0(\mathbf{r}), \phi_0^0(\mathbf{r})$and $\phi_{-1}^0(\mathbf{r})$ and propagate them in imaginary time.

Practically we first rewrite the Gross-Pitaevskii equations in dimensionless variables. We define as distance unit the characteristic length of the harmonic oscillator $a_{ho} = \sqrt{\hbar/m\omega}$, and as time unit the inverse of the trap frequency ω. These two definitions give an energy unit $\hbar\omega$ and a wavefunction unit $a_{ho}^{-3/2}$. Considering the change to imaginary times we finally do the changes of variables

$$\begin{aligned} \tilde{r} &\rightarrow r/a_{ho} \\ \tilde{t} &\rightarrow i\omega t \\ \tilde{E} &\rightarrow E/\hbar\omega \\ \tilde{\phi} &\rightarrow a_{ho}^{3/2}\phi \end{aligned}$$

and we obtain the dimensionless Gross-Pitaevskii equations in imaginary time:

$$\frac{\partial}{\partial\tilde{t}}\tilde{\phi}_{+1} = -\left(\tilde{\mathcal{H}} + \tilde{E}_{+1} - \tilde{\eta} + \tilde{c}_2(\tilde{n}_{+1} + \tilde{n}_0 - \tilde{n}_{-1})\right)\tilde{\phi}_{+1} - \tilde{c}_2\tilde{\phi}_0^2\tilde{\phi}_{-1}^* \tag{A.8}$$

$$\frac{\partial}{\partial\tilde{t}}\tilde{\phi}_{0} = -\left(\tilde{\mathcal{H}} + \tilde{E}_{0} + \tilde{c}_2(\tilde{n}_{+1} + \tilde{n}_{-1})\right)\tilde{\phi}_{+1} - 2\tilde{c}_2\tilde{\phi}_0^*\tilde{\phi}_{+1}\tilde{\phi}_{-1} \tag{A.9}$$

$$\frac{\partial}{\partial\tilde{t}}\tilde{\phi}_{-1} = -\left(\tilde{\mathcal{H}} + \tilde{E}_{-1} + \tilde{\eta} + \tilde{c}_2(\tilde{n}_{-1} + \tilde{n}_0 - \tilde{n}_{+1})\right)\tilde{\phi}_{+1} - \tilde{c}_2\tilde{\phi}_0^2\tilde{\phi}_{+1}^* \tag{A.10}$$

with:

$$\tilde{\mathcal{H}} = \frac{1}{2}\nabla^2 + \frac{1}{2}\tilde{r}^2 + \tilde{c}_0\tilde{n}_{tot} - \tilde{\mu} \tag{A.11}$$

$$\tilde{E}_i = E_i/\hbar\omega\ ,\ \tilde{\mu} = \mu/\hbar\omega\ ,\ \tilde{\eta} = \eta/\hbar\omega \tag{A.12}$$

$$\tilde{c}_0 = 4\pi N(a_0 + 2a_2)/3a_{ho} \tag{A.13}$$

$$\tilde{c}_2 = 4\pi N(a_2 - a_0)/3a_{ho} \tag{A.14}$$

$$\tilde{n}_i = |\tilde{\phi}_i^*\tilde{\phi}_i|^2 \tag{A.15}$$

In the following the drop all the tildes for clarity.

A.2 Propagation of the finite differences scheme

To propagate the initial wavefunctions according to the Gross-Pitaevskii equations we discretize the equations in time and linearize the time derivative. For the spatial coordinate on the other side the main issue is the treatment of the differential operators, here the Laplacian. Two main families of method exist: spectral methods, that propagate the wavefunction partly in the direct coordinate space and partly in the conjugated space (where the Laplacian is diagonal) after a Fourier transform, and the finite differences methods that stay in the direct space and discretize the spatial coordinate. We choose to use a finite difference method, namely the Backward Euler Finite Differences method [64].

We propagate in time the three wavefunctions $\phi_i(t,\mathbf{r}), i = \pm 1, 0$, starting from three arbitrary initial wavefunctions $\phi_i^0(\mathbf{r})$. As we consider a spherical potential the equations are rotationally symetric in space and the value of the wavefunctions of the ground state at position $\mathbf{r}$ only depends on the radius $r = \mathbf{r}$: $\phi_i(t,\mathbf{r}) = \phi_i(t,r)$. We then only have to consider a one dimensional problem in space. We discretize the time t by defining a time step Δt and a series of time $t_n = t_0 + n\Delta t$. To discretize the radial coordinate r we fix a maximum radius R and a number M. We then define a spatial step $\Delta r = 2R/(2M+1)$ and two series of points:

$$r_j = j\Delta r \ , \ r_{j+\frac{1}{2}} = (j+\frac{1}{2})\Delta r \ , \ j = 0,1,2,...,M \tag{A.16}$$

We denote by $\phi^n_{i,j+\frac{1}{2}}$ the numerical approximation of $\phi_i(t_n, r_{j+\frac{1}{2}})$. The wavefunctions at each time t_n are then represented by a vector of size $M+1$. Actually we add a component $\phi^n_{i,-\frac{1}{2}}$ whose meaning is explained in the following. The vector representing each wavefunction at a given time is thus of size $M+2$. We denote the vector $(\phi^n_{i,j+\frac{1}{2}})_{j=-1,0,1,...M}$ by ϕ^n_i. The vectors $\phi^{n=0}_i$ are obtained by the direct evaluation of the wavefunctions $\phi^0_i(r)$ at the points $r_{j+\frac{1}{2}}$. We also define the norm of the vectors by

$$||\phi^n_i||^2 = 4\pi\Delta r \sum_j |\phi^n_{i,j+\frac{1}{2}}|^2 r^2_{j+\frac{1}{2}} \tag{A.17}$$

The Backward Euler Finite Differences scheme is then given by (we give it for ϕ_{+1} only, the extension to ϕ_0 and ϕ_{-1} is straightforward)

$$\begin{aligned}\frac{\phi^{(1)}_{+1,j+\frac{1}{2}} - \phi^n_{+1,j+\frac{1}{2}}}{\Delta t} = & \Big[\frac{1}{2}\delta_r^2 - \frac{1}{2}r^2_{j+\frac{1}{2}} - c_0\left(|\phi^n_{+1,j+\frac{1}{2}}|^2 + |\phi^n_{0,j+\frac{1}{2}}|^2 + |\phi^n_{-1,j+\frac{1}{2}}|^2\right) - E_+ \\ & -c_2\left(|\phi^n_{+1,j+\frac{1}{2}}|^2 + |\phi^n_{0,j+\frac{1}{2}}|^2 - |\phi^n_{-1,j+\frac{1}{2}}|^2\right)\Big]\phi^{(1)}_{+1,j+\frac{1}{2}} \\ & -c_2(\phi^n_{0,j+\frac{1}{2}})^2(\phi^n_{-1,j+\frac{1}{2}})^*\end{aligned} \tag{A.18}$$

for $j = 0,1,...,M-1$. The operator δ_r^2 corresponds to the discretization of the Laplacian and is defined by

$$\delta_r^2\phi^{(1)}_{i,j+\frac{1}{2}} = \frac{1}{(\Delta r)^2 r^2_{j+\frac{1}{2}}}\left[r^2_{j+\frac{1}{2}}\phi^{(1)}_{i,j+\frac{3}{2}} - (r^2_{j+1} + r^2_j)\phi^{(1)}_{i,j+\frac{1}{2}} + r^2_j\phi^{(1)}_{i,j-\frac{1}{2}}\right] \tag{A.19}$$

We force the wavefunction to vanish at large radius by setting:

$$\phi^{(1)}_{+1,M} = 0 \tag{A.20}$$

Besides we ensure that the derivative of the wavefunction vanishes at $r = 0$ by imposing

$$\phi^{(1)}_{+1,-\frac{1}{2}} = \phi^{(1)}_{+1,\frac{1}{2}} \tag{A.21}$$

The points $\phi^n_{i,-\frac{1}{2}}$ do not represent the value of the wavefunction at a given point, but are numerical tricks to force the derivative to cancel at $r = 0$, which is physically required. The vector $\phi^{(1)}_i$ is not equal to the approximation of the wavefunction ϕ_i at time t_{n+1} because the total atom number and the magnetization are not conserved by the scheme (A.18). Once the three vectors $\phi^{(1)}_i, i = \pm 1, 0$ are calculated, the vectors ϕ^{n+1}_i are obtained by a projection step:

$$\phi^{n+1}_i = \sigma^n_i \phi^{(1)}_i \tag{A.22}$$

where the σ^n_i are factors chosen such that

$$\sum_{i=\pm 1,0} ||\phi^n_i||^2 = 1 \ , \ ||\phi^n_{+1}||^2 - ||\phi^n_{-1}||^2 = m_z \tag{A.23}$$

The derivation of the factors σ^n_i is done in [63]. We note $n^-_i = ||\phi^{(1)}_i||^2$ the norm of the vectors before renormalization. The expressions of the σ^n_i are:

$$\sigma^n_0 = \frac{\sqrt{1-m_z^2}}{\left[n^-_0 + \sqrt{4(1-m_z^2)n^-_{-1}n^-_{+1} + (m_z n^-_0)^2}\right]^{1/2}} \tag{A.24}$$

$$\sigma^n_{+1} = \sqrt{\frac{1 + m_z - (\sigma^n_0)^2 n^-_0}{2n^-_{+1}}} \tag{A.25}$$

$$\sigma^n_{-1} = \sqrt{\frac{1 - m_z - (\sigma^n_0)^2 n^-_0}{2n^-_{-1}}} \tag{A.26}$$

Practically, the main operation in the propagation is to solve at each step $n+1$ the equation (A.18) of unknown $\phi^{(1)}_{+1}$ knowing the three previously calculated vectors ϕ^n_i (and then do the same for $\phi^{(1)}_0$ and $\phi^{(1)}_{-1}$). For this we rewrite the equation (A.18) in the form

$$a_j \phi^{(1)}_{+1,j-\frac{1}{2}} + b_j \phi^{(1)}_{+1,j+\frac{1}{2}} + c_j \phi^{(1)}_{+1,j+\frac{3}{2}} = d_j \tag{A.27}$$

for $j = 0, 1, ...M-1$. The relations (A.20) and (A.21) give the value of the four vectors a, b, c and d for $j = M$ and $j = -1$ respectively. We now have to solve the $M+2$ dimension linear system

$$L\phi^{(1)}_i = d \tag{A.28}$$

where $d = (d_{-1}, d_0, ..., d_M)^T$ and the matrix L is defined by

$$L = \begin{pmatrix} b_{-1} & c_{-1} & 0 & \cdots & & & 0 \\ a_0 & b_0 & c_0 & 0 & \cdots & & \vdots \\ 0 & \ddots & \ddots & \ddots & & & \\ \vdots & & & & & \ddots & 0 \\ & & & & \ddots & \ddots & c_{M-1} \\ 0 & & & ... & 0 & a_M & b_M \end{pmatrix} \tag{A.29}$$

This kind of tridiagonal linear system is efficiently solve by the so-called Thomas' algorithm, whose complexity is $\mathcal{O}(M)$ (whereas the complexity of the Gaussian elimination algorithm is $\mathcal{O}(M^3)$)

A.3 Numerical implementation

Using the scheme we just described we are able to propagate the initial wavefunctions in imaginary time. An important issue that will determine the numerical precision of the calculated solution is the choice of a termination criterion. Indeed, in the mean-field approximation the spin energy is a continuous function of the three wavefunctions, and the propagation algorithm would need an infinite time to separate the ground state mode from all the others. When we stop our algorithm, the resulting spinor wavefunction will always be a packet of low-lying states, whose width in energy goes down with the propagation time. We have to find the propagation time we need such that the error we make in the determination of the ground state does not affect (at our level of approximation) the spin energy we infer from it.

An intuitive idea would be to consider the speed of the evolution of the wavefunctions by looking at the quantities $||\phi_i^{n+1} - \phi_i^n||$. The termination criterion would then be that these three quantities are smaller than a defined (small number), meaning that the wavefunctions almost do not evolve any more and that they have converged to the ground state. But this criterion can actually fail to catch the correct solution. The reason is that the effect of one step of propagation is not necessary visible in the shape of the wavefunctions, but can also consist of a change of their phase.

We actually choose as figure of merit to evaluate the convergence of the algorithm the average value of the in-time evolution operator U defined by

$$\phi_i^{n+1} = U(t_n, t_{n+1})\phi_i^n \tag{A.30}$$

As the algorithm converges, the normalized average value $\langle U \rangle = \int (\phi_i^n)^* U \phi_i^n / \int |\phi_i^n|^2$ should approach unity. We then decide to stop the propagation when the distance $|1 - \langle U \rangle|$ becomes smaller than a fixed number. We now have to choose this number. When we do the mean-fied approximation, we make an error in the spin energy we calculate of order U_s/N. To be consistent with this approximation we choose as termination criterion the verification of the condition:

$$\left| 1 - \frac{\int (\phi_i^n)^* \phi_i^{n+1}}{\int |\phi_i^n|^2} \right| \ll \frac{U_s \Delta t}{N\hbar} \tag{A.31}$$

With the parameters $N = 10^3$ and $\omega = 2\pi \times 600$ Hz, we have $U_s/\hbar\omega \approx 0.1$. If we take $\Delta t = 10^3 \omega^{-1}$ we then obtain $U_s \Delta t / N\hbar \approx 10^{-7}$.

We have checked our algorithm in various limiting cases. If we set c_2 to zero we recover the SMA solution for the three component, in particular we recover the Thomas-Fermi and the gaussian distribution in the two limits of strong and weak spin-independent interactions. We also check that the final result of the algorithm does not depend on the initial wavefunctions we input. We are then allowed to optimize the convergence time by choosing a set of initial wavefunctions as close as possible to the final solution. In particular when we want to explore the whole magnetic phase diagram, this reduces by a lot the calculation time. With the parameters N and ω we use, we expect the final solution to be close to the SMA. A good starting point of the propagation would then be the SMA solution, with three random phases and weighted by the adequate factor for each spin component in order to respect the magnetization condition. But an even better choice when calculating the phase diagram is to define as starting wavefunctions for one point

(m_z, B) the solution previously calculated at a neighbouring point. So, we first compute the solution of the Gross-Pitaevskii equations in one corner of the phase diagram with the SMA solution as guess wavefunction, and then explore the whole phase diagram in a systematic way each time using the previously calculated solution as guess for the next point.

Appendix B

Geometrical representation of a spin-1 state

B.1 Bloch-Rabi representation

As we showed in chapter 3 by considering the nematic order, mean-field state of the spin-1 Bose gas are characterized by their symmetry. To better visualize and understand the nature of these states we would like to draw a geometrical representation where symmetry considerations would be highlighted. Such a representation is well known for spin 1/2 particles which can be pictured are unit vectors in the Bloch sphere. Apart from an overall phase, a spin 1/2 state $|\psi\rangle$ can be written as:

$$|\psi\rangle = \cos\left(\frac{\theta}{2}\right) e^{i\phi/2}|+\rangle + \sin\left(\frac{\theta}{2}\right) e^{-i\phi/2}|-\rangle \tag{B.1}$$

The state $|\psi\rangle$ is obtained by rotating the state $|+\rangle$ so that it is the $+1$ eigenstate of the projected spin operator $\mathbf{S}.\mathbf{n}$ where $\mathbf{n}$ is the unit vector

$$\mathbf{n} = \begin{pmatrix} \sin(\theta)\cos(\phi) \\ \sin(\theta)\sin(\phi) \\ \cos(\theta) \end{pmatrix} \tag{B.2}$$

and can be unambiguously represented by the vector $\mathbf{n}$ on the Bloch sphere.

We now want to extend this representation to higher spins. The idea of the method, inspired by Bloch and Rabi, is to consider a spin F particle as a combination of $2F$ spin 1/2 sub-particles. Indeed, the subspace of total spin F obtained from the sum of $2F$ spin 1/2 is equivalent to the Hilbert space of a true spin F (the sum also generates subspaces of total spin $0, 1, ..., F-1$). The wavefunction of a spin F particle can then be written as the symmetrized tensor product of the $2F$ wavefunctions of its constituents. Each of the constituting spin 1/2 is represented by a vector on the Bloch sphere. A representation of a spin F particle is then a set of $2F$ vectors on the Bloch sphere. We now consider the particular case $F = 1$. The composition of two spin 1/2 gives a subspace of total spin 0 and a subspace of total spin 1 generated by the triplet states:

$$|+1\rangle = |+\rangle|+\rangle \tag{B.3}$$

$$|0\rangle = \frac{1}{\sqrt{2}}\left(|+\rangle|-\rangle + |-\rangle|+\rangle\right) \tag{B.4}$$

$$|-1\rangle = |-\rangle|-\rangle \tag{B.5}$$

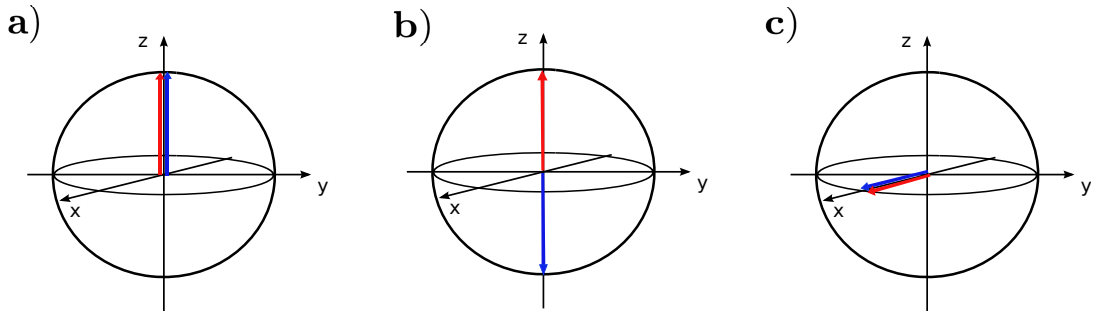

Figure B.1: Bloch-Rabi representation of three spin 1-states, given in the standard basis by: **a**): (1,0,0), **b**): (0,1,1), and **c**): $(1/2, 1/\sqrt{2}, 1/2)$.

The association of two vectors $\mathbf{n}_1$ and $\mathbf{n}_2$ defined by the angles $\theta_1, \phi_1, \theta_2, \phi_2$ describes the spin-1 states $|\Psi\rangle$ given in the standard basis by

$$\Psi_{+1} = \frac{1}{\sqrt{\mathcal{M}}} \cos\left(\frac{\theta_1}{2}\right) \cos\left(\frac{\theta_2}{2}\right) e^{i(\phi_1+\phi_2)/2} \tag{B.6}$$

$$\Psi_0 = \frac{1}{\sqrt{2\mathcal{M}}} \left[\cos\left(\frac{\theta_1}{2}\right) \sin\left(\frac{\theta_2}{2}\right) e^{i(\phi_1-\phi_2)/2} + \sin\left(\frac{\theta_1}{2}\right) \cos\left(\frac{\theta_2}{2}\right) e^{i(\phi_2-\phi_1)/2}\right] \tag{B.7}$$

$$\Psi_{-1} = \frac{1}{\sqrt{\mathcal{M}}} \sin\left(\frac{\theta_1}{2}\right) \sin\left(\frac{\theta_2}{2}\right) e^{-i(\phi_1+\phi_2)/2} \tag{B.8}$$

where the normalization constant is $\mathcal{M} = (3 + \mathbf{n}_1.\mathbf{n}_2)/4$. One then easily verifies that the average spin is given by

$$\langle \hat{\mathbf{S}} \rangle = \frac{1}{2}(\mathbf{n}_1 + \mathbf{n}_2). \tag{B.9}$$

From expression (3.34) we have

$$\langle \mathbf{S} \rangle^2 = 1 - \mathcal{N}^2 \tag{B.10}$$

$$= \frac{1 + \mathbf{n}_1.\mathbf{n}_2}{2} \tag{B.11}$$

where $\mathcal{N}$ is the nematic parameter and where we used $|\mathbf{n}_{1,2}|^2 = 1$. We then find

$$\mathcal{N}^2 = \frac{|\mathbf{n}_1 - \mathbf{n}_2|^2}{4} \tag{B.12}$$

Thus, an oriented state ($\mathcal{N} = 0$) corresponds to $\mathbf{n}_1 = \mathbf{n}_2$, and an aligned state ($|\mathcal{N}| = 1$) corresponds to $\mathbf{n}_1 = -\mathbf{n}_2$.

The treatment of the generic spin-1 state leads to quite cumbersome calculations and we directly turn to the case of the mean-field ground state with antiferromagnetic interactions that we discussed in chapter 1.

B.2 Application to the mean-field ground state

We consider a mean-field state described by the expression (1.62). Applying a global phase shift of $\Theta/2$ this state takes the form

$$|\Psi\rangle = \begin{pmatrix} \sqrt{(x+m_z)/2}e^{i\alpha/2} \\ \sqrt{1-x}e^{-i\Theta/2} \\ \sqrt{(x-m_z)/2}e^{-i\alpha/2} \end{pmatrix} \tag{B.13}$$

Comparing this expression to the previous ones we identify $\alpha = \phi_1 + \phi_2$. Besides, in the antiferromagnetic case one has $\Theta = \pi$, so that the 0 component is purely imaginary. This is realized in (B.8) by $\phi_1 - \phi_2 = \pi$. To simplify the calculations, the phase α can be set to zero without loss of generality. We then finally obtains $\phi_1 = \pi/2 = -\phi_2$. We now move to the cartesian basis. The state $|\Psi\rangle$ writes:

$$|\Psi\rangle = \frac{1}{\sqrt{2\mathcal{N}}} \begin{pmatrix} i\cos(\theta_+) \\ -\cos(\theta_-) \\ \sin(\theta_-) \end{pmatrix}_c \tag{B.14}$$

where we defined the angles $\theta_\pm = (\theta_1 \pm \theta_2)/2$. We immediately identify the two directors $\mathbf{u}_1$ and $\mathbf{u}_2$ defined in chapter 3:

$$\mathbf{u}_1 = \frac{1}{\sqrt{2\mathcal{N}}} \begin{pmatrix} 0 \\ -\cos(\theta_-) \\ \sin(\theta_-) \end{pmatrix} \ , \ \mathbf{u}_2 = \frac{1}{\sqrt{2\mathcal{N}}} \begin{pmatrix} \cos(\theta_+) \\ 0 \\ 0 \end{pmatrix} \tag{B.15}$$

We note that the vector $\mathbf{n}_1 - \mathbf{n}_2$ writes

$$\mathbf{n}_1 - \mathbf{n}_2 = 2\sin(\theta_+) \begin{pmatrix} 0 \\ -\cos(\theta_-) \\ \sin(\theta_-) \end{pmatrix} \tag{B.16}$$

so that the nematic director characterizing the spin quadrupole is parallel to $\mathbf{n}_1 - \mathbf{n}_2$. As we have seen above, the nematic parameter is determined by the modulus of this vector.

Let's consider precisely the different mean-field ground states. We start with the polar states. We easily find that the polar state along the z direction (0,1,0) is represented by two vectors pointing in opposite directions along the z axis. The family of polar states is deduced from this one by the application of any rotation, so that the polar state along a direction $\mathbf{n}$ is represented by two vectors pointing in opposite directions along the axis defined by $\mathbf{n}$.

We now consider the ground state at a given magnetization m and for a magnetic field below the critical value (i.e in the antiferromagnetic phase). This state verifies $n_0 = 0$ so that we have $\sin(\theta_-) = 0$, which implies $\theta_1 = \theta_2$. Since the relation (B.9) gives $\cos(\theta_1) + \cos(\theta_2) = 2m$ the state is represented by two vectors defined by $\cos(\theta_{1,2}) = m$. Besides, as we already said, the relation $\theta = \pi$ imposes that $\phi_1 = \phi_2 + \pi$, which means that the plane defined by the two vectors contains the z axis. Such a state is represented in the figure (B.2) for $\alpha = 0$. The angle α can take any value as a consequence of the commutation of the Hamiltonian with the spin operator $\hat{S}_z$. The representation of a state for a different α is obtained by a rotation about the z axis. Using the relation (B.9) we here clearly see that the condition $n_0 = 0$ is equivalent to $\langle \mathbf{S}_\perp = 0 \rangle$, as the components of the two vectors $\mathbf{n}_1$ and $\mathbf{n}_2$ in the $x - y$ plane exactly cancel.

The quadratic Zeeman effect favors the accumulation in the $m_F = 0$ state, and so wants to maximize θ_-. This is done by bringing the two vectors as close to the z axis as is allowed by the constraint of fixed magnetization, one vector pointing up and the other one down. This rotation of the two vectors would create some average transverse spin But as the field stays below the critical value, the spin interactions dominate, they favor the minimization of the transverse spin, and block this evolution to the z axis. At the phase

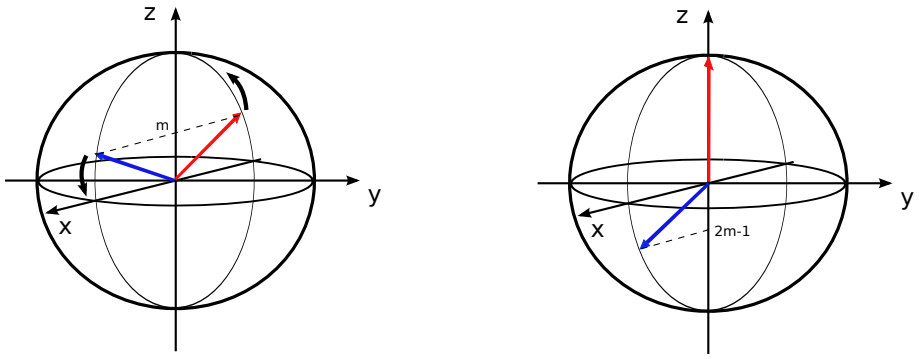

Figure B.2: Evolution of the mean-field ground state at a given magnetization m when the magnetic field increases. As long as the field is lower than the critical value, the system stays in the state represented on the left, with a vanishing transverse spin. Then, when the field increases above the critical value, the two vectors rotate in the $x-z$ plane such that the condition $\cos(\theta_1)+\cos(\theta_2)=2m$ stays true. Asymptotically one of the two vectors align along the direction $+z$ as represented on the right.

transition the field starts to dominate over the interactions, and the two vectors rotate a little in the $x-z$ plane, still verifying the condition $\cos(\theta_1)+\cos(\theta_2)=2m$. As the field increases the vectors get closer and closer to the z axis. Asymptotically, one vector is pinned along the z axis and the other is constrained by the condition on m.

For completeness we note that an other geometrical representation of high spin objects exists, which is yet very close to the one we described [103] [37]. The spin F state $|\Psi\rangle$ is here represented by the $2F$ unit vectors defining the maximally polarized spin-F state $|\Psi'\rangle$ which is orthogonal to $|\Psi\rangle$. This representation actually corresponds to inverting the orientation of the $2F$ vectors defining $|\Psi\rangle$.

Appendix C

Three-level Rabi oscillation

We consider a spin-1 system where the degeneracy of the three spin states is lifted by an external static magnetic field $\mathbf{B} = B_0\mathbf{e}_z$, so that the splitting between the states $|+1\rangle$ and $|0\rangle$ is equal to the splitting between the states $|0\rangle$ and $|-1\rangle$ and is equal to the Larmor frequency $\mu_\mathrm{B}B_0/2$. We neglect the quadratic Zeeman effect. We now couple the spin states by adding at $t = 0$ a radio-frequency magnetic field polarized along the y axis $\mathbf{B}_\mathrm{rf} = \mathbf{e}_y(Be^{i\omega_\mathrm{rf}t} + \mathrm{c.c})$ and resonant at the Larmor frequency. This field couples to the $\hat{S}_y$ spin operator and if we make the rotating-wave approximation its effect after a time t is to rotate the spinor wavefunction about the y axis:

$$|\Psi'\rangle = e^{-i\beta\hat{S}_y}|\Psi\rangle \tag{C.1}$$

Here Θ is the angle of the rotation and is given by $\beta = t\Omega$, where we defined the Rabi frequency $\Theta = \mu_\mathrm{B}B_\mathrm{rf}/2\hbar$. The rotation operator writes in the standard basis:

$$e^{-i\Theta\hat{S}_y} = \begin{pmatrix} \frac{1-\cos\Theta}{2} & \frac{\sin\Theta}{\sqrt{2}} & \frac{1-\cos\Theta}{2} \\ -\frac{\sin\Theta}{\sqrt{2}} & \cos\Theta & \frac{\sin\Theta}{\sqrt{2}} \\ \frac{1-\cos\Theta}{2} & -\frac{\sin\Theta}{\sqrt{2}} & \frac{1-\cos\Theta}{2} \end{pmatrix} \tag{C.2}$$

With this expression and using the definition (3.45) we can calculate the populations of the rotated state $|\Psi'\rangle$. Noting with primes the quantities at time t and without primes the quantities at time $t = 0$ we find:

$$\begin{aligned} n'_{+1} &= \frac{1+\cos^2\Theta}{4}(1-n_0) + \frac{\sin^2\Theta}{2}n_0 + \frac{\cos\Theta}{2}m_z + \frac{\sin^2\Theta}{2}\sqrt{n_{+1}n_{-1}}\cos\alpha \\ &\quad + \frac{\sin\Theta(1+\cos\Theta)}{\sqrt{2}}\sqrt{n_0n_{+1}}\cos(\frac{\theta+\alpha}{2}) + \frac{\sin\Theta(1-\cos\Theta)}{\sqrt{2}}\sqrt{n_0n_{-1}}\cos(\frac{\theta-\alpha}{2}) \end{aligned} \tag{C.3}$$

$$\begin{aligned} n'_{-1} &= \frac{1+\cos^2\Theta}{4}(1-n_0) + \frac{\sin^2\Theta}{2}n_0 - \frac{\cos\Theta}{2}m_z + \frac{\sin^2\Theta}{2}\sqrt{n_{+1}n_{-1}}\cos\alpha \\ &\quad - \frac{\sin\Theta(1-\cos\Theta)}{\sqrt{2}}\sqrt{n_0n_{+1}}\cos(\frac{\theta+\alpha}{2}) - \frac{\sin\Theta(1-\cos\Theta)}{\sqrt{2}}\sqrt{n_0n_{-1}}\cos(\frac{\theta-\alpha}{2}) \end{aligned} \tag{C.4}$$

$$\begin{aligned} n'_0 &= \frac{\sin^2\Theta}{2}(1-n_0) + \cos^2\Theta n_0 - \sin^2\sqrt{n_{+1}n_{-1}}\cos\alpha \\ &\quad - \sqrt{2}\sin\Theta\cos\Theta\sqrt{n_{+1}n_0}\cos(\frac{\theta+\alpha}{2}) + \sqrt{2}\sin\Theta\cos\Theta\sqrt{n_{-1}n_0}\cos(\frac{\theta-\alpha}{2}) \end{aligned} \tag{C.5}$$

where we noted $m_z = n_{+1} - n_{-1}$ the magnetization. These expressions become much simpler if the initial state is fully polarized ($n_{+1} = 1, n_0 = n_{-1} = 0$):

$$n'_{+1} = \cos^4(\frac{\Theta}{2}) \tag{C.6}$$

$$n'_{-1} = \sin^4(\frac{\Theta}{2}) \tag{C.7}$$

$$n'_0 = 2\sin^2(\frac{\Theta}{2})\cos^2(\frac{\Theta}{2}) \tag{C.8}$$

or if it is a nematic state along the z axis ($n_0 = 1, n_{+1} = n_{-1} = 0$):

$$n'_{+1} = n'_{-1} = \frac{1}{2}\sin^2\Theta \tag{C.9}$$

$$n'_0 = \cos^2\Theta \tag{C.10}$$

In particular we note that when the initial state is fully polarized the population in the state $m_F = 0$ oscillates at twice the frequency of the two others: n'_0 oscillates at the frequency $2\Omega'$ whereas the two others oscillate at Ω'. This is not the case if the initial state is the nematic state along z: the three populations then all oscillate at the frequency $2\Omega'$.

Appendix D

Generalized coherent states

Here we recall how the canonical coherent states of quantum optics are constructed, and then explain how the method can be generalized.

D.1 Construction of generalized coherent states

The concept of coherent states was first introduced by Glauber to describe states of the quantum electromagnetic radiation in a laser beam [104] [105]. We recall here their construction. We consider a quantum harmonic oscillator, and note $\hat{a}^\dagger$ and $\hat{a}$ the associated ladder operators. Due to their commutation relation $[\hat{a}, \hat{a}^\dagger] = \mathbb{1}$, these two operators together with the identity operator $\mathbb{1}$ generate a Lie algebra. The attached Lie group is obtained by exponentiation of these generators and is called the Heisenberg-Weyl group. Elements of this group are unitary and are labeled by a continuous complex parameter α. They are denoted as displacement operators $\hat{D}(\alpha)$[1]. A coherent state is generated by the action of a displacement operator on the vacuum state:

$$|\alpha\rangle = \hat{D}(\alpha)|0\rangle = e^{\alpha\hat{a}^\dagger - \alpha^*\hat{a}}|0\rangle \tag{D.1}$$

where $\alpha \in \mathbb{C}$.

The coherent states are particularly adapted to study harmonic oscillators. In such systems, a coherent state remains coherent in time and the evolution of the α parameter is given by classical equations. But quantum systems frequently obey other symmetry groups. This led to the generalization of the notion of coherent states [91].

Let us consider an arbitrary Lie group G, and let T be an irreducible unitary representation of G on the Hilbert space $\mathcal{H}$. To each element g of G the representation T associates a unitary operator $T(g)$ acting in $\mathcal{H}$. A set of generalized coherent states is then generated by the action of all these operators on some chosen reference state $|\psi_0\rangle$:

$$\{|\psi_g\rangle = T(g)|\psi_0\rangle, g \in G\}\,. \tag{D.2}$$

Sets of generalized coherent states have common properties that follow from their construction.

[1] Using the Campbell-Hausdorff-Baker formula, the group operation is easily found: $\hat{D}(\alpha)\hat{D}(\beta) = e^{\frac{1}{2}(\alpha^*\beta + \alpha\beta^*)}\hat{D}(\alpha+\beta)$.

First, the irreducibility of the representation T of the group G implies the completeness of a set of coherent states in the representation Hilbert space $\mathcal{H}$. Indeed, any operator $T(g), g \in G$, transforms a coherent state in an other coherent state (by direct application of the group action). The set of coherent states is then stable under the group action and the subspace of $\mathcal{H}$ it generates is a subrepresentation of G. Since T is irreducible, this subspace is equal to $\mathcal{H}$ and the set of coherent states form a basis of $\mathcal{H}$. It also follows from the irreducibility of T that the integration of the projectors on coherent states over the whole family gives the identity operator, providing a so-called expansion of unity.

The basis of coherent states is actually overcomplete. This implies that the decomposition of a state of the Hilbert space in this basis is not unique. This also implies that coherent states are not orthogonal.

D.2 Spin coherent states

The best known application of this construction is the set of so-called spin coherent states [106]. Let us consider the Hilbert space $\mathcal{H}^J$ of a particle of total spin J ($J > 0$). The operators $\hat{J}_\pm = \hat{J}_x \pm i\hat{J}_y$ and $\hat{J}_0 = \hat{J}_z$ verify the commutation relations $[\hat{J}_0, \hat{J}_\pm] = \pm\hat{J}_\pm$ and $[\hat{J}_+, \hat{J}_-] = 2\hat{J}_0$ and so generate a Lie algebra. The associated Lie group is the group of three-dimensional rotations $SO(3)$, and the set of operators obtained by exponentiation of the three generators $\hat{J}_{\pm,0}$ form an irreducible unitary representation T^J of this group on the Hilbert space $\mathcal{H}^J$. The spin coherent states are generated by the action of the operators $T^J(g)$ on one fixed state which is conventionally chosen to be the state of maximal spin projection $|J, J\rangle$:

$$|\alpha\rangle = \hat{D}_J(\alpha)|J, J\rangle = e^{\alpha\hat{J}_+ - \alpha^\dagger\hat{J}_-}|J, J\rangle \tag{D.3}$$

where $\alpha \in \mathbb{C}$. The operator $\hat{D}_J(\alpha)$ represents one three-dimensional rotation. Only two real parameters are needed because the third one would only account for a global phase and we can forget it. Writing $\alpha = \frac{\theta}{2}e^{i\phi}$ we obtain

$$\hat{D}_J(\alpha) = e^{i\phi\hat{J}_z}e^{i\theta\hat{J}_y}. \tag{D.4}$$

The spin coherent state $|\alpha\rangle$ thus corresponds to the rotation of Euler angles (θ, ϕ) of the state $|J, J\rangle$, and so is the eigenstate with maximal eigenvalue of the projected spin operator $\hat{\mathbf{J}}.\mathbf{n}$, where $\mathbf{n}$ is the unit vector defined by θ and ϕ.

This construction can be extended to a system of N particles. The Hilbert space is then the Fock space of total particule number N, that is a JN-dimensional irreducible representation space for the $SO(3)$ group.

Another family of coherent states is formed of the nematic (or polar) states that we introduced in chapter 1 and 3 for a spin $J = 1$. These states are indeed generated by the action of all the three-dimensional rotation operators to a fixed state, here the state of zero spin projection $|J, 0\rangle$. This similar construction explains that these two sets of states share important properties. However, the difference in the reference state alone has important consequences that led us not to use the nematic states, as we will explain in the following.

D.3 $SU(3)$ coherent states

We now apply the previous method to the $SU(3)$ group. The Lie group $SU(3)$ is formed of the set of 3×3 unitary matrices in $\mathbb{C}$ with determinant equal to one, and so corresponds to all the basis transformations of a three-level system, which makes it the natural symmetry group to study spin-1 particles. From now on we restrict to the case of spin 1 and identify the standard basis of $\mathbb{C}^3$ with the single-particle basis $\{|+1\rangle, |0\rangle, |-1\rangle\}$. The Lie algebra associated to $SU(3)$ is spanned by six generators $s_{ij} = |i\rangle\langle j|$ with $i \neq j$ and two diagonal ones s_{ii} (it is of dimension 8 because of the requirement that the determinant is one). The elements of $SU(3)$ are then obtained by exponentiation of these generators. Actually each element g of $SU(3)$ accepts a decomposition of the form [107]:

$$g = b_- \times d \times b_+ \tag{D.5}$$

where d is a diagonal matrix and b_- and b_+ are respectively lower and upper triangular matrices with unit diagonal elements:

$$b_-(\gamma) = \exp\left(\gamma_1 s_{0,-1} + \gamma_2 s_{+1,0} + (\gamma_3 - \frac{1}{2}\gamma_1\gamma_2)s_{+1,-1}\right) = \begin{pmatrix} 1 & 0 & 0 \\ \gamma_1 & 1 & 0 \\ \gamma_3 & \gamma_2 & 1 \end{pmatrix} \tag{D.6}$$

where we note $\gamma = (\gamma_1, \gamma_2, \gamma_3) \in \mathbb{C}^3$. The matrix b_+ is defined similarly (with three other complex parameters). The three matrices d, b_- and b_+ are generally not unitary. If we consider the Hilbert space describing the spin state of one spin-1 particle, then a trivial representation of $SU(3)$ acting on this space is given by $SU(3)$ itself and one generate a sets of coherent states by the action of all the elements g of this group on a chosen single-particle state. As for spin coherent states we take as reference state the state of maximal spin projection $|+1\rangle$. We note that because $s_{-1,0}|+1\rangle = s_{0,+1}|+1\rangle = s_{-1,+1}|+1\rangle = 0$, the operator of the form b_+ only acts as identity on $|+1\rangle$. Since besides the diagonal operator only amounts for a global phase, $SU(3)$ coherent states are defined by

$$|\psi(\gamma)\rangle = \frac{1}{\sqrt{\mathcal{N}}} b_-(\gamma)|+1\rangle \tag{D.7}$$

where $\mathcal{N}$ is a normalization constant. The parameter γ_2 only enters in the phase and can be ignored. We obtain the generic form

$$|\psi(\gamma)\rangle = \frac{1}{\sqrt{\mathcal{N}}} \begin{pmatrix} 1 \\ \gamma_1 \\ \gamma_3 \end{pmatrix} \tag{D.8}$$

with $\mathcal{N} = 1 + |\gamma_1|^2 + |\gamma_3|^2$.

We now consider a system of N spin-1 particles and take as Hilbert space the corresponding Fock space $\mathcal{H}^{(N)}$. Then N-particles coherent states are obtained by the same procedure, replacing the generators s_{ij} by their representation

$$S_{ij} = \sum_{n=1}^{N} s_{ij}^n \tag{D.9}$$

where s_{ij}^n acts as s_{ij} on particle number n and as identity on all the other particles. The reference state now becomes

$$|\psi_0\rangle = \frac{1}{\sqrt{N!}}(\hat{a}_{+1}^\dagger)^N|\text{vac}\rangle \tag{D.10}$$

and coherent states take the form

$$|\psi(\gamma)\rangle_N = \frac{1}{\sqrt{N!}}\left(\frac{1}{\sqrt{\mathcal{N}}}(\hat{a}^\dagger_{+1} + \gamma_1\hat{a}^\dagger_0 + \gamma_3\hat{a}^\dagger_{-1})\right)^N |\text{vac}\rangle \tag{D.11}$$

Since $SU(3)$ coherent states are generated by rotations of the mean-field state ψ_0, they are mean-field states. By performing a change of variables that we do not detail here, the previous expression can be recast in the more amenable form

$$|\psi(\gamma)\rangle_N = |N:\boldsymbol{\zeta}\rangle = \frac{1}{\sqrt{N!}}\left(\boldsymbol{\zeta}.\hat{a}^\dagger\right)^N |\text{vac}\rangle \tag{D.12}$$

where $\hat{a}^\dagger = (\hat{a}^\dagger_{+1}, \hat{a}^\dagger_0, \hat{a}^\dagger_{-1})^T$ and $\boldsymbol{\zeta}$ is a normalized complex vector. The operator $\boldsymbol{\zeta}.\hat{a}^\dagger$ creates one particle in the spin-1 state

$$|\boldsymbol{\zeta}\rangle = e^{i\phi_0}\begin{pmatrix} \sin(\theta)\cos(\nu)e^{i\phi_{+1}} \\ \cos(\theta) \\ \sin(\theta)\sin(\nu)e^{i\phi_{-1}} \end{pmatrix} \tag{D.13}$$

D.4 Diagonal representation of few-body operators in the $SU(3)$ coherent states basis

We here detail the derivation of the formula (D.17). We consider a k-body operator $\hat{O}^{(k)}$ in normal order acting in the Fock space of N spin-1 bosons:

$$\hat{O}^{(k)} = \hat{a}^\dagger_{i_1}\hat{a}^\dagger_{i_2}...\hat{a}^\dagger_{i_k}\hat{a}_{i_k}...\hat{a}_{i_1} \tag{D.14}$$

where $i_1, i_2, ..., i_k$ can take the value $+1, 0$ or -1. Using twice the expansion of unity (4.37) one find that this operator can be written in the coherent state basis:

$$\hat{O}^{(k)} = \int (d\boldsymbol{\zeta}\int \mathrm{d}\boldsymbol{\zeta'}\langle N:\boldsymbol{\zeta}|\hat{O}^{(k)}|N:\boldsymbol{\zeta'}\rangle|N:\boldsymbol{\zeta}\rangle\langle N:\boldsymbol{\zeta'}| \tag{D.15}$$

Using the relation (4.28) we calculate the matrix element

$$\langle N:\boldsymbol{\zeta}|\hat{O}^{(k)}|N:\boldsymbol{\zeta'}\rangle = N(N-1)...(N-k+1)\prod_{\lambda=1}^{k}\zeta^*_{i_\lambda}\zeta'_{i_\lambda}\langle N-k:\boldsymbol{\zeta}|N-k:\boldsymbol{\zeta'}\rangle \tag{D.16}$$

Because coherent states become quasi-orthogonal in the limit of large particle number and $k \ll N$, the scalar product $\langle N-k:\boldsymbol{\zeta}|N-k:\boldsymbol{\zeta'}\rangle$ reduces to a delta distribution and one obtains

$$\hat{O}^{(k)} \approx \int \mathrm{d}\boldsymbol{\zeta}\langle N:\boldsymbol{\zeta}|\hat{O}^{(k)}|N:\boldsymbol{\zeta}\rangle|N:\boldsymbol{\zeta}\rangle\langle N:\boldsymbol{\zeta}| \tag{D.17}$$

Appendix E

Spin fragmentation of Bose-Einstein condensates with antiferromagnetic interactions

We reproduce here the article published by our group:

- **Spin fragmentation of Bose-Einstein condensates with antiferromagnetic interactions**
  Luigi De Sarlo, Lingxuan Shao, Vincent Corre, Tilman Ziblod, David Jacob, Jean Dalibard and Fabrice Gerbier
  New Journal of Physics **15** (2013) 113039

New Journal of Physics
The open access journal for physics

Spin fragmentation of Bose–Einstein condensates with antiferromagnetic interactions

Luigi De Sarlo[1], Lingxuan Shao, Vincent Corre, Tilman Zibold, David Jacob, Jean Dalibard and Fabrice Gerbier[2]

Laboratoire Kastler Brossel, CNRS, ENS, UPMC, 24 rue Lhomond, F-75005 Paris, France
E-mail: fabrice.gerbier@lkb.ens.fr

New Journal of Physics **15** (2013) 113039 (18pp)
Received 2 July 2013
Published 19 November 2013
Online at http://www.njp.org/
doi:10.1088/1367-2630/15/11/113039

Abstract. We study spin fragmentation of an antiferromagnetic spin 1 condensate in the presence of a quadratic Zeeman (QZ) effect breaking spin rotational symmetry. We describe how the QZ effect turns a fragmented spin state, with large fluctuations of the Zeeman populations, into a regular polar condensate, where the atoms all condense in the $m = 0$ state along the field direction. We calculate the average value and variance of the population of the Zeeman state $m = 0$ to illustrate clearly the crossover from a fragmented to an unfragmented state. The typical width of this crossover is $q \sim k_B T/N$, where q is the QZ energy, T the spin temperature and N the atom number. This shows that the spin fluctuations are a mesoscopic effect that will not survive in the thermodynamic limit $N \to \infty$, but are observable for a sufficiently small atom number.

[1] Current address: SYRTE, Observatoire de Paris, CNRS, UPMC; 61 Avenue de l'Observatoire, 75014 Paris, France.
[2] Author to whom any correspondence should be addressed.

Content from this work may be used under the terms of the Creative Commons Attribution 3.0 licence. Any further distribution of this work must maintain attribution to the author(s) and the title of the work, journal citation and DOI.

© IOP Publishing Ltd and Deutsche Physikalische Gesellschaft

Contents

1. Introduction **2**
2. Single-mode description of spin-1 condensates **5**
3. Spectrum and eigenstates for $M = 0$ **5**
3.1. Continuum approximation for large q 6
3.2. Ground state 6
3.3. Excited states for $M = 0$ 7
4. Spin fragmentation at finite temperatures **8**
4.1. Spin fragmentation for $q = 0$ 9
4.2. Bogoliubov approximation for $q \neq 0$ 10
4.3. Comparison between the different approximations 11
5. Comparison with the broken-symmetry picture **12**
5.1. Zero temperature 12
5.2. Moments of N_0 at finite temperatures 14
6. Conclusion **15**
Acknowledgments **15**
Appendix A. Total spin eigenstates **16**
Appendix B. Continuum approximation **17**
References **17**

1. Introduction

The natural behavior of bosons at low enough temperatures is to form a Bose–Einstein condensate (BEC), i.e. a many-body state where one single-particle state becomes macroscopically occupied [1]. There are, however, situations where bosons can condense simultaneously in several single-particle states, forming a so-called *fragmented condensate*. Several examples are known, where fragmentation occurs due to orbital (Bose gases in optical lattices or in fast rotation) or to internal degeneracies (pseudo-spin-1/2 or spin-1 Bose gases). These examples have been reviewed in [2, 3].

The spin-1 Bose gas, first studied by Nozières and Saint James [4], is a striking example where fragmentation occurs due to rotational symmetry in spin space. For antiferromagnetic interactions of the form $V_{12} = g_s \mathbf{s}_1 \cdot \mathbf{s}_2$ between two atoms with spins $\mathbf{s}_1$ and $\mathbf{s}_2$ ($g_s > 0$), the many-body ground state is expected to be a spin singlet state [2, 5]. In such a state, the three Zeeman sublevels are occupied, leading to three macroscopic eigenvalues of the single-particle density matrix (instead of just one for a regular condensate). As pointed out in [2, 5, 6], the signature of fragmentation is then the occurrence of anomalously large fluctuations of the populations N_m in the Zeeman states $m = 0, \pm 1$ (see also [7, 8], where similar behavior is predicted in a pseudo-spin-1/2 system). In the singlet state, for instance, the expectation value and variance of N_0 are $\langle N_0 \rangle = N/3$ and $\Delta N_0^2 \approx 4N^2/45$, respectively ($N$ is the total number of particles). Such super-Poissonian fluctuations ($\Delta N_0^2 \propto \langle N_0 \rangle^2$) deviate strongly from the value expected for a single condensate or any ensemble without correlations where

$\Delta N_0^2 \propto \langle N_0 \rangle$.[3] It was pointed out by Ho and Yip [6] that such a state was probably not realized in typical experiments, due to its fragility toward any perturbation breaking spin rotational symmetry (see also [9–14]). In the thermodynamic limit $N \to \infty$, an arbitrary small symmetry-breaking perturbation is enough to favor a regular condensed state, where almost all the atoms occupy the same (spinor) condensate wave function and $\Delta N_0 \ll N$.

In this paper, we give a detailed analysis of the phenomenon of spin fragmentation for spin-1 bosons. Our analysis assumes the conservation of total magnetization m_z. The fact that magnetization is an (almost) conserved quantity follows from the rotational invariance of the microscopic spin exchange interaction, and from the isolation of atomic quantum gases from their environment. A key consequence is that in an external magnetic field B, the linear Zeeman effect only acts as an energy offset and does not play a role in determining the equilibrium state. The dominant effect of an applied magnetic field is a second-order (or quadratic) Zeeman energy, of the form $q(m^2 - 1)$ for a single atom in the Zeeman state with magnetic quantum number m.[4] The quadratic Zeeman (QZ) energy breaks the spin rotational symmetry, and favors a condensed state with $m = 0$ along the field direction. In [10–13], the evolution of the ground state with the QZ energy q was studied theoretically. Since experiments are likely to operate far from the ground state, it is important to understand quantitatively how the system behaves at finite temperatures. This is the main topic we address in this paper.

Our focus in this paper will be to calculate the first two moments (average value and variance) of N_0. These moments illustrate clearly the evolution of the system from fragmented to unfragmented and thus constitute the main experimental signature of fragmentation. The main findings are summarized in figure 1, where we plot the standard deviation of $n_0 = N_0/N$ in a q–T plane. Large fluctuations of the $m = 0$ state are observed for small q. We can distinguish three different regimes. For low $q \ll U_s/N^2$ and low temperatures $k_B T \ll U_s/N$ ($U_s \propto g_s$ is the spin interaction energy per atom), the system is close to the ground state in a regime we call 'quantum spin fragmented' [2, 5, 6, 12]. We also observe a thermal regime for $k_B T \gg Nq, U_s/N$ dominated by thermally populated excited states. We call this second regime 'thermal spin fragmented'. Finally, for q large enough and temperature low enough, the bosons condense into the single-particle state $m = 0$, forming a so-called 'polar' condensate [16, 17]. In this limit, $\langle N_0 \rangle \approx N$ and $\Delta N_0 \ll N$. We indicate this third regime as 'BEC $m = 0$' in figure 1.

The evolution from the fragmented, singlet condensate to an unfragmented condensate with increasing QZ energy q is similar to a well-known example in the literature on quantum magnetism, the Lieb–Matthis model of lattice Heisenberg antiferromagnets [18]. This model describes collective spin fluctuations of an Heisenberg antiferromagnet on a bipartite lattice. It constitutes a popular toy model for demonstrating the appearance of broken symmetry ground states in condensed matter [19–24]. The ground state of such system (in principle also a spin singlet) was found theoretically to evolve to a Néel state in the thermodynamic limit in the presence of an arbitrarily small *staggered* magnetic field (whose sign alternates from one site to the next). The underlying theory is close to the one presented here. An essential difference

[3] Note that the problem we discuss here is unrelated to the anomalous fluctuations of the *total* condensate number found for ideal gases in the grand canonical ensemble [1]. In this work, we assume implicitly the canonical ensemble, and study the fluctuations of the populations of individual Zeeman states discarding quantum and thermal depletion of the condensate.

[4] This second-order shift originates from the hyperfine coupling between electronic and nuclear spins, and corresponds to the second-order term in an expansion of the well-known Breit–Rabi formula for alkalis (see e.g. [15]).

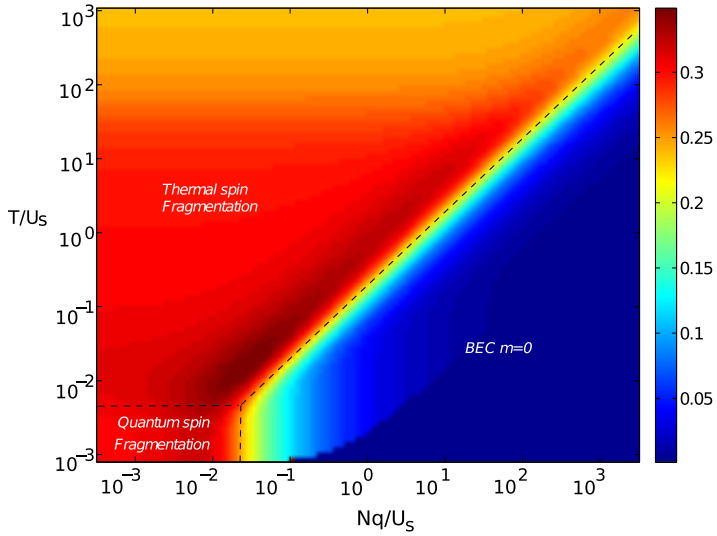

Figure 1. Standard deviation $\Delta n_0 = \Delta N_0/N$ of the population N_0 of the Zeeman state $m = 0$, normalized to the total atom number N. We mark three different regimes in the q–T plane. 'Spin fragmentation' refers to a fragmented spin state with large population fluctuations, where $\Delta n_0 \sim 1$. In the quantum regime ($Nq/U_s \ll 1/N$ and $k_B T/U_s \ll 1/N$), this is due to quantum fluctuations: the system is then close to the singlet ground state. In the thermal regime ($k_B T \gg Nq, U_s/N$), on the other hand, thermal fluctuations dominate over the quantum one and over the effect of the QZ energy. Conversely, 'BEC $m = 0$' refers to the atoms forming a regular polar condensate with almost all the atoms in $m = 0$, and $\Delta n_0 \ll 1$. The plot was drawn by numerically diagonalizing the Hamiltonian (1) and computing thermodynamic averages from the spectrum and eigenstates, using $N = 300$ particles. Note the logarithmic scales on both the horizontal and the vertical axis.

is that the present model of antiferromagnetic spin-1 BECs is expected to accurately describe actual experimental systems [25, 26]. In the antiferromagnet case, the staggered magnetic field is a theoretical object that cannot be produced in the laboratory for real solids. In contrast, the QZ energy is easily controllable in spin-1 BEC experiments. Another important difference is that experiments with ultracold quantum gases are typically conducted with relatively small atom numbers, from $N \sim 10^2$ to 10^6, so that the conclusions that hold in the thermodynamic limit do not necessarily apply and spin fragmentation can be observed experimentally.

The paper is organized as follows. In section 2, we present the basic model that describes an ensemble of spin-1 bosons with antiferromagnetic interactions condensing in the same orbital wave function irrespective of the internal state (single-mode approximation (SMA)). In section 3, we use the basis of total spin eigenstates (exact in the absence of an applied magnetic field, $q = 0$). We derive approximate solutions for the spectrum and eigenstates for $q > 0$ in section 3.1, and discuss how they evolve with increasing QZ energy. By using these results, we compute in section 4 the average value and variance of N_0 at finite temperatures, and compare the approximate solution to numerical diagonalization of the Hamiltonian. We finally present in section 5 an alternative approach, where the fragmented condensate is described as a statistical

mixture of mean-field (symmetry broken) states. We find excellent agreement with the exact diagonalization of the Hamiltonian.

2. Single-mode description of spin-1 condensates

We consider a gas of ultracold spin-1 bosons in a trap with Zeeman components $m = -1, 0$ or +1. We discuss the case of antiferromagnetic interactions and assume the validity of the SMA, i.e. that all bosons condense in the same spatial orbital irrespective of their internal state [27]. The Hamiltonian is [28]

$$\hat{H} = \frac{U_s}{2N}\hat{\mathbf{S}}^2 - q\hat{N}_0, \tag{1}$$

where $U_s > 0$ is the spin interaction energy per atom[5], $q > 0$ is the QZ energy, $\hat{\mathbf{S}}$ is the total spin operator and $\hat{N}_\alpha$ is the number operator in Zeeman state α. We assume that the number of atoms N is even for simplicity. Odd values of N could be treated in a similar way, without modifying the final results to order $1/N$. Typical experimental values for the parameters of the SMA model are $N = 10^3$–10^5, $U_s/k_B \sim 2$–5 nK, while q can be varied from zero to values much larger than U_s by changing the magnetic field [25, 26].

In the absence of an external magnetic field ($q = 0$), the Hamiltonian reduces to a quantum rotor with moment of inertia N/U_s [5, 11]. The energy eigenstates are thus simply the total spin eigenstates $|N, S, M\rangle$, with S the spin quantum number and M its projection on the z-axis. The corresponding eigenvalues are $E(S) = (U_s/2N)S(S+1)$, with a degeneracy $2S+1$. The wave functions for these states are known explicitly in the Fock basis [2, 5, 6] (see also appendix A).

When $q \neq 0$, since $[\hat{S}_z, \hat{N}_0] = 0$, the magnetic quantum number M (eigenvalue of $\hat{S}_z$) remains a good quantum number. One can diagonalize $\hat{H}$ by block in each M sector. For each M, the energy eigenstates can be expressed in the angular momentum basis

$$|\phi_M\rangle = \sum_{S=|M|}^{N} c_{S,M}|N, S, M\rangle. \tag{2}$$

To express the Hamiltonian in (1) in the $|N, S, M\rangle$ basis, we need to compute the action of $\hat{N}_0$. The non-vanishing matrix elements of $\hat{N}_0$ are $\langle N, S, M|\hat{N}_0|N, S, M\rangle$, $\langle N, S\pm 2, M|\hat{N}_0|N, S, M\rangle$ (see appendix A). The Schrödinger equation then takes the form of a tridiagonal matrix equation

$$h^M_{S,S+2}c_{S+2,M} + h^M_{S,S-2}c_{S-2,M} + h^M_{S,S}c_{S,M} = Ec_{S,M} \tag{3}$$

with E the energy eigenvalue and where the coefficients $h^M_{S,S'}$ are easily obtained from the expressions given in appendix A.

3. Spectrum and eigenstates for $M = 0$

A first approach for finding the spectrum and eigenstates is to diagonalize numerically the matrix h^M in (3). Our goal in this section is to propose an analytical approximation to better understand the structure of the spectrum and the eigenstates. The discussion allows one to describe how the

[5] The spin interaction energy U_s can be calculated from $U_s = g_s \int d\mathbf{x}|\psi(\mathbf{x})|^4$, where $\psi(\mathbf{x})$ is the spatial orbital of the condensate.

ground state evolves with q, and will also be useful to understand qualitatively the behavior of the systems at finite temperatures later in this paper. For simplicity, we focus in this section on the $M = 0$ sector. The conclusions we obtain remain qualitatively correct for $M \neq 0$ provided its value is not too large ($|M| \ll N$).

3.1. Continuum approximation for large q

We make the assumption that the thermodynamic behavior is dominated by states, such that the dominant coefficients in the $|N, S, M\rangle$ basis obey $1 \ll S \ll N$. As we will see later in this paper, this assumption is justified for large enough q at $T = 0$, and for any q at finite temperatures $k_B T \gg U_s/N$. In this limit, the matrix elements $h_{S,S}$, $h_{S,S\pm 2}$ can be simplified. We obtain to lowest order in $1/S$, S/N (see appendix B)

$$-J(x+\epsilon)c(x+\epsilon) - J(x-\epsilon)c(x-\epsilon) + \frac{NU_s}{2}x^2 c(x) = \left(E + \frac{Nq}{2}\right)c(x), \tag{4}$$

where we have set $x = S/N$, $\epsilon = 2/N$, $c(x) = c_{S,0}$. This equation maps the spin problem to a tight-binding model for a particle hopping on a lattice, with an additional harmonic potential keeping the particle near $x = 0$. The model is characterized by an inhomogeneous tunneling parameter $J(x) = Nq\,(1 - x^2/2)/4$ and a harmonic potential strength NU_s. Boundary conditions confine the particle to $0 \leqslant x \leqslant 1$.

If $c(x)$ changes smoothly as a function of x, the tight-binding model can be further simplified in a continuum approximation. We show in appendix B that the tight-binding equation reduces to the one for a fictitious one-dimensional harmonic oscillator

$$-\frac{q}{N}c''(x) + \frac{N}{4}(q + 2U_s)\,x^2 c(x) = (E + Nq)\,c(x). \tag{5}$$

The boundary condition $c(0) = 0$ selects the eigenstates of the standard harmonic oscillator with odd parity. The mass m and oscillation frequency ω of the fictitious oscillator are found from $\hbar^2/2m \equiv q/N$ and $m\omega^2 \equiv N(q + 2U_s)/2$. The oscillator frequency is thus

$$\hbar\omega = \sqrt{q(q + 2U_s)}. \tag{6}$$

This collective spectrum was also obtained by the Bogoliubov approach of [10, 12].

3.2. Ground state

In this section, we use the results established previously to examine the evolution of the ground state with increasing q. Our results reproduce the ones from [12] obtained by using a different method. The ground state of the truncated fictitious harmonic oscillator (with boundary condition $c_0(0) = 0$) is given by

$$c_0(x) = \frac{1}{\pi^{1/4}\sigma^{1/2}}\frac{x}{\sigma}\exp\left(-\frac{x^2}{2\sigma^2}\right) \tag{7}$$

with the quantum harmonic oscillator size

$$\sigma = \sqrt{\frac{\hbar}{m\omega}} = \sqrt{\frac{2}{N}}\left(\frac{q}{q + 2U_s}\right)^{1/4}. \tag{8}$$

The continuum approximation is valid only if $c(x)$ varies smoothly on the scale of the discretization step ϵ, or equivalently when $\sigma \gg 1/N$. This gives the validity criterion for this approximation

$$q \gg \frac{U_s}{N^2}. \tag{9}$$

For $q < U_s/N^2$, the ground state is very close to the singlet state, with a width $\sigma \ll 1/N$. Here, spin fragmentation occurs purely due to quantum spin fluctuations (related to antiferromagnetic interactions) of a polar BEC. We indicate this state in figure 1 as 'quantum spin fragmented'.

For $q \gg U_s/N^2$, the continuum approximation is valid. We see from (8) that as q increases, the QZ energy mixes an increasing number of S states. Asymptotically, for $q \gg U_s$, the true ground state is a superposition of $\sim N\sigma \approx \sqrt{2N}$ total spin eigenstates. In this regime, we can compute the moments of N_0 by expressing the depletion operator $N - \hat{N}_0$ in terms of the ladder operators $\hat{b}$ and $\hat{b}^\dagger$ associated with the fictitious harmonic oscillator. We find

$$N - \langle N_0 \rangle = \frac{U_s + q}{2\sqrt{q(q+2U_s)}}, \tag{10}$$

$$\Delta N_0^2 = \frac{U_s^2}{2q(q+2U_s)}. \tag{11}$$

For $U_s/N^2 \ll q \ll U_s$, the depletion $N - \langle N_0 \rangle$ and variance ΔN_0^2 are larger than unity but small compared to N, N^2, respectively, while for $q \gg U_s$, they become less than one particle: in the latter case, the ground state approaches the Fock state $(\hat{a}_0^\dagger)^N|\text{vac}\rangle$ expected from the mean field theory. We indicate both regimes as 'BEC $m = 0$' in figure 1, without marking the distinction.

3.3. Excited states for $M = 0$

We now turn to the description of the excited states, still limiting ourselves to the case $M = 0$ for simplicity. The tight-binding model (4) is characterized by a tunneling parameter $J = Nq(1 - x^2/2)/4$ and a harmonic potential strength $\kappa = NU_s$. Let us examine two limiting cases. For $q = 0$ (no hopping), the energy eigenstates coincide with the 'position' eigenstates with energy $E(S) \approx (U_s/2N)S^2$ for $S \gg 1$. Conversely, when $U_s = 0$ the energy eigenstates are delocalized states, which form an allowed energy band of width $\sim 4J \sim Nq$. The weak inhomogeneity of the tunneling parameter does not play a large role since these states are confined near $x = 0$ by the harmonic potential.

For the general case where J, $\kappa \neq 0$, the eigenstates can be divided into two groups [29, 30]:

- low-energy states with energy $E < 4J$, which are extended 'Bloch-like' states modified by the harmonic potential; the continuum approximation introduced earlier corresponds to an effective mass approximation, valid for low-energy states with $E \ll 4J = Nq$ (the requirement $q \gg U_s/N^2$ found before still holds); and
- high-energy states with $E \gg 4J$, that would be in the band gap in the absence of the potential energy term (and thus forbidden). They are better viewed as localized states, peaked around $x(E) \approx \sqrt{2E/NU_s}$ with a width $\sim 1/N$. As a result, they are very similar to the angular momentum eigenstates $|N, S, 0\rangle$ for the corresponding value of S. For these states, the continuum approximation does not hold.

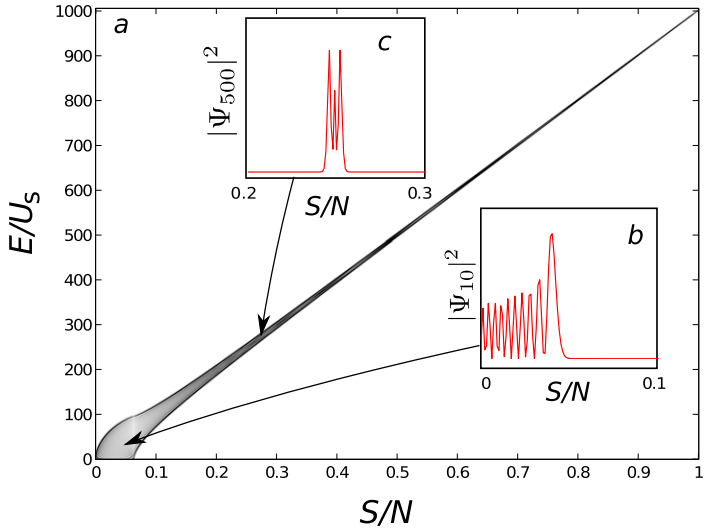

Figure 2. Probability densities (amplitude shown as gray scale) of the eigenstates of the spin-1 Hamiltonian (1) as a function of 'position' $x = S/N$ and energy E/U_s. The plot corresponds to $N = 2000$ and $Nq/U_s = 10$. At low energy, the eigenstates explore the whole available region, from the turning point down to $x = 0$. Conversely, at high energies, the eigenstates are more and more localized around the diagonal, as expected for potential energy eigenstates. We show as insets the probability densities for the 10th (b) and 500th (c) excited states for illustration.

We illustrate this classification in figure 2, where we show the probability densities $|c(S)|^2$ as a function of energy. One can see the change from a 'delocalized' regime at small energies to a 'localized' regime at large energies. The wave functions were calculated exactly by diagonalizing the Hamiltonian for $N = 1000$. We also show the corresponding energy spectrum in figure 3, showing the same crossover from delocalized states at low energies to localized states at high energies. For low energies, the spectrum is given by the harmonic oscillator model, $\epsilon_n \approx \hbar\omega(2n + 3/2)$ with n integer. For high energies, the energy eigenstates are localized around $x_n = n/N$, with a spectrum given by $\epsilon_n \approx U_s n^2/2N$ with n integer. Both expressions agree well with the numerical result in their respective domains of validity.

4. Spin fragmentation at finite temperatures

We have seen in section 3.2 that for a system in its ground state, the depletion and fluctuations of the $M = 0$ state were rapidly collapsing as q was increased above U_s/N^2, and the system turned from a fragmented to a single condensate with all the atoms in the Zeeman state $m = 0$. The energy gap to the first excited state is $3U_s/N$ near $q = 0$. For typical experimental values [25, 26], this corresponds to a few pK, vastly smaller than realistic temperatures for a typical experiment (a few tens of nK) due to the $1/N$ scaling. Therefore, it is natural to ask how the crossover from a fragmented to a single condensate is modified at finite temperatures. In the remainder of the paper, we thus consider the high temperature case $k_B T \gg U_s/N$. We will compute the first two moments of N_0 at finite temperatures, $\langle N_0\rangle_T$ and $(\Delta N_0^2)_T = \langle N_0^2\rangle_T - \langle N_0\rangle_T^2$, and use these quantities to study the fragmented to single condensate crossover.

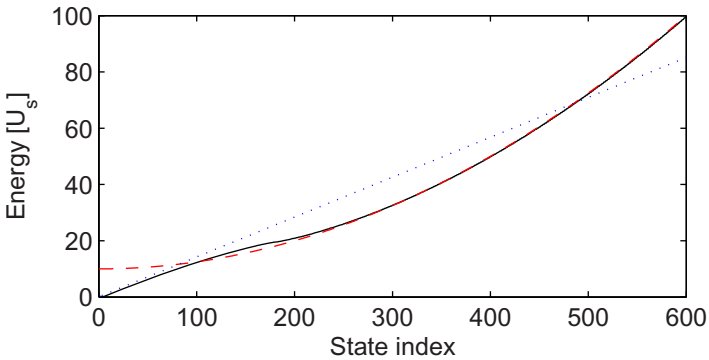

Figure 3. Energy spectrum for $N = 2000$ and $Nq/U_s = 10$. The black solid line is the spectrum calculated by numerical diagonalization of the Hamiltonian (1), shifted up by qN. The red dashed line corresponds to $E(S) = (U_s/2N)S^2 + qN/2$, the blue dotted line to the harmonic oscillator approximation.

4.1. Spin fragmentation for $q = 0$

Let us first consider the case $q = 0$. An important remark is that super-Poissonian fluctuations are not unique to the ground state, but also occur for low-energy eigenstates with $S \ll N$. This is best seen by considering values of S such that $1 \ll S \ll N$. In this limit, we find

$$\langle \hat{N}_0 \rangle_{SM} \approx (N^2 - S^2)(S^2 - M^2)/8, \tag{12}$$

$$\langle \hat{N}_0^2 \rangle_{SM} \approx (3N^2 - S^2)(S^2 - M^2)^2/8, \tag{13}$$

$$(\Delta N_0^2)_{SM} \approx (N^2 - S^2)(S^2 - M^2)^2/8, \tag{14}$$

where $\langle \hat{N}_0^p \rangle_{SM} = \langle N, S, M \mid N_0^{\mathrm{p}} \mid N, S, M \rangle$. Hence, we find super-Poissonian fluctuations for $M \ll S \ll N$, which eventually vanish as S (resp. M) increases to its maximum value N (resp. S).

We calculate now the thermally averaged $\langle n_0 \rangle_T$ and $(\Delta n_0^2)_T$ in the canonical ensemble. The average population in $m = 0$ is given by

$$\langle N_0 \rangle_T = \frac{1}{Z} \sum_{S,M} \mathrm{e}^{-\beta' S(S+1)} \langle N_0 \rangle_{SM}. \tag{15}$$

The second moment $\langle N_0^2 \rangle_T$ and the variance $(\Delta N_0^2)_T$ are given by similar expressions. Here, Z is the partition function and $\beta' = U_s/2Nk_{\mathrm{B}}T$. Assuming that the temperature is large compared to the level spacing ($k_{\mathrm{B}}T \gg U_s/N$), the thermodynamic sums over energy levels is dominated by states with large $S \gg 1$. There are two regimes to consider.

At intermediate temperatures, states with $1 \ll S \ll N$ dominate the thermodynamics. To calculate the thermal average over all S in this regime, we replace the discrete sums by integrals and send the upper bound N of the integral to infinity. A simple estimate of the mean value of S, $\langle S \rangle \sim (Nk_{\mathrm{B}}T/U_s)^{1/2}$, shows that the condition $1 \ll S \ll N$ corresponds to the boundaries

$$\frac{U_s}{N} \ll k_{\mathrm{B}}T \ll NU_s. \tag{16}$$

In this regime, we find

$$\langle N_0\rangle_T \approx \frac{N}{3}, \tag{17}$$

$$(\Delta N_0^2)_T = \langle N_0^2\rangle_T - \langle N_0\rangle_T^2 \approx \frac{4N^2}{45}, \quad k_\mathrm{B}T \ll NU_\mathrm{s}. \tag{18}$$

We note that to the leading order in $1/N$, the moments of N_0 are identical for those found in the singlet state.

The second regime arises when the temperature becomes very large ($k_\mathrm{B}T/NU_\mathrm{s} > 1$), where one expects the sum to saturate due to the finite number of states. In this limit, the upper bound of the integral cannot be taken to infinity, and one must take the restriction $S \leqslant N$ into account. On the other hand, the Boltzmann factor can be replaced by unity, and the sums can then be calculated analytically. One finds

$$(\Delta N_0^2)_{T\gg NU_\mathrm{s}} \approx N^2/18. \tag{19}$$

To summarize (see figure 1), for $q = 0$ we always find large depletion and super-Poissonian fluctuations ($\Delta N_0^2 \sim \langle N_0\rangle^2$). The average population is always $N/3$ as expected from the isotropy of the Hamiltonian. The relative standard deviation remains approximately constant (to order N) at the value $\Delta N_0/N \approx 2/3\sqrt{5} \approx 0.298$ for $k_\mathrm{B}T \ll NU_\mathrm{s}$, and changes to $1/3\sqrt{2} \approx 0.236$ for very large temperatures $k_\mathrm{B}T > NU_\mathrm{s}$ where all the states are occupied with equal probability.

4.2. Bogoliubov approximation for $q \neq 0$

For large $q > 0$ (and $\langle S_z\rangle$ constrained to vanish only in average), we expect that the system will form a condensate in the $m = 0$ Zeeman state, with small fluctuations. Such a system can be described in the Bogoliubov approximation (as described in the appendix of [12]), which extends to any M the harmonic oscillator approximation made earlier for the $M = 0$ sector. One sets $\hat{a}_0 \approx \sqrt{N_0}$, and expresses the fluctuations $\hat{a}_{\pm 1}$ in terms of new operators $\hat{\alpha}^\pm$,

$$\hat{\alpha}_\pm = u\hat{a}_{\pm 1} - v\hat{a}^\dagger_{\mp 1}. \tag{20}$$

Here, the Bogoliubov amplitudes u, v defined by

$$u \pm v = \left(\frac{q}{2U_\mathrm{s}+q}\right)^{\pm 1/4} \tag{21}$$

are chosen to put the Hamiltonian in diagonal form

$$H_\mathrm{Bogo} = \sum_{\mu=\pm} \hbar\omega\left(\hat{\alpha}^\dagger_\mu\hat{\alpha}_\mu + \frac{1}{2}\right) - (g+q). \tag{22}$$

The energy $\hbar\omega$ of the Bogoliubov mode is identical to the one previously found in the harmonic oscillator approximation for $M = 0$ (equation (6)). Note that we have now two such modes (instead of only one in the case $M = 0$).[6]

[6] We expect, in general, three modes of excitations for a spin-1 system. When the constraint of constant particle number is taken into account, this reduces the number of modes to two. The suppressed mode would correspond to the density fluctuations in an extended system, and is explicitly ruled out by the SMA. When a further constraint $M = 0$ is imposed, another mode is canceled—corresponding to magnetization fluctuations which are explicitly forbidden, thus leaving only one excitation mode.

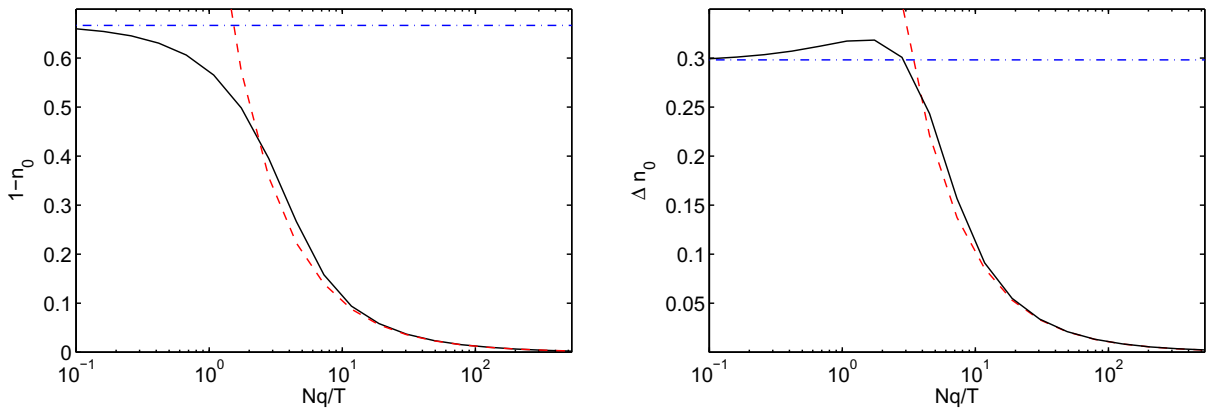

Figure 4. Depletion (left) and standard deviation (right) of N_0. The solid line shows the exact numerical result for $N = 1000$ and $T = 10U_s$, the blue dash-dotted line is the result calculated for $q = 0$ by using equations (17), (18) and the red dashed line shows the Bogoliubov approximation. Deviations are observed for $q/T \sim N$ (not visible at the scale of the figure), which is expected from our approximation: this regime corresponds to a depletion of one atom or less, and corrections $\propto 1/N$ that we neglect become important.

In the Bogoliubov approximation, the moments of N_0 can be obtained analytically. The quantum ($T = 0$) depletion of N_0 is smaller than one atom. The thermal part of the depletion and variance of $n_0 = N_0/N$ read for $k_B T \gg \hbar\omega$:

$$1 - \langle n_0 \rangle = \frac{2(U_s + q)}{q + 2U_s} \frac{k_B T}{Nq}, \tag{23}$$

$$\Delta n_0^2 = \frac{2\left[(U_s + q)^2 + U_s^2\right]}{(q + 2U_s)^2} \left(\frac{k_B T}{Nq}\right)^2. \tag{24}$$

The prefactors take values of order unity, and both the depletion $1 - \langle n_0 \rangle$ and standard deviation Δn_0 scale as $k_B T/Nq$. The above expressions are valid provided they describe small corrections to a regular polar condensate where almost all the atoms accumulate in $m = 0$ ($\langle n_0 \rangle = 1$), or in other words for temperatures

$$k_B T \ll Nq. \tag{25}$$

4.3. Comparison between the different approximations

We compare in figure 4 the predictions for the moments of N_0 obtained from the various approximations discussed in the paper, Bogoliubov approximation and $q = 0$ limit. These approximations are compared to the results obtained by diagonalization of the original Hamiltonian (1) and computing thermodynamic averages by using the exact spectrum and eigenstates.

When $Nq/k_B T \ll 1$, the localized states of section 3.3, which are dominated by their potential energy, will be populated. Since these localized states are close to the angular momentum eigenstates found in the $q = 0$ limit, to a good approximation the formula derived in section 4.1 (see (17), (18) and the continuous blue line in figure 4). On the other hand,

for $Nq/k_BT \gg 1$, thermal states mostly populate states with $E \sim qN$, i.e. 'delocalized' states within the low-energy 'Bloch band' of width $\sim Nq$. Those states correspond to small depletion and fluctuations, and they are well described by the Bogoliubov approximation presented in section 4.2 (see (23), (24) and the red dashed line in figure 4). The numerical solution of the original model (3) interpolates between the two well-defined asymptotic limits, either a thermal mixture of total spin eigenstates for $q \ll k_BT/N$ or a thermal state of Bogoliubov-like excitations for $q \gg k_BT/N$.

We note to conclude this section that in the regime $U_s/N \ll k_BT \ll NU_s$, the tight-binding model defined in equation (3) has a quasi-universal form at finite temperatures, in the sense that the model is entirely specified by two dimensionless parameters, for instance k_BT/U_s and Nq/U_s. We found that the physical quantities $\langle N_0\rangle$, (ΔN_0) depend only on their ratio Nq/k_BT, to a very good approximation. This quasi-universality, which can be explored by experiments, will be easily justified in the broken symmetry approach presented in the next section.

5. Comparison with the broken-symmetry picture

So far, we have treated the problem by the most natural method, by looking for the eigenspectrum of the Hamiltonian. Another approach [2, 3] to the problem of spin 1 bosons with antiferromagnetic interactions relies on the set of so-called polar or spin-nematic states, defined as

$$|N:\mathbf{\Omega}\rangle = \frac{1}{\sqrt{N!}}\left(\mathbf{\Omega}\cdot\hat{\mathbf{a}}\right)^N|\mathrm{vac}\rangle, \tag{26}$$

where the vector $\mathbf{\Omega}$ reads in the standard basis

$$\mathbf{\Omega} = \mathrm{e}^{\mathrm{i}\gamma}\begin{pmatrix} \frac{1}{\sqrt{2}}\sin(\theta)\mathrm{e}^{\mathrm{i}\phi} \\ \cos(\theta) \\ -\frac{1}{\sqrt{2}}\sin(\theta)\mathrm{e}^{-\mathrm{i}\phi}\end{pmatrix}. \tag{27}$$

For a single particle, the states $|\mathbf{\Omega}\rangle = \sum_{i=0,\pm1}\Omega_i|m=i\rangle$ form a continuous family of spin 1 wave functions with vanishing average spin. In fact, $|\mathbf{\Omega}\rangle$ is the eigenvector with zero eigenvalue of the operator $\mathbf{\Omega}\cdot\hat{\mathbf{s}}$, with $\hat{\mathbf{s}}$ the spin 1 operator. The states $|N:\mathbf{\Omega}\rangle$ correspond to a many-body wave function where all the particles occupy the single-particle state $|\mathbf{\Omega}\rangle$. As a result, one has $\langle N:\mathbf{\Omega}|\hat{\mathbf{S}}|N:\mathbf{\Omega}\rangle = 0$.

5.1. Zero temperature

It is interesting to connect the spin nematic states to the angular momentum eigenstates. The spin nematic states form an overcomplete basis of the bosonic Hilbert space. On writing the states $|N, S, M\rangle$ in this basis, one finds [2, 3, 12]

$$|N, S, M\rangle \propto \int \mathrm{d}\mathbf{\Omega}\; Y_{S,M}(\mathbf{\Omega})|N:\mathbf{\Omega}\rangle, \tag{28}$$

where Y_{SM} denotes the usual spherical harmonics and where $\mathrm{d}\mathbf{\Omega} = \sin(\theta)\mathrm{d}\theta\,\mathrm{d}\phi$. In particular, the singlet ground state $|N, 0, 0\rangle$ appears to be a coherent superposition with equal weights

The variance in the ensemble is thus super-Poissonian, and differs from the result in the exact ground state only by the sub-leading term $\propto N$. This is in agreement with the general statement made above.

5.2. *Moments of N_0 at finite temperatures*

We now extend the broken symmetry approach summarized above to finite temperatures. The density matrix should include a weight factor proportional to the energy of the states $|N:\Omega\rangle$. To the leading order in $1/N$, these states have zero interaction energy[7] and a mean QZ energy given by $-Nq\cos^2(\theta)$. In the spirit of the mean-field approximation, we replace the Boltzmann factor by its mean value and write the density matrix as

$$\hat{\rho}_{\mathrm{BS}} \approx \frac{1}{\mathcal{Z}} \int \mathrm{d}\mathbf{\Omega} |N:\mathbf{\Omega}\rangle\langle N:\mathbf{\Omega}| \mathrm{e}^{N\beta q \Omega_z^2} \tag{33}$$

with $\beta = 1/k_{\mathrm{B}}T$. The partition function can then be expressed as

$$\mathcal{Z} = \int_0^{2\pi} \mathrm{d}\phi \int_0^{\pi} \sin(\theta)\mathrm{d}\theta\ \mathrm{e}^{N\beta q\cos^2(\theta)} = 2\pi F_{-1/2}(N\beta q)\,. \tag{34}$$

Here, we introduced the family of functions

$$F_\alpha(y) = \int_0^1 x^\alpha\, \mathrm{e}^{yx}\, \mathrm{d}x, \tag{35}$$

which are related to the lower incomplete gamma functions. In a similar way, we can compute the moments of $n_0 = N_0/N$ to the leading order in N as

$$\langle n_0^m \rangle = \frac{F_{m-1/2}(N\beta q)}{F_{-1/2}(N\beta q)}. \tag{36}$$

From this result, one can easily deduce the average and variance of n_0. This calculation provides an explicit proof of the numerical evidence that, to the leading order in N, the moments of N_0 obey a universal curve depending only on $Nq/k_{\mathrm{B}}T$ and not on q/U_{s} or T/U_{s} separately.

From the properties of the functions F_α, we recover the results established in the previous section. When $x \to 0$, one finds $F_\alpha(x) \sim 1/(\alpha+1)$ and $\langle n_0^m \rangle \sim 1/(2m+1)$. By using this result we recover for $q=0$ the previous results, i.e. $\langle n_0 \rangle = 1/3$ and $\Delta n_0^2 = 4/45$. When $x \to \infty$, $F_\alpha(x) \sim \mathrm{e}^x/x \times [1-\alpha/x+\alpha(\alpha-1)/x^2]$. This leads to the asymptotic behavior $\langle n_0^m \rangle \sim 1 - m/(N\beta q) + m(m-3/2)/(N\beta q)^2 + \cdots$ when $N\beta q \gg 1$, which reproduces the Bogoliubov results (23), (24) for $q \ll U_{\mathrm{s}}$.[8]

We finally compare, in figure 5, the results from the broken symmetry approach to the results obtained by diagonalizing the Hamiltonian (1). We find excellent agreement between the two in the regime of thermal fragmentation, supporting the picture of mean-field states with random orientation fluctuating from one realization to the next. We note that the ansatz (33) for the density matrix is by no means obvious, and the good agreement with the numerical results is obtained only because the set of polar states is a good description for sufficiently

[7] Explicitly, one has $\langle N:\mathbf{\Omega}|\hat{\mathbf{S}}^2|N:\mathbf{\Omega}\rangle = N(1+\cos^2(\theta))$, so that the interaction energy of the state $|N:\mathbf{\Omega}\rangle$ is given by $U_{\mathrm{s}}\cos^2(\theta) \sim \mathcal{O}(1)$ compared to the QZ energy $\sim \mathcal{O}(N)$. The same argument applies to the off-diagonal matrix elements $\langle N:\mathbf{\Omega}'|\hat{\mathbf{S}}^2|N:\mathbf{\Omega}\rangle$.

[8] For $q \gg U_{\mathrm{s}}$, the depletion and standard deviation of $\hat{n}_0$ are of the order $1/N$, of the same order as the error made by using the broken symmetry approach.

The variance in the ensemble is thus super-Poissonian, and differs from the result in the exact ground state only by the sub-leading term $\propto N$. This is in agreement with the general statement made above.

5.2. *Moments of N_0 at finite temperatures*

We now extend the broken symmetry approach summarized above to finite temperatures. The density matrix should include a weight factor proportional to the energy of the states $|N:\Omega\rangle$. To the leading order in $1/N$, these states have zero interaction energy[7] and a mean QZ energy given by $-Nq\cos^2(\theta)$. In the spirit of the mean-field approximation, we replace the Boltzmann factor by its mean value and write the density matrix as

$$\hat{\rho}_{\mathrm{BS}} \approx \frac{1}{\mathcal{Z}} \int \mathrm{d}\mathbf{\Omega} |N:\mathbf{\Omega}\rangle\langle N:\mathbf{\Omega}| \mathrm{e}^{N\beta q \Omega_z^2} \tag{33}$$

with $\beta = 1/k_{\mathrm{B}}T$. The partition function can then be expressed as

$$\mathcal{Z} = \int_0^{2\pi} \mathrm{d}\phi \int_0^{\pi} \sin(\theta)\mathrm{d}\theta\ \mathrm{e}^{N\beta q\cos^2(\theta)} = 2\pi F_{-1/2}(N\beta q)\,. \tag{34}$$

Here, we introduced the family of functions

$$F_\alpha(y) = \int_0^1 x^\alpha\, \mathrm{e}^{yx}\, \mathrm{d}x, \tag{35}$$

which are related to the lower incomplete gamma functions. In a similar way, we can compute the moments of $n_0 = N_0/N$ to the leading order in N as

$$\langle n_0^m \rangle = \frac{F_{m-1/2}(N\beta q)}{F_{-1/2}(N\beta q)}. \tag{36}$$

From this result, one can easily deduce the average and variance of n_0. This calculation provides an explicit proof of the numerical evidence that, to the leading order in N, the moments of N_0 obey a universal curve depending only on $Nq/k_{\mathrm{B}}T$ and not on q/U_{s} or T/U_{s} separately.

From the properties of the functions F_α, we recover the results established in the previous section. When $x \to 0$, one finds $F_\alpha(x) \sim 1/(\alpha+1)$ and $\langle n_0^m \rangle \sim 1/(2m+1)$. By using this result we recover for $q=0$ the previous results, i.e. $\langle n_0 \rangle = 1/3$ and $\Delta n_0^2 = 4/45$. When $x \to \infty$, $F_\alpha(x) \sim \mathrm{e}^x/x \times [1-\alpha/x+\alpha(\alpha-1)/x^2]$. This leads to the asymptotic behavior $\langle n_0^m \rangle \sim 1 - m/(N\beta q) + m(m-3/2)/(N\beta q)^2 + \cdots$ when $N\beta q \gg 1$, which reproduces the Bogoliubov results (23), (24) for $q \ll U_{\mathrm{s}}$.[8]

We finally compare, in figure 5, the results from the broken symmetry approach to the results obtained by diagonalizing the Hamiltonian (1). We find excellent agreement between the two in the regime of thermal fragmentation, supporting the picture of mean-field states with random orientation fluctuating from one realization to the next. We note that the ansatz (33) for the density matrix is by no means obvious, and the good agreement with the numerical results is obtained only because the set of polar states is a good description for sufficiently

[7] Explicitly, one has $\langle N:\mathbf{\Omega}|\hat{\mathbf{S}}^2|N:\mathbf{\Omega}\rangle = N(1+\cos^2(\theta))$, so that the interaction energy of the state $|N:\mathbf{\Omega}\rangle$ is given by $U_{\mathrm{s}}\cos^2(\theta) \sim \mathcal{O}(1)$ compared to the QZ energy $\sim \mathcal{O}(N)$. The same argument applies to the off-diagonal matrix elements $\langle N:\mathbf{\Omega}'|\hat{\mathbf{S}}^2|N:\mathbf{\Omega}\rangle$.

[8] For $q \gg U_{\mathrm{s}}$, the depletion and standard deviation of $\hat{n}_0$ are of the order $1/N$, of the same order as the error made by using the broken symmetry approach.

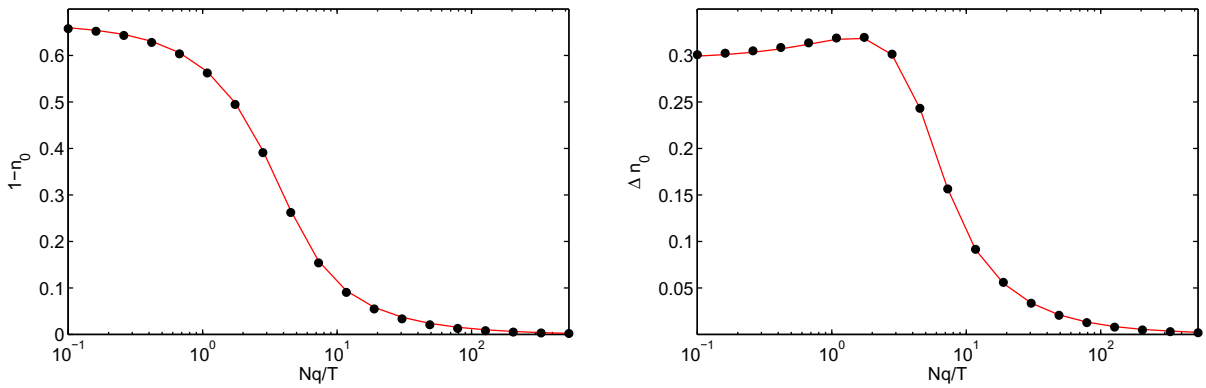

Figure 5. Exact diagonalization (red solid line) versus broken symmetry approach (black dots) for $N = 1000$, $k_B T/U_s = 10$.

low temperatures: although these states are not true eigenstates of the Hamiltonian (1), the action of $\hat{H}$ yields off-diagonal matrix elements scaling as $1/N$ [31], and thus vanishing in the thermodynamic limit. At high temperatures ($k_B T \sim N U_s$), where all the high-energy states are populated the broken-symmetry ansatz is no longer adequate.

6. Conclusion

We have studied the properties of an ensemble of antiferromagnetic spin-1 bosons with QZ energy breaking the spin rotational symmetry. The system evolves with increasing QZ energy from a super-fragmented condensate with large fluctuations to a regular polar condensate where the atoms condense in $m = 0$. We focused, in particular, on the behavior of a thermal mixture of excited states, and discussed the evolution of the moments of N_0 with increasing q. Two approaches were explored, one relying on the diagonalization of the Hamiltonian (either exactly or approximately in certain parameter regimes), and the other relying on a broken symmetry picture where the system is described as a statistical mixture of degenerate polar condensates. Both approaches were found in remarkable agreement. In this paper, we focused on the equilibrium properties and assumed thermal equilibrium from the start. An interesting question is how the physical system (i.e. also including the dynamics of non-condensed modes not described in the SMA) can reach such an equilibrium state, e.g. following a quench in q [32]. This problem, which can be linked to the more general question of thermalization of closed quantum systems [33], provides an interesting direction for future work.

Acknowledgments

We acknowledge discussions with members of the LKB, in particular Yvan Castin. This work was supported by IFRAF, by Ville de Paris (Emergences project) and by DARPA (OLE project).

Appendix A. Total spin eigenstates

The general expression of the states $|N, S, M\rangle$ in the Fock basis is

$$|N, S, M\rangle = \frac{1}{\sqrt{\mathcal{N}}}(\hat{S}^{(-)})^P(\hat{A}^\dagger)^Q(\hat{a}^\dagger_{+1})^S|\text{vac}\rangle. \tag{A.1}$$

Here, $P = S - M$, $2Q = N - S$, $\hat{S}_-$ is the spin lowering operator and $\hat{A}^\dagger = \hat{a}^\dagger_0 - 2\hat{a}^\dagger_{-1}\hat{a}^\dagger_{+1}$ is the singlet creation operator. The two operators commute. The normalization constant reads

$$\mathcal{N} = \frac{S!(N-S)!!(N+S+1)!!(S-M)!(2S)!}{(2S+1)!!(S+M)!}, \tag{A.2}$$

where !! indicates a double factorial.

The action of $\hat{a}_0$ on the angular momentum eigenstates is

$$\hat{a}_0|N, S, M\rangle = \sqrt{A_-(N, S, M)}|N-1, S-1, M\rangle + \sqrt{A_+(N, S, M)}|N-1, S+1, M\rangle, \tag{A.3}$$

where $\hat{a}_0$ is the annihilation operator of a boson in the Zeeman state $m = 0$, and where the coefficients $A_\pm$ are given by

$$A_-(N, S, M) = \frac{(S^2 - M^2)(N+S+1)}{(2S-1)(2S+1)}, \tag{A.4}$$

$$A_+(N, S, M) = \frac{((S+1)^2 - M^2)(N-S)}{(2S+1)(2S+3)}. \tag{A.5}$$

The non-zero matrix elements of $\hat{N}_0$ are

$$\langle S|\hat{N}_0|S\rangle = (A_+(N, S, M) + A_-(N, S, M)), \tag{A.6}$$

$$\langle S+2|\hat{N}_0|S\rangle = \sqrt{A_-(N, S+2, M)A_+(N, S, M)}, \tag{A.7}$$

$$\langle S-2|\hat{N}_0|S\rangle = \sqrt{A_+(N, S-2, M)A_-(N, S, M)}, \tag{A.8}$$

where we abbreviated the notation for the state $|N, S, M\rangle$ as $|S\rangle$ to simplify the notation. We then obtain the matrix elements of $\hat{H}_0$ in the $|N, S, M\rangle$ basis as

$$h^M_{S,S} = \frac{U_s}{2N}S(S+1) - q\langle S|\hat{N}_0|S\rangle, \tag{A.9}$$

$$h^M_{S,S+2} = -q\langle S+2|\hat{N}_0|S\rangle, \tag{A.10}$$

$$h^M_{S,S-2} = -q\langle S-2|\hat{N}_0|S\rangle. \tag{A.11}$$

Appendix B. Continuum approximation

We expand the matrix elements $h_{S,S}$, $h_{S,S\pm2}$ to the first order in $1/S$, S/N, M^2/S^2, and obtain

$$h^{M}_{S,S\pm2} \approx \frac{N}{4}\left[1-\frac{M^2}{(S\pm1)^2}\right]-\frac{1}{8N}\left[(S\pm1)^2-M^2\right], \tag{B.1}$$

$$h^{M\neq0}_{S,S} \approx \frac{N}{2}\left(1-\frac{M^2}{S^2}\right), \quad h^{M=0}_{S,S} \approx \frac{N}{2}. \tag{B.2}$$

For $M=0$, we obtain

$$-\frac{Nq}{4}\left[\left(1-\frac{(x+\epsilon)^2}{2}\right)c_{S+2}+\left(1-\frac{(x-\epsilon)^2}{2}\right)c_{S-2}\right]+\frac{NU_s}{2}x^2c_S=\left(E+\frac{Nq}{2}\right)c_S, \tag{B.3}$$

where we have set $x=S/N$ and $\epsilon=2/N$. We now take the continuum limit, where $\epsilon \ll 1$ is taken as a discretization step and c_s becomes a continuous function $c(S)$. We write

$$\frac{N^2}{4}\left(c_{S+2}+c_{S-2}\right) \approx \Delta c(s)+\frac{N^2}{2}c(s). \tag{B.4}$$

By substituting in (B.4) and neglecting a term $\propto (qx^2/N)\Delta c$, we arrive at (5).

This derivation is valid as long as the relevant states are well localized around $x=0$. This is always the case in the ground state, which has a width at most $\sim 1/\sqrt{N}$ for $q \gg U_s$. For the thermal states, the width is $\sim \sqrt{k_BT/[N(2U_s+q)]}$, which gives the condition $k_BT \ll N(U_s+q)$. Finally, the cross-term $\propto (qx^2/N)\Delta c$ is of the order $2E_pE_cc/[N(2U_s+q)]$ in terms of the kinetic and potential energies E_c, E_p of the harmonic oscillator. In the thermal regime, a typical order of magnitude for this term is thus $(k_BT)^2/[N(2U_s+q)]$, small compared to the energy k_BT typical for the other terms we kept in the equation provided the condition above is fulfilled.

References

[1] Pitaevskii L and Stringari S 2003 *Bose Einstein Condensation* (Oxford: Oxford University Press)
[2] Castin Y and Herzog C 2001 *C. R. Acad. Sci. Paris* **2** 419–43
[3] Mueller E J, Ho T L, Ueda M and Baym G 2006 *Phys. Rev.* A **74** 033612
[4] Nozières P and Saint James D 1982 *J. Phys. France* **42** 1133–48
[5] Law C K, Pu H and Bigelow N P 1998 *Phys. Rev. Lett.* **81** 5257
[6] Ho T L and Yip S K 2000 *Phys. Rev. Lett.* **84** 4031
[7] Kuklov A B and Svistunov B V 2002 *Phys. Rev. Lett.* **89** 170403
[8] Ashhab S and Leggett A J 2003 *Phys. Rev.* A **68** 063612
[9] Zhou F 2001 *Phys. Rev. Lett.* **87** 080401
[10] Cui X, Wang Y and Zhou F 2008 *Phys. Rev.* A **78** 050701
[11] Barnett R, Sau J D and Das Sarma S 2010 *Phys. Rev.* A **82** 031602
[12] Barnett R, Hui H Y, Lin C H, Sau J D and Das Sarma S 2011 *Phys. Rev.* A **83** 023613
[13] Lamacraft A 2011 *Phys. Rev.* A **83** 033605
[14] Tasaki H 2013 *Phys. Rev. Lett.* **110** 230402
[15] Foot C 2005 *Atomic Physics* (Oxford: Oxford University Press)
[16] Ho T L 1998 *Phys. Rev. Lett.* **81** 742

[17] Ohmi T and Machida T 1998 *J. Phys. Soc. Japan* **67** 1822
[18] Leib E and Matthis D 1962 *J. Math. Phys.* **3** 749
[19] Kaiser C and Peschel I 1989 *J. Phys. A: Math. Gen.* **22** 4257
[20] Kaplan T A, von der Linden W and Horsch P 1990 *Phys. Rev.* B **42** 4663–9
[21] Bernu B, Lhuillier C and Pierre L 1992 *Phys. Rev. Lett.* **69** 2590–3
[22] Azaria P, Delamotte B and Mouhanna D 1993 *Phys. Rev. Lett.* **70** 2483–6
[23] van Wezel J, van den Brink J and Zaanen J 2005 *Phys. Rev. Lett.* **94** 230401
[24] van Wezel J, Zaanen J and van den Brink J 2006 *Phys. Rev.* B **74** 094430
[25] Black A T, Gomez E, Turner L D, Jung S and Lett P D 2007 *Phys. Rev. Lett.* **99** 070403
[26] Jacob D, Shao L, Corre V, Zibold T, De Sarlo L, Mimoun E, Dalibard J and Gerbier F 2012 *Phys. Rev.* A **86** 061601
[27] Yi S, Müstecaplıoğlu Ö E, Sun C P and You L 2002 *Phys. Rev.* A **66** 011601
[28] Stamper-Kurn D M and Ueda M 2013 *Rev. Mod. Phys.* **85** 1191–244
[29] Hooley C and Quintanilla J 2004 *Phys. Rev. Lett.* **93** 080404
[30] Ott H, de Mirandes E, Ferlaino F, Roati G, Türck V, Modugno G and Inguscio M 2004 *Phys. Rev. Lett.* **93** 120407
[31] Anderson P W 1952 *Phys. Rev.* **86** 694–701
[32] Pu H, Law C K, Raghavan S, Eberly J H and Bigelow N P 1999 *Phys. Rev.* A **60** 1463–70
[33] Polkovnikov A, Sengupta K, Silva A and Vengalattore M 2011 *Rev. Mod. Phys.* **83** 863–83

Bibliography

[1] A Einstein. Quantentheorie des einatomigen idealen Gases. *Sitzungsberichte der Preussischen Akademie der Wissenschaften, Physikalisch-mathematische Klasse*, page 261, 1924.

[2] M. H. Anderson, J. R. Ensher, M. R. Matthews, C. E. Wieman, and E. A. Cornell. Observation of Bose-Einstein Condensation in a Dilute Atomic Vapor. *Science*, 269:198–201, 1995.

[3] K. B. Davis, M. O. Mewes, M. R. Andrews, N. J. van Druten, D. S. Durfee, D. M. Kurn, and W. Ketterle. Bose-Einstein Condensation in a Gas of Sodium Atoms. *Physical Review Letters*, 75(3969), 1995.

[4] P. Kapitza. Viscosity of liquid Helium below the λ-point. *Nature*, 141:74, 1938.

[5] V.F. Sears and E.C. Svensson. Pair Correlations and the Condensate Fraction in Superfluid ^{4}He. *Physical Review Letters*, 43:2009–2012, 1979.

[6] M. R. Andrews, H. J. Townsend, H. J. Miesner, D. S. Durfee, D. M. Kurn, and W. Ketterle. Observation of Interference between two Bose-Einstein Condensates. *Science*, 275(637), 1997.

[7] A. P. Chikkatur, Y. Shin, A. E. Leanhardt, D. Kielpinski, E. Tsikata, T. L. Gustavson, D. E. Pritchard, and W. Ketterle. A continuous surce of Bose-Einstein condensed atoms. *Science*, 296(5576), 2002.

[8] K. W. Madison, F. Chevy, W Wohlleben, and J. Dalibard. Vortex formation in a stirred Bose-Einstein condensate. *Physical Review Letters*, 84:806–809, 2000.

[9] B. DeMarco and D.D. Jin. Onset of Fermi degeneracy in a trapped atomic gas. *Science*, 285(1703), 1999.

[10] A. Truscott, K. Strecker, W. McAlexander, G. Partridge, and R. G. Hulet. Observation of Fermi pressure in a gas of trapped atoms. *Science*, 291(2570), 2001.

[11] J. Cubizolles, T Bourdel, S. J. J. M. F. Kokkelmans, G. V. Shyapnikov, and C Salomon. Production of Long-Lived Ultracold Li_2 Molecules from a Fermi Gas. *Physical Review Letters*, 91(240401), 2003.

[12] M. W. Zwierlein, C. A. Stan, C. H. Schunck, S. M. F. Raupach, A. J. Kreman, and W. Ketterle. Condensation of pairs of fermionic atoms near a feschbach resonance. *Physical Review Letters*, 92(120403), 2004.

[13] A. L. Gaunt, T. F. Schmidutz, R. P. Gotlibovych, and Z. Hadzibabic. Bose-Einstein Condensation of Atoms in a Uniform Potential. *Physical Review Letters*, 110(200406), 2013.

[14] B. Paredes, Widera. A, V Murg, O Mandel, S Foelling, G. Cirac, G. V. Shlyapnikov, T. W. Hänsch, and I. Bloch. Tonks-Girardeau gas of ultracold atoms in an optical lattice. *Nature*, 429(6989):277–281, 2004.

[15] Zoran Hadzibabic, Peter Krüger, Marc Cheneau, Baptiste Battelier, and Jean Dalibard. Berezinskii-Kosterlitz-Thouless crossover in a trapped atomic gas. *Nature*, 441:1118–1121, 2006.

[16] M. Greiner, M. O. Mandel, T. Esslinger, T. W. Hänsch, and I. Bloch. Quantum phase transition from a superfluid to a Mott insulator in a gas of ultracold atoms. *Nature*, 415(39), 2002.

[17] T. Stöferle, H. Moritz, C. Schori, M. Köhl, and T. Esslinger. Transition from a strongly interacting 1d superfluid to a mott insulator. *Physical Review Letters*, 130403, 92.

[18] G. Roati, C. D'Errico, L. Fallani, M. Fattori, C. Fort, M. Zaccanti, G. Modugno, M. Modugno, and M. Inguscio. Anderson localization of a non-interacting Bose-Einstein condenate. *Nature*, 453:895–898, 2008.

[19] Julien Chabé, Gabriel Lemarié, Benoit Grémaud, Dominiue Delande, Pascal Szriftgiser, and Jean-Claude Garreau. Experimental Observation of the Anderson Metal-Insulator Transition with Atomic Matter Waves. *Physical Review Letters*, 101(255702), 2008.

[20] P. W. Anderson. Absence of diffusion in certain random lattices. *Physical Review*, 109:1492–1505, 1958.

[21] Juliette Billy, Vincent Josse, Zhanchun Zuo, Alain Bernard, Ben Hambrecht, Pierre Lugan, David Clément, Laurent Sanchez-Palencia, Philippe Bouyer, and Alain Aspect. Direct observation of Anderson localization of matter waves in a controlled disorder. *Nature*, 453:891–894, 2008.

[22] Lester Guttman and James R. Arnold. The Nonparticipation of ^{6}He in the Superfluidity of ^{4}He. *Physical Review*, 92(3), 1953.

[23] C. J. Myatt, E. A. Burt, R. W. Ghrist, E. A. Cornell, and C. E. Wieman. Production of Two Overlapping Bose-Einstein Condensates by Sympathetic Cooling. *Physical Review Letters*, 78(586), 1997.

[24] D. S. Hall, M. R. Matthews, J. R. Ensher, C. E. Wieman, and E. A. Cornell. Dynamics of Component Separation in a Binary Mixture of Bose-Einstein Condensates. *Physical Review Letters*, 81(4531), 1998.

[25] D. S. Hall, M. R. Matthews, C. E. Wieman, and E. A. Cornell. Measurement of Relative Phase in Two-Component Bose-Einstein Condensates. *Physical Review Letters*, 81(4532), 1998.

[26] F. Schreck, L. Khaykovich, K. L. Corwin, G. Ferrari, T Bourdel, J. Cubizolles, and C Salomon. Quasipure Bose-Einstein Condensate immersed in a Fermi Sea. *Physical Review Letters*, 87(080403), 2001.

[27] Z. Hadzibabic, C. A. Stan, K. Dieckann, S. Gupta, M. W. Zwierlein, A. Görlitz, and W. Ketterle. Two-Species Mixture of Quantum Degenerate Bose and Fermi Gases. *Physical Review Letters*, 88(160401), 2002.

[28] Wheatley. Experimental properties of superfluid ^{3}He. *Reviews of Modern Physics*, 47(415), 1975.

[29] Anthony J. Leggett. A theoretical description of the new phases of liquid ^{3}He. *Reviews of Modern Physics*, 48(357), 1976.

[30] Y. Liu, S Jung, Maxwell S. E., L.D. Turner, E. Tiesinga, and P.D. Lett. Quantum Phase Transitions and Continuum Observation of Spinor Dynamics in an Antiferromagnetic Condensate. *Physical Review Letters*, 102(125301), 2009.

[31] Wenxian Zhang, D. L. Zhou, M. S. Chang, M. S. Chapman, and L. You. Coherent spin mixing dynamics in a spin-1 atomic condensate. *Physical Review A*, 72(013602), 2005.

[32] Ming-Shien Chang, Qishu Qin, Wenxian Zhang, Li You, and Michael S. Chapman. Coherent spinor dynamics in a spin-1 Bose condensate. *Nature*, 1:111–116, 2005.

[33] C. Klempt, O. Topiv, G. Gebreyesus, M. Scherer, T. Henninger, P. Hyllus, W. Ertmer, L. Santos, and J. J. Arlt. Parametric Amplification of Vacuum Fluctuations in a Spinor Condensate. *Physical Review Letters*, 104(195303), 2010.

[34] J. Stenger, S. Inouye, D. M. Stamper-Kurn, H. J. Miesner, A. P. Chikkatur, and W. Ketterle. Spin domains in ground-state Bose-Einstein condensates. *Nature*, 396(6709):345–348, 1998.

[35] H. J. Miesner, D. M. Stamper-Kurn, J. Stenger, S. Inouye, A. P. Chikkatur, and W. Ketterle. Observation of metastable states in spinor Bose-Einstein condensates. *Physical Review Letters*, 82(2228), 1999.

[36] Yuki Kawaguchi and Masahito Ueda. Spinor Bose-Einstein Condensates. *Physics Reports*, 520:253–381, 2012.

[37] Ryan Barnett, Turner Ari, and Eugene Demler. Classifying Novel Phases of Spinor Atoms. *Physical Review Letters*, 97(180412), 2006.

[38] A. Sorensen, L. M. Duan, J. I. Cirac, and P. Zoller. Many-particle entanglement with Bose-Einstein condensates. *Nature*, 409(6816):63–66, 2001.

[39] L. M. Duan, J. I. Cirac, and P. Zoller. Quantum entanglement in spinor Bose-Einstein condensates. *Physical Review A*, 65(033619), 2002.

[40] Eva M. Bookjans, Christopher D. Hamley, and Michael S. Chapman. Strong spin correlations observed in atomic spin mixing. *Physical Review Letters*, 107(210406), 2011.

[41] B. Lücke, M. Scherer, J. Kruse, L. Pezzé, F. Deuretzbacher, P. Hyllus, O. Topic, J. Peise, W. Ertmer, J. Arlt, L. Santos, A. Smerzi, and C. Klempt. Twin matter waves for interferometry beyond the classical limit. *Science*, 334(6057):773–776, 2011.

[42] Emmanuel Mimoun. *Condensat de Bose-Einstein de Sodium dans un piège mésoscopique*. PhD thesis, Université Paris 6, 2010.

[43] A. Auffeves, P. Maioli, T. Meunier, S. Gleyzes, G. Nogues, M. Brune, J. M. Raimond, and S. Haroche. Entanglement of a mesoscopic field with an atom induced by photon graininess in a cavity. *Physical Review Letters*, 91(230405), 2003.

[44] D. Leibfried, E. Knill, S. Seidelin, J. Britton, R. B. Blakestad, J. Chiaverini, D.B. Hume, W. M. Itano, J. D. Jost, C. Langer, R. Ozeri, R. Reichle, and D. J. Wineland. Creation of a six-atom "Schrödinger cat" state. *Nature*, 438(7068):639–642, 2005.

[45] E. Mimoun, L. De Sarlo, J. J. Zondy, J. Dalibard, and F. Gerbier. Sum-frequency generation of 589 nm light with near-unit efficiency. *Opt. Express*, 16(18684), 2008.

[46] E. Mimoun, L. De Sarlo, D. Jacob, J. Dalibard, and F. Gerbier. Solid-state laser system for laser cooling of Sodium. *Applied Physics B: Lasers and Optics*, 99:31–40, 2010.

[47] David Jacob, Emmanuel Mimoun, Luigi De Sarlo, Martin Weitz, Jean Dalibard, and Fabrice Gerbier. Production of Sodium Bose-Einstein condensates in an optical dimple trap. *New Journal of Physics*, 13(065022), 2011.

[48] D. M. Stamper-Kurn, M. R. Andrews, A. P. Chikkatur, S. Inouye, H.-J. Miesner, J. Stenger, and W. Ketterle. Optical Confinement of a Bose-Einstein Condensate. *Physical Review Letters*, 80(2027), 1998.

[49] M. D. Barrett, J. A. Sauer, and M.S. Chapman. All-Optical Formation of an Atomic Bose-Einstein Condensate. *Physical Review Letters*, 87(010404), 2001.

[50] C. Gross, H. Strobel, T. Zibold, N. Bar-Gill, G. Kurizki, and M. K. Oberthaler. Atomic homodyne detection of continuous-variable entangled twin-atom states. *Nature*, 480:219–223, 2011.

[51] A.T. Black, E. Gomez, L.D. Turner, S Jung, and P.D. Lett. Spinor Dynamics in an Antiferromagnetic Spin-1 Condensate. *Physical Review Letters*, 99(070403), August 2007.

[52] Franco Dalfovo, Giorgini Stefano, Pitaevskii Lev P., and Sandro Stringari. Theory of Bose-Einstein condensation in trapped gases. *Review of Modern Physics*, 71(463), 1999.

[53] C. J. Pethick and H. Smith. *Bose-Einstein Condensation in Dilute Gases*. Cambridge University Press, 2001.

[54] Sandro Stringari. Collective Excitations of a trapped Bose-Condensed Gas. *Physical Review Letters*, 77(2360), 1996.

[55] Daniel A. Steck. Sodium D line data. available online at http://steck.us/alkalidata.

[56] Ivan H. Deutsch and Poul S. Jessen. Quantum control and measurement of atomic spins in polarization spectroscopy. *Optics Communications*, 283:681–694, 2010.

[57] S. Knoop, T. Schuster, R. Scelle, AI Trautmann, J. Appmeier, M. K. Oberthaler, E. Tiesinga, and E. Tiemann. Feschbach spectroscopy and analysis of the interaction potentials of ultracold sodium. *Physical Review A*, 83(042704), 2001.

[58] B. Pasquiou, E. Marchal, L. Vernac, O. Gorceix, and B. Laburthe-Tolra. Thermodynamics of a Bose-Einstein condensate with free magnetization. *Physical Review Letters*, 106(255303), 2011.

[59] R. Kaiser, C. Westbrook, F. David, D. M. Stamper-Kurn, and W. Ketterle. *Spinor Condensates and Light Scattering from Bose-Einstein Condensates*, volume 72. Springer Berlin / Heidelberg, 2001.

[60] D.M. Brink and C.V Sukumar. Majorana spin-flip transitions in a magnetic trap. *Physical Review A*, 74(035401), 2006.

[61] C.K. Law, H. Pu, and N.P. Bigelow. Quantum spins mixing in spinor Bose-Einstein condensates. *Physical Review Letters*, 81(24), 1998.

[62] Wenxian Zhang, Su Yi, and Li You. Mean-field ground state of spin-1 condensate in a magnetic field. *Physical Review A*, 74(033612), 2006.

[63] Weizhu Bao and Yongyong Cai. Mathematical theory and numerical methods for Bose-Einstein condensation. *Kinetic and Related Models*, 6:1–135, 2013.

[64] Fong Yin Lim and Weizhu Bao. Numerical methods for computing the ground state of spin-1 Bose-Einstein condensates in a uniform magnetic field. *Physical Review E*, 78(066704), 2008.

[65] Masahito Ueda. Many-body Theory of Dilute Bose-Einstein Condensates with Internal Degrees of Freedom. *Physical Review A*, 60:013601–013604, 2000.

[66] David Jacob. *Condensats de Bose-Einstein de spin 1: étude expérimentale avec des atomes de sodium dans un piège optique.* PhD thesis, Université Paris 6, 2012.

[67] Emmanuel Mimoun, Luigi De Sarlo, David Jacob, Jean Dalibard, and Fabrice Gerbier. Fast production of ultracold sodium gases using light-induced desorption and optical trapping. *Physical Review A*, 81(023631), 2010.

[68] Harold J. Metcalf and Peter van der Straten. *Laser Cooling and Trapping.* Springer-Verlag NY, 1999.

[69] Tin-Lun Ho. Spinor Bose Condensates in Optical Traps. *Physical Review Letters*, 81(742), 1998.

[70] Matthias Scholl. *Thèse en préparation.* PhD thesis, Université Paris 6, 2014.

[71] Y. Castin and R. Dum. Bose-Einstein Condensates in Time Dependent Traps. *Physical Review Letters*, 77(27), 1996.

[72] *Making, probing and understanding Bose-Einstein condensates*, 1999.

[73] J. M. Higbie, L. E. Sadler, S. Inouye, A. P. Chikkatur, S. R. Leslie, K. L. Moore, V. Savalli, and D. M. Stamper-Kurn. Direct Nondestructive Imaging of Magnetization in a Spin-1 Bose-Einstein Gas. *Physical Review Letters*, 95(050401), 2005.

[74] Jean-Louis Basdevant and Jean Dalibard. *Mécanique quantique, Cours de l'Ecole Polytechnique.* Editions de l'Ecole Polytechnique, 2002.

[75] G. Reinaudi, T. Lahaye, Z Wang, and D. Guéry-Odelin. Strong saturation absorption imaging of dense clouds of ultracold atoms. *Optics Letters*, 32(21), 2007.

[76] C. F. Ockeloen, A. F. Tauschinsky, R. J. C. Spreeuw, and S. Whitlock. Detection of small atom numbers through image processing. *Physical Review A*, 82(061606(R)), 2010.

[77] P. G. de Gennes and J. Prost. *The Physics of Liquid Crystals.* Oxford University Press, 1974.

[78] A. F. Andreev and I. A. Grishchuk. Spin nematics. *JETP*, 87:467–475, 1984.

[79] Eugene Demler and Daniel Podolsky. Properties and detection of spin nematic order in strongly correlated electron systems. *New Journal of Physics*, 7(59), 2005.

[80] J. Zaanen and Z. Nussinov. Stripe fractionalization: the quantum spin nematic and the Abrikosov lattice. *Physica Status Solidi b*, 236:332–339, 2003.

[81] Lingxuan Shao. *Theoretical and experimental study of an antiferromagnetic spin-1 Bose-Einstein condensates.* PhD thesis, Ecole Normal Supérieure Paris, 2014.

[82] Wenxian Zhang, Su Yi, and Li You. Bose-Einstein condensation of trapped interacting spin-1 atoms. *Physical Review A*, 70(043611), 2004.

[83] Yuki Kawaguchi, Nguyen Thanh Phuc, and P. Blair Blakie. Finite-temperature phase diagram of a spin-1 Bose gas. *Physical Review A*, 85(053611), 2012.

[84] J. M. McGuirk, D. M. Harber, H. J. Lewandowski, and E. A. Cornell. Normal-Superfluid Interaction Dynamics in a Spinor Bose Gas. *Physical Review Letters*, 91(150402), 2003.

[85] Erich J. Mueller, Tin-Lun Ho, Masahito Ueda, and Gordon Baym. Fragmentation of Bose-Einstein Condensates. *Physical Review A*, 74(033612), 2006.

[86] O. Penrose and L. Onsager. Bose-Einstein Condensation and Liquid Helium. *Physical Review*, 104(576), 1956.

[87] P. Nozières. *Bose-Einstein Condensation.* Cambridge University Press, 1995.

[88] Luigi De Sarlo, Lingxuan Shao, Vincent Corre, Tilman Zibold, David Jacob, Jean Dalibard, and Fabrice Gerbier. Spin fragmentation of Bose-Einstein condensates with antiferromagnetic interactions. *New Journal of Physics*, 15(113039), November 2013.

[89] Yvan Castin and Christopher Herzog. Bose-Einstein Condensates in symmetry breaking states. *C.R. Académie des sciences Paris*, 2(419-43), 2001.

[90] John R. Klauder and Bo-Sture Skagerstam. *Coherent States: Applications in Physics and Mathematical Physics.* World Scientific Publishing Company, 1985.

[91] A. M. Peremolov. Generalized coherent states and some of their applications. *Soviet Physics Uspekhi*, 20(9)(703), 1977.

[92] G. Yaffe, Laurence. Large N limits as classical mechanics. *Review of Modern Physics*, 54(2), 1982.

[93] Jasper van Wezel and Jeroen van den Brink. Spontaneous Symmetry Breaking in Quantum Mechanics. *American Journal of Physics*, 75:635–638, 2007.

[94] C. Kaiser and I. Peschel. Ground state properties of a quantum antiferromagnet with infinite-range interactions. *Journal of Physics A: Mathematical and General*, 22(4257), 1989.

[95] P. W. Anderson. An Approximate Quantum Theory of the Antiferromagnetic Ground State. *Physical Review*, 84(694), 1952.

[96] Laurent de Forges de Parny, Hongyu Yang, and Frédéric Mila. Anderson tower of states and nematic order of spin-1 bosonic atoms on a 2D lattice. arXiv:1403.2952v2, 2014.

[97] Gerhard Bohm and Günter Zech. *Introduction to Statistics and Data Analysis for Physicists*. Verlag Deutsches Elektronen-Synchroton.

[98] George I. Mias, Nigel R. Cooper, and S. M. Girvin. Quantum noise, scaling and domain formation in a spinor Bose-Einstein condensate. *Physical Review A*, 77(023616), 2008.

[99] Marcos Rigol, Vanja Dunjko, and Maxim Olshanii. Thermalization and its mechanism for generic isolated quantum systems. *Nature*, 452:854–858, 2008.

[100] Anatoli Polkovnikov, Krishendu Sengupta, Alessandro Silva, and Mukund Vengalattore. *Colloquium*: Nonequilibrium dynamics of closed interacting quantum systems. *Reviews of Modern Physics*, 83(863), 2011.

[101] Ryan Barnett, Anatoli Polkovnikov, and Mukund Vengalattore. Prethermalization in quenched spinor condensates. *Physical Review A*, 84(023606), 2011.

[102] Nguyen Thanh Phuc, Yuki Kawaguchi, and Masahito Ueda. Effects of thermal and quantum fluctuations on the phase diagram of a spin-1 ^{87}Rb Bose-Einstein condensate. *Physical Review A*, 84(043645), 2011.

[103] Dan M. Stamper-Kurn and Masahito Ueda. Spinor Bose gases: symmetries, magnetism and quantum dynamics. *Reviews of Modern Physics*, 85(1191), 2013.

[104] R. J. Glauber. The Quantum Theory of Optical Coherence. *Physical Review*, 130(2529), 1963.

[105] R. J. Glauber. Coherent and Incoherent States of the Radiation Field. *Physical Review*, 131(2766), 1963.

[106] J. M. Radcliffe. Some properties of coherent spin states. *Journal of Physics A: General Physics*, 4(313), 1971.

[107] Sven Gnutzmann and Marek Kus. Coherent states and the classical limit on irreducible SU_3 representations. *Journal of Physics A: Mathematical and General*, 31:9871–9896, 1998.